Calibration and use of the Petroelastic Model for 4D Seismic interpretation

Angel Eduardo Briceño Yañez

Thesis presented for the degree of Doctor of Philosophy.

Heriot-Watt Institute of Petroleum Engineering
School of Energy, Geoscience, Infrastructure and Society
Heriot-Watt University, Edinburgh. UK

June, 2017

Abstract

One of the major objectives of 4D studies is to understand and quantify changes in the seismic response, related to pressure and saturation changes in the reservoir. A key ingredient of such interpretation is the petroelastic model (PEM), which links fluid saturations and pore pressure changes in the reservoir rock to the elastic property changes required for seismic modelling, time-lapse feasibility studies, 4D inversion and also seismic history matching. Many previous studies have pointed out the difficulty of selecting a PEM, the challenges in calibrating the model to the in situ response, and in particular the uncertainties involved. In this work I study the use of different deterministic PEMs for simulator to seismic modelling. The models are applied to three fields in the UKCS, Norwegian Sea and offshore Brazil with distinctly different geological settings. For each model, the static components are calibrated against a range of wireline log data acquired prior to production using an optimization algorithm. The dependence on pressure change is then added separately using coefficients derived from core data in the laboratory. All PEMs for the clastic datasets as well for the carbonate reservoir, are found to yield similar responses making the choice of the "best" challenging; however even when an appropriate well calibrated model is used, it may not be adequate for time-lapse seismic studies. In addition, the large number of input parameters for each model makes the process of model fitting particularly non-unique. To reduce the input parameters for computing the time lapse seismic response a linear two parameter equation has been suggested which gives similar results to the multi-parameter models, specifically for an oil-water system. When working with maps of 4D seismic attributes in particular, the work presented in this research advocate that a simple model which is linear with respect to the pressure and saturation changes, and is "primed" by any conventional deterministic PEM may be an adequate alternative for time-lapse seismic interpretation.

The non-unique nature of the rock physics models, together with data and model uncertainties creates the need for time-consuming comparisons in the Seismic History Matching (SHM) workflow. This study presents a simple and interactive way of visualizing all of these uncertainties, whilst optimizing the SHM. It consists of a simple

cross-plot of all changes in water saturation and pore pressure between at least two time periods of interest in the reservoir history (usually pre-production baseline and a monitor) from the simulation model and colour coded based with the 4D seismic signature from the “predicted” models or “observed” data. Therefore it allow us to discriminate between regions in the reservoir that are dominated by pressure or saturation, from which a boundary line associated with the controlling parameters (C_P/C_S) from the simplified proxy model PEM can be drawn. Application to synthetic examples and field datasets verified the usefulness of this approach and the sensitivities to both data and the model.

This thesis is dedicated to my family

Acknowledgements

If you could only see my face while writing these words, there is a big smile and exhausted eyes, which summarises the perfect mix of emotions and feelings I have felt through my PhD, it was a roller coaster but I enjoyed it and I am so thankful for of the experience and for so many incredible people that were part of this journey, they supported me, they shared intellectual conversations with me, they laughed with me and probably I also ugly cried with them. You were all there being part of this journey, from my family, to my supervisor, my colleagues, my friends from back home and the ones I made here in Europe I only can say MUCHAS GRACIAS!

I am extremely grateful to my supervisor, Professor Colin MacBeth, your dedication to your students is admirable, thank you for giving me the opportunity to be part of the ETLP group and sharing your knowledge with me. Thank you for your patience and your unconditional support you are just an incredible person and role model. I also want to thank to Dr Maria Daphne Mangriotis, you are a mentor, you are a friend, you are one of my rocks in this group, and you believe in me. Honestly there are not enough words to express my gratitude towards both of you, Colin and Maria!

I thank the Edinburgh Time Lapse Project (ETLP) sponsors of Phase V and VI, for their support and for providing the datasets used in my research (BG, BP, Chevron, CGG, ConocoPhillips, ENI, ExxonMobil, Hess, Ikon Science, Landmark, Maersk, Nexen, Norsar, RSI, OMV, Petoro, Petrobras, Shell, Statoil, Suncor, TAQA, TGS and Total).

My dear colleagues from ETLP, I couldn't survive this journey without you guys, we had technical and intellectual discussions that made me expand my knowledge but also we bonded over our successes, and stressful times, complaining, lunch, coffee breaks and the list goes on. It wouldn't have been the same without mi pana (normally never use that word but he is special!) Ricardo, my fave Malaysian Chinese Ming, sweet Lu, Miss Niki, Phung that is unintentionally hilarious, Veronica the last few months we have been living in this office, David, Dennis and Justin. A special shout out to Dr Hamed Amini, you shared unselfishly all your knowledge with me, merci! Probably I have too many friends to thanks because even when this PhD scammed my social life I

still made time for a coffee or a glass of wine here and there, so really to my boo boos Marta, Sara, Gonzalo, Andrea, Clementyne, Stuart, Sarah, Nat and Colette you are my extended family here in Europe and the appreciation for you guys is endless.

Finally but not least, my family! Mamá te amo infinito gracias por el apoyo incondicional, eres mi inspiración. Papá gracias por llamarme todos los dias. Both of you taught me to be strong and independent and to deal with challenges in life! Mama Tati, Tia Caro, Mama Deya and Rita thank you so much for caring and loving me, you are all my rock and I am so lucky to have you all. Now I am finishing this short acknowledgment, the smile on my face is still there but now I have teary eyes.

Mil Gracias, and looking forward to the future…

Angel Briceño, 2017

Declaration Statement

ACADEMIC REGISTRY
Research Thesis Submission

Name*:*	Angel Eduardo Briceño Yañez		
School:	Energy, Geoscience, Infrastructure and Society		
Version: *(i.e. First, Resubmission, Final)*	Final	Degree Sought:	PhD, Petroleum Engineering

Declaration

In accordance with the appropriate regulations I hereby submit my thesis and I declare that:

1) the thesis embodies the results of my own work and has been composed by myself
2) where appropriate, I have made acknowledgement of the work of others and have made reference to work carried out in collaboration with other persons
3) the thesis is the correct version of the thesis for submission and is the same version as any electronic versions submitted*.
4) my thesis for the award referred to, deposited in the Heriot-Watt University Library, should be made available for loan or photocopying and be available via the Institutional Repository, subject to such conditions as the Librarian may require
5) I understand that as a student of the University I am required to abide by the Regulations of the University and to conform to its discipline.
6) I confirm that the thesis has been verified against plagiarism via an approved plagiarism detection application e.g. Turnitin.

* *Please note that it is the responsibility of the candidate to ensure that the correct version of the thesis is submitted.*

Signature of Candidate*:*		Date:	

Submission

Submitted By *(name in capitals):*	Angel Eduardo Briceño Yañez
Signature of Individual Submitting:	
Date Submitted:	

For Completion in the Student Service Centre (SSC)

Received in the SSC by *(name in capitals):*			
Method of Submission *(Handed in to SSC; posted through internal/external mail):*			
*E-thesis Submitted (**mandatory for final theses)***			
Signature:		Date:	

Table of Contents

Chapter 1

Introduction – The role of the Petroelastic Model in 4D seismic studies

This chapter focuses on the integration of 4D seismic and reservoir engineering for the practical interpretation of 4D data, with particular interest in the role of the petroelastic model. Challenges and uncertainties are identified, which set the stage for the development of this work.

1.1 Synergy between 4D Seismic and simulation model in Reservoir Management

Wiggins and Startzman (1990) define reservoir management as "that set of operations and decisions by which a reservoir is identified, measured, produced, developed monitored and evaluated, from its discovery through depletion and final abandonment". Ideal management requires up-to-date quantitative information throughout the entire reservoir. Access to the latest data, including 4D seismic technology as a surveillance tool, allows engineers to develop cost-effective strategies to optimize recovery and maximize profitability of the field at the lowest risk (Johnston 2013).

The concept behind time-lapse seismic is quite simple. The term 4D seismic expresses that calendar time represents the fourth dimension. Time-lapse consist of 3D seismic surveys repeated over certain production periods in order to monitor production changes in the reservoir. Production activities in hydrocarbon fields cause changes in reservoir parameters such as pore pressure, fluid saturation, temperature and even layer thickness in the presence of compacting reservoirs. All these changes will directly affect seismic properties, such as impedance, seismic wave travel time, reflection amplitudes, and seismic velocities. By comparing the differences in measurements of seismic properties, changes in the elasticity of the subsurface can be monitored over time through understanding of the principles of rock physics (Fanchi et al., 1999; Landrø 2015). Indeed, Time-lapse seismic shows great potential in reservoir monitoring and management for mapping bypassed oil, monitoring fluid contacts and injection fronts, identifying pressure compartmentalization, and characterizing the fluid-flow properties of faults (Lumley and Behrens 1998).

Reservoir elasticity is affected by different factors including lithology, fluid content, and changes in pore pressure. Velocity contains information on the fluid distribution in the reservoir. For example, the ratio of compressional to shear velocity (V_P/V_S) is related to porosity and fluid content in the pore space (Fanchi et al., 1999). Using 4D seismic to monitor the changes in reservoir elasticity can provide spatially resolved fluid changes inside the reservoir. This link yields useful information to improve the validity of fluid-flow models and the reservoir-management decisions that rely on simulation model forecasts (Waggoner et al., 2002).

Reservoir flow simulation modelling provides synthetic production profiles to generate cash flow forecasts (Fanchi 2006) as well as predict saturation and pressure distribution in the intra-well space as a function of production time. The predictions are based on explicit prior knowledge of the 3D flow model and they are history-matched to well production data. Nevertheless, such models are constructed from deterministic data, which are often sparse and hampered with a high degree of uncertainty (Little et al., 2006). The successful application of time-lapse seismic reservoir monitoring can provide unique information regarding the dynamic reservoir properties of the reservoir between wells. Therefore, the combination of 4D seismic and reservoir simulation offers an attractive scheme to reduce the uncertainty of the reservoir models and thereby prepare more accurate production forecasts.

1.2 Bringing together 4D seismic and reservoir engineering data

The success of 4D interpretation relies on the integration between the 4D seismic and reservoir engineering domain, such that they can be practically used by asset teams for field development. This is achieved by making 4D seismic an integral part of exploration, development and production stages throughout the field's lifecycle (figure 1.1). The exploration stage consists of discovery and appraisal activities, which are the main avenues for the assessment of 4D applicability. In the development stage, a more detailed 4D feasibility study can be carried out to estimate the possible chances of success for changes due to production to be seismically detected. The production stage focuses on enhancing the predictability of the reservoir model by matching its dynamic predictions to the observed 4D seismic data (figure 1.2). This phase involves petroelastic modelling, seismic forward modelling and inversion. This thesis sits between the two latter stages; specifically investigating and developing an effective rock physics model for time-lapse interpretation.

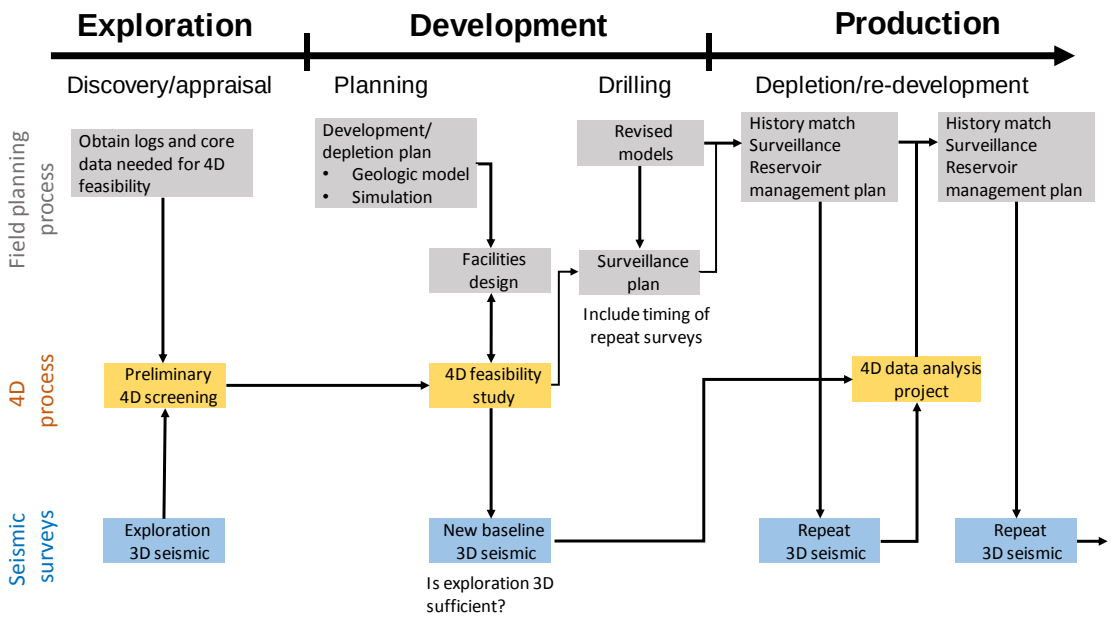

Figure 1.1 *4D Seismic data utility at different stages of a field lifecycle (after Johnston 2013)*

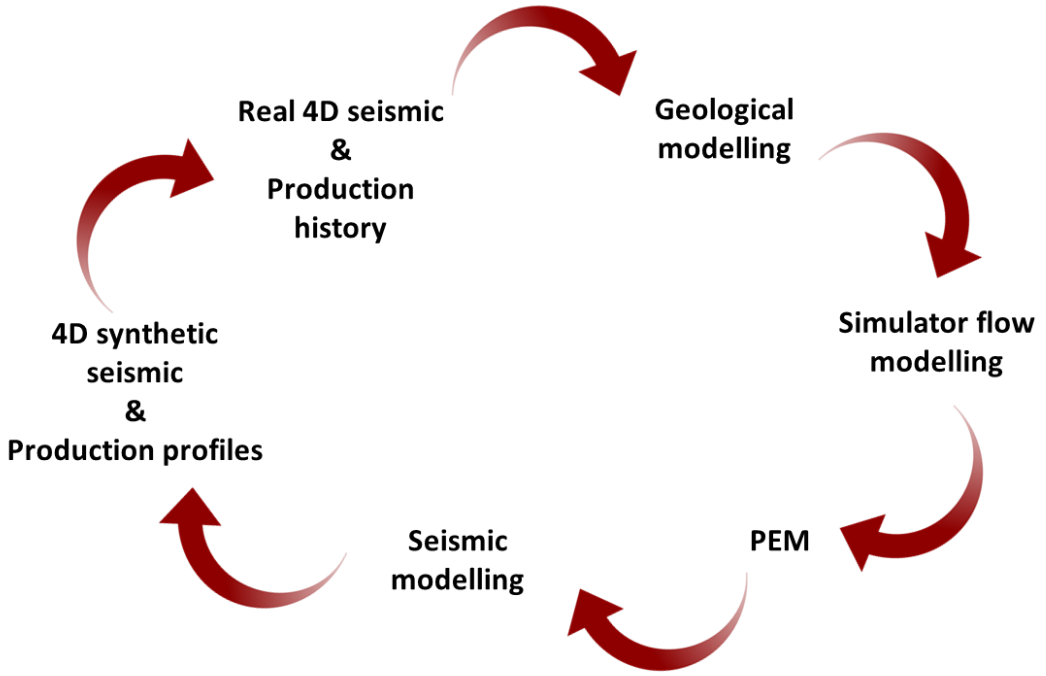

Figure 1.2 *Workflow for integrating geology, seismic and engineering data (after Landa and Kumar 2011)*

1.2.1 From qualitative to quantitative analysis of 4D seismic data

The integration of 4D seismic and engineering data has been primarily developed in a qualitative sense (Lumley and Behrens, 1998; Elde et al., 2000; Pagano et al., 2000; Hatchell et al., 2002; Pannett et al., 2004), through simple visualisation of the seismic signature compared to changes associated to production in the reservoir, mainly by mapping reservoir compartmentalization, identifying fluid contact movements or map flow paths and fault barriers. However, the interest and development towards a more quantitative use of time lapse seismic data in the reservoir modelling workflow has increased in the geoscience industry and research community. Linking reservoir flow simulator output data to seismic data is a step forward to go from qualitative analysis to quantitative analysis of dynamic changes within the reservoir (Waggoner, 1998a). This requires solid understanding of the relationship between reservoir rock and fluid parameters with the seismic response.

A fundamental element in evaluating time-lapse seismic data involves the comparison of observed seismic differences with predicted seismic differences generated from multiple possible reservoir model scenarios, thereby constraining the latter (Floricich 2006). This process of making time-lapse observations and updating the model is referred to as closing-the-loop (Waal and Calvert 2003). The growth of history matching involving not only production data but also 4D seismic data is a very active field (Gosselin et al. 2003; Lygren et al. 2005; Roggero et al. 2007; Landa and Kumar 2011; Alerini et al. 2014; Obidegwu 2015; Trani et al. 2017). This integration helps to add lateral constraints of the final reservoir model solutions and improve the reliability of production forecasts (Walker et al. 2006). Seismic history matching (SHM) closes the loop and minimizes the misfit between the observed data and that predicted by the reservoir model (figure 1.3) as a result of incorporating production and time-lapse data. In general the 4D seismic data response can be delivered in different form or levels in the time or depth domains, including seismic amplitudes, impedances and pressure and fluid saturation. Indeed the comparison of misfits between “observed” and “predicted” models in the SHM loop can be measured at any of the levels previously mentioned across the seismic and reservoir-engineering domains, as illustrated in figure 1.4, each level has associated its own challenges and uncertainties.

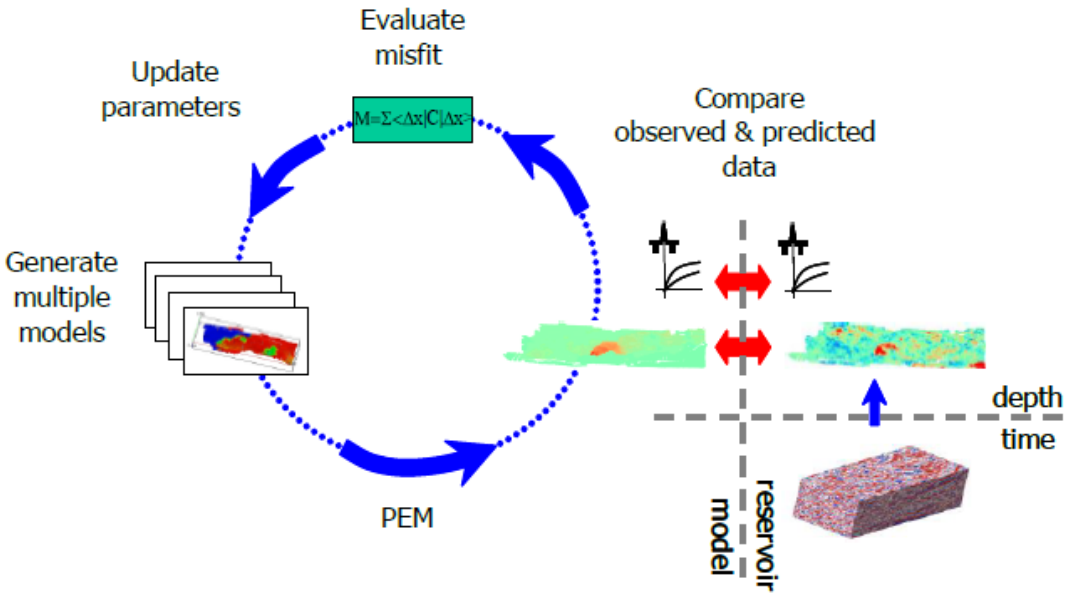

Figure 1.3 *Seismic History Matching (SHM) workflow. SHM is a combination of well data and time-lapse seismic data to yield better update of the reservoir model and improve trustworthiness of production forecasts. (Stephen and MacBeth, 2006)*

At the simulation model domain, a comparison is done between the pore pressure and saturation changes from the 4D observed data and to those predicted by the simulation model. This type of comparison is very complex as it requires two inversions that involve non-uniqueness issues (Landrø, 2001; Machado, 2009; Souza et al. 2010; Trani et al. 2011). The comparison at the level of seismic impedances requires an inversion for impedances of the observed seismic amplitude data, and the synthetic impedances require computed through a petroelastic model (PEM), using the saturation and pressure distribution from the fluid flow simulation model as inputs (Gosselin et al. 2001; Gosselin et al. 2003; Stephen et al. 2006; Roggero et al. 2007; Ayzenberg et al. 2013). Finally, if we are comparing at the level of seismic traces there is no need for seismic inversions of the observed seismic data, but to generate the synthetic seismic an additional procedure of seismic modelling is required after elastic properties calculation using a PEM coupled to a simulator model. The generated synthetic seismic is then compared to the observed seismic data (Dadashpour et al. 2007; Landa and Kumar, 2011).

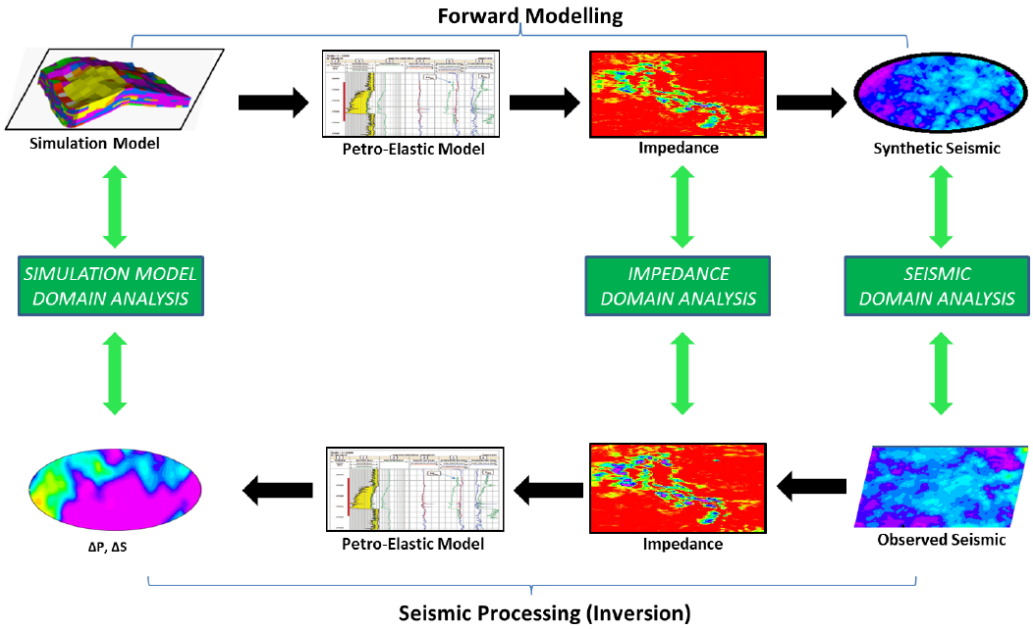

Figure 1.4 *Possible different domains at which 4D seismic and reservoir engineering data can be compared: the simulation model, acoustic impedances and seismic domain (after Obidegwu 2015).*

1.2.2 Importance of the Petroelastic Model (PEM)

One of the main focuses of the oil and gas industry is to constrain reservoir models to 3D and 4D seismic data using quantitative workflows, which are suitable for model updating and history matching. Workflows that include computation of synthetic seismic must rely on a petroelastic model (PEM), such models comprise of a chain of mathematical equations and empirical relationships relating fluid and rock properties to the elastic moduli distribution in the reservoir and hence determine P-wave and S-wave velocities and density. Within the 4D seismic framework, the main objective is to transform the time-lapse seismic data into a quantitative tool for field management, which requires linking the time-lapse response to changes in pressure and saturation in the reservoir with confidence. This link is known as the 4D petroelastic model (4D PEM) and requires identification of the effective stress sensitivity and dynamic reservoir behaviour over time. The use of petroelastic attributes has different applications, such as in the feasibility of 4D seismic monitoring, the optimization of a 4D seismic monitoring program and prediction of more accurate production forecasts.

The main shared feature for most of the inversion schemes for pressure and saturation estimation using time-lapse data (Landrø 2001; Trani et al. 2011; Ayzenberg et al. 2013) is that they rely on petroelastic modelling to compute elastic rock properties. Nevertheless the scope of this research covers essentially the simulator to seismic process, where the 3D and 4D PEMs represent fundamental constituents in seismic constrained modelling (figure 1.5). In a general sense, simulator to seismic modelling, hereafter referred to as sim2seis, connects two different domains together, the fluid flow simulation and the seismic domains. Sim2seis modelling is a process that creates the synthetic seismic response from a reservoir simulator during different stages of production.

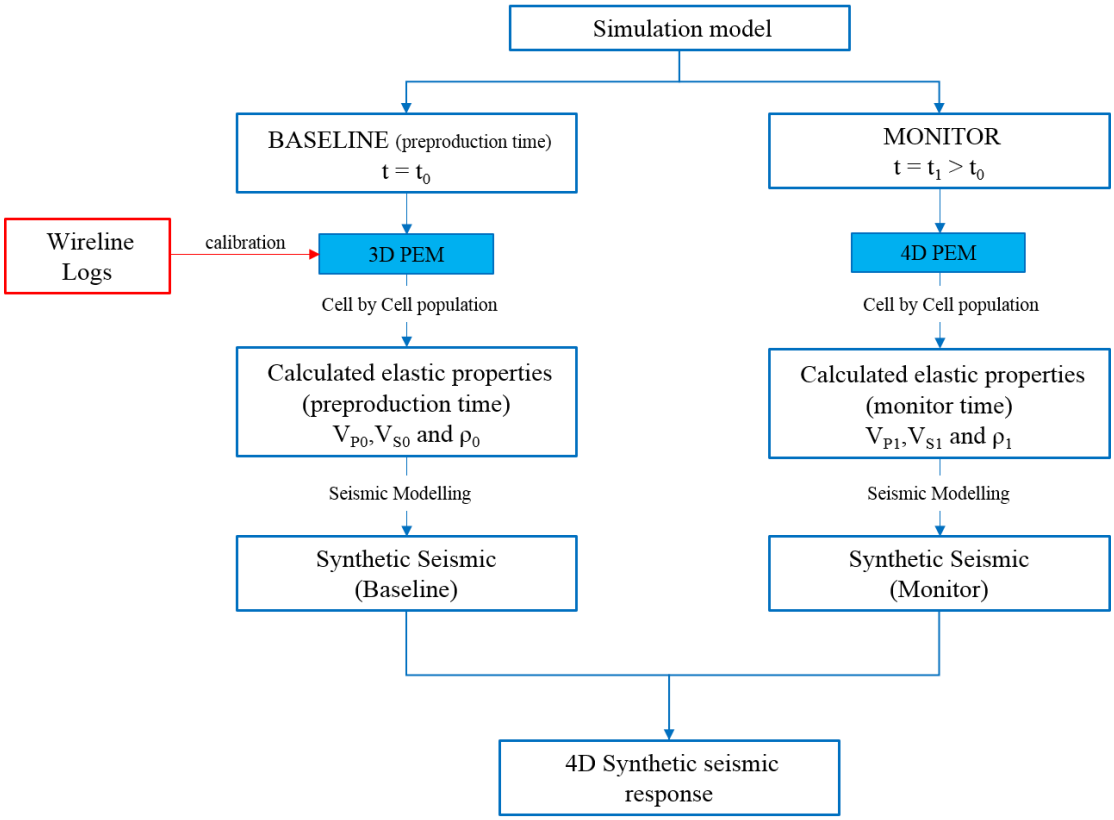

Figure 1.5 *The simulator to seismic scheme (sim2seis), highlighting the importance of the 3D and 4D PEM.*

Within the forward modelling workflow, sim2seis relies on the PEM relationships between static properties (porosity and clay content), effective stress sensitivity term and dynamic changes (pressure and saturation) in the reservoir at the geocellular model scale. Sim2Seis is a multi-disciplinary tool which combines petrophysics, geophysics and the engineering disciplines, however, in this thesis the focus of interest is its rock

physics aspect. The 3D and 4D PEM parameters are generally calibrated from a forward modelling perspective using wireline log data and laboratory measurements and must be computed on a case by case study since the rock physics models are fabric and lithology dependent (Alfred et al. 2008); therefore, different parameters and/or models must be used for different fields. In practice the PEM is uncertain and without calibration of the input data (lithology, porosity, and fluid saturation) it becomes more so (Amini 2014), with the uncertainty carried on through the entire process of the synthetic seismic computation.

1.3 Motivation

In most of the literature it is found that the analysis of the seismic data through rock physics modelling and fluid substitution is a characteristic part of any 4D seismic investigation. The PEM links fluid saturation and pore pressure changes in the reservoir rock to the elastic property changes required for seismic modelling, time-lapse feasibility studies, 4D inversion and seismic history matching. Certainly, having an accurate and robust PEM is indispensable and useful, nevertheless the process of building it can be complex and time-consuming (Chao et al., 2009; Amini 2014).

Despite the development in the integration between 4D seismic and reservoir engineering data, there are still challenges inside 4D seismic workflows that affect and could complicate the 4D interpretation results. It is well understood that an objective of the industry is to constrain the reservoir model to 3D and 4D seismic data using quantitative workflows, which rely on rock physics modelling. The role and context of the PEM in 4D seismic studies has been previously highlighted and sets the tone for this thesis. In the current section I exhibit a more critical motivation statement in terms of the "need" for this project based on challenges, uncertainties and general treatment of the rock physics models for time-lapse seismic interpretation.

Much of the current literature focuses on reporting the accomplishment of history matching using 4D seismic data, seismic forward modelling, and inversion of pressure and saturation changes for 4D interpretation while keeping the importance and challenges in PEM understanding most often than not in a tacit way. The PEM is not a means to an end in most 4D seismic studies, since such a model is mentioned as a

technicality instead of actually addressing its own research challenges in term of the physical principles, calibration of its multiple parameters and practicality.

1.3.1 Maturity of the PEM in 4D studies

Table 1.1 lists a number of 4D seismic history matching applications reported in the literature, where the minimization of the objective function between "observed" and "predicted" is obtained through different algorithms and the delivery of the 4D seismic data is shown at different domains including: seismic domain provided as amplitude or time-shift, impedance domain and the simulation domain. A common denominator from the aforementioned domains is the petroelastic modelling which is uncertain, and non-unique and mainly based on assumptions for the use of Gassmann fluid substitution equations, and laboratory measurements to deal with the stress sensitivity effect.

Data set (field)	Authors	4D seismic data	SHM algorithm	PEM contribution
Tordis	Fagervik et al. 2001	Amplitude maps	Gradient-based algorithm	
PunqS3 model	Gosselin et al. 2001	Impedance	Gradient-based algorithm	$\kappa_{dry}(V_{Pdry}, V_{Sdry}, \rho_{dry})$; $\mu_{dry}(V_{Sdry}, \rho_{dry})$ $V_{Pdry}=a_0+a_1\phi_0+a_2P_{eff}+a_3\phi_0P_{eff}^2$ $V_{Sdry}=b_0+b_1\phi_0+b_2P_{eff}+b_3\phi_0^3+b_4\phi_0^3$ $a_0=3699.445$; $a_1=4500$; $a_2=-18.6667$; $a_3=-3.23765$ $b_0=3579.5$; $b_1=-20430$; $b_2=6.9277$; $b_3=-132000$; $b_4=82600$
Grand Isle block 102 (Gulf of Mexico)	Waggoner et al. 2002	Impedance	Greedy algorithm	Gassmann fluid substitution model integrated with critical porosity and stress model for the dry properties.
Oseberg (North Sea) Amelia (Adriatic Sea)	Gosselin et al. 2003	Impedance	Gradient-based algorithm	
PUNQ-MONITOR	Mezghani et al. 2004	Impedance	Least-squares objective function	$\kappa_{dry}= \kappa_m(3.88\phi^2 -3.9\phi+1)$ $\mu_{dry}= \mu_m(2.19\phi^2 -3.48\phi+1)$ Hertz model to model pressure variation on V_p and V_s Herzt coefficient P-wave =0.05 Herzt coefficient S-wave =0.20
Girassol	Falcone et al. 2004	Impedance	Gradient-based algorithm	

Valhall	Kjelstadli et al. 2005	Time-shift Impedance	Genetic algorithm	$\kappa_{dry}= \kappa_{norm}(1+A_K\log(P_{eff}/P_{eff\_norm})$ where A_K is a parameter determined from core measurements. And κ_{norm} P_{eff_norm} are the normalized dry frame modulus and effective pressure at reference conditions
Semisynthetic model from a middle East oil field	Dong and Oliver 2005	Impedance	Gradient-based algorithm	$\text{Log}_{10}\kappa_{dry}= \log_{10}\kappa_m - 4.25\phi$ And for Vs it was used Han eq. $V_s=3520 - 4910\phi – 1890V_{sh}$
Norne	Lygren et al. 2005	Impedance	Gradient-based algorithm	
Norne	Khazanehdari et al. 2005	Impedance Pressure/saturation	RMS analysis	
North Sea field	Haverl et al. 2005	Impedance	Gradient-based algorithm	The flexibility of the PEM is limited. And the inputs may not be fully representative of the field.
Schiehallion	Stephen et al. 2005	Impedance	Gradient-based algorithm	Dry bulk modulus was calculated using MacBeth (2004) equations and parameters. After Gassmann to obtain the saturated moduli
Synthetic data North Sea field	Skjervheim et al. 2007	Impedance Amplitude	EnKF (Ensemble Kalman Filter)	
Girassol	Roggero et al. 2007	Impedance	Gradual deformation algorithm	PEM parameters named “overpressure” and “underpressure” are introduced in the history matching loop to account for a better impact of the pressure on the 4D seismic impedance
Synthetic data	Dadashpour et al. 2007	Seismic amplitude	Gauss-Newton optimization	Gassmann equation and the Hertz Mindlin model are used for estimating the elastic properties of the reservoir, in this study coordination number = 9 and the degree of the root n = 5 was used in the Hertz Mindlin model
Synthetic data Carbonate (Campos basin) Sandstone (Campos basin)	Emerick et al. 2007	Impedance	Quasi-Newton optimization algorithm	Polynomial correlations between effective porosity and the dry rock elastic properties $\kappa_{dry} = -21.79\phi +13.753$ $\mu_{dry} = -8.0066\phi +6.205$
Nelson	Stephen et al. 2007	Impedance	Neighbourhood algorithm	
Enfield	Ali et al. 2008	Amplitude maps	-	

Schiehallion	Sedighi and Stephen 2009	Impedance	Neighbourhood algorithm	
Gullfaks	Fahimuddin et al. 2010	Impedance	EnKF	
Synthetic data	Souza et al. 2010	Impedance Pressure/Saturation	Conjugate-Gradient method	
Marlim	de Brito et al. 2010	Impedance	Least-squares objective function	Polynomial correlations between effective porosity and the dry rock elastic properties $\kappa_{dry} = -21.79\phi + 13.753$ $\mu_{dry} = -8.0066\phi + 6.205$
North Sea field data (Tarbert units)	Gervais et al. 2010	Impedance	Gradient-based algorithm	Highlights that modifying the PEM parameters is not enough to reduce the mismatch between computed model and observed model.
Valhall	van Gestel et al. 2011	Time-shift Amplitude maps	Genetic algorithm Match quality factor	
Synthetic data	Davolio et al. 2011	Pressure/saturation	Gradient-based algorithm	Dry moduli was computed using the uncemented sand model, which uses the Hertz Mindlin contact theory and the modified Hashin-Shtrikman lower bound
Namorado (adapted synthetic data set)	Souza et al. 2011	Impedance Pressure/Saturation	Global objective function	The impact of PEM parameters on impedance change distributions can hamper the history matching results.
Ekofisk	Tolstukhin et al. 2012	Time-shift	Evolutionary algorithm	Upper Hashin-Shtrikman model to describe the porosity effect on velotcity and additionally, the Hertz-Mindlin theory accounts for the pressure effect.
Synthetic based on Brugge field	Trani et al. 2012	Travel times Saturation	EnKF	
Turbidite reservoir (Campos basin)	Emerick and Reynolds 2013	Impedance	Ensemble smoother with multiple data assimilation (ES-MDA)	End member PEM construction (sand and clay) mixing both components with the Hashin-Shtrikman bound. $\kappa_{qtz} = 37.5$; $\kappa_{clay} = 22.78$ GPa $\mu_{qtz} = 45.5$; $\mu_{clay} = 12.62$ GPa
Delhi	Cui et al. 2013	Impedance	-	
North Sea Field	Ayzenberg et al. 2013	Impedance V_P ratio	-	
Gimle	Alerini et al. 2014	V_P ratio	Iterative ensemble smother	

Schiehallion	Fursov 2015	Saturation and Pressure	CMA-ES	MacBeth (2004) stress sensitivity model together with Gassmann equations.
Brugge	Luo et al. 2016	Amplitude versus angle (AVA)	Iterative ensemble smoother	Soft sand model to compute the dry frame moduli of the rock, which later is used in Gassmann fluid substitution

Table 1.1 *Uses of Seismic History Matching (SHM) in the research community. It is important to mention that the blank spaces in the PEM contribution column mean that the PEM has been mentioned as a formality in the work, or just a simple review of its equations have been shown, and lookup value from literature have been used for the bulk and shear moduli of the mineral.*

Based on a small indicative statistic (table 1.1), the majority of the 4D seismic studies mention the word PEM or rock physics model as part of their workflow, however they don't go into details since it is not part of the objectives of their studies. Figure 1.6 shows a histogram constructed out of the articles displayed in table 1.1. The histogram break down the different depth level in which the PEM is treated in the literature. 74% of the previous works report the set of equations, theoretical and empirical models used to build up the PEM. It is important to have in mind that there are a vast numerous relationships published in the literature to link elastic properties to the fluid saturation, porosity, pressure and lithology (Mavko et al. 2009). Nevertheless, a comprehensive study on different PEM paradigms in the 4D seismic framework is not yet to be found on the literature; from what I have observed, all the authors assume a model that may work for their specific cases (synthetic or field data) without exhausting the models in terms of their sensitivity and uncertainties. Only 40% actually reported the input parameters used to calculate the elastic properties of the reservoir (V_P, V_S and ρ) and from that statistic, 32% used look up tables values for the elastic moduli and density of the grain minerals (quartz, clay, calcite). On the other hand, it is known that the PEM is calibrated against log data and core measurements, still only 44% of the authors from table 1.1 reported such calibration. The calibrations were performed mainly to obtain:

- Coefficients for empirical relationship between dry frame moduli, porosity and effective pressure (Emerick et al., 2007) using log data.
- Coefficients for a polynomial function of effective pressure and initial porosity on the compressional and shear velocity obtained using core measurements (Gosselin et al., 2001).

- Coefficients that define a theoretical stress sensitivity model using core data to calculate the bulk and shear modulus for a sandstone rock (MacBeth 2004; Stephen et al. 2005).

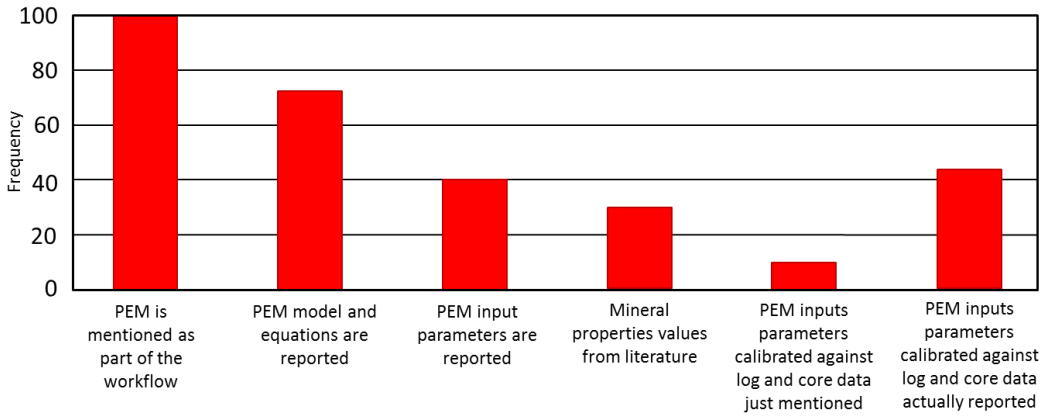

Figure 1.6 *Histogram based on literature review (table 1.1) that breaks down the role and treatment of the PEM in the research community.*

1.3.1.1 Calibration of the PEM

There is an imminent necessity to calibrate the PEM parameters to the in-situ response; therefore, using values from look-up tables in the literature might yield erroneous results that will be carry out through the entire forward modelling process and jeopardize the qualitative and quantitative interpretation of the 4D seismic. Selection of the appropriate inputs parameters of the PEM remain ambiguous, only few authors have designed strategies to overcome this challenge. Generally, calibration of the PEM parameters is performed deterministically by fitting the PEM outputs (V_P, V_S and ρ) against log data and core measurements. Amini and Alvarez (2014) work shows the result of an optimization algorithm, which was designed using Gassmann fluid substitution and the modified MacBeth (2004) model (Alvarez and MacBeth, 2013) that accounts for lithology and porosity effect in the dry frame moduli characterization. Figure 1.7a shows the results of the optimization performed over an appraisal well in a clastic reservoir in the North Sea where a 4D feasibility study was performed with their associated calibrated input properties.

On the other hand, Escobar et al. 2006 tried to automate the calculations by re-casting the PEM as an inverse problem using a global optimization based on simulated annealing algorithm (figure 1.8), the advantage of this approach is the reduction of time required to build and update the PEM. Nevertheless, the numerical coefficients of the PEM tested on well data from two clastic fields in the North Sea and West Africa were not reported.

a)

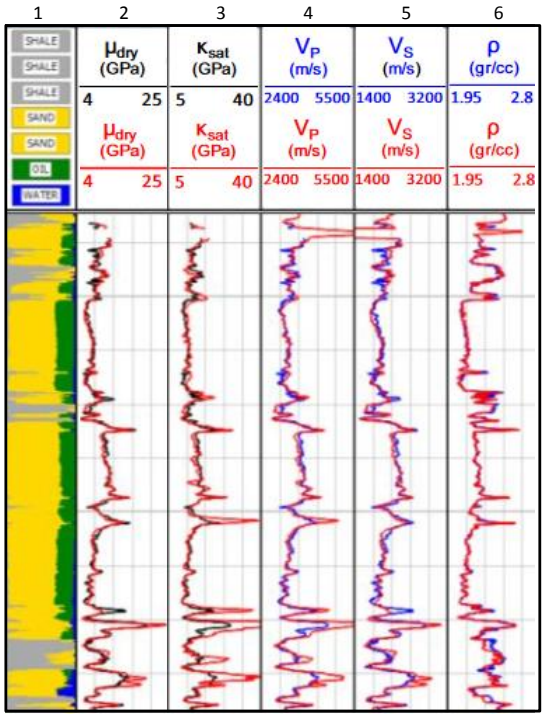

Optimised PEM parameters. Reconstructed V_P, V_S and ρ logs. Measured logs.

b)

	SAND	SHALE
κ (GPa)	31	12
μ (Gpa)	22	7
ρ (g/cc)	2.64	2.37
ε = $0.42V_{sand} + 0.19V_{sh} + 0.66\phi_e$		

Figure 1.7 *(a) Results of PEM calibration for 4D seismic studies. Track description: (1) sand/shale model based on effective porosity. (2) Dry frame shear modulus curve. Black (optimized) versus red curve (measured). (3) Saturated bulk modulus obtained through Gassmann fluid substitution. Black (optimized) versus red curve (measured). (4) Reconstructed compressional velocity log (blue) through PEM equations versus the measured V_P log (red). (5) Reconstructed shear velocity log (blue) through PEM equations versus the measured V_S log (red) and (6) Reconstructed bulk density log (blue) through PEM equations versus the measured ρ log. (b) Calibrated inputs PEM parameters, where ε is the inverse of the critical porosity ($\varepsilon = 1/\Phi_C$) and represent a lithology dependent parameter, calculated through a multi-linear regression as a function of clay content and porosity. (Modified from Amini and Alvarez 2014).*

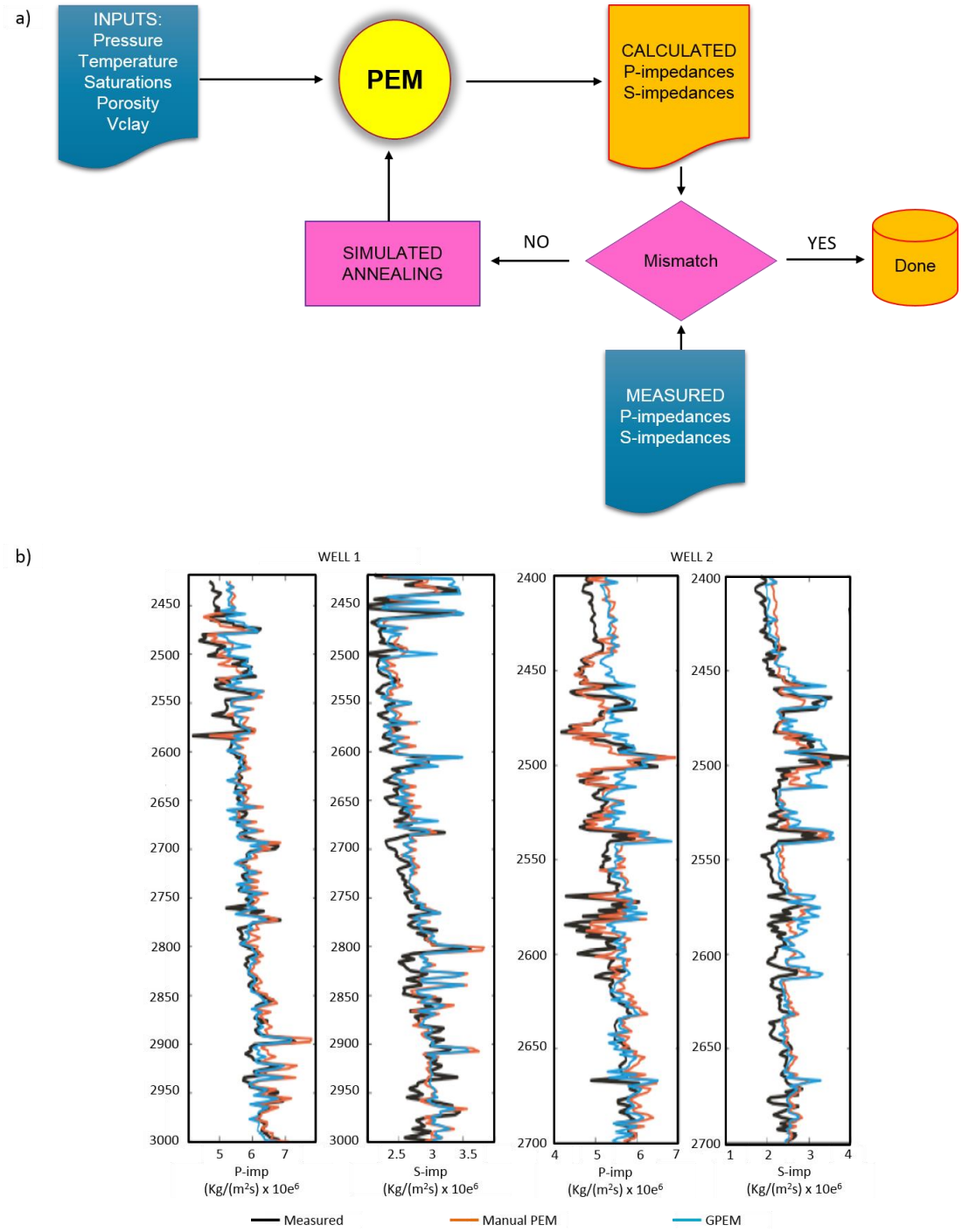

Figure 1.8 *(a) Global petroelastic model (gPEM) workflow, starting from an initial guess, a simulated annealing algorithm searches globally for a minimum between the calculated and measured impedances. (b)Example and comparison of gPEM and manual model fit for two wells in West Africa, the correlation of both fitted models versus the measured logs in bigger than0.8. (Redrawn from Escobar et al. 2006)*

A statistical methodology is presented by Chao et al. (2009), which aim is to quantify and develop an uncertainty workflow for the PEM parameters (figure 1.9) through probabilistic density functions (PDF). The calibration of the coefficients considered in

the depth-trend laws included in the rock physics model against log data was based on simulated annealing (Escobar et al., 2006)

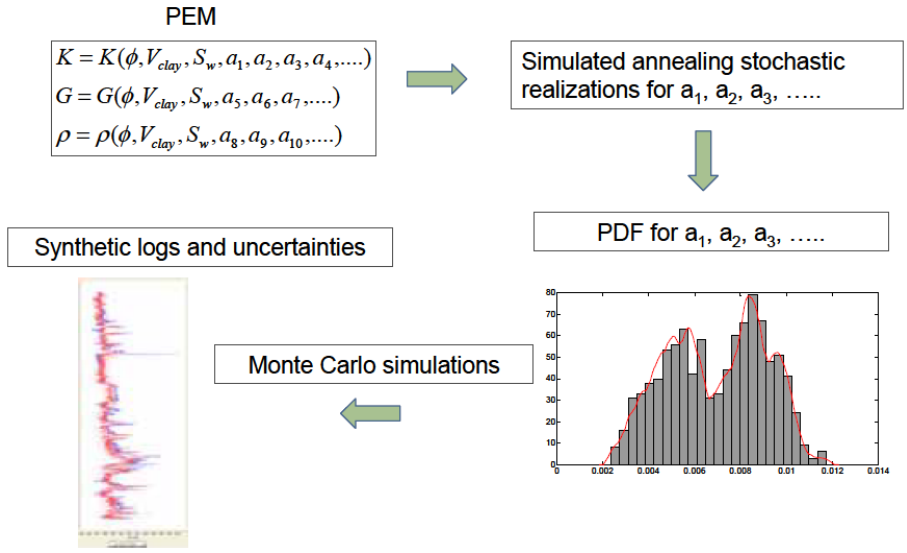

Figure 1.9 *Workflow for optimization and uncertainty of PEM based on depth-trend relationships, a total of 19 coefficients based on log data are calibrated. The method computes probability density functions (PDF) which are employed in Monte Carlo simulations to obtain synthetic elastic logs which are compared against the measured wireline logs (Chao et al. 2009).*

1.3.1.2 Pressure/Saturation domain

Going from seismic domain to the simulation model means estimation of the pressure and saturation changes based on the 4D seismic, for which several approaches have been reported in the literature. Landrø (2001) introduced a mathematical expression to invert for water saturation and pore pressure changes in the Gullfaks field from time-lapse AVO attributes, prior to the inversion a PEM is calibrated. The PEM was based on modified Gassmann model which take into consideration cementation effect and clay content, the saturation effect between pre and postproduction times was studied through available repeated logs in the wells, and the pressure effect was derived from ultrasonic lab measurements on the core samples (Landrø et al., 1999). Figure 1.10 summarises the results of the PEM feasibility study performed by Landrø et al. (1999). Landrø (2001) addresses then the importance of the calibration of the rock physics model and pointed out that is a necessary input to obtain the equations to compute saturation and pressure related changes from 4D seismic data.

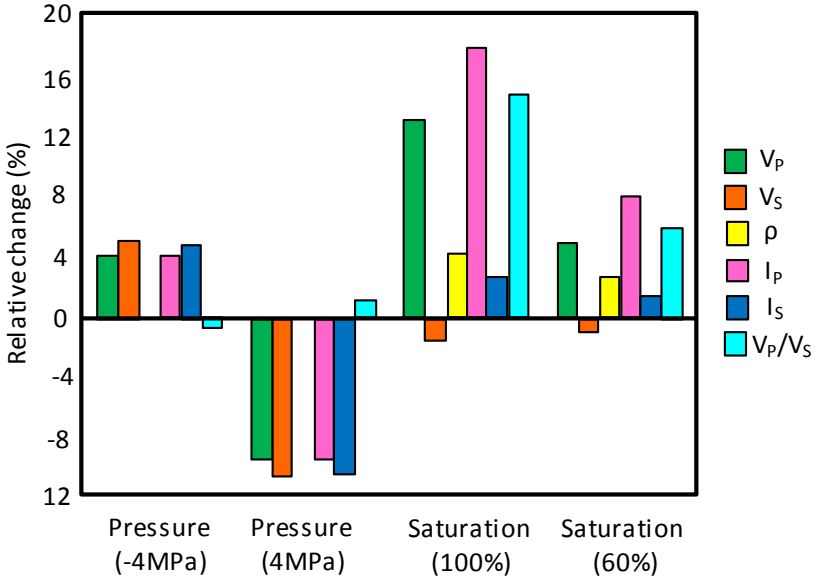

Figure 1.10 *Relative changes in seismic parameters, including velocities, impedances and density, due to changes in water saturation taken from wells and pore pressure taken from core samples in the Gullfaks field (Redrawn from Landrø et al., 1999).*

In the framework of seismic history matching, when comparing "observed and "predicted" data in the pressure and saturation domain is very complex as it requires two inversions that involve non-uniqueness issues. Souza et al. (2010) presented an integrated history matching to update the simulator flow models regarding seismic derived saturation and pressure maps. Davolio et al. (2011) used the pressure and saturation maps inverted from P and S-impedances for history matching of a synthetic model.

1.3.1.3 Impedance domain

When the impedance domain is employed in seismic history matching, it means that the observed seismic volumes are inverted to the impedances, which are compared with the impedances obtained from the simulation model through rock physics modelling. This approach appears to be the most popular in SHM literature, probably related to the robustness of the method compared to the complexity of inversion procedure for pressure and saturation or wave interference during seismic modelling. Indeed, from all the studies cited on table 1.1, 70% of them used the impedance domain to perform the

mismatch calculation between observed and predicted data. One of the drawbacks that face such approach is the reliability of the input parameters of the PEM, the assumptions behind the theoretical or empirical relationships that make up the model, and the calibration of the PEM, since using lab data is not fully reliable to reproduce the in-situ response of the reservoir (Landrø 2001; MacBeth 2004; Falcone et al. 2004; Haverl et al. 2005; MacBeth and Schuett 2007).

Falcone et al. (2004) dedicated all their effort on the assessment of the impact of PEM within the framework of 4D SHM, by addressing the scale at which the rock physics modelling should be performed (log scale versus simulation grid scale) and a sensitivity analysis on the acoustic properties predicted by the PEM when coupled to a simulator model. The PEM is defined at the fine log scale but applied at the coarse simulation grid scale, upscaling or downscaling petrophysical properties and/or dynamic properties of the reservoir is an issue with its own challenges. Using up-scaled petrophysical parameters with cut-off values may result modelling different lithologies in the same way due to lack of heterogeneity in the simulation model domain.

Roggero et al. (2007) used gradient deformation algorithm for history matching with 4D seismic data to the Girassol Field, offshore Angola. This research recognised that the uncertainty associated with the PEM may have a strong impact on history matching results, indeed stress sensitivity parameters were introduced as SHM parameters. Using the new calibrated PEM impacts the 4D seismic signature response significantly, by reinforcing or attenuating the change of P-impedance in high pressure zones, released gas zones and water injection areas. After PEM calibration a better agreement with the observed data can be seen in figure 1.11a and 1.11b

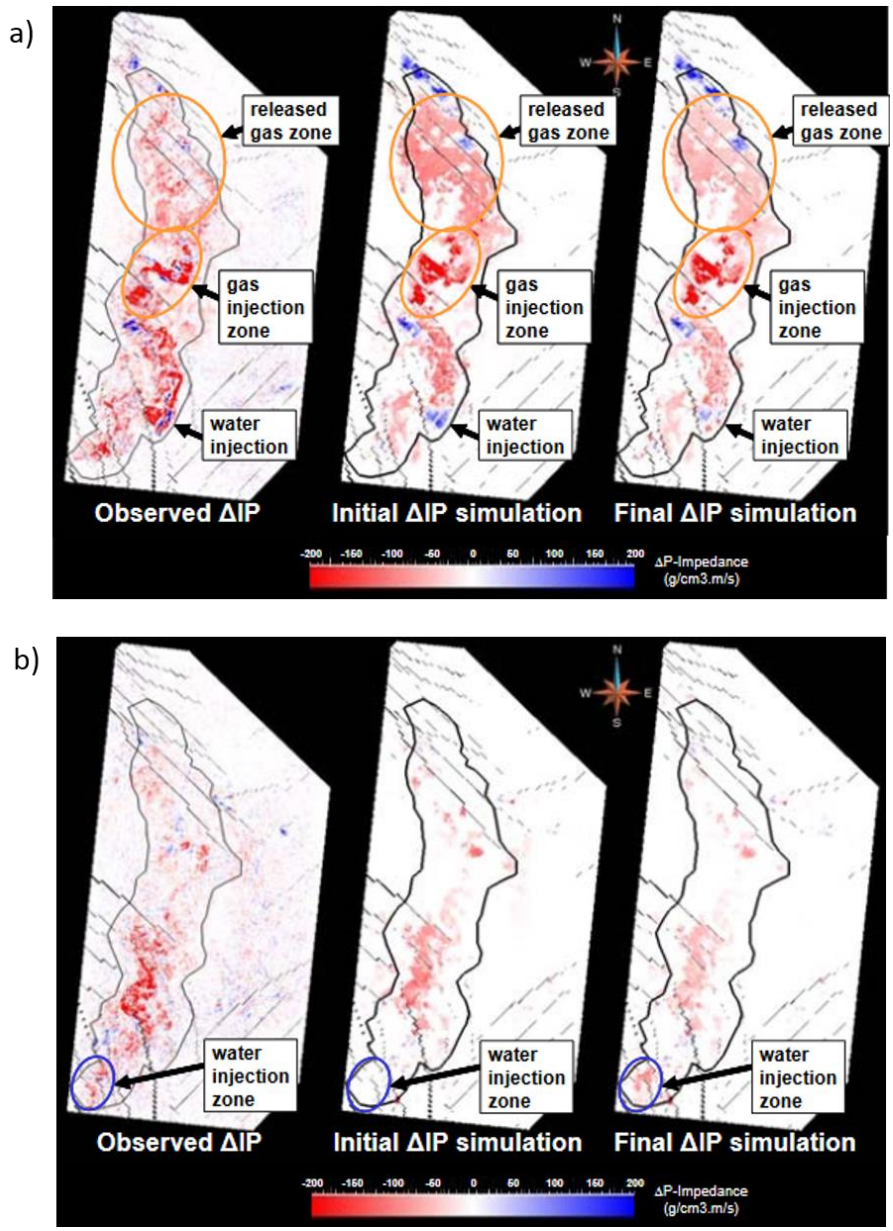

Figure 1.11 *Maps of P-impedance change of the Girasson Field: observed data (left); initial PEM result (middle); and after calibration of PEM parameters (right). (a) Map for the top reservoir and (b) bottom of the upper complex. (From Roggero et al., 2007)*

While there are reports of better history matching performance by taking into account PEM parameters into the history match loop (Roggero et al., 2007; Souza et al., 2011), authors like Gervais et al. (2010) state that by only modifying the PEM parameters is not enough to reduce the mismatch between the simulated seismic attributes and the observed ones. Indeed, parameters influencing the distribution of the pressure and fluid saturation dynamics inside the simulator must be considered; including, fault transmissibility, porosity and permeability multipliers, fracture network to name a few.

1.3.1.4 Seismic domain

In a general sense, simulator to seismic modelling (sim2seis) connects two different domains together, the fluid flow simulation and the seismic domains. Sim2seis modelling is a process that creates the synthetic seismic response from a reservoir simulator during different stages of production. To generate the synthetic seismic an additional procedure of seismic modelling is required after the reservoir rock impedances and density obtained with a PEM. Amini (2014) performed sim2seis to two North Sea case studies, revealing that the PEM is easy to implement but should be adjusted and calibrated properly especially if the goal is to use the 4D seismic data in a semi or quantitative manner.

A quantitative application of sim2seis in automated model updating in SHM was performed in Valhall field by van Gestel et al. (2011), where fault transmissibility, pore volume multipliers and permeability were the updating parameters in the SHM loop. The synthetic data was generated using Valhall specific rock physics and seismic forward modelling software (Askim 2003, Kjelstadli et al. 2005). Even though the PEM equations are reported in the work of Kjelstadli et al. (2005), there is a lack of visibility in term of values of the input parameters used, and the general calibration of the PEM performed. In general, after an extensive literature review, most of the articles do not exhaust the rock physics modelling in term of sensitivity for 4D seismic response. It is assumed that a specific rock physics model may work for their data set, however it will be instructive to report what is the PEM, the input parameters values used and associated uncertainties for future developments and comparison of fields with similar geological settings.

1.3.2 Opportunities

In this thesis, I want to highlight the rock physics modelling aspect that often is overlooked in the literature, including choices available and uncertainties. Even though there is an extensive variety of rock physics models in the literature, and research that have addressed important aspects of the PEM to my knowledge, there is no published study that comprehensively reports rock physics modelling in term of different types of paradigms, individual parameters, uncertainties and non-uniqueness applied to time-

lapse studies, which creates an opportunity for this work to explore the relationship between 4D seismic interpretation and PEM in a general sense. The core of this work evolves from the perspective of the simulator to seismic modelling (sim2seis) workflow which is the natural first step in assessing PEM non-uniqueness prior to any inversion assessment. It is important to be aware that either qualitative or quantitative methods to integrate 4D seismic and engineering data, the source of mismatch need to be recognised. Amini (2014) condenses in table 1.2 the list of parameters and hierarchy of uncertainties for the process of updating the simulation model using sim2seis.

Simulation Model

• Model Geometry
  o Active/Inactive geobody distribution (NTG)
  o Fluid contacts
  o Reservoir top and base
• Connectivity of reservoir units
• …
• …
• …
Production History matching hierarchy of uncertainty

Observed Seismic
• Noise (acquisition) • Processing and imaging
PEM

• Dry Frame characterization
  o Stress-sensitivity
  o Sand/shale properties
• Fluid Properties
• Overburden/Underburden properties

Seismic Modelling
• Wavelet

Table 1.2 *Hierarchy of uncertainty in updating the model using simulator to seismic modelling (Amini 2014).*

The ever present objective and challenge of this thesis is to build a PEM suitable for sim2seis applications within the time-lapse framework. The specific PEM must be sufficiently accurate, which stresses the importance of such model. To make a contribution to the wide knowledge of PEM in the research community, I will interrogate a variety of models in term of calibration against logs and lab measurements, the number of inputs parameters, its non-uniqueness nature and the resultant outputs in the time-lapse impedance domain.

The preferred PEMs in this thesis, follows three criteria stated in Amini's (2014) work:

- The PEM must honour the rock and fluid physics.
- It must have the ability to capture changes in the reservoir related to saturation changes through a fluid substitution model, and to recognize the effect of changes in pore pressure using a stress-sensitivity model.
- , and it must be applicable to simulator to seismic modelling, therefore needs to be compatible with the parameters of the simulator in the engineering domain.

In principle, 4D PEM selection should be based on efficiency, robustness and a general awareness of the petrophysics and geology of the field honouring both the static and dynamic domains. Hence, in this work I look at PEM consistency between time lapse seismic data, simulation flow data, logs and core data; however, how can we choose the best model since different theories for the PEM are proposed in the literature and validation of such models remains one of the biggest challenges in PEM studies? Using a deterministic approach for a rock physics model based on effective medium theory and Gassmann fluid substitution comes at the cost of using many reservoir dependent variables, and is an under-determined problem, numerous past studies have now pointed to the limitations and uncertainties that can exist within current models (Falcone et al., 2004; Roggero et al., 2007; Amini, 2014). Beside the difficulty of selecting an appropriate model, there is the need to calibrate to the in situ response; indeed one of the main challenges is to set the correct field dependent input parameters into the equations, since values from lookup tables in the literature might yield erroneous results.

This thesis focuses on the assessment of the implications and impact of petroelastic modelling within the framework of time lapse data interpretation and its applicability in seismic forward modelling using sim2seis. To address the difficulty of selecting an appropriate model and the need to calibrate to the in situ response, here I investigate twelve (12) different plausible PEM paradigms applied to two clastic North Sea fields with different geological setting, United Kingdom Continental Shelf (UKCS) field and Norwegian Sea field, and four (4) PEM paradigms applied to a carbonate field. For each model, the static rock frame components are calibrated using a range of wireline log data acquired prior to production, and the dependence on pressure change is then added using coefficients derived from laboratory. The value of each calibrated PEM is

assessed through a comparison of the predicted changes of impedance maps between monitor and baseline by coupling the rock physics model to a flow simulation model. Based on comparisons across field and model, the number of parameters, degree of utility, and overall accuracy of the PEMs, conclusions are drawn on their effectiveness for 4D seismic interpretation guided by simulator to seismic modelling. Finally the uncertainties of the PEM, together with the ones from the seismic data and simulation model creates the need for time-consuming comparisons in the SHM workflow. This study presents a simple and interactive way of visualizing all of these uncertainties, whilst optimizing seismic history matching. The approach is illustrated by application initially to synthetic data and then to three different fields from the UKCS, Norwegian Sea and offshore Brazil.

1.4 Outline of this thesis

This thesis focuses on the assessment of the implications and impact of petroelastic modelling within the framework of time lapse data interpretation and its applicability in seismic forward modelling using sim2seis. The remainder of this thesis is divided into six chapters. Chapter 2 presents a general background on petroelastic modelling applied to reservoir engineering within the framework of 4D seismic, including deterministic and new approaches. Chapter 3 is dedicated to description of suitable PEMs for sim2seis, concentrating on Gassmann's fluid substitution model in conjunction with the effective medium theories for solid and fluid components specifically used in this thesis. A major part of this chapter addresses the dry frame modelling, which together with the rock stress sensitivity remains the highest uncertainty in the PEM. So far 4D seismic has mostly been used for clastic reservoirs and only rarely for carbonate reservoirs. This because carbonate reservoirs are stiffer, apart from chalks, and the effect on seismic parameters of substituting oil with water is far less pronounced (Landrø 2015). In this chapter, I am looking to extend the PEM knowledge, since Gassmann fluid substitution may need modifications in order to be applicable to carbonate rocks. This is due to the internal pore structures unique in carbonate rocks that are far more complicated that in siliciclastic rocks.

Chapter 4, focuses on the necessity of calibration of the PEM parameters to the in-situ response for each specific field presented in this work. For the calibration an

optimization algorithm is proposed to fit each rock physics model previously explained in chapter 3 to the sonic, shear and density logs data acquired prior production. After this statistical analysis, in chapter 5 each set of estimated input parameters are now used in simulator to seismic modelling. Thus, each cell in the flow simulation model specified by a particular shale volume (V_{sh}) and porosity (ø) together with saturation and pressure changes can be transformed into a corresponding V_P, V_S, and ρ. The calculation of the acoustic elastic properties of the reservoir leads to the resultant impedance change maps for producing units in each field to assess and interpret the 4D response. A second part of this chapter, aims at reducing the amount of parameters from the conventional PEM and moving into a simplified proxy model with two parameters, which previous research (Alvarez 2014) suggested can still capture the main 4D response. This mathematical equation is attractive in particular for time-lapse seismic maps.

Chapters 6 further explore the two parameter a proxy model in relationship to PEM, with the objective to translate these two parameters into an interactive SHM domain, thereby helping to discriminate and visualize the uncertainties associated with the observed seismic data, the simulation model and the PEM itself whilst optimizing the SHM. The approach is tested initially on several synthetic data and finally to three different observed field applications. The final chapter (7) summarises the conclusions of this entire work, and gives recommendations and suggestions for future research.

1.5 Publications

Specific aspects of this thesis have been published and presented in conferences:

- Briceño A., MacBeth C. and M.D. Mangriotis. [2016] Towards an effective petroelastic model for simulator to seismic studies. *78th EAGE Conference and Exhibition*, Extended Abstracts, Th LHR2 08.
- Briceño A., MacBeth C. and M.D. Mangriotis. [2017] A Practical Tool for Simultaneous Analysis of 4D Seismic Data, PEM and Simulation Model. *79th EAGE Conference and Exhibition*, Extended Abstracts, Th A1 08.

Chapter 2

Petroelastic model in the research community: from conventional to novel approaches

In 4D seismic studies any workflow that requires synthetic seismic computation must rely on a PEM, which by definition and parameterization will define the accuracy and understanding of the 4D seismic signature. In the research community, there is a vast amount of equations and relationships that related rock and fluid properties to pore space, pressure changes in the reservoir and rock composition. The following chapter displays a summary of knowledge on rock physics model having as a framework 4D seismic interpretation studies.

2.1 Introduction

Any quantitative workflow designed to predict reservoir properties from seismic must rely on a petroelastic model (PEM) which brings together the petrophysical properties and the simulation model domain to the seismic response. Within the time-lapse seismic framework, the PEM represents a crucial element since it links fluid saturation and pore pressure changes in the reservoir rock to the elastic property changes required for seismic modelling, time-lapse feasibility studies, 4D inversion and seismic history matching. The PEM is a series of equations and relationships based on theoretical principles and empirical laws (Menezes and Gosselin 2006) with parameters calibrated against well logs and core data. In this chapter all PEMs consist of two parts: first the static rock components by which the saturated rock frame moduli and density in their initial state are specified, and secondly the dynamic component which is defined by the fluid substitution model, effect of pressure changes on each fluid phase, and finally the stress dependency of the rock frame density and moduli.

2.2 The conventional Petroelastic model

The set of equations which comprised the conventional (3D and 4D) PEM is used to transform the rock and fluid properties of the reservoir into elastic attributes (P-wave and S-wave velocities and density or impedances) and it can be applied at different scales, from laboratory cores and well logs to the geological model and fluid flow simulators grids (Falcone et al. 2004; Menezes and Gosselin, 2006). Such elastic property changes obtained from the PEM are required for seismic modelling, time-lapse feasibility studies, 4D inversion and also seismic history matching (Falcone et al. 2004); as our ultimate end-goal is simulator to seismic modelling for the reservoir prior and after production and recovery.

There are two principal elastic parameters that affect seismic velocities: the bulk modulus and the shear modulus. Shear wave velocities (V_S) are affected by bulk density and shear modulus, while compressional wave velocities (V_P) are affected by bulk density and both shear and bulk moduli, the bulk modulus is related to rock and fluid compressibility. The equations for compressional and shear velocities of fluid saturated rocks in a homogeneous isotropic medium are well known and can be written as:

$$V_p = \sqrt{\frac{K_{sat} + \frac{4}{3}\mu_{sat}}{\rho_{sat}}} \tag{2.1}$$

$$V_s = \sqrt{\frac{\mu_{sat}}{\rho_{sat}}} \tag{2.2}$$

where K_{sat}, μ_{sat} and ρ_{sat} are the bulk modulus, shear modulus and density of the fluid saturated rock. The elastic moduli can be estimated through a fluid substitution model, meanwhile the bulk density is a well understood quantity and it is calculated as the volume average of the solid and liquid phase as:

$$\rho_{sat} = \rho_{fluid}\,\phi + (1-\phi)\,\rho_{matrix} \tag{2.3}$$

$$\rho_{matrix} = \rho_{sand}(1-V_{sh}) + \rho_{sh}V_{sh} \tag{2.4}$$

$$\rho_{fluid} = \rho_w S_w + \rho_o S_o + \rho_g S_g \tag{2.5}$$

The PEM has been comprehensively investigated in the literature; in fact, there are numerous quantitative relationships to link rock properties with pore space, fluid saturation, and pressure and rock composition (Mavko et al. 2009). In particular it is found various fluid substitution models (Gassmann 1951; Geertsma and Smit, 1961; Brown and Korringa, 1975; Berryman and Milton, 1991), fluid substitution in heterogeneous matrix-clay mixtures (Gurevich and Carcione, 2000), calculation of acoustic properties of fluids (Batzle and Wang 1992; Han and Batzle, 2000a,b), fluid-mixing (Domenico, 1974; Dvorkin and Nur 1998; MacBeth and Stephen 2008) and mineral-mixing theories (Hill 1952; Backus 1962; Mavko et al. 2009) and dry frame rock modelling (Krief et al. 1990; Nur et al. 1998; MacBeth 2004; Pride 2005; Amini 2014).

A deterministic 3D PEM commonly includes the acoustic properties of the fluid components as a function of pressure, temperature and salinity based on empirical correlations (Batzle and Wang, 1992; Han and Batzle, 2000a, b) and oil and gas PVT

data including API, Bo, GOR and Gg. As well as relations that show the porosity dependence on the dry frame moduli (Krief et al. 1990; Nur et al. 1998; Pride 2005), averaging laws to describe the fluid and mineral mixing and a fluid substitution model.

2.2.1 Gassmann Fluid Substitution and its parametrization

A key component of any 3D and 4D PEM refers to a fluid substitution model used to calculate the rock/fluid interaction. Fluid substitution is a reliable tool for modelling and quantifying different fluid scenarios that might give rise to an observed AVO or 4D response. Gassmann's equations (Gassmann, 1951) for fluid substitution are widely used in the industry because of their simplicity, robustness and mainly because all the required inputs are measured or obtained from wireline logs. Gassmann's equations are strictly valid for isotropic, homogeneous media, fully saturated and are free of assumptions about the pore geometry. According to Mavko et al (2009), the equation is valid only at sufficiently low frequencies such that the induced pore pressures are equilibrated throughout the pore space, allowing sufficient time for the pore fluid to flow and eliminate wave induced pore pressure gradients. This limitation to low frequency range explains why Gassmann works best for very low frequency in-situ seismic data (<100Hz). However, the reality of a reservoir is much more challenging than a perfectly isotropic medium, since reservoir rocks are anisotropic. This is particularly true at the scale of the cell of a fluid flow simulator, due to stratigraphic layering and non-uniform porosity distribution (Falcone et al. 2004).To calculate the saturated moduli of the rock (K_{sat}, μ_{sat}), Gassmann equations are formulated in the following form:

$$K_{sat} = K_{dry} + \frac{\left(1 - \frac{K_{dry}}{K_m}\right)^2}{\frac{\phi}{K_{fl}} + \frac{1-\phi}{K_m} - \frac{K_{dry}}{K_m^2}} \tag{2.6}$$

$$\mu_{sat} = \mu_{dry} \tag{2.7}$$

where K_{dry} is the dry frame bulk modulus, K_m is the bulk modulus of the mineral components, K_{fl} is the fluid bulk modulus and μ_{dry} is the dry frame shear modulus.

2.2.1.1 Fluid

The density and bulk modulus of the single phase fluids are calculated using the empirical correlation from Batzle and Wang (1992), based on temperature, salinity and pressure. Black oil properties such as oil API, solution gas-oil ratio and oil-formation volume factor and gas gravity are used to characterise the hydrocarbon properties. Table 2.1 illustrates the basic dependencies (velocity and density) for hydrocarbon gas, oil and brine in combination when values of compositional vary with pressure and temperature. The fluid mixing of the in-situ properties of the reservoir fluids is performed using a harmonic averaging (Domenico, 1974) written as:

$$K_{fl} = \left(\frac{V_w / \phi}{K_w} + \frac{V_{HC} / \phi}{K_{HC}} \right)^{-1} \tag{2.8}$$

where V_w and V_{HC} are the volume fractions of water and hydrocarbon respectively, and K_w and K_{HC} the bulk modulus of water and hydrocarbon.

Fluid acoustic properties	Velocity	Density
Hydrocarbon Gas		
Pressure	Increase	Increase
Temperature	Decrease	Decrease
Gas Gravity	Increase	Decrease
Oil		
Pressure	Increase	Increase
Temperature	Decrease	Decrease
Solution GOR	Decrease	Decrease
API gravity	Decrease	Decrease
Brine		
Salinity	Increase	Increase
Pressure	Increase	Increase
Temperature	Slight increase	Decrease

Table 2.1 *Relative changes of fluid acoustic properties, in connection with increasing values of key environmental and compositional variables (Johnston 2013)*

2.2.1.2 Mineral

To calculate the effective elastic moduli of the mineral mixture we can specify the volume fractions and the constituent moduli to predict the upper and lower bounds (figure 2.1). According to Mavko et al. (2009) the best bounds for an isotropic linear elastic composite without specifying the geometry details of how the constituents are arranged relative to each other is the Hashin-Shtrikman lower and upper bounds (Hashin and Shtrikman, 1963), written as:

$$\kappa_{HS\pm} = \kappa_1 + \frac{f_2}{(\kappa_2 - \kappa_1)^{-1} + f_1\left(\kappa_1 + \frac{4}{3}\mu_1\right)^{-1}} \tag{2.9}$$

$$\mu_{HS\pm} = \mu_1 + \frac{f_2}{(\mu_2 - \mu_1)^{-1} + \frac{2f_1(\kappa_1 + 2\mu_1)}{5\mu_1\left(\kappa_1 + \frac{4}{3}\mu_1\right)}} \tag{2.10}$$

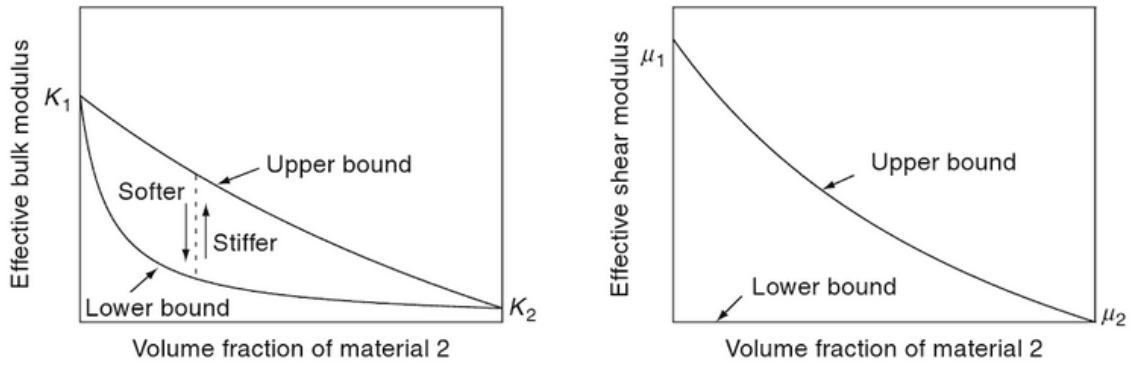

Figure 2.1 *Schematic representation of the upper and lower bounds of the elastic moduli between a mixture of a mineral (quartz or calcite) and water (Mavko et al. 2009)*

On the other hand, we find the simplest and most widely used bounds in the literature, Voigt (M_V) upper and Reuss (M_R) lower bounds. Afterward using an arithmetic average of the bounds (Hill, 1952), it estimates the elastic modulus of the mineral mixing that lies between the upper and lower bounds (Mavko et al. 2009). The arithmetic Voigt-Reuss-Hill average of the bounds (Hill, 1952) M_{VRH} lies exactly halfway between the

Voigt upper and Reuss lower bounds. An understandable extension of the Voigt-Reuss-Hill average is to perform the arithmetic moduli estimate on the previously mentioned Hashin-Shtrikman lower and upper bounds.

$$M_V = \sum_{i=1}^{N} f_i M_i \tag{2.11}$$

$$\frac{1}{M_R} = \sum_{i=1}^{N} \frac{f_i}{M_i} \tag{2.12}$$

$$M_{VRH} = \frac{M_V + M_R}{2} \tag{2.13}$$

where f_i is the volume fraction and M_i is the elastic modulus for each phase i. For the fields presented in this research only two phases are applicable, sand and shale. In a finely layered medium as a single homogenous medium, Backus average (Backus 1962, Mavko et al., 2009) is used to obtain the elastic media properties weighted by their volumetric proportions.

2.2.1.3 Dry Frame

Finally, the dry frame modulus (K_{dry}) can be obtained from laboratory measurements, empirical relationships with dependency on porosity (Krief et al., 1990; Nur et al. 1998; Mavko et al., 2009) or wireline log data. In the log domain, based on the density (ρ) log and sonic logs (V_P and V_S) the bulk modulus of a rock saturated with a fluid is determined; then by rewriting the Gassmann equation (equation 2.6) the dry frame modulus can be determined, generally assuming values for the elastic moduli of the mineral components from look up tables.

$$K_{dry} = \frac{K_{sat}\left(\frac{\phi K_m}{K_{fl}} + 1 - \phi\right) - K_m}{\frac{\phi K_m}{K_{fl}} + \frac{K_{sat}}{K_m} - 1 - \phi} \tag{2.14}$$

Nevertheless, when working in the simulation domain, the dry frame moduli in each cell must be modelled, like in the case of seismic forward modelling. The characterization of the dry frame moduli normally calibrated against log data can follow an empirical correlation, which takes into account the porosity effect. Different polynomial correlations between porosity and dry rock properties are proposed in the literature (Ramamoorthy et al., 1995; Mezghani et al., 2004; Emerick et al., 2007) of the form:

$$\kappa_{dry} = \kappa_m(a\phi^2 - b\phi + c) \tag{2.15}$$

$$\mu_{dry} = \mu_m(d\phi^2 - e\phi + f) \tag{2.16}$$

where the constants from *a* to *f* are calculated through polynomial regression of log data, as can be seen in the example from figure 2.2.

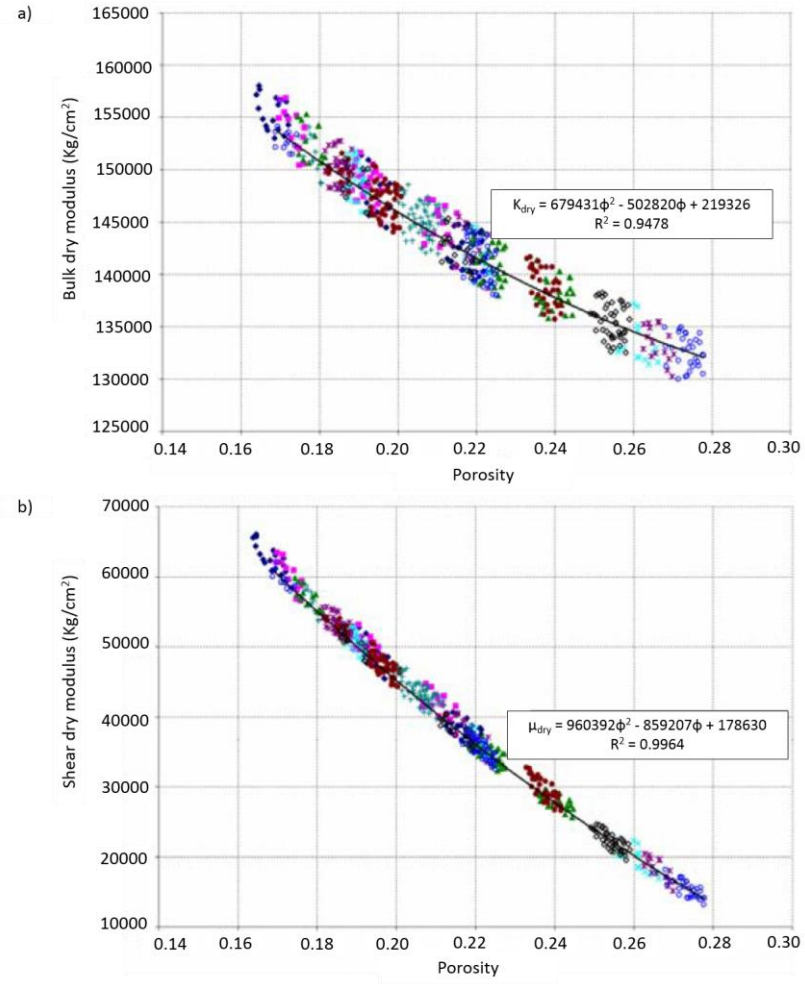

Figure 2.2 *Polynomial correlation between the effective porosity and (a) dry bulk shear modulus, (b) dry shear modulus. (After Emerick et al. 2007)*

As we have seen in the previous section, theoretical estimates of effective moduli of composite material depends on properties of the individual components, volume fractions of the components and the geometric description of the shapes and spatial distribution of the components. Most of the models assume an isotropic and homogenous media, nevertheless is known that reservoir rocks have complex pore shapes and are heterogeneous. Indeed in the presence of velocity dispersion and anisotropy that may be present in shaley sandstone and carbonate reservoirs such assumptions of simple models fail, thus more complex effective elastic media models must be selected. An alternative model include the T-matrix inclusion, based on the integral equation of quantum scattering theory, taking into account the interaction between inclusions based on multiple-point correlation functions (Mavko et al. 2009) This approach is used to estimate elastic properties of anisotropic ellipsoidal shape inclusion in an anisotropic background. It has been previously applied to model the elastic properties of anisotropic shales (Mavko et al. 2009). On the other hand, Jakobsen et al. (2003b) extended the T-matrix approach to take into consideration the fluid effect on the rock, such formulation can be used to model velocity dispersion due to fluid and attenuation in the porous media (For more mathematical detailed description of the model refer to Mavko et al. 2009).

2.3 Rock Physics of 4D seismic

From a time-lapse point of view, the PEM consists of three main categories: fluid substitution model, fluid related pressure effects and the stress-dependency of the rock frame (Floricich et al. 2006). The 4D PEM should take into consideration the effective stress dependency of the rock frame density (figure 2.3) and moduli; this need is addressed through theory and core based laboratory measurements (Ebenhart-Phillips et al., 1989; MacBeth 2004). Some researchers have developed empirical correlations to estimate the rock stress sensitivity directly from well log data (Fürre et al., 2009) or core data (Vernik and Hamman, 2009), while others have based their prediction of the pressure sensitivity using theoretical models (Mindlin, 1949; MacBeth, 2004). The stress sensitivity term of the dry rock frame remains the highest uncertainty in the PEM (Amini 2014) especially since the majority of studies on stress sensitivity are based on laboratory core measurements and they may not represent the in-situ field scale stress response (Ness et al., 2000, Fürre et al., 2009, Alvarez 2014).

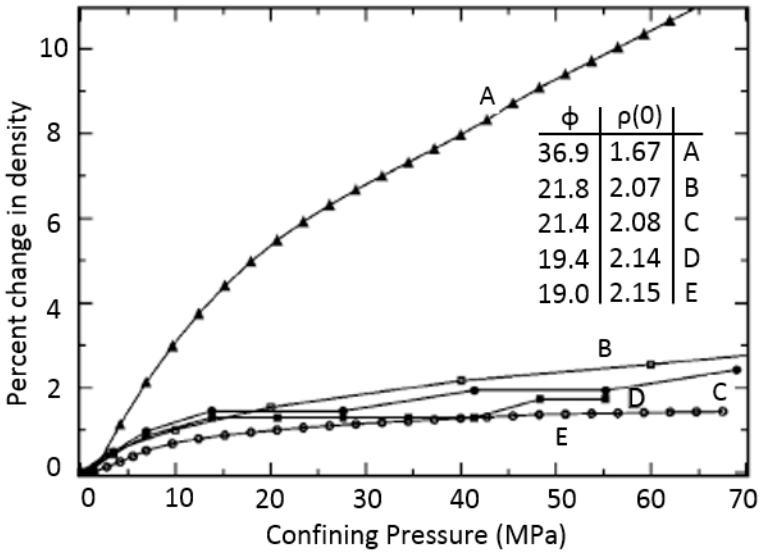

Figure 2.3 *Percentage change in density with pressure for 5 core samples: A) disaggregated Lochaline; B) Rotliegend, Facies A; C) Berea; D) Unconsolidated Lochaline and E) Rotliegend, Facies B. Most density variations are underestimated by less than 3% with pressure, thus MacBeth (2004) concluded that the impact of porosity on the stress sensitivity model proposed is insignificant. (MacBeth 2004)*

2.3.1 Rock Stress Sensitivity

2.3.1.1 Pressure dependence on velocity

It is known that acoustic velocities increase with effective stress and tend toward a flat asymptotic behaviour at high effective pressure (figure 2.4). Indeed, rock stress sensitivity models can be represented in form of velocities that is an appealing physical measurement to fit, however the use of elastic moduli, as previously explained, is of direct benefit because is a closer representation of the true physical changes and thus should lead to a more accurate treatment of the stress sensitivity. Eberhart-Phillips et al. (1989); Freund (1992) and Jones (1995) have demonstrated that the velocity-effective stress relationship could be expressed by an empirical equation consisting of a constant, a linear part and an exponential member.

$$V(P_{eff}) = A + KP_{eff} - Be^{-DP_{eff}} \tag{2.17}$$

where *A*, *K*, *B* and *D* are parameters determined by statistical analysis for a set of rock samples with a given porosity and clay content. Khaksar et al. (1999) simplified equation 2.17 by setting the parameter *K* at zero, since it was demonstrated that the coefficient *K* is frequently small or unstable, producing unphysical behaviour. Khaksar et al. (1999) have shown that such relationships (equations 2.18 and 2.19) provides stability and more realistic velocity predictions at high effective stress.

$$V_p = A_p - B_p e^{-D_p P_{eff}} \tag{2.18}$$

$$V_s = A_s - B_s e^{-D_s P_{eff}} \tag{2.19}$$

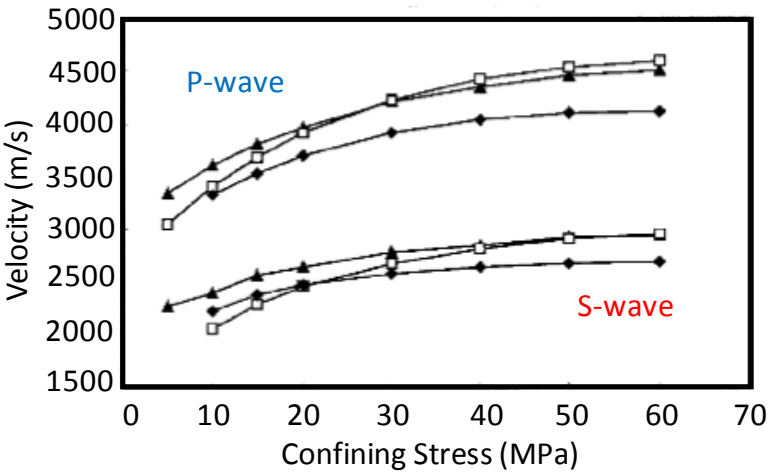

Figure 2.4 *Compressional and shear wave velocities as function of confining stress for three sandstones with different porosity values (after Khaksar et al. 1999).*

Continuing in the velocity domain, the pressure dependence of the compressional and shear velocities can be approximated by a power law. The exponent of this power law, is commonly known as Hertz exponent (Wang and Nur, 1989; Mezghani et al., 2004; Rasolofosaon and Zinszner, 2012)

$$V_P(P_c - P_p) = V_P(\Delta P_a)\left(\frac{P_c - P_p}{\Delta P_a}\right)^{h_p} \tag{2.20}$$

$$V_S(P_c - P_p) = V_S(\Delta P_a)\left(\frac{P_c - P_p}{\Delta P_a}\right)^{h_S} \tag{2.21}$$

where P_c is the confining pressure, P_p the pore pressure, ΔP_a is the asymptotic differential pressure, h_p and h_s the Hertz coefficient for compressional and shear waves respectively. In Mezghani et al. (2004) the Hertz coefficients used for the PUNQ-MONITOR case was 0.05 for compressional wave and 0.20 for shear wave.

2.3.1.2 Pressure dependence on elastic moduli

From Gassmann's equations we can observe that there are three parameters we need to consider which depend on pressure changes and are part of a conventional petroelastic model: the bulk and shear modulus of the rock frame (K_{dry}, μ_{dry}), which define the rock stress sensitivity, and the bulk modulus of the fluid (K_{fl}) which controls the effect of pressure on fluids (Alvarez 2014). One of the most problematic areas in the application of Gassmann fluid substitution model is in the calculation of the dry frame moduli; in the 4D domain, studies on dry frame modelling must incorporate the static dependence of the dry-rock moduli on porosity (Krief et al. 1990; Nur et al. 1998; Pride 2005); as well as relations that show the pressure dependence in the dry frame moduli (Mindlin. 1949, Shapiro and Troyan, 2002; Dvorkin and Gutierrez, 2002; MacBeth, 2004; Lee, 2005; Alvarez and MacBeth, 2014).

MacBeth (2004) proposed a three-parameter formula to describe the sensitivity of the bulk and shear modulus for a sandstone rock frame under isotropic loading.

$$K_{dry} = \frac{\kappa_\infty}{1 + E_\kappa e^{-P_{eff}/P_\kappa}} \tag{2.22}$$

$$\mu_{dry} = \frac{\mu_\infty}{1 + E_\mu e^{-P_{eff}/P_\mu}} \tag{2.23}$$

Where κ_∞ and μ_∞ are the background, high-pressure asymptotes, E_κ, P_κ, E_μ and P_μ are the rock stress sensitivity constants from core measurements that define the shape of the stress sensitivity curve (figure 2.5), and P_{eff} is the effective stress of the reservoir at different times during production, which is related to pore pressure given the following equation:

$$P_{eff} = \sigma_{ob} - n P_{pore} \tag{2.24}$$

where σ_{ob} is the overburden stress and n is the effective stress coefficient ($n \leq 1$) (Berryman 1992a; Gurevich, 2004), the negative sign on the pore pressure indicates that the pore pressure counteracts the effects of the confining pressure (Mavko et al. 2009). MacBeth equations (2004) were tested against 179 sets of laboratory measurements on reservoir core and outcrop sandstones from different depositional environments, geographic locations and with variable range of porosities, such wide data set helped to demonstrate the robustness of the equations.

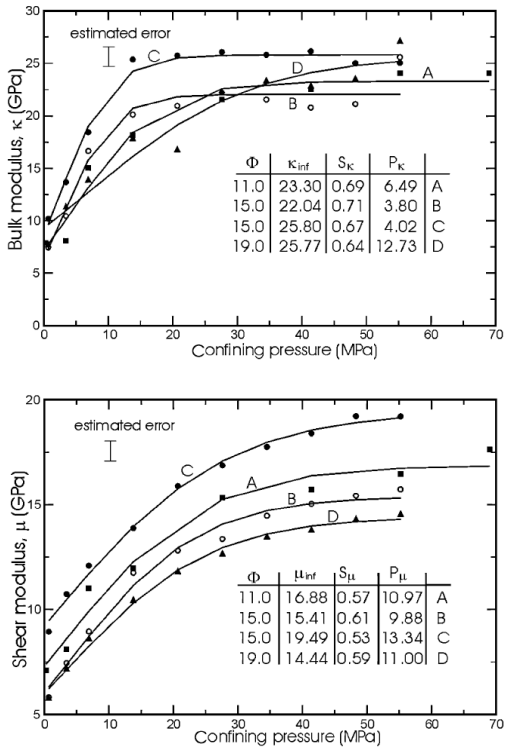

Figure 2.5 *Example of behaviour of the stress sensitivity curves for different porosity sandstones samples (MacBeth 2004)*

MacBeth work (2004) shows a solid dependency between intergranular porosity and the asymptotes κ_∞ and μ_∞ which almost clear linear trend can be seen in figure 2.6, such results is consistent with the empirical critical-porosity trend model (Mavko et al. 2009).

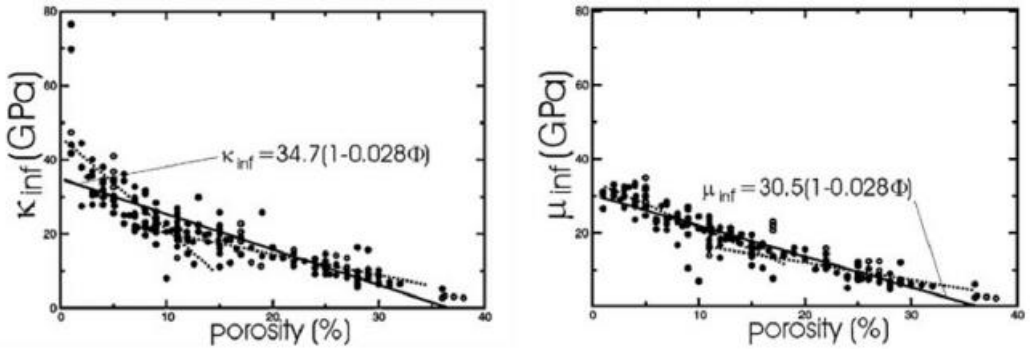

Figure 2.6 *Intergranular porosity dependence of κ_∞ and μ_∞ (Modified from MacBeth, 2004)*

The bulk and shear moduli of dry frame can be also computed using empirical relationships (Dong and Oliver 2008), and through laboratory measurements the corresponding empirical coefficients (a through d) are obtained.

$$K_{dry} = a_0 + a_1 P_{eff} + a_2 \sqrt{P_{eff}} + \left(b_0 + b_1 P_{eff} + b_2 \sqrt{P_{eff}}\right)\phi \tag{2.25}$$

$$\mu_{dry} = c_0 + c_1 P_{eff} + c_2 \sqrt{P_{eff}} + \left(d_0 + d_1 P_{eff} + d_2 \sqrt{P_{eff}}\right)\phi \tag{2.26}$$

Also popularly used in 4D seismic literature is the Hertz-Mindlin model (Mindlin 1949), such model is used to describe the effective bulk and shear modulus or a dry, random, identical-sphere packing, which takes into consideration the effective stress sensitivity in the rock.

$$\kappa_{dry} = \sqrt[n]{\frac{c^2 (1-\phi)^2 \mu_m^2 P_{eff}}{18\pi^2 (1-\nu)^2}} \tag{2.27}$$

$$\mu_{dry} = \frac{5-4\nu}{5(2-\nu)}\sqrt[n]{\frac{3c^2(1-\phi)^2\mu_m^2 P_{eff}}{2\pi^2(1-\nu)^2}} \tag{2.28}$$

where *c* is the average number of contact per grain. In the original Hertz-Mindlin theory the degree of the root (*n*) is 3. However, Vidal et al. (2000) found *n*=5.6 for the compressional wave and *n*= 3.8 for shear wave in gas sand, meanwhile Landrø (2001) used n = 5 for oil sands.

A more simple Hertz formula (Mindlin 1949) has been as well reported in the literature (Lerat et al., 2010; Gervais et al. 2010), which brings together the static component of the dry frame moduli with the effective pressure that varies over time.

$$\kappa_{dry}(t) = \kappa_{dry}\left(\frac{P_{eff}(t)}{P_{eff}^{i}}\right)^{h_\kappa} \tag{2.29}$$

$$\mu_{dry}(t) = \mu_{dry}\left(\frac{P_{eff}(t)}{P_{eff}^{i}}\right)^{h_\mu} \tag{2.30}$$

where $P_{eff}\ (t)$ is the effective pressure at monitor times, and P^{i}_{eff} is the intial reservoir effective pressure. The dry bulk modulus the Hertz coefficient (h_k) is in the range of 0.05 - 0.5, and between 0.03 - 0.5 for the dry shear modulus Hertz coefficient (h_μ).

2.4 Proxy models for Time-lapse seismic interpretation

Changes in both pressure and saturation are expected during productions, the magnitude of these changes are controlled by the rock and fluid properties of the reservoir. Figure 2.7 illustrates the combine effects of pore pressure and saturation changes on acoustic P-wave impedances, which relates to bulk density and compressional velocity. The time-lapse response is indeed a combination of both changes, therefore has been an urge in the industry to discriminate both effects (pressure and saturation) that characterized the seismic signature.

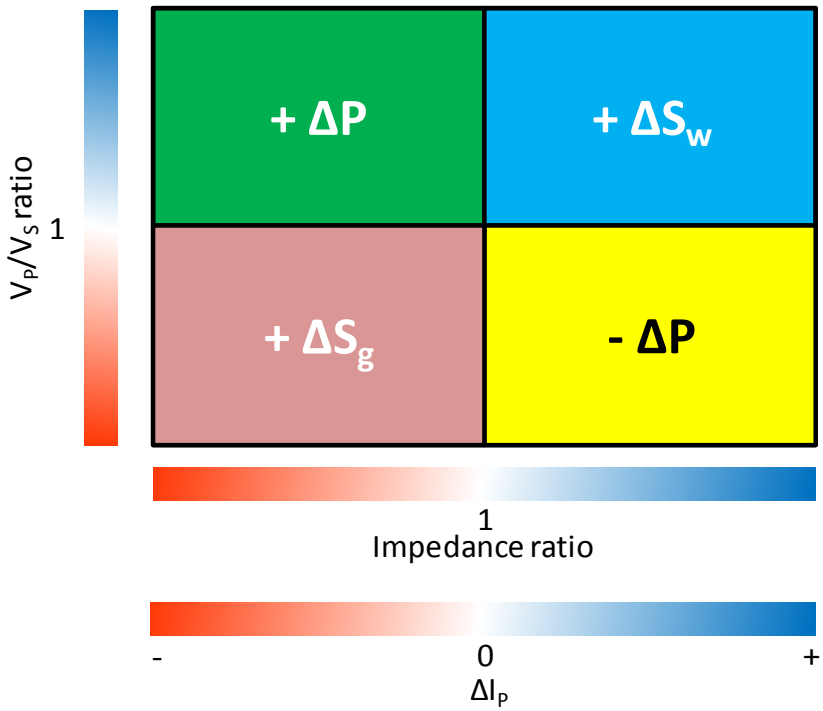

Figure 2.7 *Change of P-Impedances, V_P/V_S and acoustic impedance ratio variations due to changes in the reservoir during production (Modified after Gervais et al. 2010).*

Petro elastic modelling relies on laboratory measurements to estimate the stress sensitivity dependence of the rock frame. However there is a strong need to obtain independent evidence with which to evaluate the PEM recipe (Floricich, 2006). Floricich et al (2006) established a trend equation to predict the 4D seismic response from pressure and saturation changes in the reservoir. Thus the time lapse change for any particular seismic attribute ΔA between the baseline and a preproduction survey can be expressed as:

$$\Delta A = a(1 - e^{b\Delta S_g}) + c\Delta S_w + d\Delta P^2 + f\Delta P \tag{2.31}$$

where ΔS_g, ΔS_w and ΔP are the changes in gas saturation, water saturation and reservoir pressure respectively for a specific monitor-baseline pair, and *a*, *b*, *c*, *d*, and *f* are constants to be determined by calibration to the engineering measurements of production and downhole pressure. To solve for the coefficients a simulated annealing (SA) algorithm is employed to minimize the misfit function between the observed and estimated values. When applied to the Schiehallion Field, it shows a good agreement for water and gas saturation changes, but a discrepancy for pore pressure changes. This can be seen in figure 2.8 where there is a good qualitative agreement for the hardening areas

and the softening areas due to gas coming out of solution, however there is a disagreement in areas of pressure build up; by taking into account the prediction of the simplified equation related to the stress sensitivity, the conventional PEM is updated, thus a more accurate comparison between observed and synthetic data obtained from the simulation model is obtained.

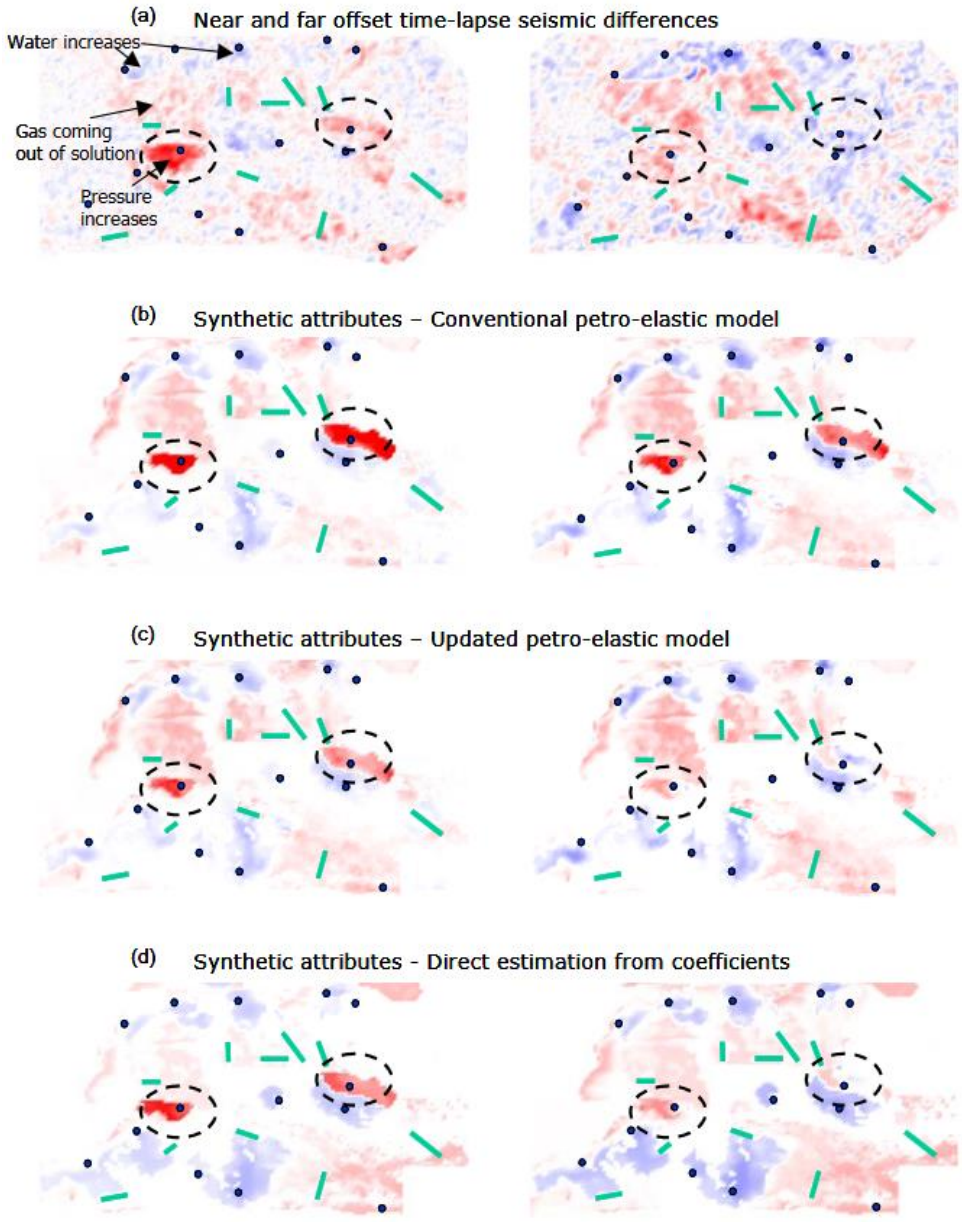

Figure 2.8 *Comparison between observed 4D seismic and synthetic for near and far offset stacks. (a) Observed 4D seismic; (b) synthetic seismic differences using a conventional PEM; (c) synthetic seismic differences updating the stress sensitivity curve in the conventional PEM; (d) synthetic seismic differences using the trend equation for rock and fluid properties. Red represents softening and blue hardening. (Floricich et al., 2006)*

Alvarez and MacBeth (2013) developed a simplified equation where the elastic constants from such equations are related to the petroelastic model. The overall objective of Alvarez (2014) work was to devise a simple formula that can relate seismic, engineering and rock/fluid physic domains for ease of interpretation. Such simplified mathematical expressions and assumptions are attractive for time-lapse studies, but their utility is limited to map based analyses. Indeed, use of 4D maps for visual comparison and understanding of time lapse data, lack the representation of the vertical heterogeneity from the simulation model and seismic domain. The empirically based proxy model described by Alvarez and MacBeth (2013) can be written as:

$$\Delta A = C_S \Delta S_w - C_p \Delta P \tag{2.32}$$

where C_S and C_P are the controlling parameters, which provide the balance between the relative contributions of saturation (ΔS_w) and pore pressure (ΔP) change to the overall time-lapse seismic signature (ΔA) (Alvarez and MacBeth 2013). The negative sign in the equation is preserved whether the impedance contrast at the event is low to high or high to low, forcing both coefficients C_S and C_P to remain positive, C_S is unit less whereas the unit of C_P is MPa^{-1}. Alvarez (2014) validates this simplified equation on a North Sea clastic reservoir, figure 2.9 shows the comparison between the resulting map of the simplified formulation, a full modelling computation using a conventional rock physics model and the observed time-lapse response. The comparison between the observed seismic and the proxy model maps validates Alvarez's approach with normalised errors in the maps of less than 5% despite tuning effects and wave interferences.

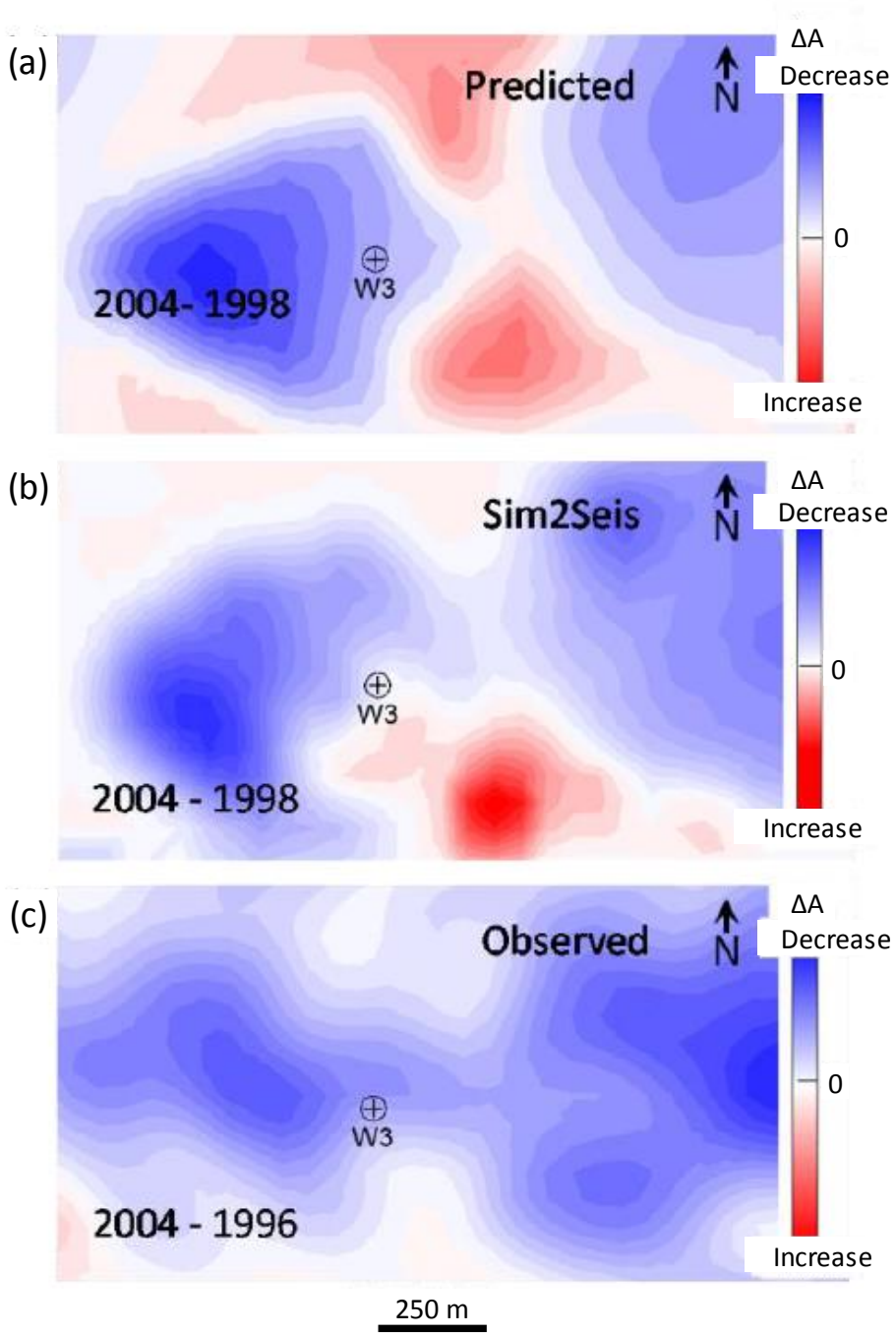

Figure 2.9 *(a) 4D seismic response prediction using the proxy model equation 1.20; (b) Synthetic 4D map using simulation to seismic modelling and (c) Observed 4D seismic response. (Alvarez 2014)*

Even though in the research community there has been an interest in obtaining the 4D seismic response independently from the conventional PEM recipe by using trend or simplified equations, like in the work of Floricih et al. (2006). Alvarez (2014) has

extended the use of the simplified equation (Equation 2.32) to derive the time-lapse response by associating the coefficients of the simple mathematical model to the conventional PEM, which means constants with a clear physical meaning. Hence, it is an attractive model to calibrate and constraint the conventional PEM, especially the stress sensitivity term, which remains the highest uncertain term in any rock physics model.

2.5 Summary

From the literature, it is observed that models can be classified based on geometrical idealization of the rock, however it is far from the complex reality. Such models include simple layer, sphere pack and inclusion models, which help us to build up the set of equations for any conventional PEM. Figure 2.10 shows an overview of the models used in rock physics community.

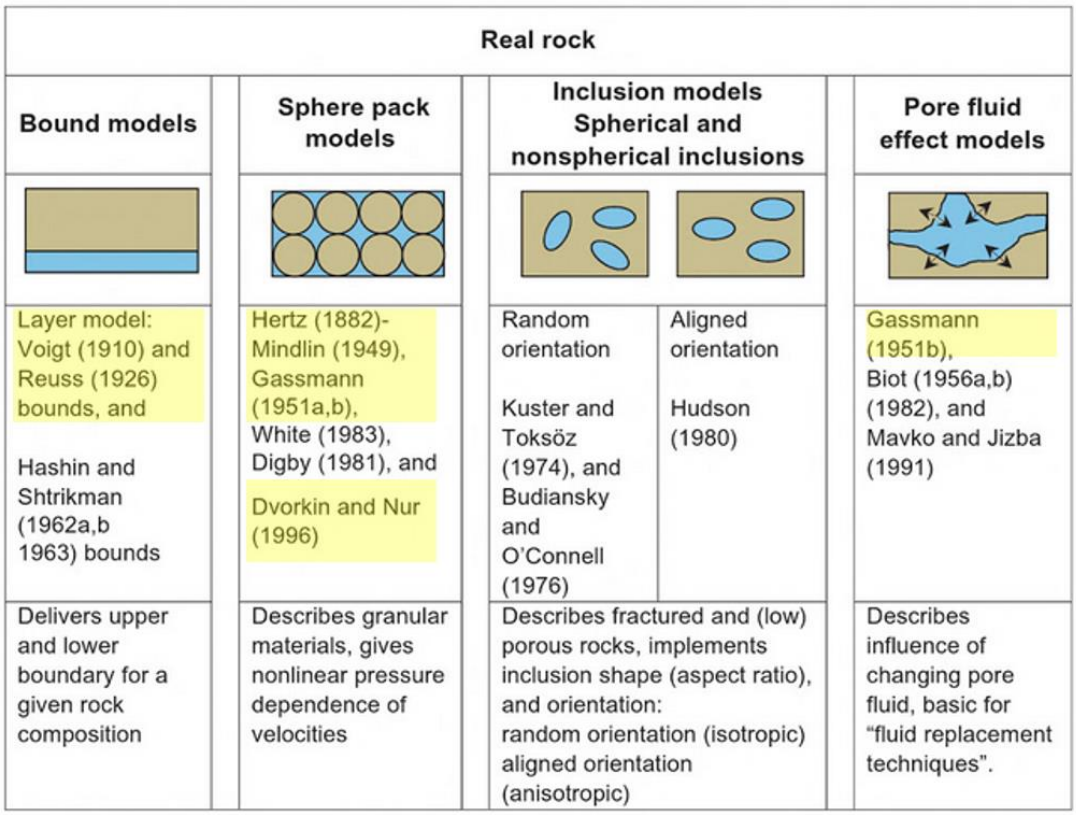

Figure 2.10 *Types of models for elastic properties. Highlighted in yellow are some of the models used in the development of this thesis, which detailed description can be found in the following Chapter 3. (Schön 2015)*

PEM equations are generally developed in the log domain, yet for 4D studies such model must be transferable and used in the simulation model domain. The cells in the flow simulator model are coarser compared to the high frequency logs, which means the cells represent average properties (porosity, NTG, pressure, fluid saturation) within the same volume, that translates in a loss of heterogeneity as is observed in the logs. However the wireline log data does not necessarily capture the lateral variability inside the reservoir. Table 2.2 shows a small summary based on the knowledge acquired of the conventional deterministic PEM and the proxy model used for 4D seismic interpretation studies.

Deterministic PEM	**Proxy PEM**
• Set of equations • Theoretical + Empirical + Heuristic models • Multiple parameters to be determined and calibrated • Underdetermined system • The model has physical meaning in terms of the rock and fluid properties.	• Single Equation • Several coefficients to be determined, using different approaches, like simulated annealing or multilinear regression. • Coefficients can have or not a physical meaning

Table 2.2 Summary of deterministic PEMs versus Proxy models used on 4D seismic studies

Having in mind the objective of this thesis is building a comprehensive PEM for seismic forward modelling, hence needs to be compatible with the parameters of the simulator in the engineering domain. For the purpose of this current thesis, I am going to develop twelve different deterministic PEMs for two clastic fields, and six PEM paradigms for a carbonate reservoir, where the stress sensitivity model proposed by MacBeth (2004) is going to be used, since the static term related to the porosity dependence of the elastic moduli can be explicitly included, for which different heuristic model are considered (more detailed in the following Chapter 3). And more important, equations 2.22 and 2.23 are defined using the same parameters that go into Gassmann fluid substitution model, hence there is a compatibility for their incorporation in the 4D modelling workflow.

Chapter 3

Towards an effective petroelastic model for 4D seismic studies

"All models are wrong but some are helpful" is a recurrent phrase found in rock physics literature. In 4D seismic studies any workflow that requires synthetic seismic computation must rely on a PEM. This chapter focuses on the integration of conventional but appropriate rock physics models used for clastic and carbonate fields, in the context of simulation to seismic modelling.

3.1 Introduction

Any quantitative workflow designed to predict reservoir properties from seismic must rely on a petroelastic model (PEM) which brings together the petrophysical properties and the simulation model domain to the seismic response. Within the time-lapse seismic framework, the PEM represents a crucial element since it links fluid saturation and pore pressure changes in the reservoir rock to the elastic property changes required for seismic modelling, time-lapse feasibility studies, 4D inversion and seismic history matching. The PEM is a series of equations and relationships based on theoretical principles and empirical laws (Menezes and Gosselin 2006) with parameters calibrated against well logs and core data. In this chapter all PEMs consist of two parts: first the static rock components by which the saturated rock frame moduli and density in their initial state are specified, and secondly the dynamic component which is defined by the fluid substitution model, the effect of pressure changes on each fluid phase, and finally the stress dependency of the rock frame density and moduli. For the purpose of our study, six different paradigms described here as models A, B, C and D for clastic reservoirs and E and F for carbonate reservoirs, are used to build the static component that is then calibrated directly by wireline logs. All models have some aspects in common: Gassmann fluid substitution equations and semi-empirical relations for reservoir fluid properties (Batzle and Wang 1992). They also have in common the volume averaging of the solid and liquid phases for calculation of the density, and the Voigt-Reuss-Hill averaging of the mixing of the mineral moduli (figure 3.1).

The preferred PEMs in this thesis, follow three criteria stated in Amini's (2014) work:

1) The PEM must honour the rock and fluid physics.
2) They must capture changes in the reservoir related to saturation changes through a fluid substitution model, and recognize the effect of changes in pore pressure using a stress-sensitivity model.
3) They must be applicable to simulator to seismic modelling, therefore need to be compatible with the parameters of the simulator in the engineering domain.

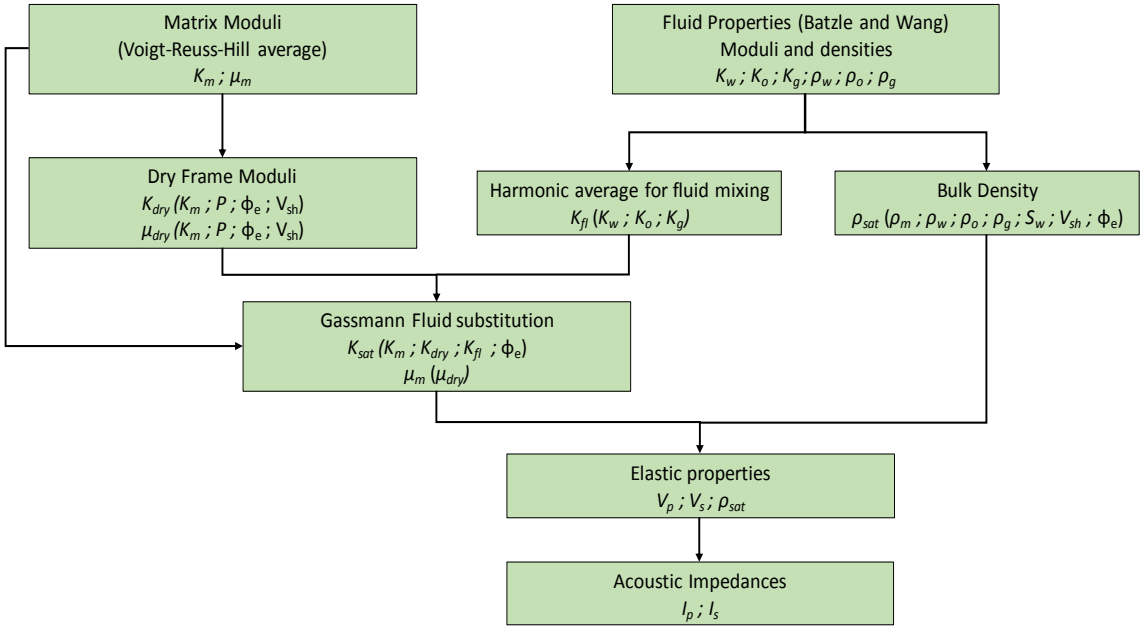

Figure 3.1 *PEM simplified workflow*

3.2 How many PEMs do we need?

As PEMs are lithology and rock fabric specific, it may be necessary to distinguish between different categories of rock physics models, which display significantly different elastic behaviour. Indeed the PEM must be aware of the petrophysics and geology of the field and consequently it is influenced by the choices made when building the cellular fluid simulation model and its subsequent predictions. A different PEM can be constructed for each elastically distinct lithofacies (Alfred et al. 2008) or alternatively a simple but useful approach is to construct a PEM that defines the properties of the mineral for the mixture of two phases using conceptual end member values for density, bulk and shear modulus of the solid constituents. For most clastic reservoirs the main lithologies are sand and shale, meanwhile for carbonate reservoirs are calcite and shale.

In this thesis I show two examples of PEMs following both approaches mentioned. First example when the model cell is specified by a net-to-gross NTG (or volume of shale V_{SH} = 1-NTG). This therefore assumes that the geology and facies variations for a clastic reservoir can be represented by only introducing varying sand/shale fraction within the sand bodies (figure 3.2a); or by varying calcite/shale fraction within the carbonate reservoir layers. However, it is important to highlight that there are other

ways to define the NTG distribution in the geocellular grid, for example the model can be divided into reservoir and non-reservoir cells based on porosity cut-off or facies distribution. In this case, the NTG in the reservoir cells are set to one (1), while for the rest the NTG is set to zero (0).

On the other hand, a second example displays the simulation model cells built by regions with specific NTG and porosity distribution, which represents different geological major formations (figure 3.2b), therefore a representative value for bulk and shear modulus of the matrix for each lithofacies is appropriate to build up the PEM.

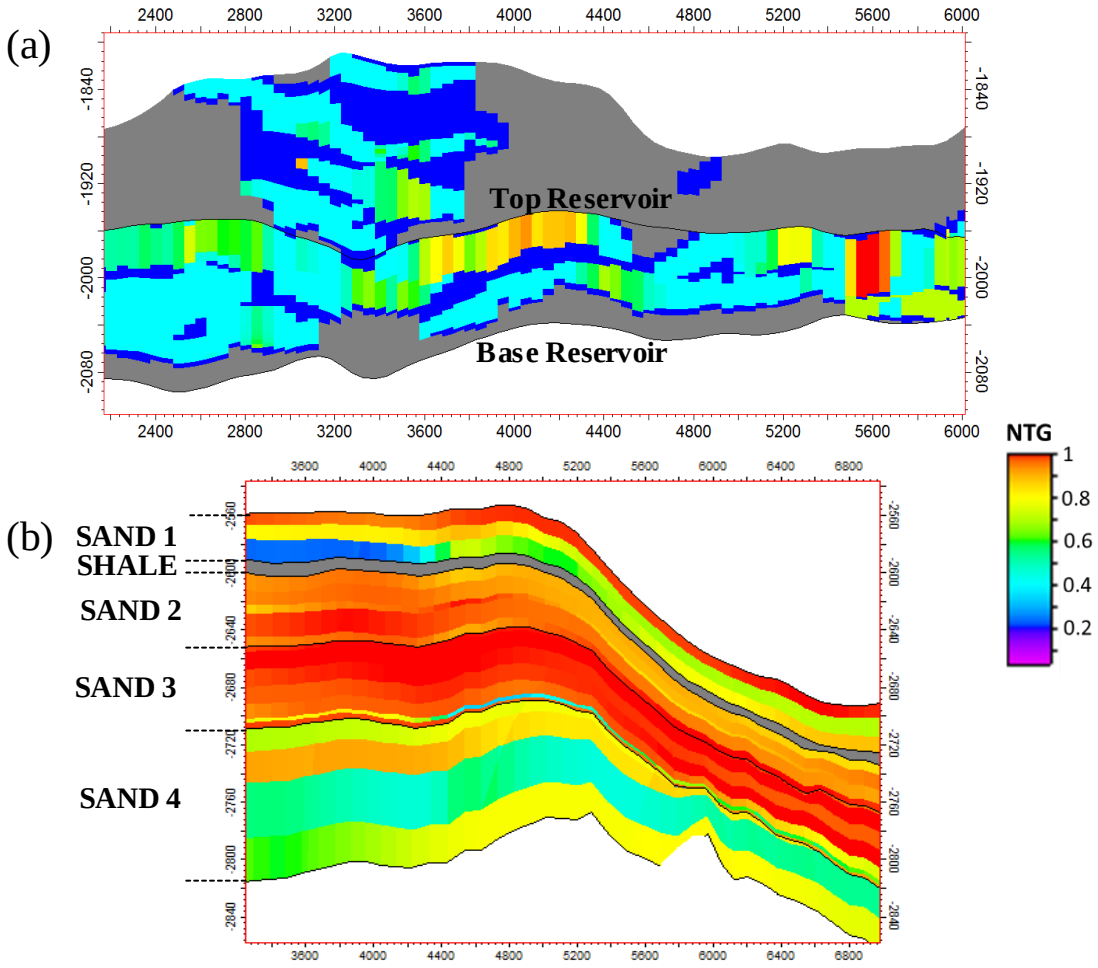

Figure 3.2 *Net-to-Gross (NTG) distribution of the facies in the simulation model. (a) Example 1 for conceptual end members PEM and (b) Example 2 for single lithofacies PEM definition.*

3.3 PEMs for clastic reservoirs

The PEM has been broadly investigated in the literature, especially for siliciclastic rocks; in fact, there are numerous quantitative relationships to link rock properties with pore space, fluid saturation, and pressure and rock composition (Mavko et al., 2009). In this research the exploration of deterministic PEMs is based on the following aspects: dry frame characterization and Gassmann modelling for sand-clay mixtures. The remaining aspects of the rock physics models are kept the same between all the paradigms and they have been already addressed in the literature review in chapter 2. Another important aspect to discuss is the porosity concept, which is understood at multidisciplinary domains, from laboratory to petrophysics and engineering domain. In this thesis, the effective porosity (total porosity less clay-bound water) is used on the construction of all rock physics models. Indeed, effective porosity is lower than total porosity when shale components are present in the rock (Dvorkin et al. 2007) which is the case of most heterogeneous complex reservoirs. Dvorkin et al. (2007) proposed an approach to apply Gassmann fluid substitution in the presence of shaley sediments by using effective porosity which results yielded more sensitivity of the elastic properties of sediment to changes in the pore fluid. Such results translate in better agreement between wells data, 3D seismic and 4D seismic data. The different PEMs in the following chapters (4 and 5) are calibrated against well logs to investigate how each rock physics model balances the changes in pressure and saturation, as reflected in the calculated elastic attributes and resulting 4D seismic models. Hence, this work challenges each PEM within the framework of time lapse data interpretation, in term of their practicality and usefulness.

3.3.1 Dry Frame Characterization

Deriving sensible fluid substitution results in shaly sands using Gassmann fluid substitution model requires a fitting that efficiently stiffens at low porosity rock. This could be achieved by varying the mineral, fluid or dry rock moduli. The most sensible solution is to condition the dry rock model that is used in fluid substitution (Simm 2007). One of the most problematic areas in the application of Gassmann fluid substitution model is in the calculation of the dry frame moduli; in the 4D domain, studies on dry frame modelling must incorporate the static dependence of the dry-rock

moduli ($K_{dry(st)}$, $\mu_{dry(st)}$) on porosity, as well as models that show the dynamic dependency on effective stress ($K_{dry(dyn)}$, $\mu_{dry(dyn)}$). All the PEMs showed in this work have the same modified equation based on MacBeth (2004) to address the stress sensitivity term (equations 3.1 and 3.2).

$$K_{dry(dyn)} = K_{dry(st)}\left(\frac{1+E_{\kappa}\, e^{-P_{res\_eff}/P_{\kappa}}}{1+E_{\kappa}\, e^{-P_{eff}/P_{\kappa}}}\right) \tag{3.1}$$

$$\mu_{dry(dyn)} = \mu_{dry(st)}\left(\frac{1+E_{\mu}\, e^{-P_{res\_eff}/P_{\mu}}}{1+E_{\mu}\, e^{-P_{eff}/P_{\mu}}}\right) \tag{3.2}$$

where E_K, P_K, E_μ and P_μ are the rock stress sensitivity constants from core and laboratory measurements that define the shape of the stress sensitivity curve (MacBeth 2004), P_{res_eff} is the initial effective pressure of the reservoir at preproduction time, P_{eff} is the effective stress of the reservoir at different times during production. Nevertheless, the main difference between each PEM paradigms lies in the static component of the dry frame bulk and shear moduli ($K_{dry(st)}$, $\mu_{dry(st)}$) in terms of the corresponding mineral moduli K_m and μ_m, porosity Φ and volume of shale V_{SH}.

Amini and Alvarez (2014) proposed a calibration of the PEM parameters for 4D seismic studies in multi-mineral rocks, specifically it pays important attention to how the static dependence on porosity and lithology heterogeneity affect the 4D response. For this, two different PEMs were used, PEM-1 considers only the dynamic dependence of the dry frame on the effective stress, and PEM-2 incorporates the variation of shale and matrix volume as well as porosity. Figure 3.3 shows a map of impedance change for PEM-2 and the error difference between both models concluding that a simplification of the dry frame characterization in 4D seismic studies leads to errors of the same magnitude as the 4D seismic signal. PEM 1 over-estimates the water flooding signal by less than 55% and also under-estimates the gas breakout signal by up to 30% (Amini and Alvarez, 2014). Based on this finding, the PEMs presented in this thesis include the dependency of dry frame characterization on porosity and lithology in addition to effective stress.

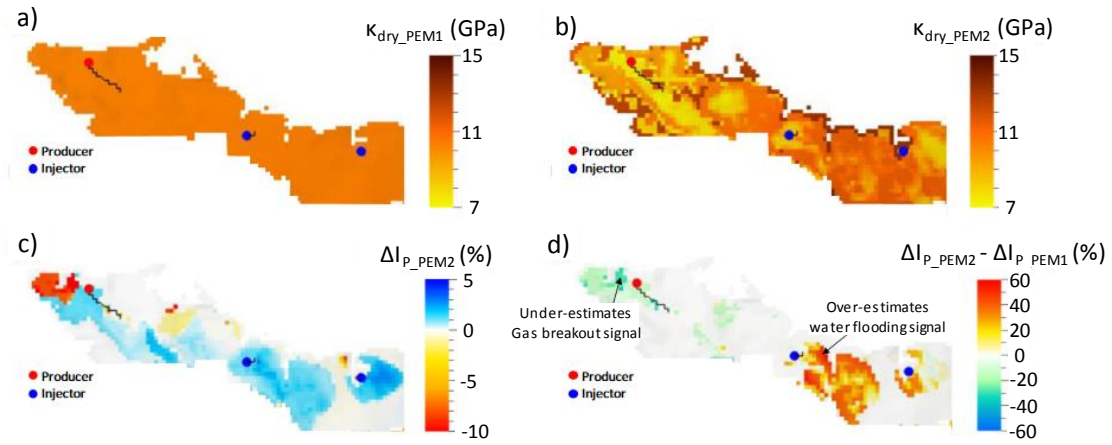

Figure 3.3 *(a) Dry frame at pre-production baseline time without lithology dependency (PEM-1). (b) Dry frame at pre-production baseline time with lithology dependency (PEM-2). (c) 4D response as change of impedance map between monitor and baseline from PEM-2. (d) Difference in predictions between PEM-1 and PEM-2. (After Amini and Alvarez 2014)*

The dry frame characterization calibrated to the log data ($K_{dry(st)}$, $\mu_{dry(st)}$) must be chosen based on the suitability for the field of study which in this case are siliciclastic reservoirs. When in the presence of shaley sandstones, different models have been published with their own assumptions, limitations and complexity. It is worthy to mention Xu-White (1995) model which accounts not only for the effect of porosity and fluid on the calculation of the elastic properties of rock but as well on the pore geometry or pore aspect ratio, although this is not always a known data in any study. The estimation of dry rock bulk and shear moduli for the sand/shale mixture is implemented by applying the differential effective medium method to the Kuster-Toksöz equations for ellipsoidal pores (Xu and White 1995). However, its implementation is computationally intensive, for which Keys-Xu (2002) model was proposed as a solution. Keys and Xu (2002) provided approximations for dry rock bulk and shear modulus, even showing that the critical porosity model can be seen as first-order estimate to the dry rock approximation. Such relevant but complex models help to justify the choice of more simple PEMs in this thesis. The rock physics models used are well known and broadly used in the literature and research community, each paradigm (A, B C and D) is hereafter explained.

3.3.1.1 PEM A

Amini (2014) developed a PEM for sand-shale system in the petrophysical domain by use of well-logs and the laboratory measurements using a dry frame moduli adapted from Lee (2005) based on the consolidation factor α. Instead of using a single value for the consolidation factor, a multilinear regression was engaged to create a consolidation factor aware of the lithology that varies with shale and sand volume and porosity. For clastic fields the consolidation factor lies in the approximate range 2< α <20 (Pride 2005; Lee 2005).

$$K_{dry(st)} = K_m \frac{1-\phi}{1+\alpha\phi} \tag{3.3}$$

$$\mu_{dry(st)} = \mu_m \frac{1-\phi}{1+\alpha\phi} \tag{3.4}$$

$$\alpha = a V_{sand} + b V_{sh} + c\phi \tag{3.5}$$

3.3.1.2 PEM B

Nur et al. (1998) introduced the concept of critical porosity as a key definition to relate physical properties in rocks. Critical porosity ϕ_c separates the mechanical and acoustic behaviour of the rock into two distinct domains (figure 3.4). For porosities lower than ϕ_c, the mineral grains are load-bearing, whereas for porosities greater than ϕ_c, the rock becomes a suspension, in which the fluid phase is load-bearing (Mavko et al. 2009).

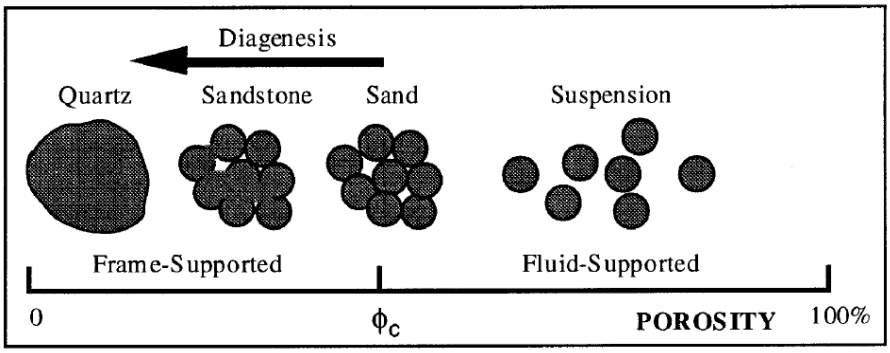

Figure 3.4 *Physical meaning of Critical Porosity (Nur et al. 1998)*

In the load bearing domain, $\phi < \phi_c$ the moduli decrease rapidly from the mineral value at zero porosity to the suspension values at the critical porosity as can be seen in figure 3.5. The geologic interpretation is that for clastic rocks, the weak suspension state at critical porosity describes the sediment when it is first deposited before compaction and diagenesis. The grain sorting and angularity at deposition determine the value of ϕ_c. For sandstones a typical value of critical porosity varies between 36 and 40% (Mavko et al. 2009).

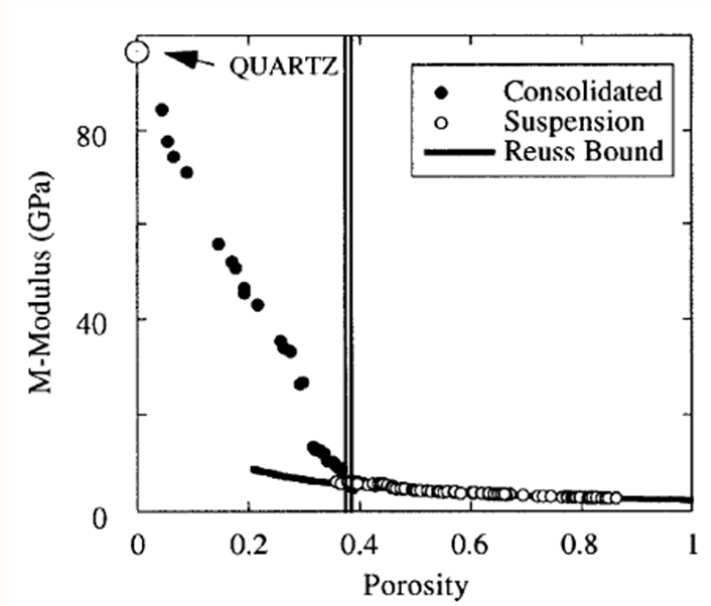

Figure 3.5 *Critical porosity in clean sandstones separates the consolidated rock domain from the suspension domain. (Nur et al. 1998)*

For dry rocks, the bulk and shear modulus can be expressed as the following linear functions:

$$\mu_{dry(st)} = \mu_m \left(1 - \frac{\phi}{\phi_c}\right) \tag{3.6}$$

$$K_{dry(st)} = K_m \left(1 - \frac{\phi}{\phi_c}\right) \tag{3.7}$$

For this thesis, instead of using a constant value for critical porosity through the entire reservoir, I generated a variable critical porosity that represents the heterogeneity of the

lithology, based on the volumes of shale and sand and effective porosity (Amini and Alvarez 2014).

$$\phi_c = aV_{sand} + bV_{sh} + c\phi \tag{3.8}$$

3.3.1.3 PEM C

PEM C is based on Krief et al. (1990) model who suggested a velocity prediction approach similar to the critical porosity model where the dry frame is modeled as porous elastic solid using the Biot coefficient (β) with an empirical relationship against porosity. The dry rock bulk modulus can be written as:

$$K_{dry(st)} = K_m(1-\beta) \tag{3.9}$$

where β is the Biot's coefficient, Krief et al. (1990) found a relation for β versus ϕ empirically based on the low-to-high sandstone data from Raymer et al. (1980)

$$(1-\beta) = (1-\phi)^{m(\phi)} \tag{3.10}$$

$$m(\phi) = \frac{3}{(1-\phi)} \tag{3.11}$$

The empirical fit of $\beta(\phi)$ was performed against shaley sand data (Raymer et al. 1980) which might not be entirely appropriate to the lithology of the clastic fields presented in this work. Instead I generated a modified Krief model that incorporates the variation of lithology centred around the volumes of shale and sand and effective porosity (equation 3.12) obtained using wireline log data for each specific clastic field.

$$m(V_{sh}, V_{sand}, \phi) = \frac{aV_{sand} + bV_{sh} + c\phi}{(1-\phi)} \tag{3.12}$$

3.3.1.4 PEM D

PEM D is based on the intermediate stiff-sand model using the functional form of the soft sand model with Hertz-Mindlin contact theory (equations 3.13 and 3.14) taking into account the pressure effect in the reservoir rocks and the modified Hashin-Shtrikman lower bound to capture the porosity dependence (equations 3.16 and 3.17). The intermediate stiff sand model uses the functional form of the soft sand model but with the high-porosity end point situated on the stiff sand model curve (figure 3.6). The easiest way to generate this model is by increasing the coordination number (*n*) in the soft sand model, which it may not be representative of the actual coordination number of the grain pack at the high porosity end point (Mavko et al. 2009). For this work, the coordination number is kept constant (*n*=20), even though it is known the coordination number varies with porosity. The log fitting by using both approaches (chapter 4 and Appendix B) shows very small error differences between them, less than 0.1%.

$$K_{HM} = \left[\frac{P\left(n\left(1-\phi_c\right)\mu_m\right)^2}{18\left(\pi\left(1-\nu\right)\right)^2} \right]^{1/3} \tag{3.13}$$

$$\mu_{HM} = \frac{5-4\nu}{5\left(2-\nu\right)} \left[\frac{3P\left(n\left(1-\phi_c\right)\mu_m\right)^2}{2\left(\pi\left(1-\nu\right)\right)^2} \right]^{1/3} \tag{3.14}$$

where, ν is the Poisson ratio, defined as:

$$\nu = \frac{3K_m - 4\mu_m}{2\left(3K_m + \mu_m\right)} \tag{3.15}$$

Finally the dry frame moduli are defined with the following equations:

$$K_{dry} = \left(\frac{\phi/\phi_c}{K_{HM}+\frac{4}{3}\mu_{HM}} + \frac{1-\phi/\phi_c}{K_m+\frac{4}{3}\mu_{HM}} \right)^{-1} - \frac{4}{3}\mu_{HM} \tag{3.16}$$

$$\mu_{dry} = \left(\frac{\phi / \phi_c}{\mu_{HM} + \frac{1}{6}\xi \mu_{HM}} + \frac{1 - \phi / \phi_c}{\mu_m + \frac{1}{6}\xi \mu_{HM}} \right)^{-1} - \frac{1}{6}\xi \mu_{HM} \tag{3.17}$$

where ξ is,

$$\xi = \frac{9K_{HM} + 8\mu_{HM}}{K_{HM} + 2\mu_{HM}} \tag{3.18}$$

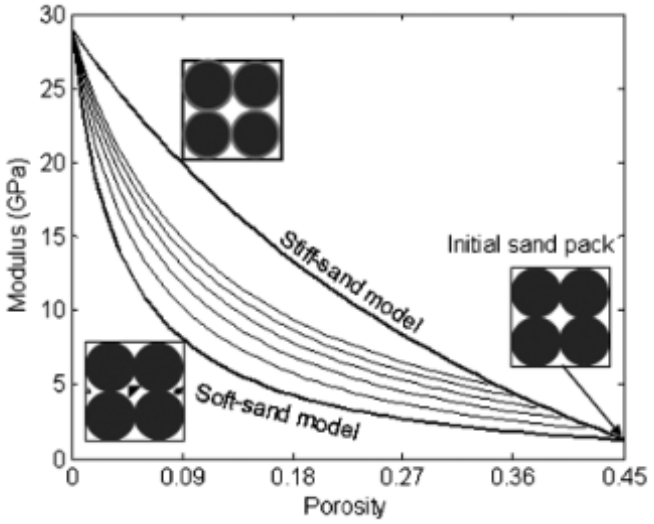

Figure 3.6 *Illustration of the soft and stiff sand model based on the modified Hashin-Shtrikman bounds. The curves between both bounds represent the intermediate-stiff sand model, obtained by increasing the coordination number (Hossain et al 2011).*

3.3.2 Gassmann modelling for sand-clay mixtures

Gassmann's equations are strictly valid for isotropic, homogeneous media, fully saturated and are free of assumptions about the pore geometry. However, the reality of a reservoir is much more challenging than a perfectly isotropic medium, since reservoir rocks are heterogeneous. This is particularly true at the scale of the cell of a fluid flow simulator, due to stratigraphic layering and non-uniform porosity distribution (Falcone et al. 2004). In a sand-clay mixture the application of Gassmann is not straightforward (Smith et al., 2003; Han and Batzle, 2004; Skelt 2004; Simm 2007), since the equations are not valid in a strict sense. In the literature, the computation of the elastic properties

from such a composite rock (sand and shale) has been covered by Gurevich and Carcione (2000) and Amini (2014), who suggested two schemes based on the same scientific reasoning. In a simplified manner, the first scheme mixes the moduli of the two single constituents and then computes fluid substitution to obtain the saturated moduli of the composite rock. In the second scheme, fluid substitution is applied to the single constituents separately (only sand, for the clay component is assigned a single value to the wet clay) to obtain the saturated moduli of each component and later uses a mixing law to determine the final fluid saturated moduli of the multi-mineral rock.

Following Amini's work (2014) it is decided to perform sand-clay mixing prior to fluid substitution and a second approach, mixing after fluid substitution to the models A, B, C and D previously explained. For mixing before fluid substitution, the elastic moduli of the dry composite rock matrix are computed by mixing the mineral moduli of dry sand and clay matrices using Voigt-Reuss-Hill (VRH). Then the saturated moduli are computed using Gassmann. On the other hand, the second approach, mixing after fluid substitution, uses Gassmann equations to compute independently the elastic moduli of the saturated sand and clay from their respective dry moduli. The saturated sand and clay components are then mixed using the same composite mixing law used in the first approach. It is important to highlight that the fluid substitution in the clay component assigns a single modulus value to the wet clay (figure 3.7).

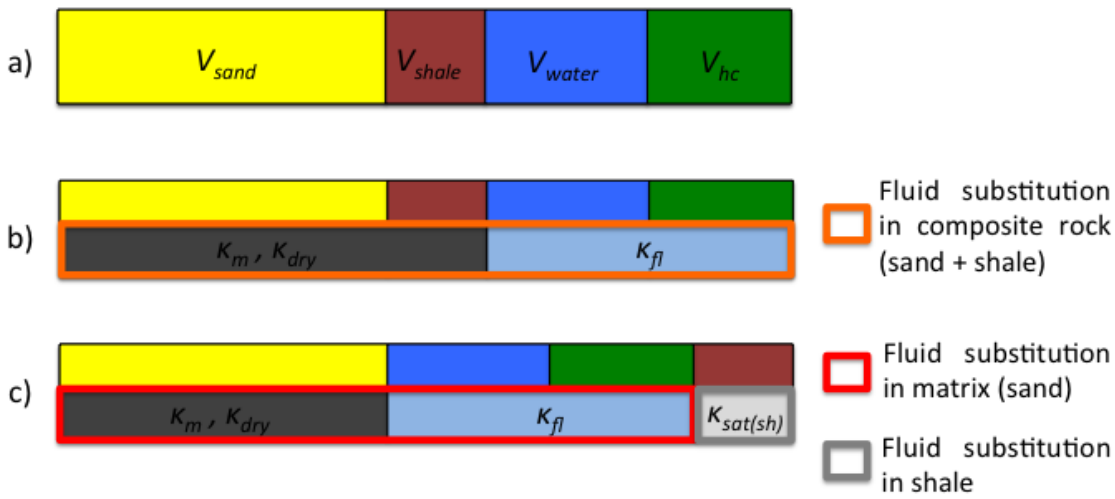

Figure 3.7 *Fluid substitution modelling for sand-shale mixture. (a) Rock components model, (b) sand-shale mixing before fluid substitution and (c) sand-shale mixing after fluid substitution (After Amini 2014).*

In a sand-clay mixture the seismic response is influenced by the clay distribution inside the reservoir, such distribution will impact the effective elastic medium used to obtain the elastic moduli of the grain mixture. Figure 3.8 shows a clastic system, which consists of clean sands, shales, sand with dispersed clay, or sand with laminar clay distribution (Mavko et al. 2009). In a homogenous dispersed clay distribution the VRH average is the most common mixing law used; nevertheless, if the clay distribution is laminar, it violates the assumption that the rock is isotropic, hence the VRH average must be substituted by a different averaging law appropriate for sands with laminated clay or a different solution for fluid substitution for laminar shales must be found (Skelt, 2004; Katahara, 2004; Dejtrakulwong and Mavko, 2011). Even though, core data and thin section analysis are necessary to understand the clay distribution, such data are not always available. To capture how laminar clay will affect the PEMs in this study, it is decided to apply Backus averaging (1962) after fluid substitution for the models A, B, C and D, since the Backus average allows a prediction of the elastic moduli of a laminated composite in term of the individual layer properties (Mavko et al., 2009).

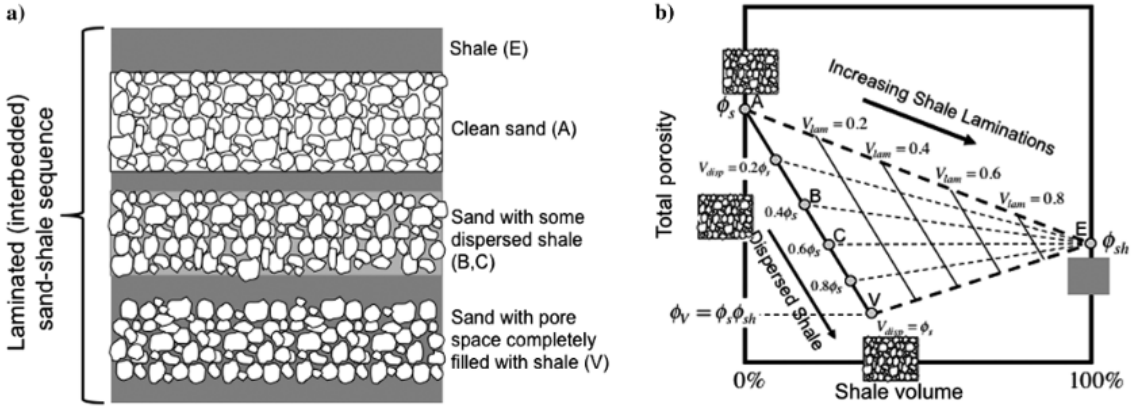

Figure 3.8 *(a) Models of sand-shale system. (b) Thomas-Stieber model for porosity versus shale volume, which shows the different distribution of clay in a sand-clay system (After Dejtrakulwong and Mavko 2016)*

Backus average is the last step when building the PEM, since the saturated moduli of each rock components (sand and shale) are calculated using Gassmann fluid substitution. The brackets <.> in the following equations indicate averages of the enclosed properties weighted by their volumetric proportions (Mavko et al. 2009). Although Backus takes into consideration anisotropy of the effective medium, for the

current work, I am only interested in the vertical component of the compressional and shear wave velocities. The Backus equations are written as follows:

$$V_{p,v} = \sqrt{\frac{\left\langle \kappa + \frac{4}{3}\mu \right\rangle}{\rho}} \tag{3.19}$$

$$V_{s,v} = \sqrt{\frac{\langle \mu \rangle}{\rho}} \tag{3.20}$$

$$\left\langle \kappa + \frac{4}{3}\mu \right\rangle = \left[\frac{V_{sh}}{\kappa_{sat(shale)} + \frac{4}{3}\mu_{sat(shale)}} + \frac{(1 - V_{sh})}{\kappa_{sat(sand)} + \frac{4}{3}\mu_{sat(sand)}} \right]^{-1} \tag{3.21}$$

$$\langle \mu \rangle = \left[\frac{V_{sh}}{\mu_{sat(shale)}} + \frac{(1 - V_{sh})}{\mu_{sat(sand)}} \right]^{-1} \tag{3.22}$$

3.4 PEMs for carbonate reservoirs

So far 4D seismic studies has been almost exclusively applied to clastic reservoirs and seldom to carbonates, since such reservoirs are stiffer and the effect on the seismic parameters due to production are less pronounced than on clastic rocks (Landrø 2015). Developing a robust, practical and accurate rock physics model for carbonate reservoirs is crucial for geophysical applications and 4D seismic studies (Xu et al. 2007). Application of a Gassmann fluid substitution model can be used for relatively homogenous sandstone reservoir rocks, yet they may need modifications in order to be applicable to carbonate rocks. This is because the internal pore structure in carbonates are far more complex than in siliciclastic rocks. Gassmann equations are not only widely used because of their simplicity and since the inputs parameters can be obtained from log measurements, but moreover they are free of assumptions about pore geometry, although the pore system must be completely connected. This assumption is violated in low porosity rocks, including carbonate rocks, where porosity ranges from

15% to more than 30% and they exhibit high complexity of pore structures where pore shape, pore size, pore and matrix connectivity affect the elasticity of the rock and the fluids (Eberli et al. 2003). Certainly, the effects of pore structures on elastic moduli should be considered either explicitly or implicitly in any PEM used for 4D seismic studies. A second assumption is that the fluid saturation affects only the bulk modulus and not the shear modulus. In carbonates, however, studies have shown that the shear modulus changes between 5 and 20% from dry to brine saturated carbonates (Japsen et al., 2002, Assefa et al. 2003, Baechle et al 2005).

In the literature, there exist authors that question the applicability of Gassmann (Wang 1997; Baechle et al. 2005), while others state that Gassmann works well in most applications (Adam et al. 2006; Bhakta and Landrø 2013). de Paula et al. (2010) showed results of a carbonate reservoir in Santos Basin, offshore Brazil, demonstrating that Gassmann fluid substitution in carbonates using ultrasonic measurements on dry samples yields elastic moduli that are in a good agreement with the compressional wave moduli derived from sonic and bulk density logs (figure 3.9). This good agreement provides validation that the Gassmann equations can be applied not only in siliciclastic reservoirs, but also in the complex carbonates reservoirs.

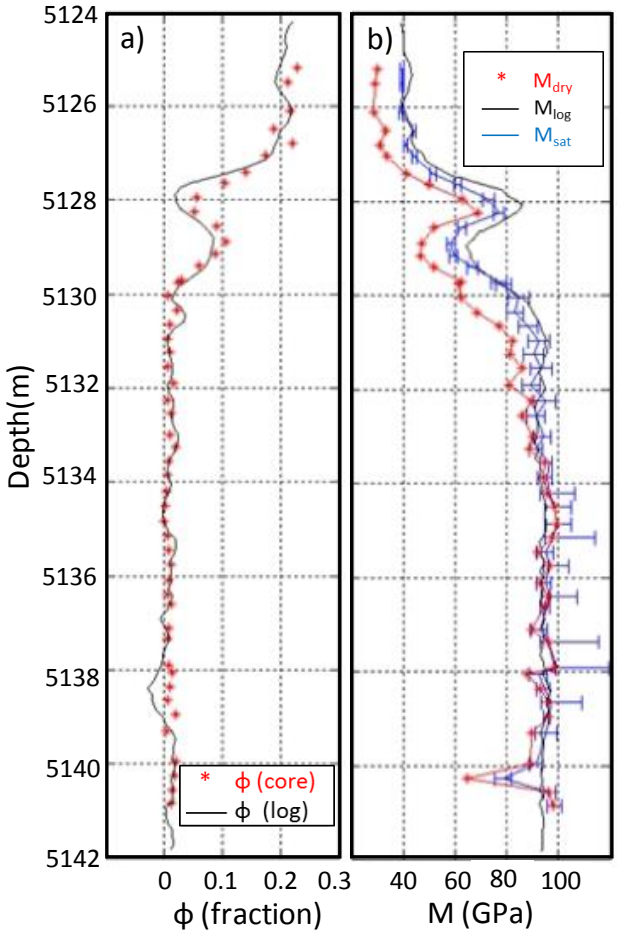

Figure 3.9 *(a) Porosity measured in 50 carbonate samples (red) showing good agreement with the porosity obtained from the bulk density log (black). (b) Comparison between the P-wave modulus (M= κ + (4/3)*μ) obtained from lab measurements (red), well logs (black) and the saturated modulus resultant from Gassmann fluid substitution (blue). (de Paula et al. 2010)*

For the purpose of this work, two different PEMs (E and F) are constructed based on theoretical and heuristic models that consider the complex internal structure of carbonates rocks. First I compute the dry frame moduli using the modified upper Hashin-Shtrikman (PEM E) and then the Self-Consistent Approach (PEM F) which combine with Gassmann fluid substitution give an approximation of the low frequency saturated rock. The rock physics models used for a carbonate field in this thesis are hereafter explained.

3.4.1.1 PEM E

The Modified Upper Hashin-Shtrikman model (Walls et al., 1998; Anderson 1999; Bahkta and Landrø 2013) connects two end members in the elastic modulus-porosity

plane, one end member (κ_o, μ_o) is at critical porosity while the other end member is at zero porosity which refers to the mineral moduli (κ_m, μ_m) (figure 3.10).

$$\kappa_{dry} = \kappa_m + \frac{\phi / \phi_c}{(\kappa_o - \kappa_m)^{-1} + \left(1 - \phi / \phi_c\right)\left(\kappa_m + \frac{4}{3}\mu_m\right)^{-1}} \tag{3.23}$$

$$\mu_{dry} = \mu_m + \frac{\phi / \phi_c}{(\mu_o - \mu_m)^{-1} + \frac{2\left(1 - \phi / \phi_c\right)(\kappa_m + 2\mu_m)}{5\mu_m\left(\kappa_m + \frac{4}{3}\mu_m\right)}} \tag{3.24}$$

At critical porosity the dry frame bulk and shear modulus (κ_o, μ_o) is modelled as cavities saturated with air, where the shear modulus (μ_o) is set to zero and the bulk modulus (κ_o) is obtained through Reuss average at critical porosity.

$$\kappa_o = \frac{\kappa_m \kappa_{air}}{(1 - \phi_c)\kappa_{air} + \phi_c \kappa_m} \tag{3.25}$$

$$\mu_o = 0 \tag{3.26}$$

The critical porosity in carbonates is variable depending on the lithology from 40% up to 65%, to include the lithology dependency it was decided to calculate a variable critical porosity through a multi-linear regression as can be seen in chapter 4, from which coefficients a, b and c can be related to the volumetric proportions of calcite and shale and the effective porosity.

$$\phi_c = aV_{calcite} + bV_{sh} + c\phi \tag{3.27}$$

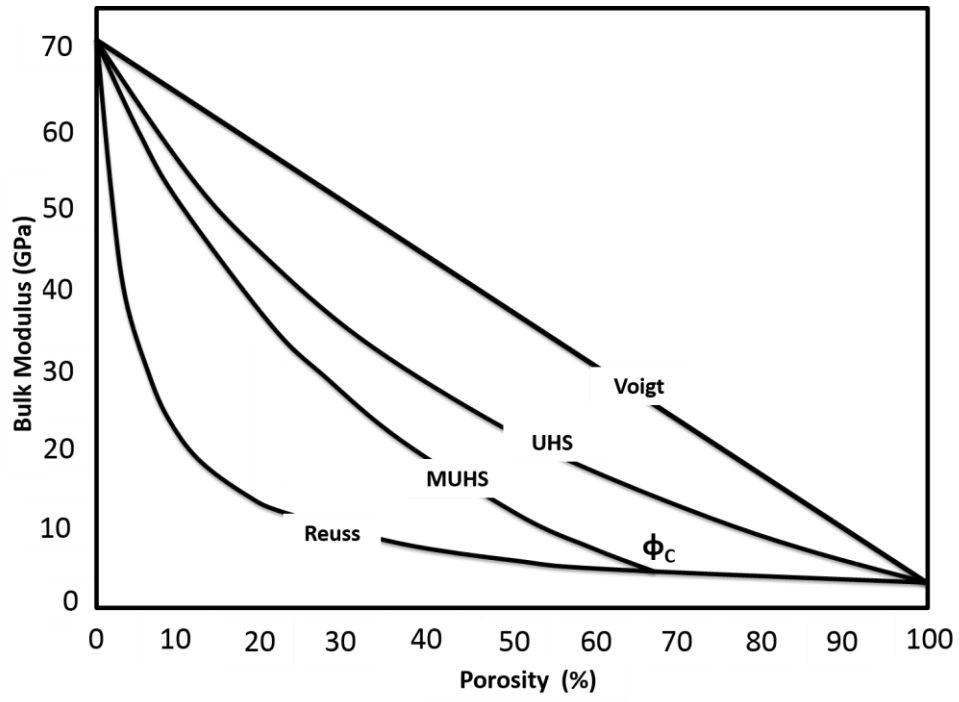

Figure 3.10 *Effective elastic bulk modulus predictions of a brine-bearing chalk versus porosity. Upper Hashin–Shtrikman bound (UHS), and the modified upper Hashin-Shtrikman bound (MUHS) together with Voigt and Reuss bounds are included. (Redrawn from Gommesen et al. 2007)*

3.4.1.2 PEM F

Theoretical estimates of the effective moduli depend on the properties of the individual components of the composite rock, their respective volume fractions and the geometric descriptions related to the shape details and spatial distribution of the components in the rock. The afore-explained rock physics model (PEM E) doesn't include geometric details. Therefore a second PEM that takes into consideration pore shapes is presented in this research. Wu's Self-Consistent Approximation (Wu, 1966; Mavko et al. 2009; Bahkta and Landrø 2013) estimates the effective moduli for two-phase composites of the form:

$$\kappa_{dry} = \kappa^*_{SC} = \kappa_m + x_i(\kappa_i - \kappa_m)P^{*i} \tag{3.28}$$

$$\mu_{dry} = \mu^*_{SC} = \mu_m + x_i(\mu_i - \mu_m)Q^{*i} \tag{3.29}$$

At low frequencies, the effective dry frame of dry cavities is modelled by setting the inclusion moduli to zero, and then saturating them and performing Gassmann fluid substitution (Mavko et al. 2009). A more general form of the Self-Consistent Approximation for N-phase composites was proposed by Berryman (1980b)

$$\sum_{i=1}^{N} x_i \left(\kappa_i - \kappa_{SC}^{*}\right) P^{*i} = 0 \tag{3.30}$$

$$\sum_{i=1}^{N} x_i \left(\mu_i - \mu_{SC}^{*}\right) Q^{*i} = 0 \tag{3.31}$$

Where P and Q are geometric factors for specific shapes including spheres, needles disk and penny cracks. The subscripts *m* and *i* refer to the matrix and the inclusion materials (Mavko et al. 2009). The application of the Self Consistent Approach is limited due to the lack of information about the volume fraction, the aspect ratio for each pore type, and the geometrical description of the pores (Bahkta and Landrø 2013). Table 3.1 shows the equations used for the geometric factors of spheres and needles used in this work.

Inclusion Shape	P^{*i}	Q^{*i}
Spheres	$\dfrac{\kappa_m + \frac{4}{3}\mu_m}{\kappa_i + \frac{4}{3}\mu_m}$	$\dfrac{\mu_m + \zeta_m}{\mu_i + \zeta_m}$
Needles	$\dfrac{\kappa_m + \mu_m + \frac{1}{3}\mu_i}{\kappa_i + \mu_m + \frac{1}{3}\mu_i}$	$\dfrac{1}{5}\left(\dfrac{4\mu_m}{\mu_m + \mu_i} + 2\dfrac{\mu_m + \gamma_m}{\mu_i + \gamma_m} + \dfrac{\kappa_i + \frac{4}{3}\mu_m}{\kappa_i + \mu_m + \frac{1}{3}\mu_i}\right)$
$\gamma = \mu\dfrac{(3\kappa + \mu)}{(3\kappa + 7\mu)}$		$\zeta = \dfrac{\mu}{6}\dfrac{(9\kappa + 8\mu)}{(\kappa + 2\mu)}$

Table 3.1 *Coefficients P and Q for spheres and needles shape. The subscripts m and i refer to the background matrix and inclusion material respectively (Mavko et al. 2009).*

3.5 Summary

A key ingredient of time lapse seismic interpretation is the petroelastic model (PEM), which links fluid saturations and pore pressure changes in the reservoir rock to the elastic property changes. All conventional deterministic PEMs consist of two parts: the static rock components by which the saturated rock frame moduli and density in their initial state are specified, and the dynamic component which is defined by the fluid substitution model, effect of pressure changes on each fluid phase, and finally the stress dependency of the rock frame density and moduli. The characterization of the PEMs and their parametrization will help to define the accuracy and confidence of 4D seismic interpretation studies. The necessity of calibration of the PEM parameters to the in-situ response for each fields is accessible in chapter 4. Indeed for each PEM a large number of free parameters are required to be determined (nine parameters for PEMs A, B, C and E. eight for model D and six for model F), plus four laboratory coefficients in common since all the PEMs share the same stress sensitivity model (table 3.2).

	Clastic Reservoirs				**Carbonate Reservoirs**	
	PEM A	**PEM B**	**PEM C**	**PEM D**	**PEM E**	**PEM F**
Static	9 Parameters $\kappa_{sand,shale}$ $\mu_{sand,shale}$ $\rho_{sand,shale}$ $\alpha \rightarrow$ a,b,c	9 Parameters $\kappa_{sand,shale}$ $\mu_{sand,shale}$ $\rho_{sand,shale}$ $\phi_c \rightarrow$ a,b,c	9 Parameters $\kappa_{sand,shale}$ $\mu_{sand,shale}$ $\rho_{sand,shale}$ $m(\phi) \rightarrow$ a,b,c	8 Parameters $\kappa_{sand,shale}$ $\mu_{sand,shale}$ $\rho_{sand,shale}$ ϕ_c *n*	9 Parameters $\kappa_{calcite,shale}$ $\mu_{calcite,shale}$ $\rho_{calcite,shale}$ $\phi_c \rightarrow$ a,b,c	6 Parameters $\kappa_{calcite,shale}$ $\mu_{calcite,shale}$ $\rho_{calcite,shale}$
Dynamic	4 Parameters for the stress sensitivity model E_K, P_K, E_μ and P_μ					

Table 3.2 *Rock properties parameters for each deterministic PEM, to be calibrated against wireline log data.*

As for the properties of the fluids (table 3.3), all the PEMs commonly include them as function of pressure, temperature and salinity based on empirical correlations (Batzle and Wang, 1992; Han and Batzle, 2000a, b).

Fluid and reservoir properties	Units
Reservoir Temperature	^{o}C , ^{o}F
Water Salinity	ppm
Oil gravity	API
Gas gravity (Gg)	unitless
Bubble point pressure (Pbp)	psi, bars, MPa
Initial reservoir pressure	psi, bars, MPa

Table 3.3 *Fluid parameters for the deterministic PEM.*

Chapter 4

Calibration of the Petroelastic model

The definition and parameterization of the PEM will define its ultimate accuracy and the understanding of 4D seismic interpretation studies. This chapter emphasises the necessity of calibration of the PEM parameters to the in-situ response. Since the PEM is fabric and lithology dependent, using values from look-up tables in the literature might yield erroneous results that will carry forward through the entire forward modelling process and jeopardize the qualitative and quantitative interpretation of the 4D seismic.

4.1 Introduction

Seismic petrophysics integrates laboratory and well-derived rock and fluid properties data, guaranteeing the development of a rock physics model with predictive capability (Kittridge et al. 2008). The PEM in the 3D and 4D domains uses the products of a petrophysical evaluation (porosity, shale volume, fluid saturations) as inputs, together with the results of laboratory measurements to understand how the seismic signal responds to changes in the reservoir properties due to production (Hall and Alvarez 2014).

Using a conventional deterministic PEM comes at the cost of using many reservoir dependent variables, as it is an under-determined problem. Numerous past studies have now pointed to the limitations and uncertainties that can exist within current models (Falcone et al. 2004; Roggero et al. 2007; Amini 2014). The PEM is lithology dependent therefore needs to be calibrated to the in situ response. Indeed one of the main challenges is to set the correct field dependent input parameters into the equations, since values from lookup tables in the literature might yield erroneous results. Coléou et al. (2005) recognises that the PEM calibration is a critical step, since it reconciles different static measurements (cores, logs and seismic) obtained at different scales and domains (depth and TWT). The calibration performed against well data, predicts V_p, V_s and ρ through forward modelling, that are then compared to the measured compressional and shear sonic and density logs. A wide amount of relationships are available in the literature to assist with the generation of pseudo density and velocity data. Approaches for estimating V_p, V_s and ρ logs from seismic petrophysics can be grouped into: 1) application of effective medium models, 2) application of heuristic models and 3) application of empirical models (Smith 2011).

Aleardi and Ciabarri (2017) evaluate different methods in developing a robust static PEM conducted in log data from offshore Nile Delta, using a deterministic approach with elastic moduli parameters for sand and clay are reported from the literature (Avseth et al. 2005; Mavko et al. 2009; Moyano et al. 2012). Moreover, three empirical relationships to obtain V_p, V_s and ρ using multilinear stepwise regression, neural networks and genetic algorithm were tested (figure 4.1). By using literature values for the inputs parameters of the theoretical PEM, the model becomes data-independent and

it might yield good predictions if only the assumptions made in deriving the model are substantiated and the inputs parameters are in good agreement with the true ones (Aleardi and Ciabarri 2017). In contrast, the work presented in this chapter expects the calibration of the different PEM paradigms to be data driven. It is important to be aware that all published coefficients and parameters are lithology specific, and do not apply on a global scale

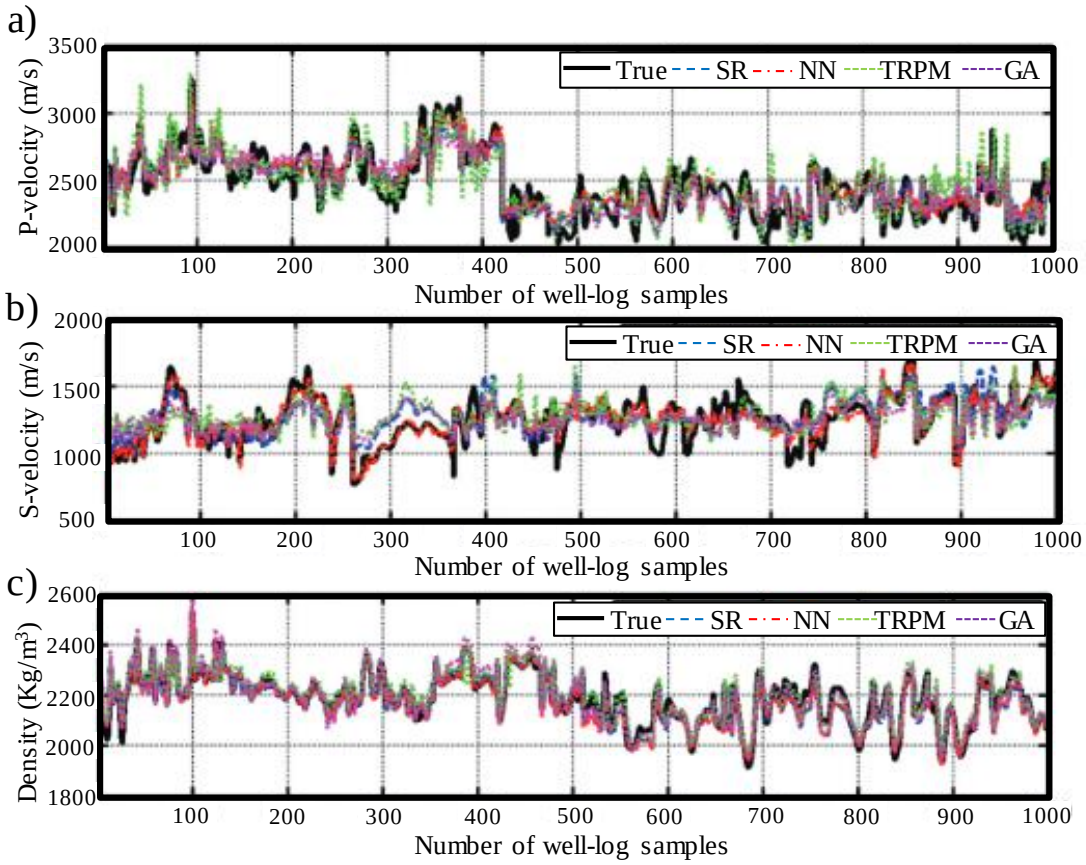

Figure 4.1 *Comparison between the measured log data and the predicted elastic properties from four PEMs. SR: stepwise regression, NN: neural network, GA: genetic algorithm and TRPM: theoretical rock physics model. a) Compressional velocity (V_p), b) shear velocity (V_s) and c) bulk density (ρ). (After Aleardi and Ciabarri 2017)*

In this chapter, wireline log data from three different fields (two clastic and one carbonate field) is used to calibrate the static parameters of the PEMs. Those have been previously explained in detail in Chapter 3 based on effective medium theory together with heuristic models that require estimation of dry frame moduli and Gassmann fluid substitution equations. The calibration is performed through reconstruction of the compressional and shear sonic (V_p, V_s) logs as well as the bulk density (ρ) log using the

calculated porosity, water saturation and shale volume logs from the petrophysical evaluation which carry intrinsic uncertainties using an optimization algorithm.

4.2 Log optimization algorithm

One of the main challenges in developing a robust and accurate PEM is to set the correct input parameters (density, bulk and shear modulus) into the set of equations. To solve the under-determined problem of finding the right inputs for each PEM, an optimization algorithm based on the models previously mentioned in chapter 3 is implemented. The optimization algorithm is described in Figure 4.2, where the inputs to the algorithm, are the porosity, water saturation and volume of shale logs that come from petrophysical analysis, in-situ properties of the fluids including salinity, temperature and API gravity; the initial pore pressure log which is extracted from the simulation model along a well trajectory, and a reasonable range for density and bulk/shear moduli of the solid components (sand and shale for the clastic reservoirs; calcite and shale for the carbonate reservoir). For all the possible combinations of the input parameters, the PEM is evaluated and the predicted V_p, V_s and ρ logs are compared against the measured sonic and density logs within the depth interval(s) of interest. The optimization algorithm is based on statistical criteria for the evaluation of the parameterization performances by using the percent mean relative error (PMRE) between measured (m) and predictive elastic logs (e) as objective function (equation 4.1) (Amini 2014; Amini and Alvarez 2014).

$$PMRE = \frac{100}{N} \sum_{i=1}^{N} \left| \frac{e_i - m_i}{m_i} \right| \tag{4.1}$$

The optimization predicts first the bulk density log, which outputs the density of the solid components associated with the least misfit error between measured and predicted logs ($PMRE_\rho$). Finally, it performs the reconstruction of the compressional and shear sonic logs where the outputs are the set of elastic moduli (bulk and shear) of the solid components and coefficients related to the specification of each PEM (A, B, C, D, E and F). They are associated with the least misfit of the sum of both velocities errors of the form $min(PMRE_{Vp} + PMRE_{Vs})$. All calibrated parameters are used later when I implement the PEM in simulator to seismic modelling (sim2seis) in the next Chapter 5.

Amini (2014) shows that the main advantage of the optimization is that can be performed over several wells simultaneously to capture the most representative values of the entire reservoir. However, in this work the optimization is performed well by well to create different scenarios in order to understand the possible variability of the inputs related to the geology, and to assess confidence of the reconstructed logs and investigate the non-uniqueness of the rock physics models. Three fields with different geological setting and lithology are used for the calibration of the rock physics model to the data. A general description of each field is given in Chapter 5. For the Schiehallion field five wells are used, two of those wells are divided into specific depth intervals (figure 4.3a). For the Norne field, four wells (figure 4.3b), meanwhile for the carbonate field, there are five wells in total (figure 4.3c)

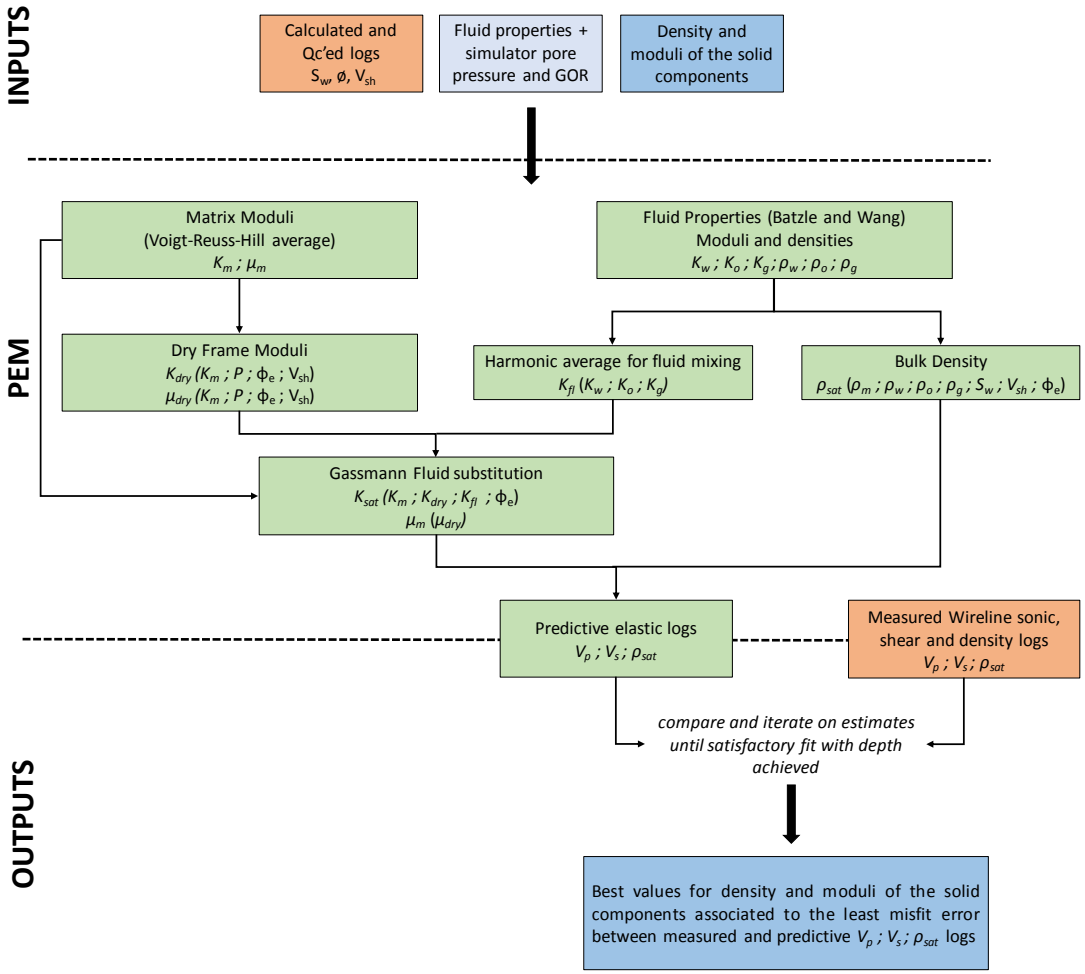

Figure 4.2 *The PEM optimization workflow (After Amini, 2014)*

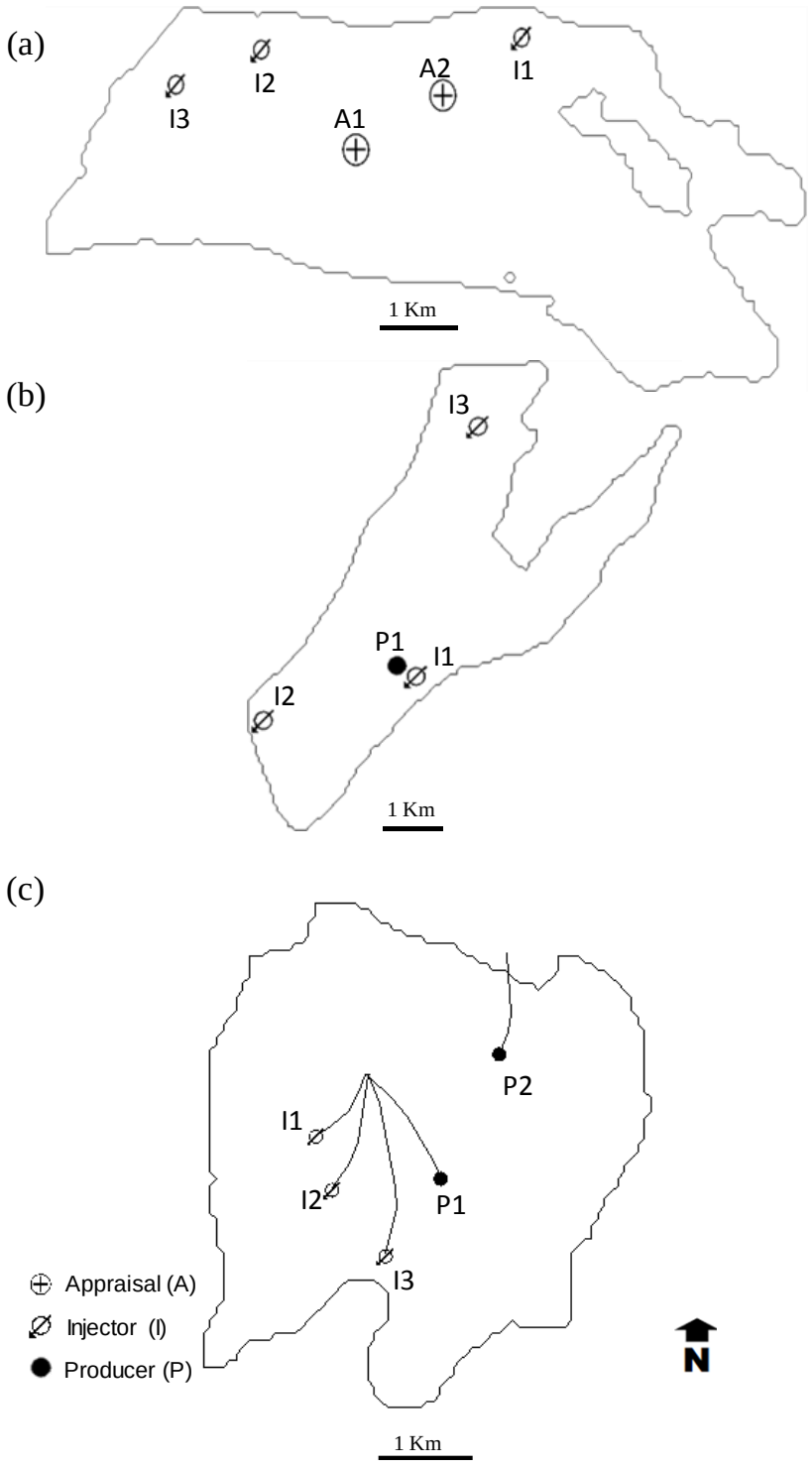

Figure 4.3 *Location of wells used for the log optimization algorithm, a more detailed description of each field can be found in Chapter 5. a) Shiehallion field, b) Norne field and c) carbonate Field X.*

4.3 Calibration to field data

4.3.1 Static calibration to the log data

In practice the PEM is uncertain and without calibration of the input data and parameters it becomes more so (Amini, 2014). It is important to be aware of the geology and petrophysics of the fields under study, mainly to put realistic constraints on the log calibration, and to be able to link the geology to the simulation model. Since the PEM is calibrated using log data, it is key to have a careful conditioning of the log data by avoiding oversimplification and to be attentive to the intrinsic uncertainties of the calculated petrophysical properties (porosity, lithology and fluid saturation) that are the main inputs (figure 4.4) in the calibration process and will impact the field results.

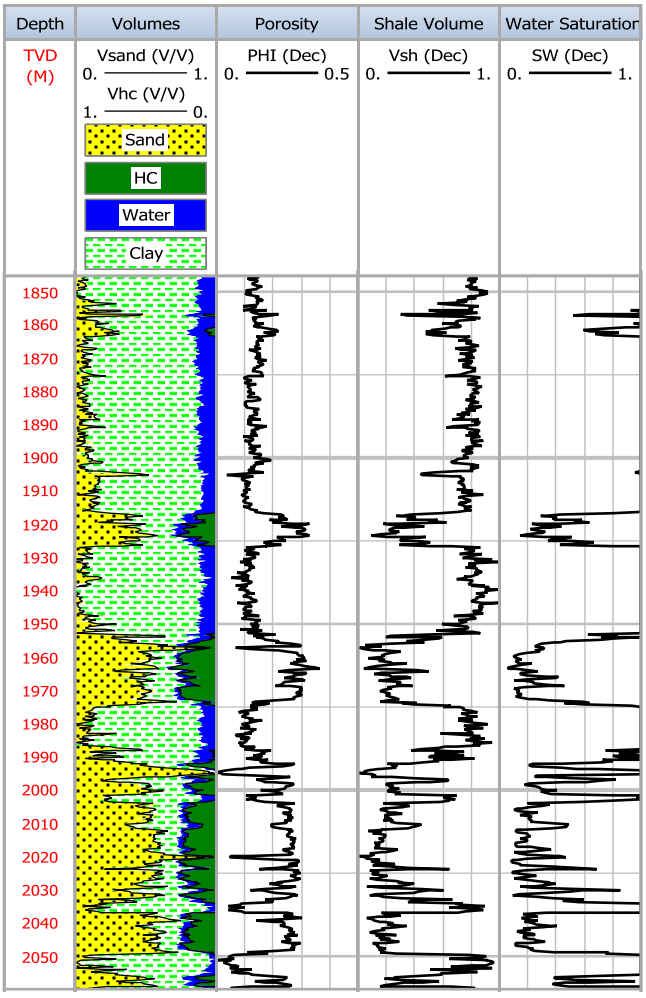

Figure 4.4 *Porosity, lithology and fluid saturation logs obtained from petrophysical evaluation from an appraisal well in the Schiehallion field.*

As I previously stated, before performing the optimization, it is important to question the logs, how they describe the geology and how this is translated at the simulation model domain, since my end goal is forward modeling using the simulator flow model to obtain our synthetic impedances and seismic as a final product. For example in the Schiehallion field, discrete, tightly calcite cemented intervals of thickness generally less than 1m occur occasionally in the reservoir. Such intervals are observed in the logs as high peaks in the density, velocity and resistivity logs (figure 4.5). These are believed to be laterally restricted given the non-parallel and often strongly convergent attitudes of their boundaries seen in core. A more detailed geological description of the three fields of study is shown in chapter 5. Those high peaks from the logs are removed from the optimization since the calcite is not included in the simulation model although affects the seismic signature.

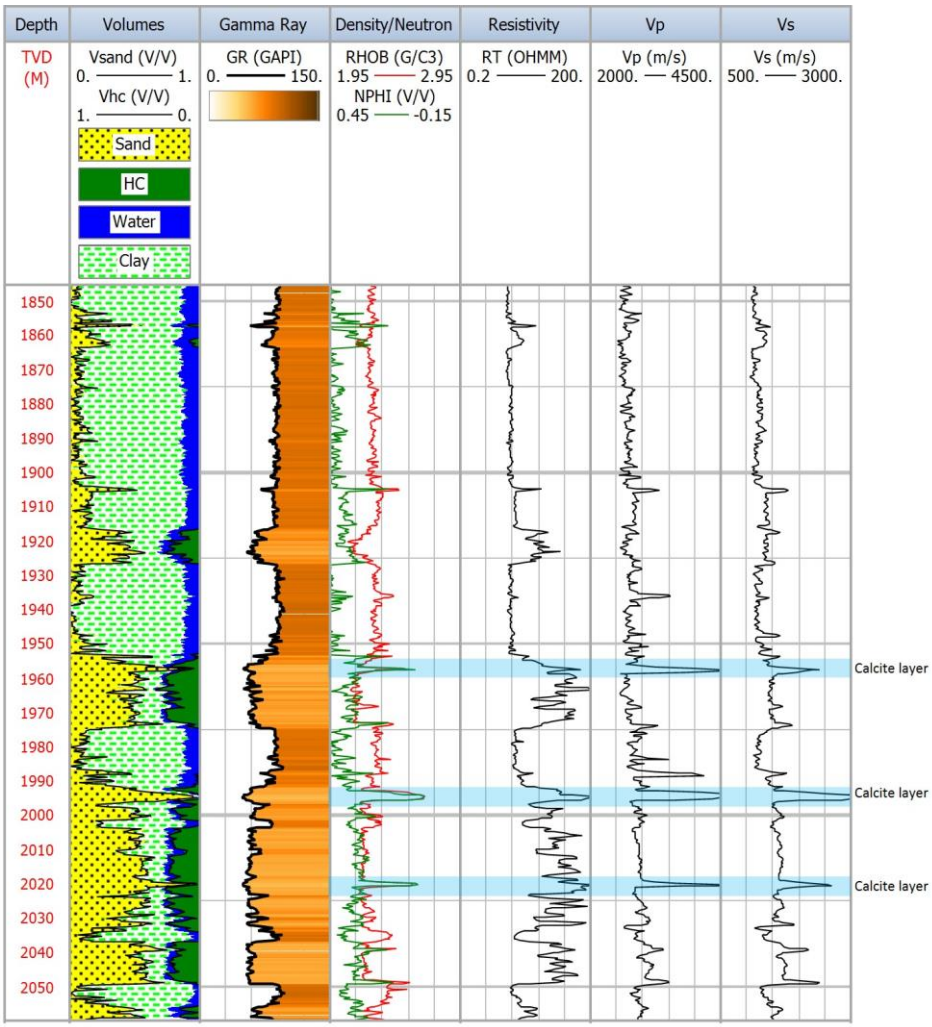

Figure 4.5 *Example of discrete calcite layers observed in density, resistivity and sonic logs in a well from the Schiehallion field.*

The static rock components of any conventional PEM by which the saturated rock frame moduli and density in their initial state are specified, consists of two groups of equations, one group related to the calculation of the density and bulk modulus of each fluid phase and second, a set of equations that describe the rock properties including its dry frame and saturated moduli and the bulk saturated density. For each field, in-situ properties of the fluids including salinity, temperature and API gravity are specified in Tables 4.1, 4.2 and 4.3; the initial pore pressure log and the gas to oil ratio log (GOR) are extracted from the simulation model along a well trajectory, and the oil formation volume factor (Bo - defined as the ratio of the volume of oil at in-situ reservoir conditions to that at surface conditions) is obtained from the PVT data in the simulation model files (figures 4.6a, b and c). Below bubble point pressure, Bo increases with pressure, due to more gas going into solution causing the oil to swell as can be seen in figure 4.6a.

Fluid and reservoir properties	
Reservoir Temperature	136 ^{o}F
Water Salinity	18000 ppm
Oil gravity	25 API
Gas gravity (Gg)	0.5864
Bubble point pressure (Pbp)	21.4565 MPa
Initial reservoir pressure	20 MPa

Table 4.1 *Fluid parameters for Schiehallion Field*

Fluid and reservoir properties	
Reservoir Temperature	208.4 ^{o}F
Water Salinity	15000 ppm
Oil gravity	32.7 API
Gas gravity (Gg)	0.645
Bubble point pressure (Pbp)	-
Initial reservoir pressure	27.3 MPa

Table 4.2 *Fluid parameters for Norne Field*

Fluid and reservoir properties	
Reservoir Temperature	170 ^{o}F
Water Salinity	110000 ppm
Oil gravity	30 API
Gas gravity (Gg)	0.957
Bubble point pressure (Pbp)	15 MPa
Initial reservoir pressure	32 MPa

Table 4.3 *Fluid parameters for Carbonate Field X*

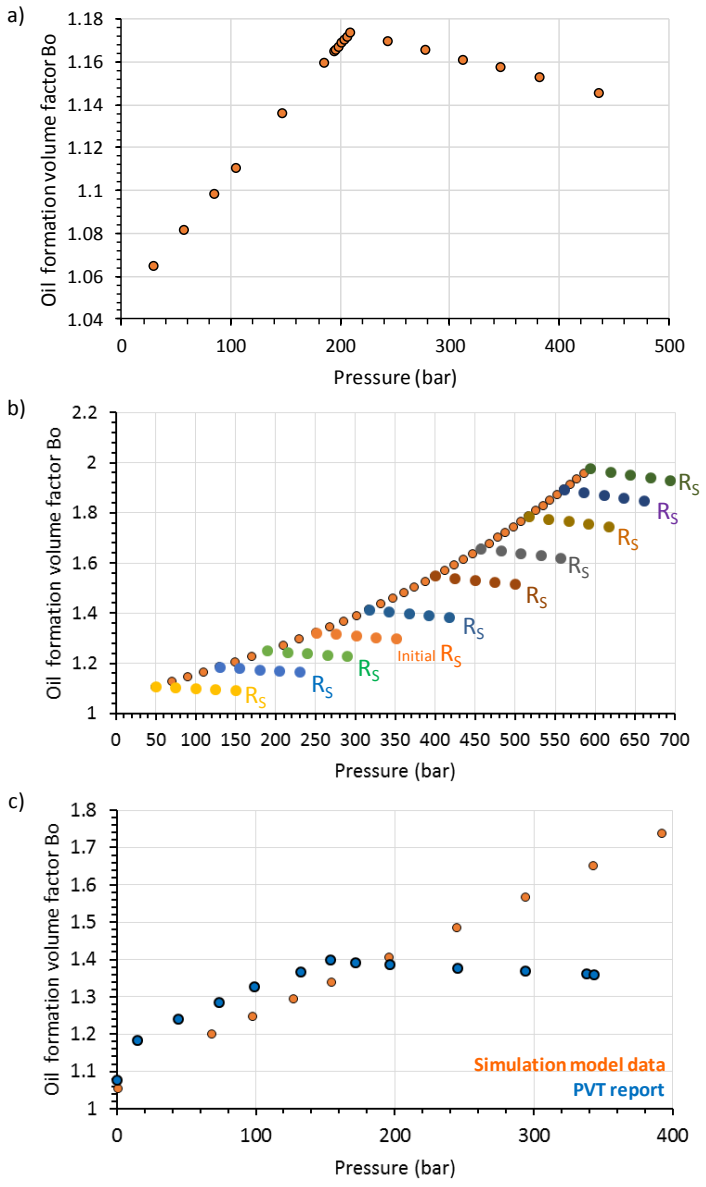

Figure 4.6 *Pressure data versus Bo factor obtained from the PVT tables included in the simulation model for: a) Schiehallion field, b) Norne field and c) Carbonate Field X where the monotonic increase of Bo obtained from the simulation model indicates that more gas goes into solution as the pressure increase compared to the actual PVT report, affecting the resulting fluid bulk modulus.*

For the carbonate Field X, the lack of measured shear sonic log on the LAS files represents an uncertainty to take into consideration for calibration of the rock physics models used against the log data. To overcome the lack of this important data, an empirical relationship (figure 4.7) that defines V_s is obtained by using five core samples at different depths for which velocities (compressional and shear) were measured in the laboratory.

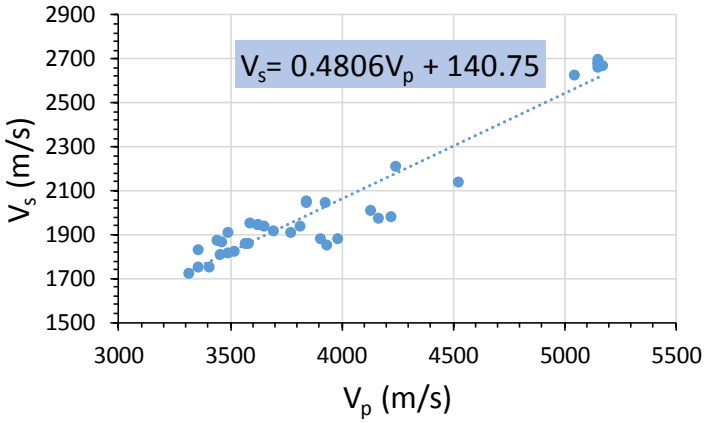

Figure 4.7 *Cross-plot of laboratory measured compressional versus shear wave velocities for the carbonate Field X.*

Figure 4.8, 4.9 and 4.10 show examples of log prediction from the optimization algorithm for all three study fields (for more log prediction results see Appendix B), with the corresponding model parameters highlighted in tables from 4.4 to 4.13, where all the calibrated parameters for each PEM for the three fields are displayed. In general, there is a good fit between predicted and measured logs for both clastic fields (Schiehallion and Norne). With errors of less than 3%, 5% and 1% for V_P, V_S and ρ respectively for all the rock physics models A, B, C, and D.

For the carbonate Field X, PEM E (modified upper Hashin-Shtrikman) shows the smallest error fit between measured log data and the reconstructed logs compared to the results obtained using PEM F (self-consistent approach) since the former takes into consideration the lithology (volume of calcite, shale and porosity) contribution. However, both models shows a reasonable good fit. On the other hand the self-consistent approach (PEM F) was performed using just two simple approximations of the internal pores of the rock, first all pores are considered spheres and second all the pores are described as needles (which it may be far from the real complex internal

structure). Log prediction errors based on PEM E are less than 3% for both V_P and V_S, meanwhile using PEM F with only spheres as the inclusion shape the error is less than 4% and 6% for V_P and V_S respectively. When merely using needles as the inclusion shape the error becomes approximately 5% for both V_P and V_S. The close similarity between the predicted and measured logs errors for both acoustic velocities in this field, is due to the nature of the shear velocity (*Vs*) log definition previously stated, that empirically depends on the compressional sonic log (figure 4.7).

The set of model parameters obtained from the optimization algorithm for each PEM are different and yet still produce a good match to the observed log data. This can be explained with a simple mathematical statement $f(x_1) = I(x) \exists\ g,\ x_2 \neq x_1$ such that $g(x_2) = I(x)$. Where the functions f and g represent the PEM, x_1 and x_2 the input parameters and I(x) the log prediction.

In terms of the geological variability in the reservoir, it should be understood that the logs are sampling the same geology for each field, nevertheless, results obtained from the calibration imply a lateral variation since there is variability for the bulk (*K*) and shear (μ) moduli of the solid components. This means that PEMs created from a single well data may not adequately sample the variety of rock and fluids within the reservoir necessary for a realistic-accurate seismic forward modelling perspective. To assess the strength of the PEM calibration based on the different scenarios, we need to look at the standard deviation of the variables (bulk and shear moduli) involved in our calculation. To this end, the coefficient of variation (CV) as a standardized measure of dispersion of a frequency distribution is used, which is defined as the ratio of the standard deviation (σ) to the mean (μ) ($CV = \sigma/\mu$) for each of the variables optimized. For the clastic fields, coefficient of variations values range from 0.01 to 0.4 (tables 4.14 and 4.15), indicating a reasonable overall consistency between fits laterally across each field and with depth. As might be anticipated, the shear moduli are observed to be more variable than the bulk moduli. The elastic properties of clay minerals are extensively variable (Mavko et al., 2009), this is represented in the high values of the coefficient of variation for the bulk and shear moduli of shale compared to the values obtained for the sand component for the Schiehallion field (table 4.14). Interestingly however, no model shows a particularly strong tendency of either low or high dispersion.

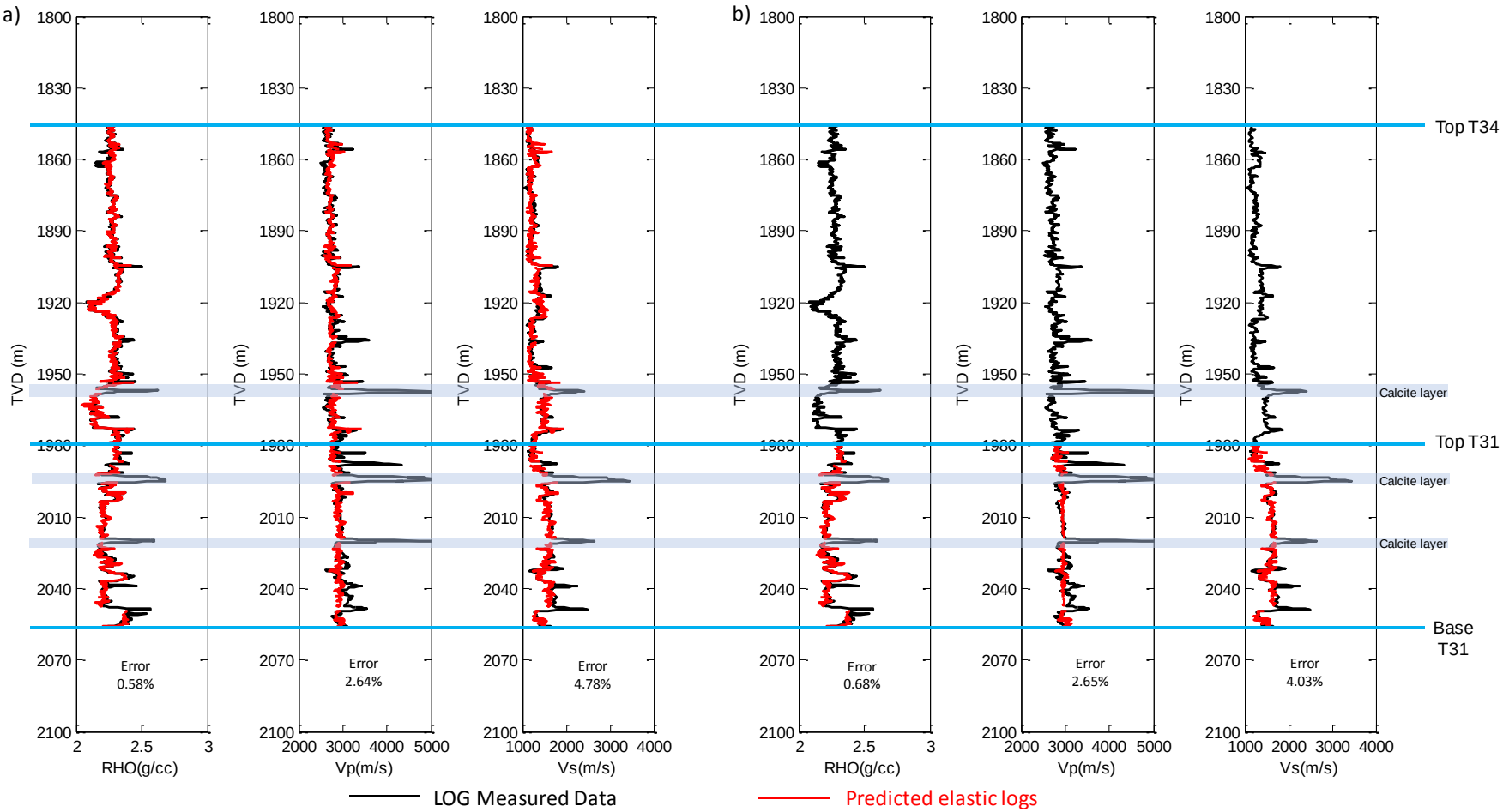

Figure 4.8 *Example of the PEM fits to log segments for well A1 (figure 4.3a) from the Schiehallion field. (a) mixing before fluid substitution PEM A for the entire log segment (A1 Table 4.4) and (b) PEM B only for the lower reservoir sands ($A1_{low}$ Table 4.5).*

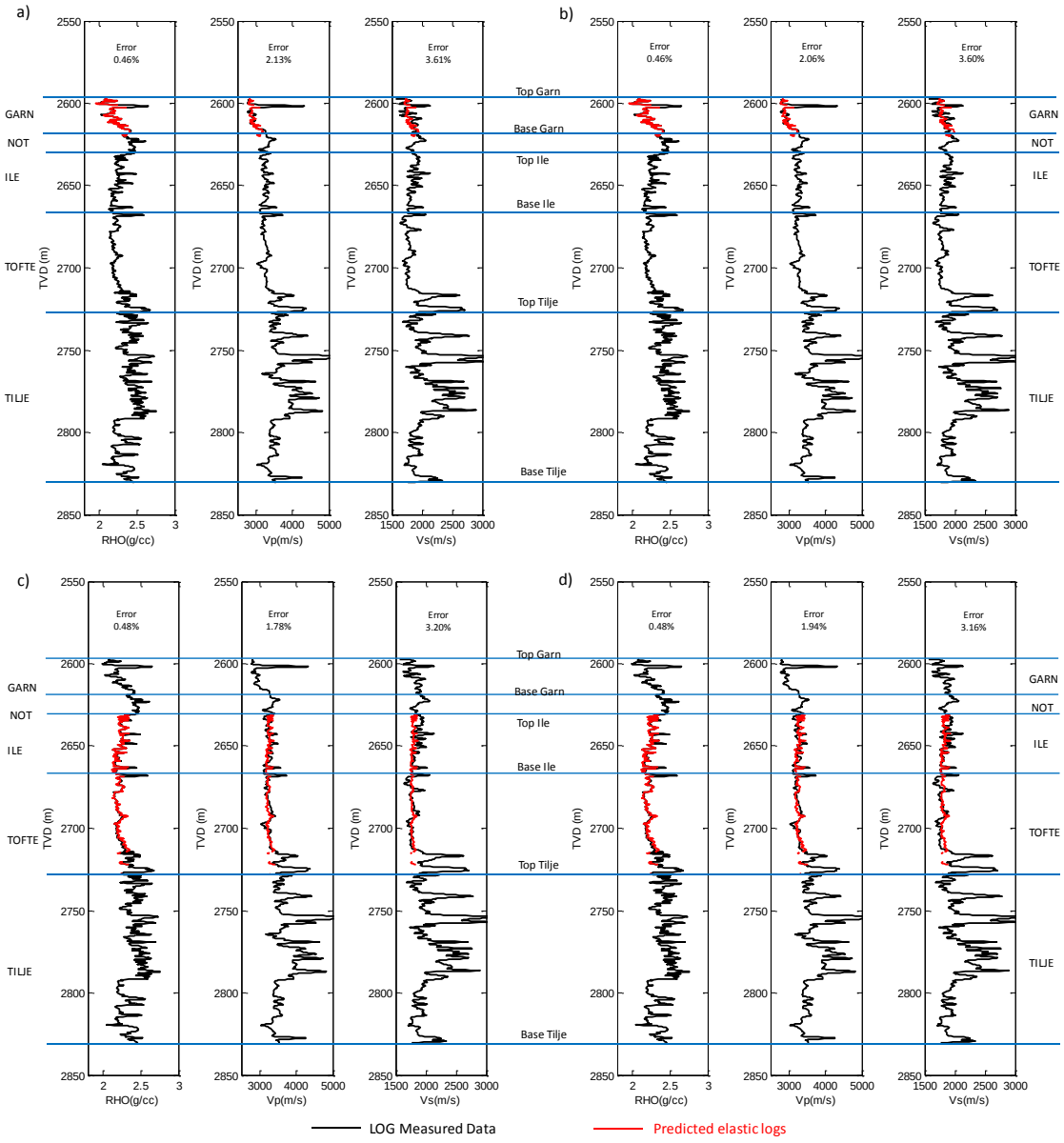

Figure 4.9 *Example of PEM fits to log segments for well I1 (figure 4.3b) from the Norne field. (a) Mixing before fluid substitution PEM A for only the top sand (Garn formation) (I1, Table 4.8), (b) PEM B for only the top sand (Garn formation) (I1, Table 4.9), (c) PEM A only for the second and third sands (Ile and Tofte formations) (I1, Table 4.8) and (d) PEM B only for the second and third sands (Ile and Tofte formations) (I1, Table 4.9).*

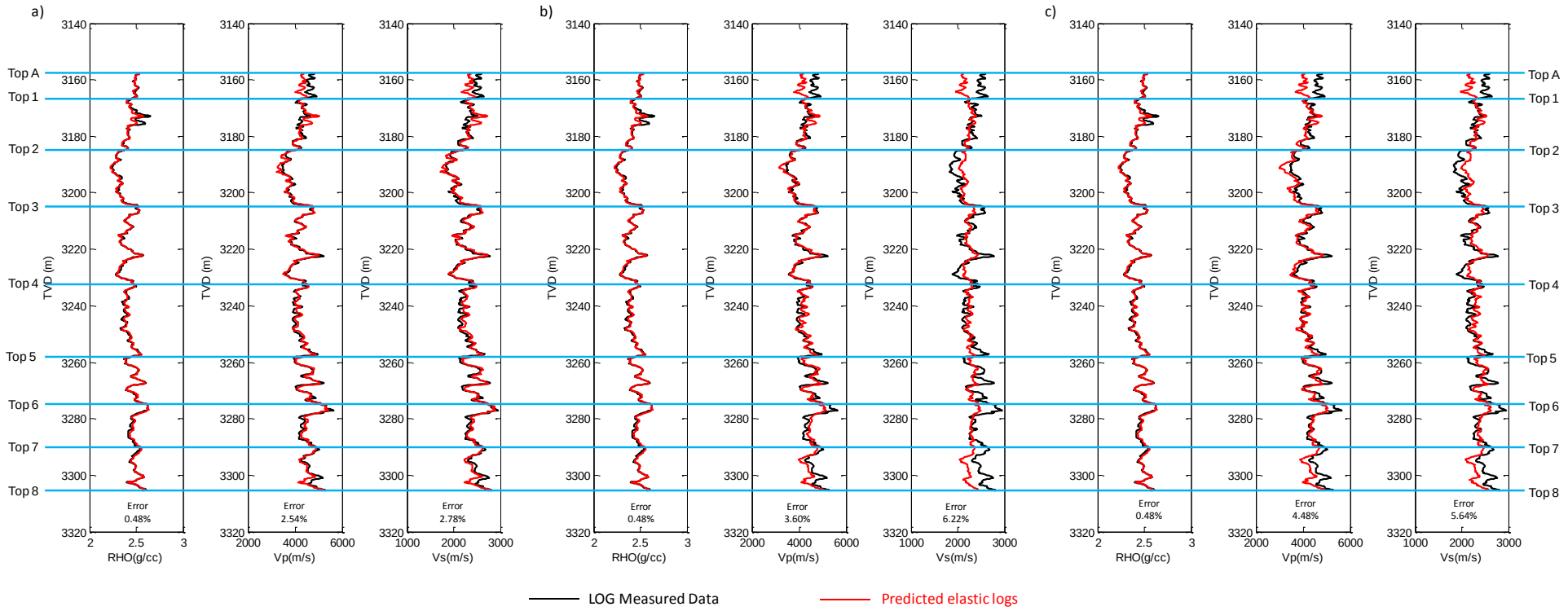

Figure 4.10 *Example of PEM fits to log segments of well I2 (figure 4.3c) from the carbonate Field X. (a) mixing before fluid substitution PEM E for the entire log segment (I2, Table 4.12), (b) PEM F using only spheres shape inclusions for the entire log segment (I2, Table 4.13) and (c) PEM F using only needles shape inclusions for the entire log segment (I2, Table 4.13).*

	Well	κ_{sand} (GPa)	κ_{shale} (GPa)	μ_{sand} (GPa)	μ_{shale} (GPa)	ρ_{sand} (g/cc)	ρ_{shale} (g/cc)	a	b	c
Mixing before Fluid Substitution	A1	24	15	20	4	2.718	2.403	2.113	1.728	4.421
	$A1_{low}$	30	16	29	4	2.722	2.407	10.954	3.912	-9.938
	A2	28	19	19	6	2.685	2.578	5.407	2.972	0.519
	$A2_{low}$	24	19	16	6	2.669	2.579	4.831	3.056	-3.408
	I1	27	15	21	4	2.684	2.393	4.988	3.168	0.883
	I2	26	15	16	5	2.656	2.421	0.587	2.820	7.389
	I3	36	16	28	5	2.624	2.404	14.004	5.376	-12.64
Mixing after Fluid Substitution	A1	28	12	22	3	2.718	2.403	-9.349	11.820	33.797
	$A1_{low}$	29	13	25	3	2.722	2.407	2.633	12.576	10.626
	A2	32	13	22	3	2.685	2.578	-7.092	6.257	33.431
	$A2_{low}$	31	13	17	4	2.669	2.579	-3.142	12.974	15.678
	I1	27	13	19	3	2.684	2.393	-6.675	12.620	28.468
	I2	29	13	18	4	2.656	2.421	-0.694	13.696	14.350
	I3	26	14	14	5	2.624	2.404	-3.876	13.475	14.718
Backus averaging	A1	24	12	26	3	2.718	2.403	-8.995	9.383	36.489
	$A1_{low}$	27	12	23	4	2.722	2.407	5.548	13.273	1.419
	A2	28	13	27	3	2.685	2.578	-7.118	5.511	36.950
	$A2_{low}$	30	13	18	4	2.669	2.579	-3.923	12.246	18.033
	I1	23	13	16	4	2.684	2.393	-3.467	16.129	15.593
	I2	28	13	17	5	2.656	2.421	-1.281	16.791	13.186
	I3	25	14	14	5	2.624	2.404	-1.047	13.099	7.795

Table 4.4 *Calibrated parameters, obtained from model fit to the logs using PEM A for Schiehallion Field. The coefficients a, b and c are related to the dependency on lithology and porosity of the consolidation factor used for this specific paradigm (see Equations 3.3, 3.4 and 3.5 in Chapter 3).*

	Well	κ_{sand} (GPa)	κ_{shale} (GPa)	μ_{sand} (GPa)	μ_{shale} (GPa)	ρ_{sand} (g/cc)	ρ_{shale} (g/cc)	a	b	c
Mixing before Fluid Substitution	A1	30	16	27	5	2.718	2.403	0.118	0.179	1.118
	$A1_{low}$	32	16	32	4	2.722	2.407	0.047	0.227	1.223
	A2	37	20	26	7	2.685	2.578	0.114	0.194	1.022
	$A2_{low}$	31	21	21	8	2.669	2.579	0.052	0.134	1.257
	I1	34	14	29	4	2.684	2.393	0.039	0.123	1.213
	I2	34	14	24	5	2.656	2.421	0.192	0.271	0.857
	I3	34	15	24	5	2.624	2.404	0.103	0.233	1.080
Mixing after Fluid Substitution	A1	24	12	26	2	2.718	2.403	0.343	0.248	0.501
	$A1_{low}$	28	12	23	3	2.722	2.407	0.334	0.171	0.596
	A2	27	14	16	5	2.685	2.578	0.276	0.027	0.913
	$A2_{low}$	26	13	15	4	2.669	2.579	0.348	0.149	0.713
	I1	37	12	30	4	2.684	2.393	0.129	0.001	0.939
	I2	30	17	22	5	2.656	2.421	0.217	-0.008	0.861
	I3	35	13	25	6	2.624	2.404	0.162	0.004	0.917
Backus averaging	A1	22	12	25	3	2.718	2.403	0.287	0.155	0.702
	$A1_{low}$	27	12	22	4	2.722	2.407	0.415	0.146	0.442
	A2	24	13	21	3	2.685	2.578	0.396	0.195	0.555
	$A2_{low}$	26	13	14	4	2.669	2.579	0.363	0.186	0.660
	I1	25	13	22	3	2.684	2.393	0.158	0.149	0.939
	I2	33	12	22	6	2.656	2.421	0.218	-0.005	0.846
	I3	26	14	19	4	2.624	2.404	0.305	0.175	0.649

Table 4.5 *Calibrated parameters, obtained from model fit to the logs using PEM B for Schiehallion Field. The coefficients a, b and c are related to the dependency on lithology and porosity of the critical porosity definition used for this specific paradigm (see Equations 3.6, 3.7 and 3.8 in Chapter 3)*

	Well	κ_{sand} (GPa)	κ_{shale} (GPa)	μ_{sand} (GPa)	μ_{shale} (GPa)	ρ_{sand} (g/cc)	ρ_{shale} (g/cc)	a	b	c
Mixing before Fluid Substitution	A1	21	15	17	4	2.718	2.403	1.763	2.149	1.692
	$A1_{low}$	23	15	19	4	2.722	2.407	3.041	2.227	-1.082
	A2	24	17	15	5	2.685	2.578	2.566	2.054	0.002
	$A2_{low}$	21	17	13	5	2.669	2.579	3.037	2.813	-2.144
	I1	19	15	13	4	2.684	2.393	1.832	2.244	0.812
	I2	23	15	15	5	2.656	2.421	1.111	2.221	2.516
	I3	26	15	15	5	2.624	2.404	1.750	2.073	1.499
Mixing after Fluid Substitution	A1	16	13	17	2	2.718	2.403	-0.495	0.728	7.362
	$A1_{low}$	14	15	14	3	2.722	2.407	1.204	1.671	2.234
	A2	19	13	19	2	2.685	2.578	1.326	0.499	5.897
	$A2_{low}$	27	12	17	3	2.669	2.579	3.555	1.980	3.069
	I1	12	16	12	3	2.684	2.393	-2.339	1.819	9.638
	I2	18	17	18	2	2.656	2.421	0.185	1.608	7.145
	I3	12	17	12	4	2.624	2.404	-1.379	1.773	8.004
Backus averaging	A1	14	12	14	3	2.718	2.403	-0.311	1.105	5.719
	$A1_{low}$	14	14	14	3	2.722	2.407	0.885	1.356	2.548
	A2	14	13	14	3	2.685	2.578	-0.357	0.510	6.379
	$A2_{low}$	12	14	13	3	2.669	2.579	-0.003	0.715	4.669
	I1	13	14	13	3	2.684	2.393	-1.728	1.416	8.986
	I2	17	15	17	3	2.656	2.421	-0.082	2.091	7.251
	I3	12	16	12	4	2.624	2.404	-1.546	1.522	8.240

Table 4.6 *Calibrated parameters, obtained from model fit to the logs using PEM C for Schiehallion Field. The coefficients a, b and c are related to the dependency on lithology and porosity of the modified Krief model used for this specific paradigm (see Equations 3.9, 3.10 and 3.12 in Chapter 3)*

	Well	κ_{sand} (GPa)	κ_{shale} (GPa)	μ_{sand} (GPa)	μ_{shale} (GPa)	ρ_{sand} (g/cc)	ρ_{shale} (g/cc)
Mixing before Fluid Substitution	A1	37	19	41	4	2.718	2.403
	$A1_{low}$	37	19	44	4	2.722	2.407
	A2	37	26	31	7	2.685	2.578
	$A2_{low}$	37	26	25	8	2.669	2.579
	I1	37	15	34	3	2.684	2.393
	I2	37	18	38	3	2.656	2.421
	I3	37	17	33	5	2.624	2.404
Mixing after Fluid Substitution	A1	29	12	35	2	2.718	2.403
	$A1_{low}$	36	12	37	2	2.722	2.407
	A2	44	12	22	3	2.685	2.578
	$A2_{low}$	39	13	22	2	2.669	2.579
	I1	44	12	24	2	2.684	2.393
	I2	44	12	28	2	2.656	2.421
	I3	44	13	19	4	2.624	2.404
Backus averaging	A1	31	11	32	3	2.718	2.403
	$A1_{low}$	24	13	39	3	2.722	2.407
	A2	37	12	27	3	2.685	2.578
	$A2_{low}$	23	13	31	3	2.669	2.579
	I1	37	12	23	3	2.684	2.393
	I2	37	13	24	4	2.656	2.421
	I3	37	14	21	4	2.624	2.404

Table 4.7 *Calibrated parameters, obtained from model fit to the logs using PEM D for Schiehallion Field. The model equations can be found in Chapter 3 (Equations 3.13- 3.18)*

	Well	Region	κ_{matrix} (GPa)	μ_{matrix} (GPa)	ρ_{sand} (g/cc)	ρ_{shale} (g/cc)	a	b	c
Mixing Before Fluid Substitution	I2	Garn	37	37	2.739	2.629	25.165	25.522	-25.682
		Ile-Tofte	29	21	2.725	2.653	6.722	7.908	-3.637
	I1	Garn	25	24	2.697	2.692	9.555	10.143	-3.250
		Ile-Tofte	33	19	2.721	2.657	5.922	7.812	-1.264
	I3	Garn	27	17	2.679	2.662	7.448	8.865	-8.894
		Ile-Tofte	30	20	2.641	2.704	6.241	6.413	-4.590
	P1	Garn	26	22	2.659	2.655	8.009	7.744	2.223
		Ile-Tofte	44	31	2.682	2.808	14.428	17.184	-3.543
Mixing After Fluid Substitution	I2	Garn	19	15	2.739	2.629	6.498	4.841	-7.364
		Ile-Tofte	25	18	2.725	2.653	4.474	5.349	-1.827
	I1	Garn	19	17	2.697	2.692	4.203	4.395	0.644
		Ile-Tofte	34	20	2.721	2.657	6.627	8.581	-1.699
	I3	Garn	27	17	2.679	2.662	7.313	8.357	-7.667
		Ile-Tofte	29	20	2.641	2.704	6.198	6.419	-4.497
	P1	Garn	22	18	2.659	2.655	4.903	4.668	3.866
		Ile-Tofte	44	31	2.682	2.808	14.427	17.244	-3.507
Backus Averaging	I2	Garn	20	16	2.739	2.629	7.761	6.253	-10.066
		Ile-Tofte	17	11	2.725	2.653	0	0	0
	I1	Garn	21	19	2.697	2.692	5.965	6.216	-2.511
		Ile-Tofte	33	19	2.721	2.657	6.146	7.878	-3.251
	I3	Garn	29	18	2.679	2.662	8.472	9.829	-11.001
		Ile-Tofte	31	21	2.641	2.704	7.073	7.292	-6.860
	P1	Garn	23	18	2.659	2.655	5.398	5.167	1.184
		Ile-Tofte	44	31	2.682	2.808	14.653	17.3667	-6.572

Table 4.8 *Calibrated parameters, obtained from model fit to the logs using PEM A for Norne Field. The coefficients a, b and c are related to the dependency on lithology and porosity of the consolidation factor used for this specific paradigm (see Equations 3.3, 3.4 and 3.5 in Chapter 3)*

	Well	Region	κ_{matrix} (GPa)	μ_{matrix} (GPa)	ρ_{sand} (g/cc)	ρ_{shale} (g/cc)	a	b	c
Mixing Before Fluid Substitution	I2	Garn	38	38	2.739	2.629	0.019	0.019	1.165
		Ile-Tofte	41	34	2.725	2.653	0.061	0.045	1.127
	I1	Garn	25	25	2.697	2.692	0.098	0.090	1.109
		Ile-Tofte	44	28	2.721	2.657	0.085	0.054	1.097
	I3	Garn	32	24	2.679	2.662	0.066	0.049	1.208
		Ile-Tofte	39	33	2.641	2.704	0.053	0.053	1.173
	P1	Garn	38	38	2.659	2.655	0.045	0.047	1.066
		Ile-Tofte	44	34	2.682	2.808	0.066	0.048	1.064
Mixing After Fluid Substitution	I2	Garn	37	38	2.739	2.629	0.020	0.019	1.165
		Ile-Tofte	40	34	2.725	2.653	0.061	0.045	1.127
	I1	Garn	24	24	2.697	2.692	0.109	0.102	1.098
		Ile-Tofte	44	28	2.721	2.657	0.086	0.055	1.095
	I3	Garn	31	23	2.679	2.662	0.072	0.055	1.210
		Ile-Tofte	38	33	2.641	2.704	0.053	0.053	1.173
	P1	Garn	35	35	2.659	2.655	0.063	0.066	1.040
		Ile-Tofte	44	34	2.682	2.808	0.066	0.048	1.063
Backus Averaging	I2	Garn	39	39	2.739	2.629	0.014	0.016	1.184
		Ile-Tofte	42	35	2.725	2.653	0.055	0.040	1.151
	I1	Garn	34	38	2.697	2.692	0.040	0.038	1.124
		Ile-Tofte	44	29	2.721	2.657	0.077	0.047	1.127
	I3	Garn	34	25	2.679	2.662	0.055	0.039	1.239
		Ile-Tofte	40	34	2.641	2.704	0.044	0.043	1.206
	P1	Garn	39	38	2.659	2.655	0.050	0.052	1.065
		Ile-Tofte	44	33	2.682	2.808	0.068	0.049	1.081

Table 4.9 *Calibrated parameters, obtained from model fit to the logs using PEM B for Norne Field. The coefficients a, b and c are related to the dependency on lithology and porosity of the critical porosity definition used for this specific paradigm (see Equations 3.6, 3.7 and 3.8 in Chapter 3)*

	Well	Region	κ_{matrix} (GPa)	μ_{matrix} (GPa)	ρ_{sand} (g/cc)	ρ_{shale} (g/cc)	a	b	c
Mixing Before Fluid Substitution	I2	Garn	17	12	2.739	2.629	2.881	2.753	-2.503
		Ile-Tofte	17	11	2.725	2.653	0.929	1.199	0.679
	I1	Garn	16	14	2.697	2.692	2.658	2.662	-0.899
		Ile-Tofte	22	12	2.721	2.657	1.798	2.435	-0.008
	I3	Garn	20	11	2.679	2.662	2.124	2.289	-1.281
		Ile-Tofte	19	11	2.641	2.704	0.739	0.757	0.945
	P1	Garn	19	15	2.659	2.655	3.219	3.129	-0.843
		Ile-Tofte	23	14	2.682	2.808	2.397	2.976	0.192
Mixing After Fluid Substitution	I2	Garn	17	16	2.739	2.629	4.092	4.277	-3.488
		Ile-Tofte	24	23	2.725	2.653	4.598	4.828	-3.115
	I1	Garn	17	17	2.697	2.692	3.511	3.653	-1.772
		Ile-Tofte	29	25	2.721	2.657	4.329	3.896	-0.964
	I3	Garn	21	18	2.679	2.662	4.955	4.826	-3.795
		Ile-Tofte	26	24	2.641	2.704	4.442	4.227	-2.113
	P1	Garn	19	19	2.659	2.655	4.033	3.982	-1.407
		Ile-Tofte	31	21	2.682	2.808	2.918	3.868	2.448
Backus Averaging	I2	Garn	16	11	2.739	2.629	2.298	2.097	-2.093
		Ile-Tofte	17	11	2.725	2.653	0.912	1.179	0.300
	I1	Garn	16	14	2.697	2.692	2.624	2.632	-1.246
		Ile-Tofte	24	13	2.721	2.657	2.312	2.939	-1.089
	I3	Garn	20	11	2.679	2.662	2.096	2.196	-1.457
		Ile-Tofte	21	12	2.641	2.704	1.341	1.365	-0.344
	P1	Garn	22	19	2.659	2.655	4.258	4.214	-2.205
		Ile-Tofte	24	15	2.682	2.808	2.744	3.445	-0.604

Table 4.10 *Calibrated parameters, obtained from model fit to the logs using PEM C for Norne Field. The coefficients a, b and c are related to the dependency on lithology and porosity of the modified Krief model used for this specific paradigm (see Equations 3.9, 3.10 and 3.12 in Chapter 3)*

	Well	Region	κ_{matrix} (GPa)	μ_{matrix} (GPa)	ρ_{sand} (g/cc)	ρ_{shale} (g/cc)
Mixing Before Fluid Substitution	I2	Garn	32	23	2.739	2.629
		Ile-Tofte	44	32	2.725	2.653
	I1	Garn	30	27	2.697	2.692
		Ile-Tofte	44	29	2.721	2.657
	I3	Garn	39	20	2.679	2.662
		Ile-Tofte	44	30	2.641	2.704
	P1	Garn	40	23	2.659	2.655
		Ile-Tofte	44	24	2.682	2.808
Mixing After Fluid Substitution	I2	Garn	31	23	2.739	2.629
		Ile-Tofte	44	31	2.725	2.653
	I1	Garn	31	26	2.697	2.692
		Ile-Tofte	44	28	2.721	2.657
	I3	Garn	42	20	2.679	2.662
		Ile-Tofte	44	30	2.641	2.704
	P1	Garn	40	23	2.659	2.655
		Ile-Tofte	44	24	2.682	2.808
Backus Averaging	I2	Garn	32	24	2.739	2.629
		Ile-Tofte	44	34	2.725	2.653
	I1	Garn	32	28	2.697	2.692
		Ile-Tofte	44	31	2.721	2.657
	I3	Garn	43	21	2.679	2.662
		Ile-Tofte	44	32	2.641	2.704
	P1	Garn	44	25	2.659	2.655
		Ile-Tofte	44	26	2.682	2.808

Table 4.11 *Calibrated parameters, obtained from model fit to the logs using PEM D for Norne Field. The model equations can be found in Chapter 3 (Equations 3.13- 3.18)*

	Well	$\kappa_{calcite}$ (GPa)	κ_{shale} (GPa)	$\mu_{calcite}$ (GPa)	μ_{shale} (GPa)	$\rho_{calcite}$ (g/cc)	ρ_{shale} (g/cc)	a	b	c
Mixing Before Fluid Substitution	I3	69	21	29	9	2.701	2.761	0.471	1.490	-0.047
	I2	65	21	31	9	2.710	2.689	0.368	1.190	0.419
	I1	73	25	35	9	2.706	2.729	0.361	1.151	0.614
	P2	73	25	35	10	2.729	2.685	0.239	0.956	0.811
	P1	67	21	31	10	2.714	2.615	0.332	0.927	0.583
Mixing After Fluid Substitution	I3	60	21	28	9	2.701	2.761	0.518	1.042	-0.139
	I2	57	21	27	9	2.710	2.689	0.490	0.881	0.092
	I1	65	21	30	9	2.706	2.729	0.487	0.758	0.385
	P2	58	21	28	9	2.729	2.685	0.445	0.707	0.347
	P1	62	21	29	9	2.714	2.615	0.379	0.561	0.491

Table 4.12 *Calibrated parameters, obtained from model fit to the logs using PEM E for Field X. The coefficients a, b and c are related to the dependency on lithology and porosity of the critical porosity term in the modified Hashin-Shtrikman model (see Equations 3.23-3.23 in Chapter 3)*

		Spherical inclusion shape				Density		Needle inclusion shape			
	Well	$\kappa_{calcite}$ (GPa)	κ_{shale} (GPa)	$\mu_{calcite}$ (GPa)	μ_{shale} (GPa)	$\rho_{calcite}$ (g/cc)	ρ_{shale} (g/cc)	$\kappa_{calcite}$ (GPa)	κ_{shale} (GPa)	$\mu_{calcite}$ (GPa)	μ_{shale} (GPa)
Mixing Before Fluid Substitution	I3	65	21	19	9	2.701	2.761	51	21	23	9
	I2	62	21	19	9	2.710	2.689	55	21	22	9
	I1	64	21	22	9	2.706	2.729	54	21	26	9
	P2	61	21	20	9	2.729	2.685	58	21	23	9
	P1	47	21	17	9	2.714	2.615	45	21	20	9
Mixing After Fluid Substitution	I3	59	21	18	9	2.701	2.761	50	21	21	9
	I2	58	21	18	9	2.710	2.689	51	21	21	9
	I1	58	21	21	9	2.706	2.729	51	21	24	9
	P2	57	21	18	9	2.729	2.685	51	21	21	9
	P1	44	21	16	9	2.714	2.615	40	21	20	9

Table 4.13 *Calibrated parameters obtained from model fit to the logs using PEM F with two scenarios using only sphere and only needle inclusions shape for carbonate Field X.*

PEM paradigm	Elastic Moduli	Coefficient of Variation (CV)		
		Mixing Before Fluid Substitution	Mixing After Fluid Substituiton	Backus Averaging
PEM A	κ_{sand}	0.1389	0.0679	0.0878
	μ_{sand}	0.2298	0.1746	0.2365
	κ_{shale}	0.1022	0.0411	0.0497
	μ_{shale}	0.1715	0.2040	0.1890
PEM B	κ_{sand}	0.0654	0.1500	0.1217
	μ_{sand}	0.1284	0.2221	0.1542
	κ_{shale}	0.1575	0.1254	0.0550
	μ_{shale}	0.2578	0.3006	0.2566
PEM C	κ_{sand}	0.0729	0.2879	0.1151
	μ_{sand}	0.1295	0.1711	0.1051
	κ_{shale}	0.0580	0.1295	0.0958
	μ_{shale}	0.1083	0.2578	0.1113
PEM D	κ_{sand}	-	0.1343	0.1834
	μ_{sand}	0.1656	0.2399	0.2067
	κ_{shale}	0.2000	0.0368	0.0719
	μ_{shale}	0.3720	0.2999	0.1375

Table 4.14 *Coefficient of variation (CV) for the elastic bulk and shear modulus of the solid components for the Schiehallion field.*

PEM paradigm	Elastic Moduli	Coefficient of Variation (CV)		
		Mixing Before Fluid Substitution	**Mixing After Fluid Substituiton**	**Backus Averaging**
PEM A	$\kappa_{m(Garn)}$	0.1675	0.1503	0.1502
	$\kappa_{m(Ile\text{-}Tofte)}$	0.1752	0.2153	0.3072
	$\mu_{m(Garn)}$	0.2953	0.0651	0.0614
	$\mu_{m(Ile\text{-}Tofte)}$	0.2117	0.2300	0.3475
PEM B	$\kappa_{m(Garn)}$	0.1611	0.1565	0.0685
	$\kappa_{m(Ile\text{-}Tofte)}$	0.0505	0.0626	0.0390
	$\mu_{m(Garn)}$	0.2163	0.2198	0.1654
	$\mu_{m(Ile\text{-}Tofte)}$	0.0771	0.0771	0.0695
PEM C	$\kappa_{m(Garn)}$	0.0878	0.0896	0.1404
	$\kappa_{m(Ile\text{-}Tofte)}$	0.1178	0.0979	0.1336
	$\mu_{m(Garn)}$	0.1216	0.0639	0.2378
	$\mu_{m(Ile\text{-}Tofte)}$	0.1021	0.0636	0.1160
PEM D	$\kappa_{m(Garn)}$	0.1226	0.1403	0.1526
	$\kappa_{m(Ile\text{-}Tofte)}$	-	-	-
	$\mu_{m(Garn)}$	0.1070	0.0922	0.1020
	$\mu_{m(Ile\text{-}Tofte)}$	0.1025	0.0949	0.0959

Table 4.15 *Coefficient of variation (CV) for the elastic bulk and shear modulus for the Norne field.*

PEM paradigm	Elastic Moduli	Coefficient of Variation (CV)	
		Mixing Before Fluid Substitution	Mixing After Fluid Substituiton
PEM E	$\kappa_{calcite}$	0.0461	0.0475
	$\mu_{calcite}$	0.0745	0.0359
	κ_{shale}	0.0867	-
	μ_{shale}	0.0521	-
PEM F_1 Spheres	$\kappa_{calcite}$	0.1096	0.1021
	$\mu_{calcite}$	0.0838	0.0879
	κ_{shale}	-	-
	μ_{shale}	-	-
PEM F_2 Needles	$\kappa_{calcite}$	0.0838	0.0888
	$\mu_{calcite}$	0.0850	0.0634
	κ_{shale}	-	-
	μ_{shale}	-	-

Table 4.16 *Coefficient of variation (CV) for the elastic bulk and shear modulus of the solid components for the carbonate Field X.*

For the Schiehallion field after log optimization algorithm is performed, extremely values for sand bulk modulus are obtained (especially using PEM C, table 4.6), as low as 14 GPa have been estimated, which cannot be justified with the mineralogy of sand. Therefore, such find is a way to discriminate or discard the rock physics model as not good since will affect the 4D response once we move into the simulation model domain.

On the other hand, for the carbonate field, values of coefficient of variation are smaller therefore are less dispersive than the values obtained for the clastic reservoirs. The coefficient of variation for Field X varies between 0.04 and 0.11, representing a stability between fits laterally across the field and with depth and between the examined PEMs,

even when the complex internal structure of the carbonate rock is not fully described and comprehended in the models. Based on the calibration and this analysis I conclude that no model in the clastic and carbonate examples can in fact be considered as the best and all fit well in the log domain.

4.3.2 Dynamic calibration

The response of the seismic to pressure is not known, and can only be measured and calibrated in the laboratory. The logs cannot assess the stress sensitivity term, as it does not sample a wide enough range of pressures. In fact, the stress sensitivity term carries the highest uncertainty in the petro elastic model. To address the stress sensitivity in this thesis, the modified MacBeth (2004) equations describe the dependency between effective pressure and the dry bulk and shear modulus, where E_K, P_K, E_μ and P_μ are the rock stress sensitivity constants from core measurements that define the shape of the stress sensitivity curve and should be specified for each field.

4.3.2.1 Clastic Fields

From the 179 sandstones samples used in MacBeth (2004) to study the pressure sensitivity, many of the reservoir rocks were from the North Sea, specifically a set corresponds to Paleocene sandstones from the West of Shetlands with range of porosity that varies between 15 and 36% which agrees with the Schiehallion field reservoir rock. The curves displayed in figure 4.11 obtained using the parameters from table 4.17 and the equations 3.1 and 3.2 (chapter 3), show that this rock has lower sensitivity to pressure depletion and higher sensitivity to pressure build up. Conventionally, shales are considered inactive reservoir material, however the presence of clay in the active cells in the simulation model could affect the stress sensitivity of the shaly sands (MacBeth and Schuett, 2007). Nevertheless in this current work, shales are regarded as equally stress sensitive as sand (HajNasser, 2012). For the Norne field, due to the lack of laboratory measurements to calibrate the pressure response of the dry moduli, it was decided to use the same stress sensitivity parameters as in Schiehallion, even though both fields have a different geological setting and different initial reservoir pressure.

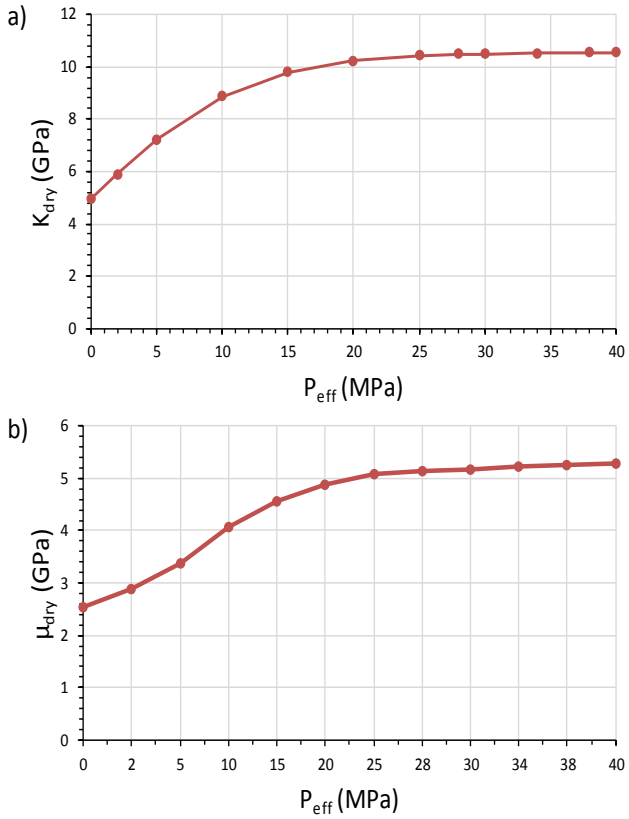

Figure 4.11 *Stress sensitivity curves for the Schiehallion field, based on the modified MacBeth (2004) equations (Equations 3.1 and 3.2 in Chapter 3).*

E_K (unitless)	P_K (MPa)	E_μ (Unitless)	P_μ (MPa)
1.1277	5.62	1.0833	7.97

Table 4.17 *Rock stress sensitivity constants from core measurements for Schiehallion field (MacBeth 2004)*

4.3.2.2 Carbonate Field

For field X, I reconstruct the effect of the stress sensitivity based on five sample measurements using the modified MacBeth (2004) equations (Equations 3.1 and 3.2). The five samples obtained at different depth and pressure, have porosity that varies between 11 and 26%. The rock stress sensitivity parameters from table 4.18 were obtained from the reconstruction of the stress sensitivity curves displayed in figure 4.12.

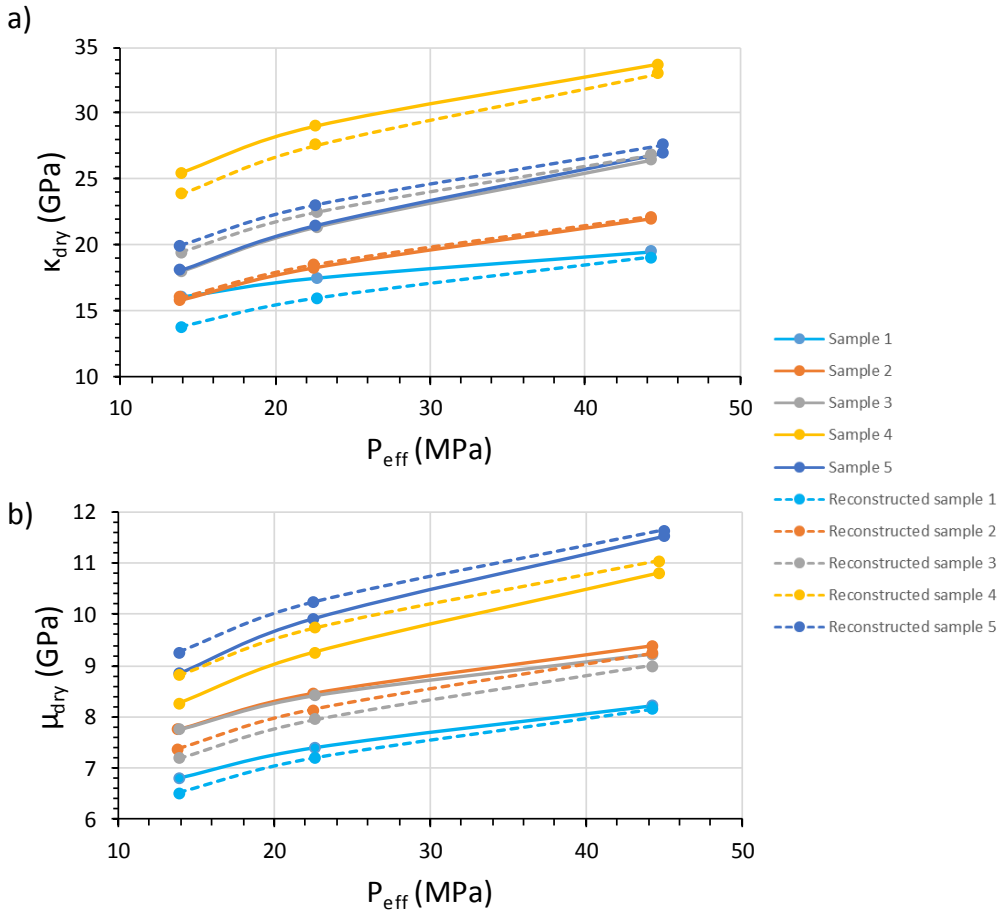

Figure 4.12 *Stress sensitivity curves for the Field X, using five samples from the laboratory and based on modified MacBeth (2004) equations.*

E_K (unitless)	P_K (MPa)	E_μ (Unitless)	P_μ (MPa)
1.124	16.54	0.7095	17.98

Table 4.18 *Rock stress sensitivity constants from core measurements for Field X*

4.4 Summary

All conventional deterministic PEMs consist of two parts: the static rock components by which the saturated rock frame moduli and density in their initial state are specified, and the dynamic component which is defined by the fluid substitution model, effect of

pressure changes on each fluid phase, and finally the stress dependency of the rock frame density and moduli. The parameterization of the PEM will help to outline the accuracy and confidence of time-lapse studies. This chapter focuses on the calibration of the PEM parameters to the in-situ response for each field that I will analyze further. The static calibration against log data is performed through an optimization algorithm to reconstruct the elastic logs (velocities and bulk density) and derive the calibrated input parameters of each rock physics model. For all three fields studied there is a reasonably good fit between measured and predicted logs, implying that no rock physics model can in fact be considered as the best and all fit well. As for the dynamic section, all the PEMs share the same stress sensitivity model with four laboratory coefficients calibrated for each field.

After the statistical analysis using wireline log data presented in this chapter, each set of estimated input parameters are now used in simulator to seismic modelling. Thus, each cell in the flow simulation model specified by a particular V_{shale} and porosity together with saturation and pressure changes can be transformed into V_P, V_S, and ρ. The results and analysis from this modelling are the focus of the following Chapter 5.

Chapter 5

Sim2Imp modelling application to field datasets

After the statistical analysis presented in the previous chapter, this new chapter focuses on modelling of impedances, mainly transforming the static and dynamic properties from the simulation model into a corresponding V_P, V_S, and ρ. The calculation of the elastic properties of the reservoir leads to the resultant impedance change maps for the producing units in each field, which can be used to assess and interpret the 4D response.

5.1 Introduction

A cornerstone in the integration of time-lapse data with reservoir engineering is the simulator to seismic modelling approach, hereafter referred to as sim2seis. This connects two different domains together, the fluid flow simulation and the seismic domain. Sim2seis modelling is a process by which simulator flow model predictions along with rock properties information are used to create the synthetic seismic response from a reservoir during different stages of production. Within this forward modelling workflow, sim2seis relies on the PEM relationships between static properties (porosity and clay content), effective stress sensitivity term and dynamic changes in the reservoir at the geocellular model scale. An essential requirement for a successful 4D sim2seis, is to ensure a good 3D sim2seis (Whitcombe et al. 2002) before 4D differences take place. In this step it is necessary to calibrate the PEM parameters to the in-situ response since the PEM is fabric and lithology dependent (Bogan at al. 2003; Alfred et al. 2008; Alvarez and Amini 2014).

After the statistical analysis using log data and calibration of the input parameters from the optimization in chapter 4, each PEM is incorporated into the sim2seis. Sim2seis modelling consist of two steps, first conversion of the simulation data into impedances (sim2imp), and second converting the calculated impedances into synthetic seismic volumes. In the ETLP in-house sim2seis code the latter process is performed through 1D convolution with the primary reflection coefficient series Zoeppritz equations, introduced to handle angle dependence. Sim2imp bring two domains together: the petrophysical domain as is represented through the PEM calibrations to the wireline logs, and the flow simulation domain, from which the static properties (porosity and *net-to-gross* NTG) are extracted, along with the simulated pressure and saturation for the baseline and monitor, all of which are entered as inputs into the calculation of elastic properties (V_P, V_S and ρ) of each grid cell of the model.

Although the end product of the sim2seis algorithm is synthetic seismic at different stages of production which can then be compared to observed seismic data, it is more instructive to compare PEM paradigms in terms of their predicted impedance values, which are free of wave interference phenomena. The use of the P-impedances domain in seismic history matching (SHM) is well known and highly used in the industry and the

research community (Mezghani et al. 2004; Falcone et al. 2004; Roggero et al. 2007) as can be seen in Table 1.1 from Chapter 1. In a 4D sense, for this thesis, the comparison of each PEM paradigm change in impedance predictions presented in this thesis is defined as:

$$\frac{\Delta I_P}{I_{P(baseline)}} = \frac{I_{P(monitor)} - I_{P(baseline)}}{I_{P(baseline)}} \tag{5.1}$$

In this chapter, once each grid cell in the simulation model has the elastic properties calculated (V_P, V_S, ρ or impedances) using the different PEMs, the 4D change of P-impedances maps are created from the simulation model using weighted averaging between specific reservoir depths of interval, which represents the producing units for each field of study.

5.2 Modelling application to the Schiehallion field

5.2.1 Field Description

The Schiehallion field is situated on the Atlantic margin of the UK Continental Shelf, about 200 km to the west of the Shetland Islands (figure 5.1a), and lies in water depth of approximately 300-500m (Chapin et al. 2000). The reservoir is a deep water turbidite of Tertiary age deposited in the Faroe-Shetland basin and shows varying degree of channelization in different parts of the field. The turbidite channel sands are 10-50m thick at a depth of about 2000m (Chapin et al. 2000)

The multiple stacked reservoir sands are siliciclastic turbidites, with the seismic interpretation suggesting that they are highly channelized units, amalgamated channels and unconfined sheet-like sands within a largely submarine slope system (figure 5.1b) (Martin and Macdonald, 2010). The reservoir is heavily compartmentalised with structural faults in the East-West direction. Individual channel complexes are up to 70m thick and 100-1000m wide, the channel complexes fill consists of both sandstone and mudstone. In general thicker and higher net to gross pay is encountered in the centre of channel complexes and thinner, more interbedded pay on the margins.

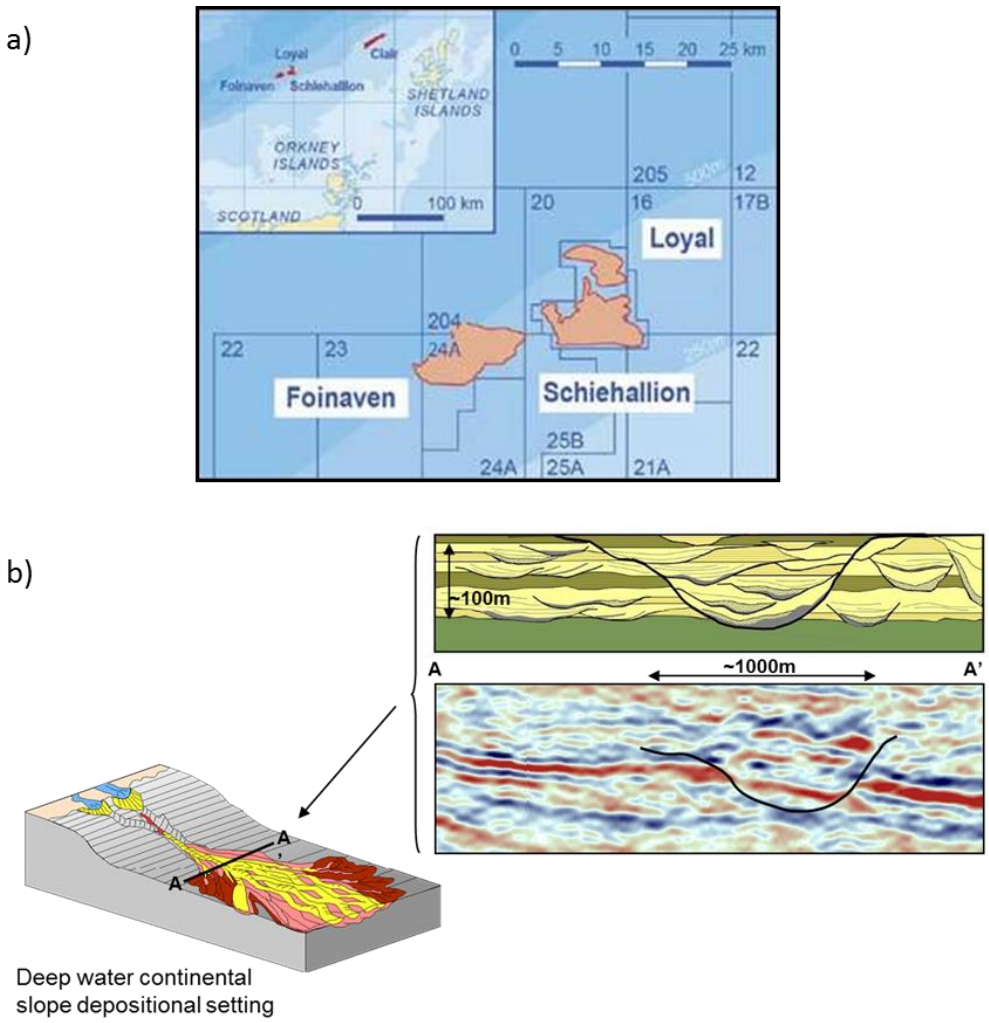

Figure 5.1 *(a) Schiehallion field location. (b) Depositional setting and seismic facie (channelized) (Martin and Macdonald 2010)*

Reservoir quality varies in character from thinly interbedded sands to massive sands, with the massive sands being of better quality. Typically, the sands are fine to medium grained, with 25-30% of average porosity and 200-2000 mD permeability. The UKCS reservoir fluids are geochemically mixed source oils, with oil gravity in the range 22-28 degrees API.

BP uses a regional stratigraphic framework (the T-sequence scheme) for the Paleocene-Early Eocene representative of the West of Shetlands (figure 5.2). The UKCS reservoir sits within the BP T30 Paleocene group of sequences, approximately equivalent to the Andrew Member of North Sea lithostratigraphy. The T30 reservoirs are siliciclastic turbidite sandstones classified as sublithic to lithic arenite, which were derived from the uplifted Scottish Massif to the southeast (Leach et al., 1999).

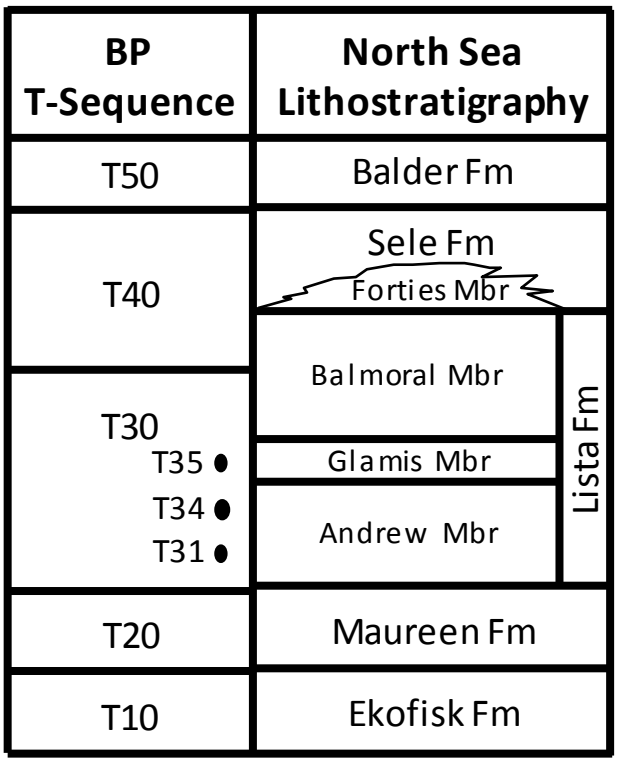

Figure 5.2 *Comparison between BP West of Shetland sequence stratigraphic nomenclature and the North Sea lithostratigraphy (Leach et al. 1999)*

The T30 interval is also subdivided into a number of sequences (e.g. T31A, T31B T34). This subdivision was based upon well logs and seismic data interpretation. Most of the reservoir sands in the UKCS field of our interest for this study are in the T31A unit. The sequences T31B and T31A are separated by the deposition of a thin shale interval as can be seen in figure 5.3. The T31A deposits are more extensive compared to the spatial distribution of the T31 sands, covering the whole area of segment 1, which suggests amalgamation between channels and overbank deposits from different flows. Texturally, the T31 sandstones are generally upper fine-grained and moderately well sorted, and the T34 sandstones are lower to medium-grained and well sorted. From well analysis, the massive packages of sandstones have homogenous density and are comprised of predominantly rigid framework grains, but with some ductile components and authigenic material. The most common authigenic phase is calcite observed on the well logs, accompanied by minor trace amounts of kaolinite, chlorite, silica, K-feldspar and pyrite (Leach et al 1999).

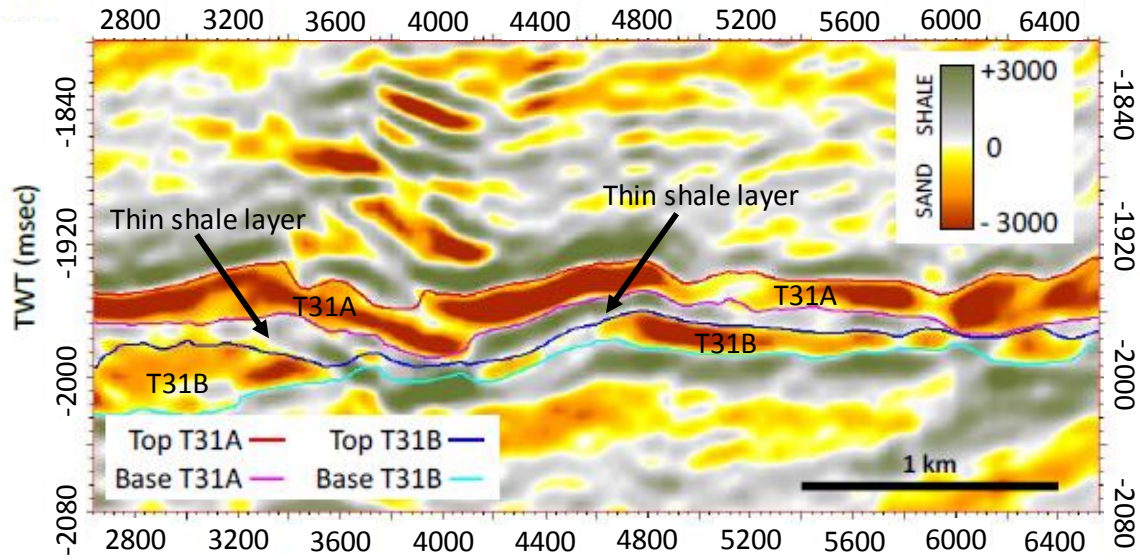

Figure 5.3 *Vertical section from the coloured inversion seismic data (1996 preproduction data), showing the distribution of the turbidite sequences T31A and T31B of the Schiehallion field. The top and base horizons of the sand layers are picked as zero crossing by the data provider (BP). (Amini 2014)*

5.2.2 Datasets

Figure 5.4 shows the timeline of the seismic surveys in the Schiehallion field over the years. In this thesis four seismic vintages are available, including the baseline in 1996 and three monitor surveys (2004, 2006 and 2008). Other datasets available consist of wireline log data and a simulation model with a dimension of 193x99x84 cells, with a grid cell size of 50x50m and cell height ranging from 2m to 5m. The connectivity across the reservoir is the primary factor in understanding the well performances and the reservoir sweep in the Schiehallion field, therefore the simulation model available for this study allows the adjustment of the connectivity and shows the lithological heterogeneity through a detailed geobody characterization (figure 5.5a). From a simulation point of view, each geobody is a group of contiguous cells in the model, characterized as being in the same transmissibility region, as for the NTG distribution in the geobodies, this was populated using seismic NTG (Connolly, 2007). Connolly's (2007) method uses the apparent thickness and average band-limited impedance measured between zero-crossing picks (Seismic NTG = Net pay thickness/Apparent thickness). One of Connolly's (2007) requirement for the implementation of the method is that the sands have lower impedance than the shales, which is the case of Schiehallion. For our Schiehallion field the model cell is specified by a net-to-gross

NTG (or volume of shale V_{SH} = 1-*NTG*) as can be seen in figure 5.5b where the higher NTG geobodies correspond to the sand turbidite channels and represent brighter amplitudes in the seismic section.

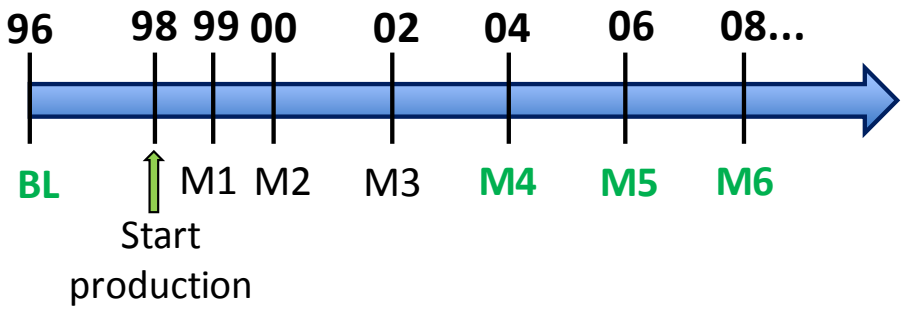

Figure 5.4 *Timeline of the seismic surveys in the Schiehallion field over the years. Highlighted in green the seismic surveys available for this thesis. 1996 baseline and three monitor seismic volumes (2004, 2006 and 2008)*

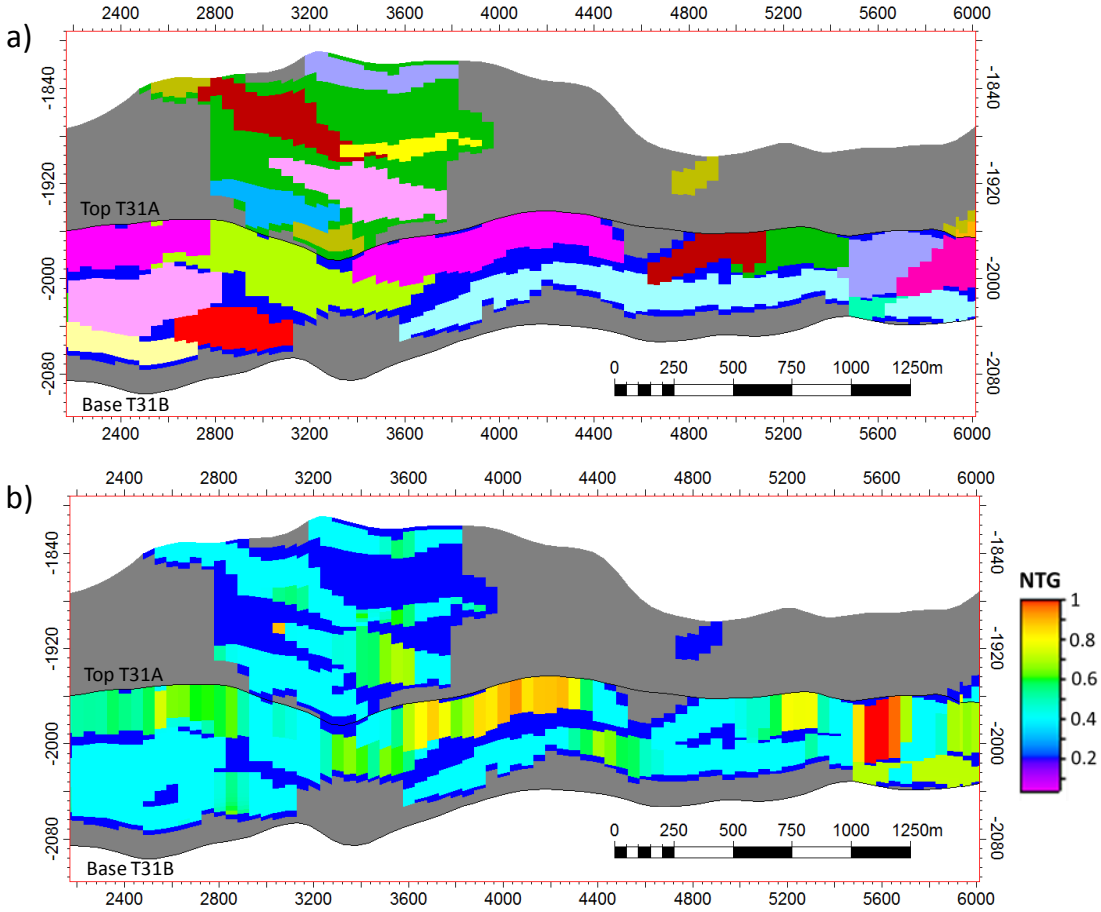

Figure 5.5 *(a) Geobody section from the simulation model, a total of 361 geobodies describe the sand bodies of the Schiehallion field, which connectivity between them is defined through transmissibility multiplier in the simulation model. (b) Net-to-gross (NTG) distribution section in the geobodies, based on Connolly's (2007) method.*

5.2.3 Simulation to Impedances (sim2imp) modelling

Each cell in the flow simulation model specified by a particular V_{shale} and porosity (ϕ) together with saturation and pressure changes can be transformed into a corresponding elastic properties (V_P, V_S, and ρ). Figure 5.6 shows the resultant impedance change maps for the producing T31 unit in the Schiehallion Field for all the PEMs described in chapter 3. The log calibration deals with the dry fame characterisation in the static domain and impacts the amplitudes via Gassmann fluid substitution but it will not impact strongly on the pressure sensitivity. Qualitatively, all twelve time-lapse maps calculated between the 2004 monitor and the baseline display an obvious static structure imprint, but in most areas in the maps, the modelled 4D response (P-impedance changes) is consistent with the maps of pressure (figure 5.7a) and saturation changes (figure 5.7b), with areas showing hardening (blue zones) due to pressure depletion or oil being replaced by water and softening (yellow/red zones) due to pressure build up.

Previous work by BP (Allan et al 2011) shows that the water signal is clearly visible in the Schiehallion field, around 6% of impedance change is expected for 50% change in water saturation. However, this is not the case, 4D map based on PEM C show less contrast in the hardening areas in comparison to the other PEM outputs. This implies that the set of input parameters, even though they were optimized and showed a good fit to the logs, do not necessarily translates in a good 4D impedance response in the simulation domain, and might affect the entire synthetic seismic computation and its direct comparison to the observed data. In the southeast of the field, the transmissibility multipliers of the geobody highlighted in figure 5.6 act as pressure sealers, which results in the strongest softening signature due to pressure build up in the geobody, where the pore pressure change reaches +13MPa (figure 5.7a). The maps achieved through PEM A, B and C show a stronger and laterally wider softening (red zone) response due to pressure build up than PEM D, even though all PEMs have in common the same stress sensitivity model. Yet PEM D includes the initial pressure of the reservoir inside the model equations (see chapter 3) for the calculation of the dry effective moduli, which will affect the entire 4D seismic signature response in general. In terms of the hardening response, the maps based on PEM D show the strongest effect due to water-flood compared to the remaining maps. Such observations will be restated when heading into a more quantitative analysis later on this current chapter, and on Chapter 6.

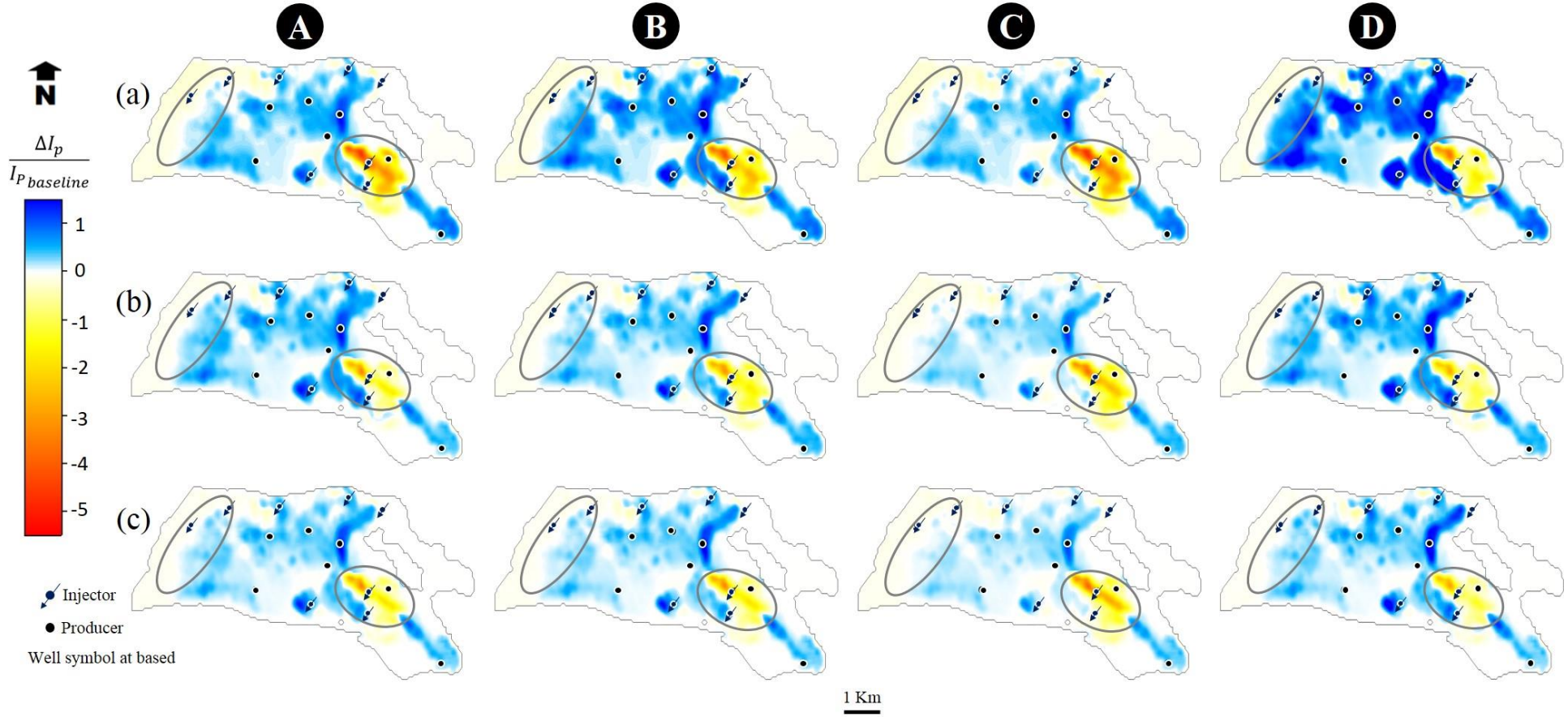

Figure 5.6 (a) Maps of impedance change predicted by calibrated PEMs A, B C and D based on mixing the solid components before fluid substitution approach for the T31 sands of the Schiehalliion Field.(b) as in (a) but maps based on mixing the solid components after fluid substitution, and (c) as in (a) but maps of impedance change predicted using Backus averaging. (blue = hardening ; yellow/red = softening).

Towards the west of the field, from all the 4D maps (figure 5.6), it can be observed a clear portrayal of the competition between the softening effect and the effect of hardening due to water-flood, which are consistent with the dynamic maps from the simulation model, and display how each rock physics model balances such competition. The time lapse change of impedances can be cast as a function of pressure and saturation changes, simulation model properties such as porosity, NTG, SATNUM (saturation regions), and the PEM. Certainly, each of the PEMs balances the changes of the dynamic properties of the reservoir differently, which is reflected in the 4D amplitudes response.

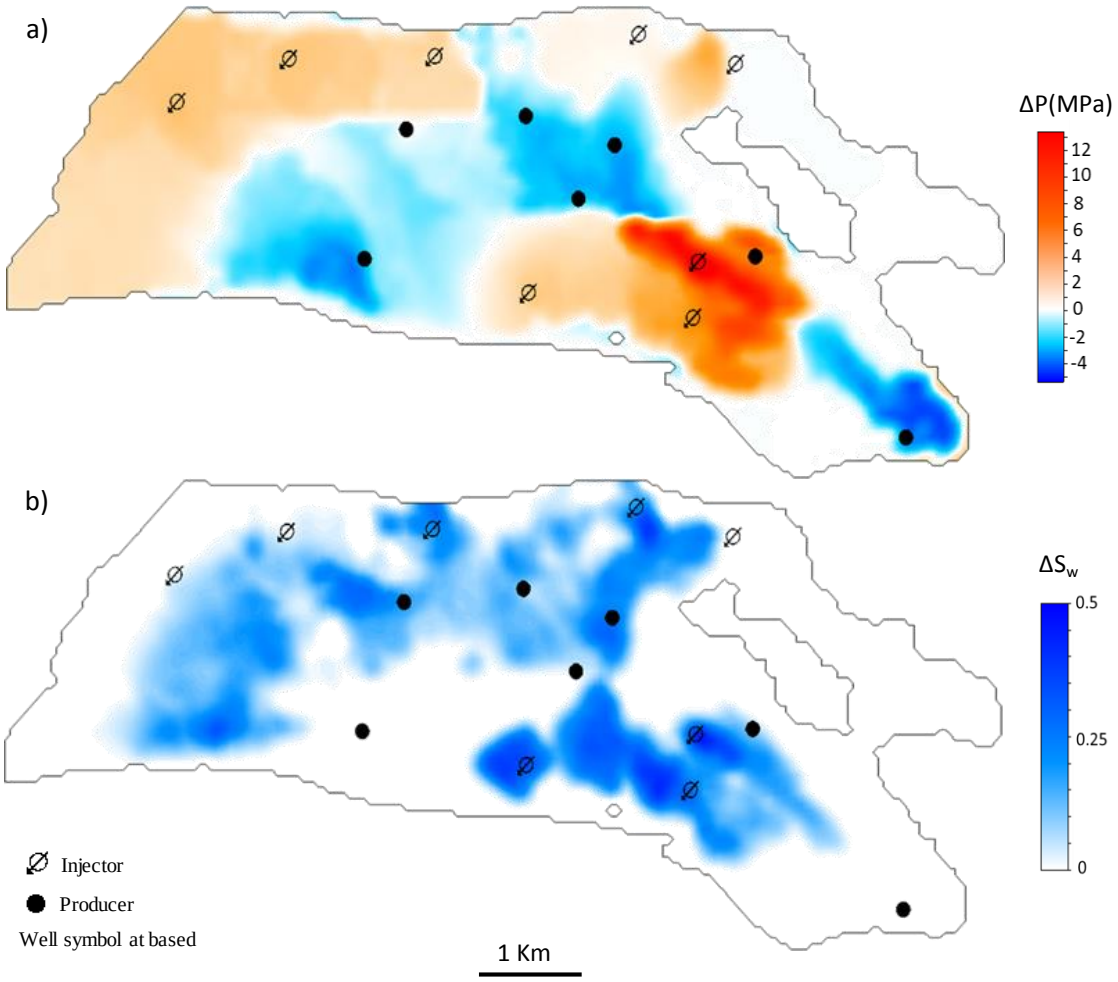

Figure 5.7 *Change in dynamic property maps between the 2004 monitor and 1996 baseline obtained from the simulation model. (a) Pore pressure change map. (b) Water saturation change map for the T31 reservoir sands of the Schiehallion Field.*

5.3 Modelling application to the Norne Field

5.3.1 Field Description

The Norwegian Sea Field, discovered in December 1991 is located on blocks 6608/10 and 6508/10 on a horst block in the southern part of the Norland II area in the Norwegian Sea (figure 5.8a) and lies beneath water depths of about 380m. The size of the horst block is approximately 9km x 3km (Ouair et al. 2005). The field consists of two separate oil compartments, the main structure corresponding to the segments C, D and E which production started in 1997 (Osdal and Alsos 2002) and the North-East Segment known as G segment (figure 5.8b).

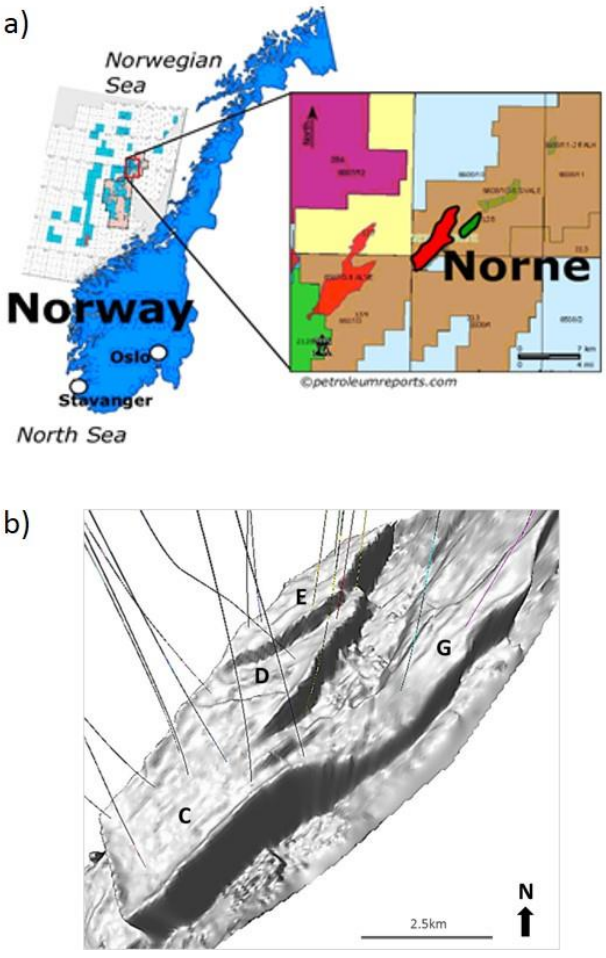

Figure 5.8 *(a) Location of the Norne Field in the Norwegian Sea. (b) Horst block structure showing four different segments C, D, E and G.*

The reservoir sandstones of Late Triassic to Middle Jurassic age in the formations Garn, Ile, Tofte and Tilje (figure 5.9) are dominated by fine-grained and well sorted sub-arkosic arenites. The sandstones are buried at a depth of 2500-2700m, with a porosity range of 25-30% and permeability values between 20 to 2500 mD (Verlo and Hetland 2008; Statoil 2001c).The entire reservoir thickness varies over the Norwegian Sea Field from 260m in the southern parts to 120m in the northern parts (Verlo and Hetland 2008). The reservoir is reasonably well connected even though the presence of shale and calcite permeability barriers and faulting has a big impact on the reservoir production and connectivity (Aarre, 2006).

The Garn Formation deposited during the Late Aalenian and Early Bajocian has a thickness of 35m and its depositional environment was near shore with some tidal influence. The reservoir quality increases upward within the formation. The Garn Formation is divided in three reservoir zones; Garn 1 is a sandstone unit, whose lower part is muddy as is the continuance of the Not Formation, and the upper part has an increased sand content. Garn 2 consists of fine grained sandstones and at the top shows calcareous cemented sandstone. Garn 3 is made up of low angled cross bedded fine grained sandstones (Verlo and Hetland, 2008).

The Not Formation, deposited during the Aalenian in a quiet marine environment, is a 7.5m thick, dark grey to black claystone with siltstone lamina. The Not Formation has a coarsening upward trend which continues into the Garn Formation. The Ile Formation, corresponds to a sandstone of 32-40m thickness with generally good reservoir quality, deposited during the Aalenian in the shoreface environment. It consists of fine to very fine grained sand which is coarsening to the north, and displays cemented calcareous layers results of minor flooding in a regressive period. The sandstones of the Tofte Formation has a mean thickness across the field of 50m and were deposited in a marine from foreshore to offshore environment; and finally the Tilje Formation consists of sand with some clay and conglomerates deposited in a marginal marine, tidally influenced environment (Verlo and Hetland, 2008).

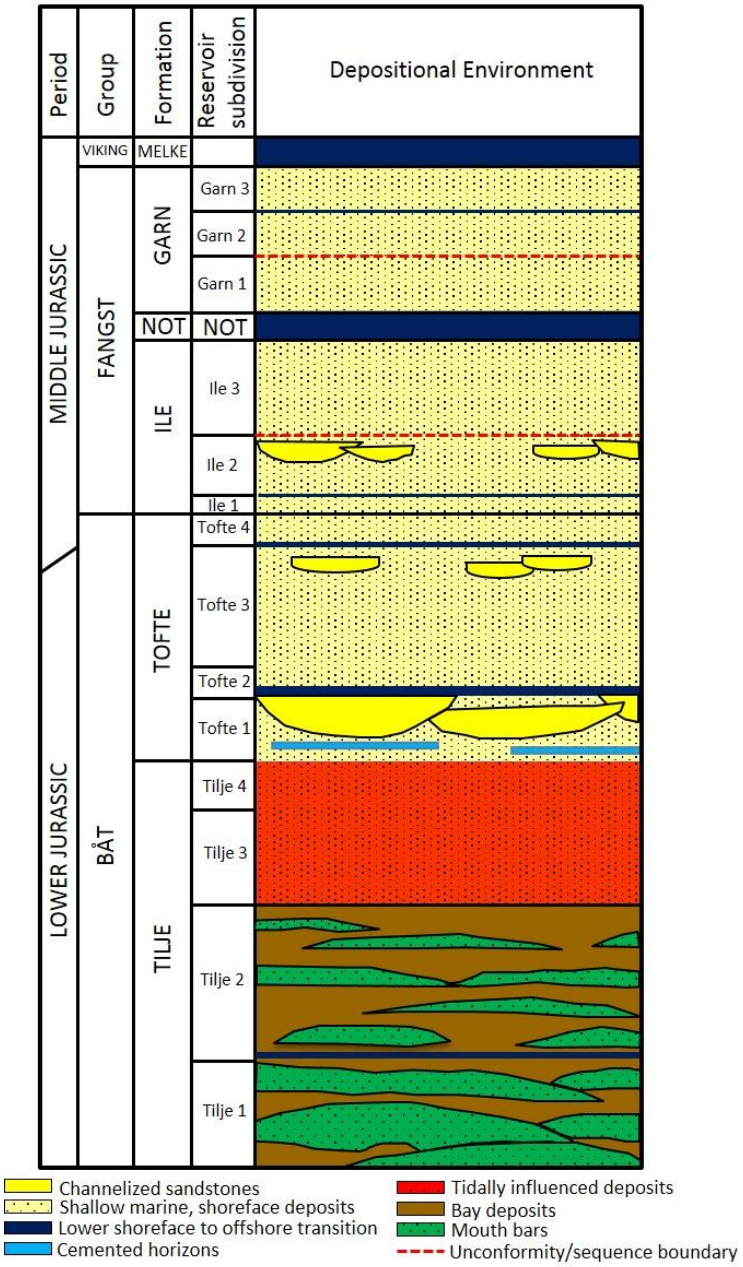

Figure 5.9 *Stratigraphical division of the Norne Field (redrawn from Statoil 2001c; Verlo and Hetland 2008)*

5.3.2 Datasets

The first seismic survey was acquired in 1992. Production started in 1997 in CDE segments and in 1999 for G-segment. The seismic surveys available for this study were shot in 2001, 2003, 2004 and 2006 (figure 5.10). Besides the seismic volumes, a range of wireline logs from several wells is available and a flow simulation model with dimension of 46x112x22 cells, with a grid cell size of 50x50m and cell height ranging from 2m to 20m.

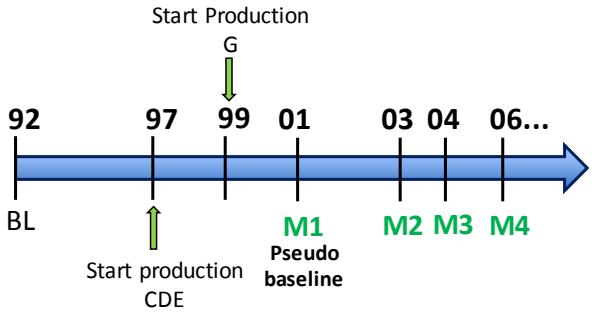

Figure 5.10 *Timeline of the seismic surveys in the Norne field over the years and start of production dates. Highlighted in green the seismic surveys available for this thesis. 2001 pseudo-baseline after production and three monitor seismic volumes (2003, 2004 and 2006)*

In this work, 2001 survey is considered as the baseline and the rest of the surveys as monitors, however this should affect the 4D seismic signature, since there is gas present in the pseudo-baseline survey post production that needs to be taken into account. The polarity of the seismic data implies that an increase in acoustic impedance is plotted as a peak, figure 5.11 shows a vertical section from the 2001 pseudo-baseline seismic survey, troughs in red and negative values represents the sand bodies. The top of Garn is picked as troughs by Statoil, which represent the decrease in acoustic impedances at the boundary between the claystones from the cap rock and the soft sandstones of the Garn formation.

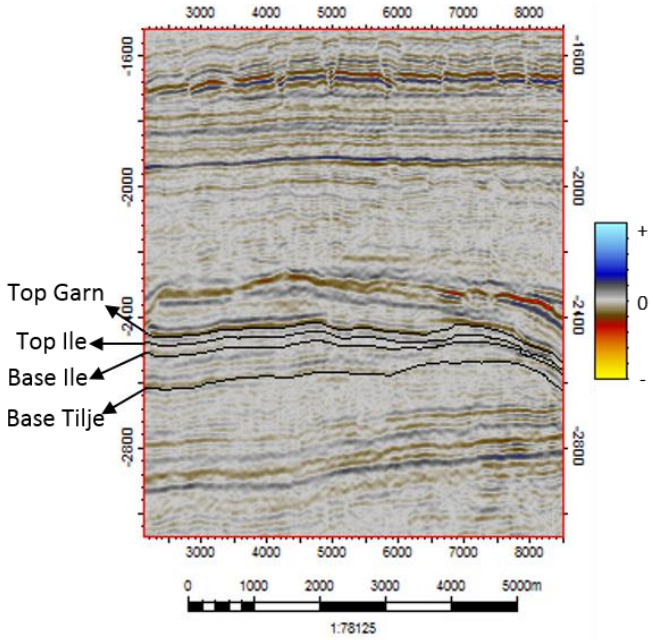

Figure 5.11 *Vertical section from the 2001 post-production seismic survey of the Norne Field. The top and base horizons (Garn and Tilje) of the sand layers are picked as the strong negative reflectors by the data provider. The top and base of Ile formation shown in this picture were obtained from the simulation model, later used for the attribute mapping in chapter 6.*

5.3.3 Sim2Imp modeling

Each cell in the flow simulation model can be transformed into corresponding elastic properties (V_P, V_S, and ρ) for each of the rock physics models (A, B C and D). Figure 5.12 shows the resultant depth average impedance change maps for the producing sands of the Ile formation, which in the simulation model is defined between layers 5 to 11. The twelve time-lapse maps calculated between the 2004 monitor and the 2001 pseudo-baseline display an obvious static structure imprint, but in most areas in the maps, the modelled 4D response (P-impedance changes) shows consistency with the change of dynamic properties maps obtained from the simulation model (figure 5.13). Qualitatively all twelve maps display hardening (blue areas) where the oil is being replaced by water or gas coming back into solution, and softening zones (yellow/red areas) due to pressure build up or increase in gas saturation.

In the northwest of the field from figure 5.12 the strongest softening signature is displayed, where the pore pressure change reaches up to +15MPa (figure 5.13a). Meanwhile in the southwest area it is found a released gas zone (figure 5.13c) which determine the softening response observed in the impedance change maps. Based on the observation of the hardening signature, the maps obtained through PEM D show the strongest effect due to water-flood compared to the remaining maps, with the time-lapse maps obtained using PEM C showing the less contrast in the hardening areas. Similar way as in the Schiehallion field, such remarks will be reiterated when moving into a more quantitative analysis later in the discussion. When comparing the results between the clastic fields, the 4D response maps of both fields seems to point out that the PEM D is more sensitive to saturation, while PEM C is more sensitive to pressure, even though the fields have different geological settings.

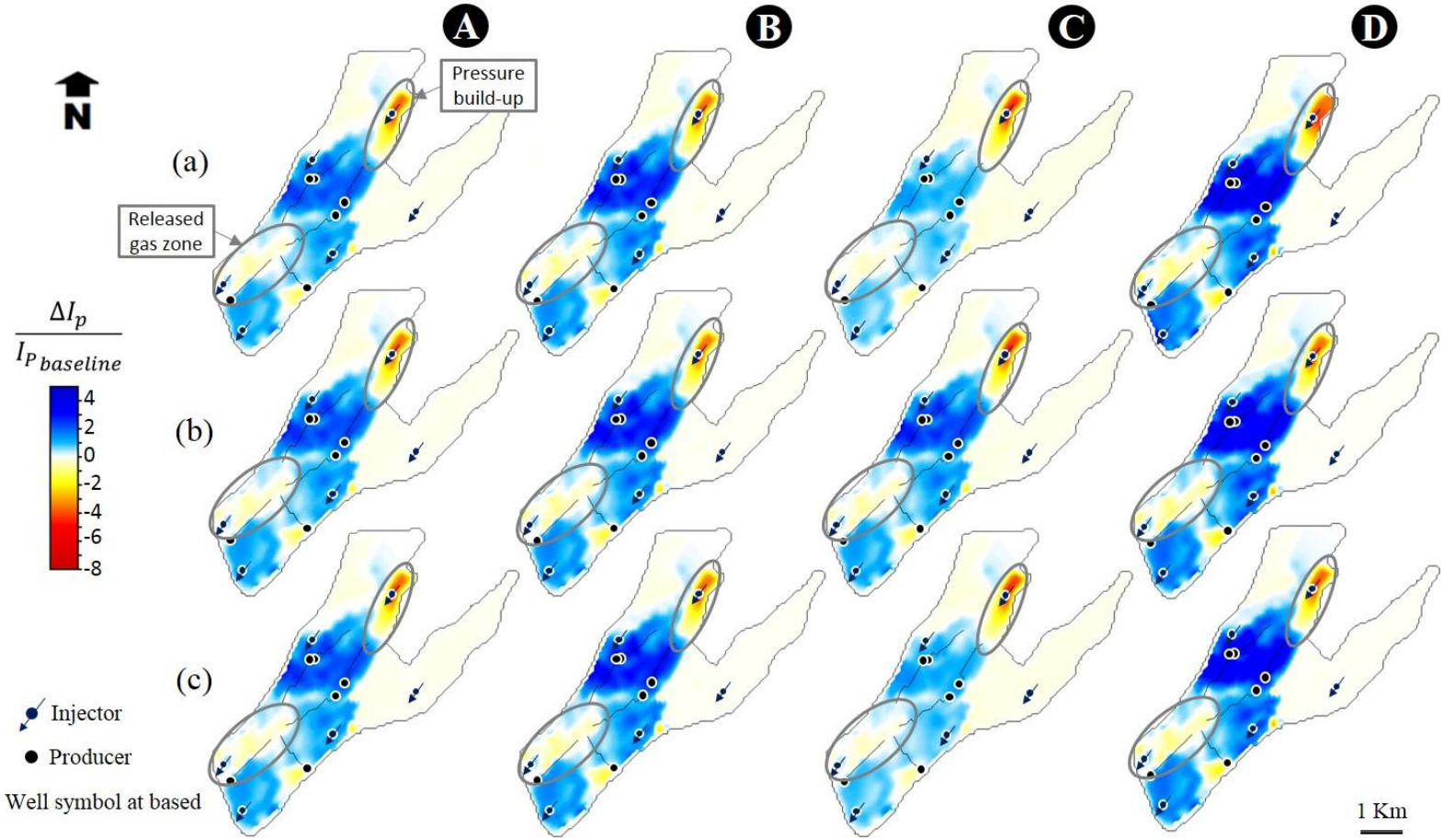

Figure 5.12 *(a) Maps of impedance change predicted by calibrated PEMs A, B C and D based on mixing the solid components before fluid substitution approach for the Ile sand formation of the Norne Field.(b) as in (a) but maps based on mixing the solid components after fluid substitution, and (c) as in (a) but maps of impedance change predicted using Backus averaging.* (Blue = hardening; Yellow/Red = softening).

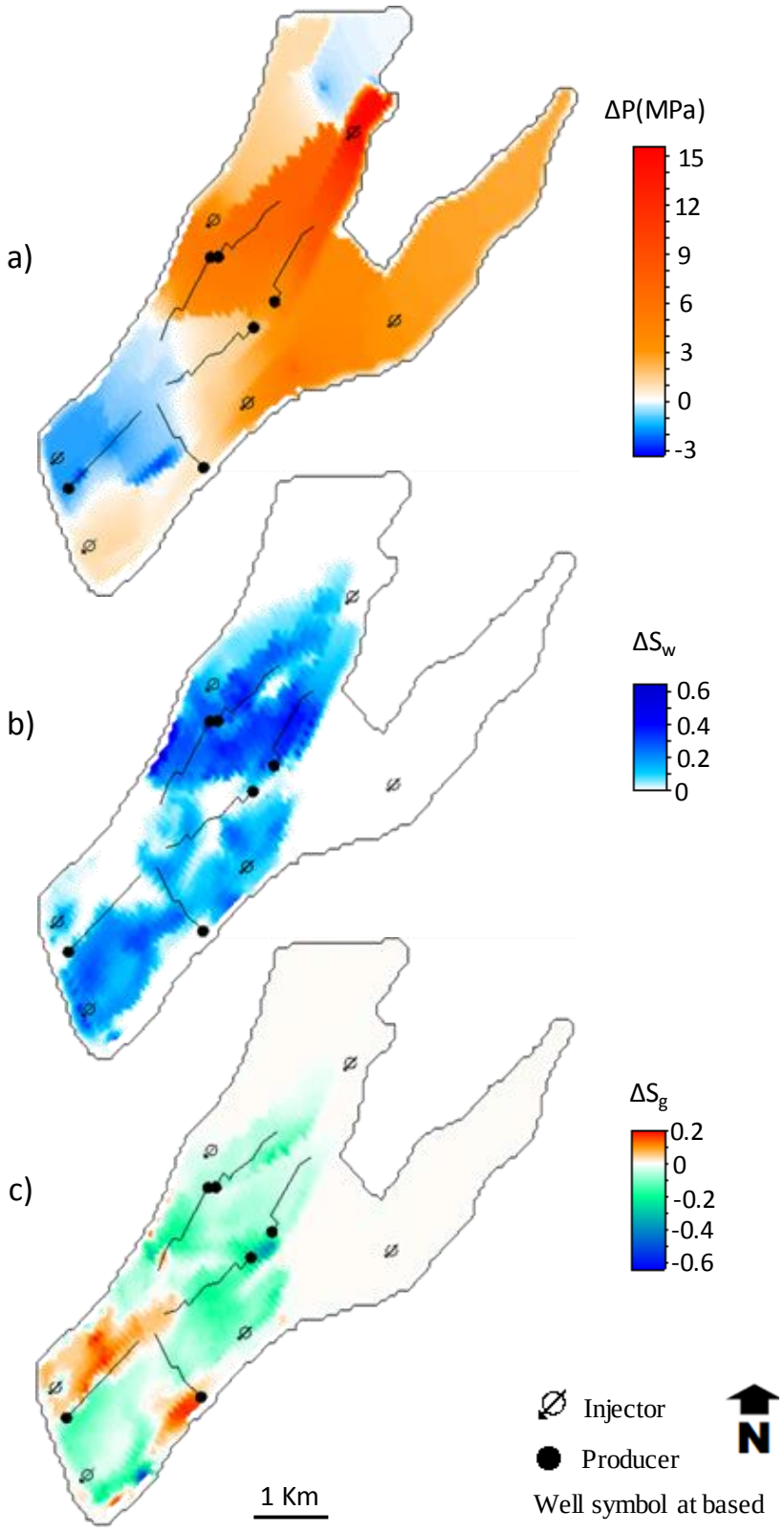

Figure 5.13 *Change in dynamic property maps between 2004 monitor and 2001 pseudo-baseline obtained from the simulation model. (a) Pore pressure change map. (b) Water saturation change map and (c) gas saturation change map for the Ile formation of the Norne field.*

5.4 Modelling application to the Carbonate Field X

5.4.1 Field Description

The carbonate Field X was discovered in 1974 and is located in the central part of the Campos Basin, Brazil (figure 5.14a) and lies beneath water depths of about 124m. The net reservoir interval is approximately 70-90m thick of light oil column with an API gravity of 30º contained in shallow marine platform carbonate bars (figure 5.14b), which are mainly composed of intertidal oncolytic packstones of the Albian Macaé Formation, other facies found in the field include crinoid and bryozoan packstones and lime mudstones as secondary and tertiary facies type respectively.

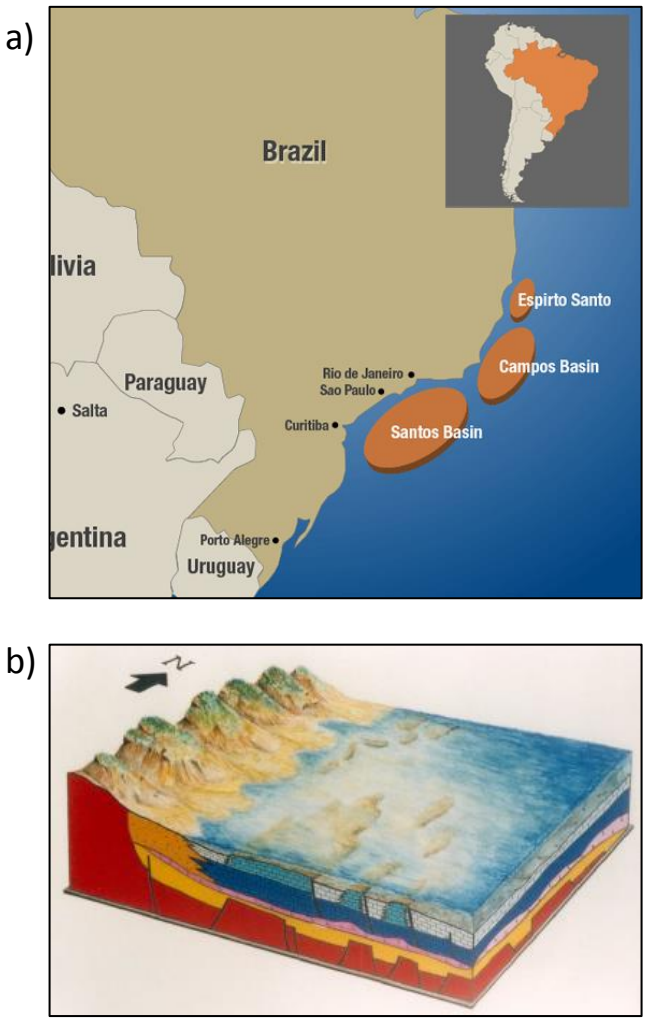

Figure 5.14 *(a) Location of the Field X in Campos Basin. (b)Depositional setting of the shallow marine platform carbonate bars.*

The field is 5Km long and 3Km wide and exhibits a layer-cake architecture and display narrow distribution ranges of porosity and permeability. Porosity ranges between 16 and 25% with a mean porosity of 19%, meanwhile permeability average is 175 mD with a range of 126-200 mD (Carozzi and Falkenheim, 1985). Field X came on-stream in 1979 and the production was supported by a strong bottom-water aquifer drive. The reservoir has good lateral continuity and no major compartmentalization. The high reservoir quality of the topmost zone is due to coarser grain size and effective secondary porosity generated from dissolution of intergranular calcite cement.

5.4.2 Datasets

For this study, the available datasets consisted of wireline log data from several wells, a flow simulation model with dimension of 65x74x72 cells, with a grid cell size of 75x75m and cell height ranging from 2m to 20m. Two seismic surveys, namely the 2002 pseudo-baseline seismic survey and 2011 seismic monitor survey are also accessible (figure 5.15).

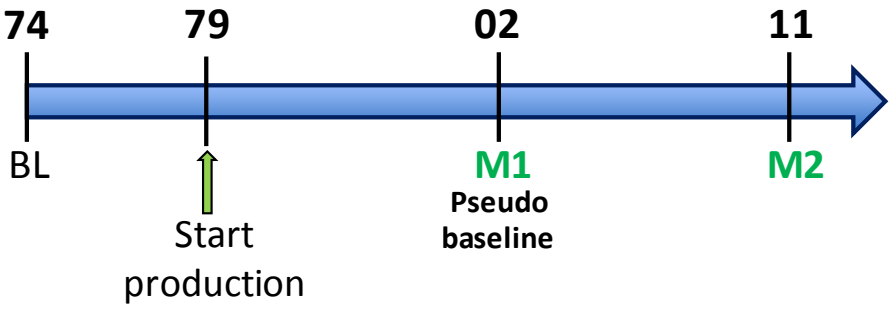

Figure 5.15 *Timeline of the seismic surveys in the Field X over the years and start of production date. Highlighted in green the seismic surveys available for this thesis. 2002 pseudo-baseline after production and one monitor seismic volume (2011)*

The convention for the seismic section shown in figure 5.16 is that an increase in acoustic impedance is plotted as a peak. Figure 5.16 shows a vertical section from the 2002 pseudo-baseline seismic survey where the reservoir thickness varies between 100 and 140 ms. The troughs from the strong negative reflector in the reservoir is picked as the top by the data provider, which represents a decrease in acoustic impedances at the boundary between the overburden and the carbonate reservoir rock.

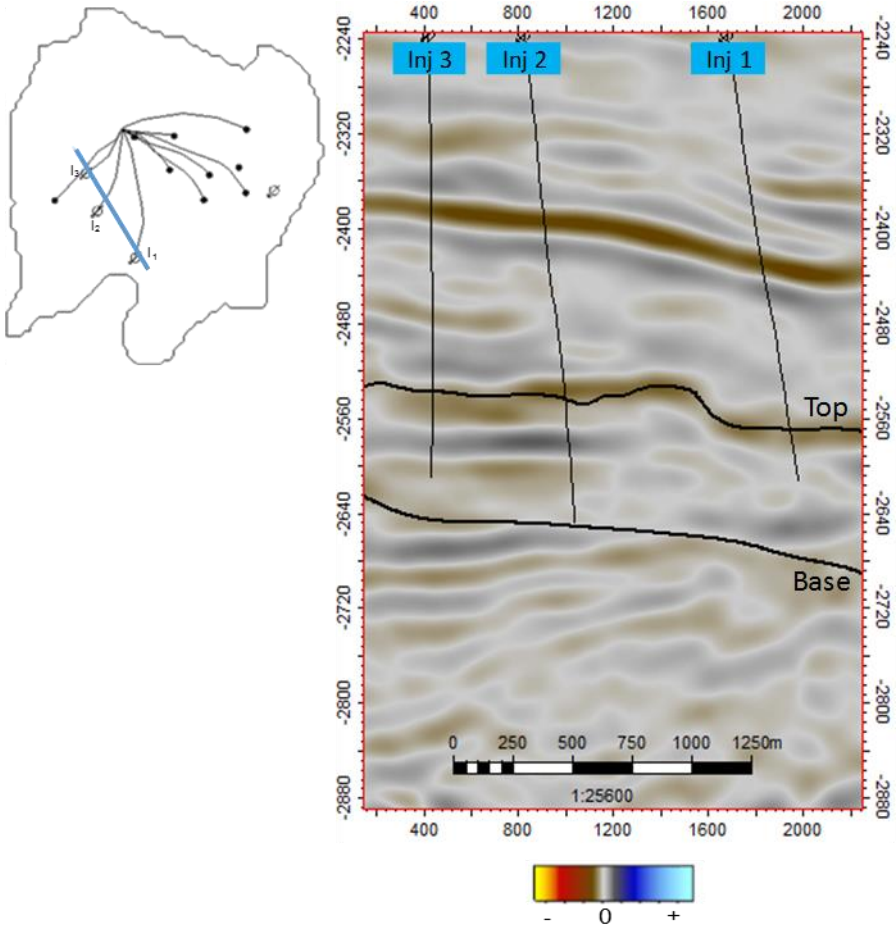

Figure 5.16 *Vertical section from the 2002 post-production seismic survey of the carbonate Field X. The top and base horizons of the reservoir are picked as troughs by the data provider.*

5.4.3 Sim2imp modeling

Each cell in the flow simulation model is transformed into corresponding elastic properties (V_P, V_S, and ρ) based on PEMs E, F_1 and F_2. Figure 5.17 shows the resultant depth average impedance change maps for the producing packstones. The average maps for this field were calculated for an optimal window of 15ms below the top reservoir, which translates in the simulation model as the first thirteen layers. The six time-lapse maps calculated between the 2011 monitor and the 2002 pseudo-baseline display an obvious static structure imprint. Qualitatively, all six maps display same hardening areas where gas is coming back into solution and the pore pressure change is relatively small which is consistent with the maps of pore pressure and gas saturation changes displayed in figures 5.18a and 5.18c respectively.

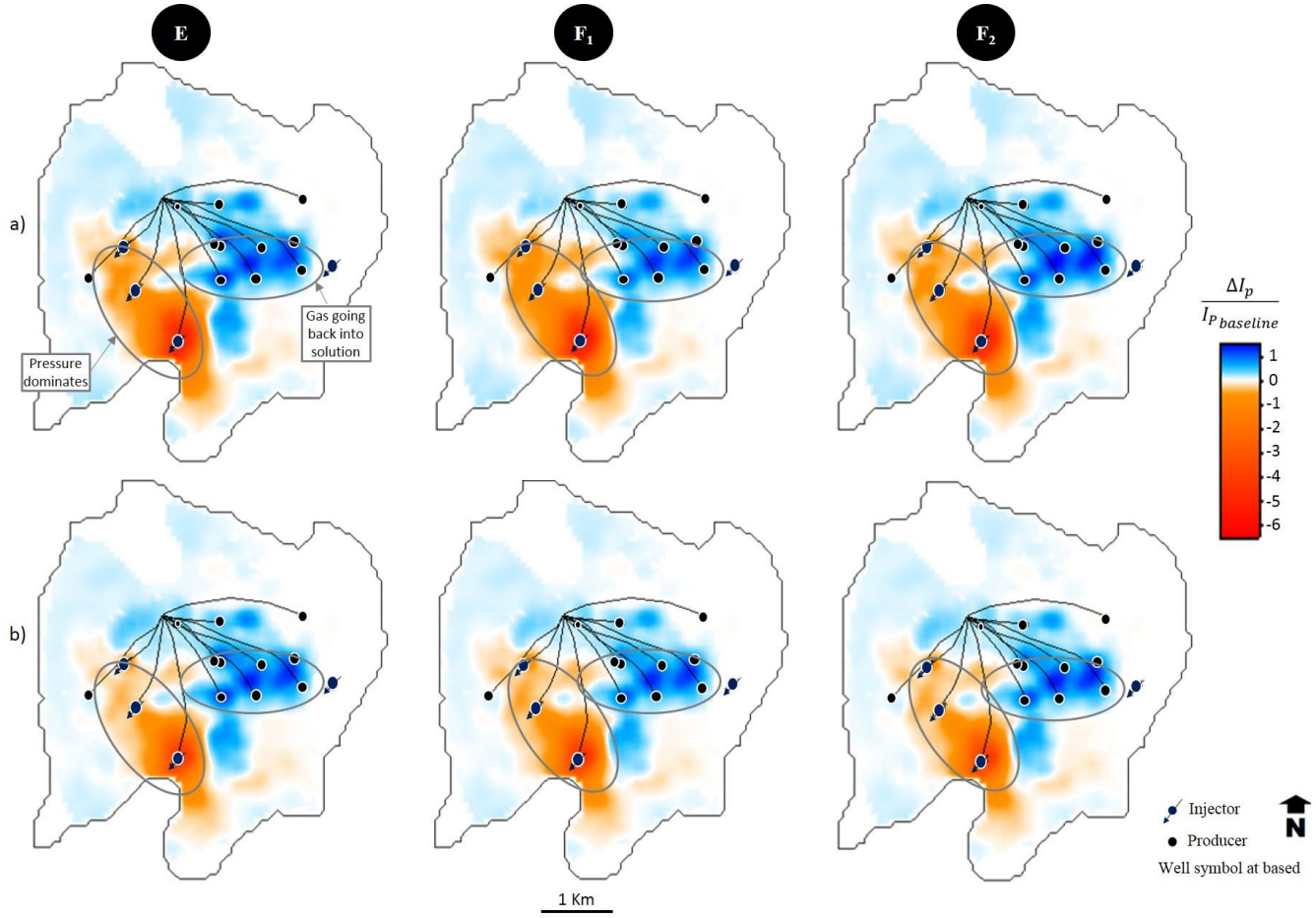

Figure 5.17 *(a) Maps of impedance change predicted by calibrated PEMs E, F_1 (spheres inclusions) and F_2 (needles inclusions) based on mixing the solid components before fluid substitution approach for a 15ms window below top of the reservoir of the Field X .(b) as in (a) but maps based on mixing the solid componets after fluid substitution. (Blue = hardening ; Red = softening)*

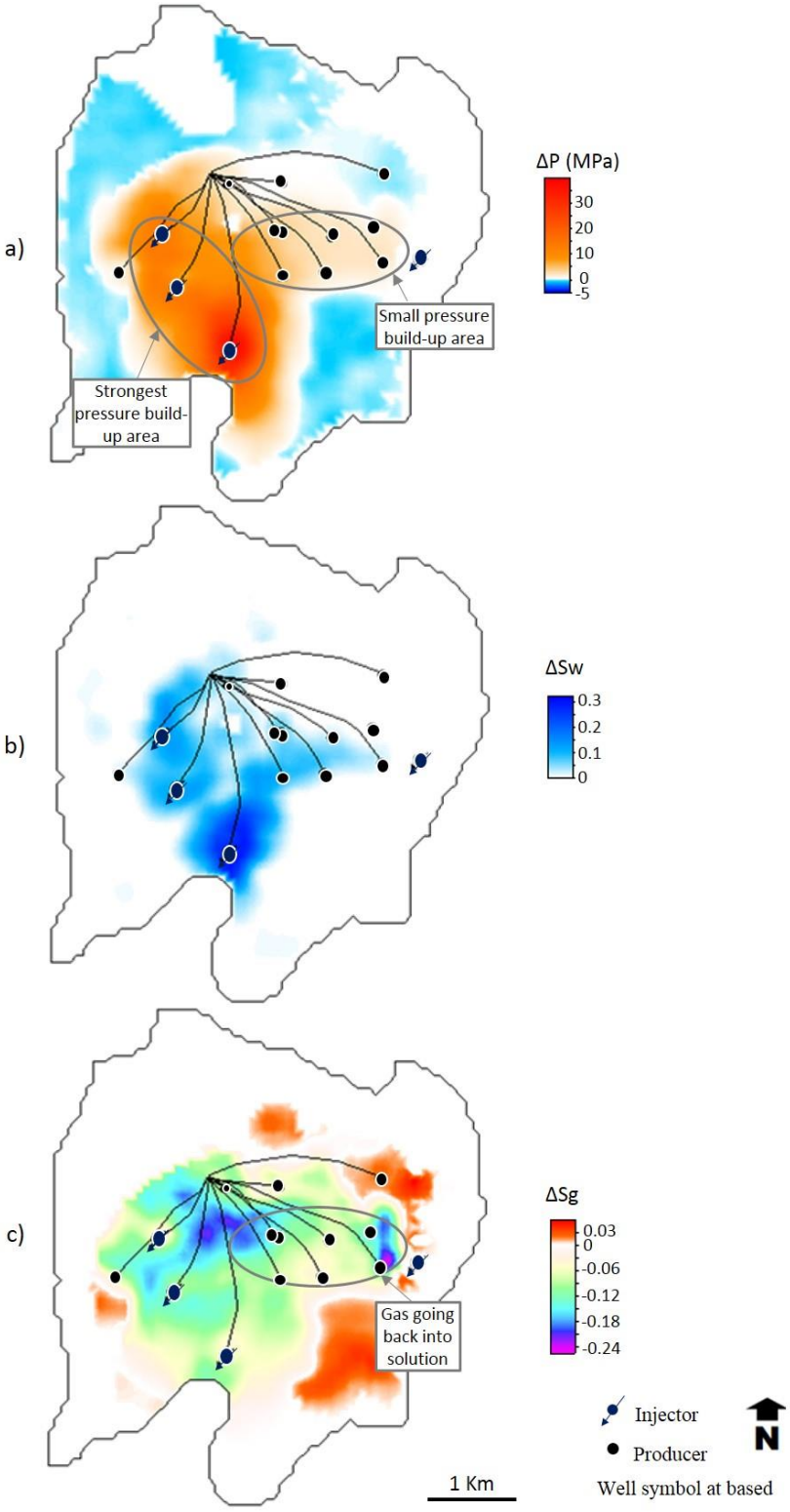

Figure 5.18 *Change in dynamic property maps between the 2011 monitor and 2002 pseudo-baseline time obtained from the simulation model. (a) Pore pressure change map. Bearing in mind the strongest pressure build up area (>+40MPa), means that in the calculation of effective pressure for each time-step negative pressure will be obtained. Suggesting that the pressure distribution in the simulation model is not correct, to avoid such negative values, a cut off for pore pressure was introduced manually inside the sim2imp code. All pore pressure higher than 64MPa, are overwritten manually and kept as 64 MPa. (b) Water saturation change map and (c) Gas saturation change map for top reservoir of the carbonate Field X.*

As for the softening zones (red areas), all 4D maps show the strongest response around the injectors in the west side of the field, where the pressure build up ranges between 10 to 35MPa (figure 5.18a), therefore dominating the 4D seismic signature and winning over water and gas saturation effects. From my observations for the carbonate Field X, there is no rock physics model which displays more sensitivity to pressure or saturation effects, since all the paradigms balance such dynamic changes in a similar way, which is translated in same shape or boundary where both effects are competing and comparable magnitude of the 4D response in the resultant maps.

5.5 Discussion

For each PEM presented in this work a large number of free parameters are determined by the log optimisation procedure, and also relies on laboratory measurements to estimate coefficients related to the stress sensitivity dependence of the rock frame using the modified MacBeth (2004) equations. Despite the data points available with which to calibrate effectively and the adequate degree of fit to almost all log segments as was shown in chapter 4. All PEMs are found to yield similar responses, as can be seen in the resultant 4D change of impedance maps for producing units of each field, which thus makes the choice of the "best" challenging, with any appropriate well-calibrated model. Nevertheless, the large number of inputs parameters for each model makes the process of model fitting particularly non-unique, such high degree of uncertainty of the rock physics model makes the 4D seismic interpretation less intuitive.

On the other hand, there is a strong need to obtain independent evidence with which to evaluate the PEM recipe (Floricich, 2006) moving away from the challenging and uncertain multi-parameter deterministic PEMs. For time-lapse seismic maps in particular, it has been suggested that the main response may be captured by a simple two parameter equation (Equation 2.32, Chapter 2) (Alvarez and MacBeth, 2013) that can relate seismic, engineering and rock/fluid physic domains for ease of interpretation. Indeed, using 4D maps for visual comparison and understanding of time lapse data, lack the representation of the vertical heterogeneity from the simulation model and seismic domain.

5.5.1 Proxy model for impedances (synthetic data)

The controlling parameters (C_S and C_P) of the proxy model ($\Delta A = C_S \Delta S_w - C_P \Delta P$) provide the balance between the relative contributions of saturation (ΔS_w) and pore pressure (ΔP) change to the overall time-lapse seismic signature (ΔA) (Alvarez and MacBeth 2013). Given that in this work, the simplified equation is a proxy model for the rock and fluids physics only, it is therefore used to estimate the change of P-impedance data between monitor and baseline for the synthetic computed data as the time-lapse seismic signature. Even though gas is present in the field data and is included in the previous 4D impedances map for PEM comparisons, in the proxy model space we are excluding all the cells where gas has been predicted in the flow simulator model data.

The controlling parameters C_S and C_P, which are unitless and MPa^{-1} respectively, for all the scrutinised fields are calculated using the previously stated deterministic PEMs (A, B, C and D for the clastic fields and E and F for the carbonate reservoir) at baseline and monitor times, using the static and dynamic (pore pressure and saturations changes) properties from the simulation model, and the set of log calibrated inputs parameters for each rock physics model. In order to determine the controlling parameters C_S and C_P, an end member study of the PEM strategies is performed; this means, assuming there is no pressure change between baseline and monitor, we can calculate the change of P-impedances equivalent to a pure saturation signal response. In the same way as when there is no water saturation change between baseline and monitor we obtain the change of P-impedances for the pure pressure signal response. Of course the effect of pressure and saturation is convolved, because they are coupled when the fluid flow equations are solved.

Once the independent scenarios where the impedances under constant pressure and also impedances under constant fluid saturations are computed, then C_S and C_P can be calculated respectively through local gradient, using cross-plots of change in P-impedances of each end member study ($\Delta I_{P(\Delta Sw=0)}$; $\Delta I_{P(\Delta P=0)}$) versus changes in dynamic properties (water saturation and pore pressure change) from the simulation model between the two time periods of interest in the reservoir history (usually pre-production baseline and a monitor) and excluding all cells containing gas. The cross-plots only

represent the producing units of each field, figure 5.19a and 5.19b show an example for the calculation of the controlling parameters for the T31 sands of the Schiehallion field, for which impedance changes ($\Delta I_{P(\Delta Sw=0)}$; $\Delta I_{P(\Delta P=0)}$) were calculated using the PEM A "mixing before fluid substitution" paradigm.

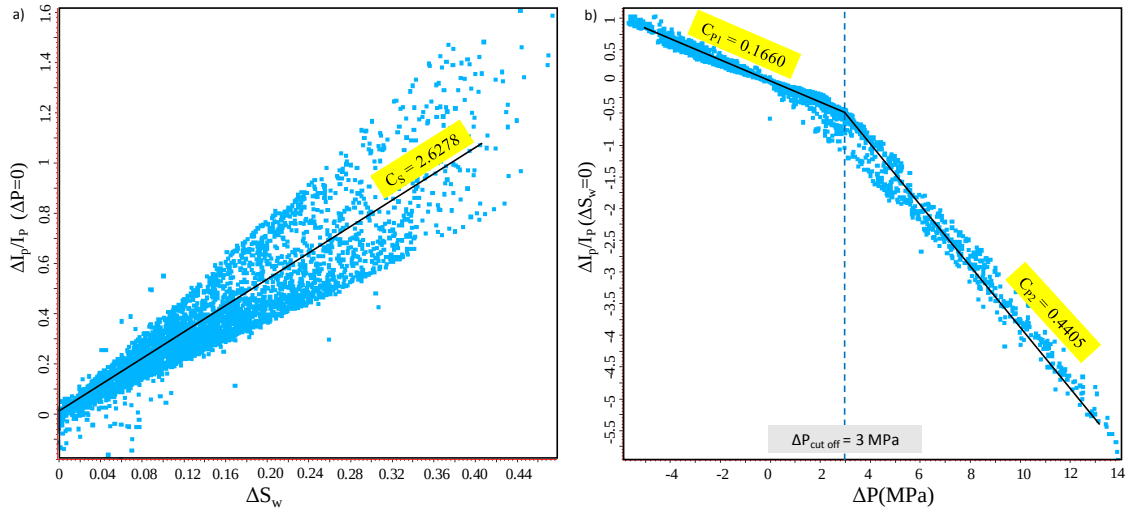

Figure 5.19 *(a) Cross-plot of change of impedances calculated keeping pressure constant in monitor and baseline versus change of water saturation for the T31 sands of Schiehallion field. (b) Cross-plot of change of impedances calculated keeping saturation constant in monitor and baseline versus change of pore pressure.*

The stress sensitivity model used for the four PEMs might not be appropriate or it is exaggerated strongly, because it shows a non-linearity in the cross-plot of change in P-impedance versus change in pore pressure (figure 5.19b), for such reason the calculation of C_P is divided into two different slope regions (C_{P1}, C_{P2}) with the cut off between both slopes at +3MPa for the Schiehallion field. A similar behaviour is observed for the remaining fields. For the Norne field the change of slope occurs around +8MPa while for the carbonate Field X around +15MPa pore pressure change. This observation increases the number of parameters and to some extent the complexity and understanding of the proxy model.

Previous work (Alvarez, 2014) states that the controlling parameters C_P and C_S have a strong dependency on porosity. In terms of saturation changes, they become stronger as porosity gets larger, which explains the more scatter behaviour in figure 5.19a. Therefore C_S is proportional to porosity, however for pressure this is not obvious since

the pressure has two elements to take into consideration, rock stress sensitivity and fluid pressure sensitivity. Nevertheless, the controlling parameters in this thesis are not calculated with distinction in porosity ranges (low, medium, high). Once the controlling parameters are obtained, it is straightforward to obtain the new time-lapse maps based on the equation 5.2 for each producing units of the investigated fields.

$$\frac{\Delta I_P}{I_P} = C_S \Delta S_w - \begin{cases} C_{P1} \Delta P \rightarrow for \quad \Delta P < cutoff \\ C_{P2} \Delta P \rightarrow for \quad \Delta P > cutoff \end{cases} \tag{5.2}$$

Figures 5.20a, 5.21a and 5.22a display the 4D P-impedance change maps for the proxy model, corresponding to the Schiehallion field (2004-baseline), Norne field (2004-2001) and Field X (2011-2002) respectively, with the controlling parameters given in table 5.1. The required C_S and C_P displayed in table 5.1 were calculated for all the PEMs (A, B, C, D, E and F) based on mixing before fluid substitution and using only one set of calibrated input parameters from the optimization algorithm (chapter 4), specifically the ones highlighted in yellow in tables 4.4 until 4.13.

Field	**PEM**	**Cut off ΔP**	**C_P**		**C_S**
			C_{P1}	**C_{P2}**	
Schiehallion	A	+ 3 MPa	0.1660	0.4405	2.6278
	B		0.1765	0.4212	3.6046
	C		0.1745	0.4561	2.1242
	D		0.1786	0.3641	5.4590
Norne	A	+8 MPa	0.0754	0.4966	4.7778
	B		0.0805	0.4604	6.0011
	C		0.0641	0.5468	2.6921
	D		0.0926	0.4434	9.6380
Field X	E	+15MPa	0.1333	0.2988	4.3470
	F_1		0.1336	0.3010	4.3488
	F_2		0.1346	0.2918	4.4094

Table 5.1 *Proxy model controlling parameters obtained from the model predictions obtained from each deterministic PEM for the Schiehallion Field, Norne Field and Carbonate Field X.*

From a qualitative point of view, the maps produced with the three parameters proxy model still preserve the internal variation between the changes of pressure and saturation, which implies that the proxy model, compared to the deterministic PEMs containing a larger amount of inputs, still obey to the trend of the time lapse response. Differences in the 4D impedance change maps calculated using C_P and C_S are due to non-linearity in the calculation of the gradient of the change of impedance for each deterministic PEM. It is important to point out where the variability in C_S and C_P for the different PEMs and scenarios comes from. C_S is PEM dependent meanwhile C_P has a strong dependence on the stress sensitivity model and since all the PEMs studied share a common model for stress sensitivity, the C_P term obtained has small variability between PEMs for each field (table 5.1). It is known that C_P carries more uncertainty than C_S (MacBeth, 2004; Eiken and Tøndel, 2005). Certainly pressure sensitivity is calibrated using core laboratory measurements which does not translate to the real in-situ field-scale reservoir response (Fürre et al. 2009; Alvarez and MacBeth 2014).

From Table 5.1, it is observed that C_S obtained from PEM D is higher from both clastic fields than the one obtained through the remaining PEMs, which agrees with the observation previously stated in sections 5.3.2 and 5.3.3 that the 4D maps based on PEM D shows the strongest hardening effect response due to water-flood. Meanwhile, C_S obtained from PEM C is the lowest in both fields, meaning that shows the weakest hardening signature out of all the PEM results. As for the Field X, the controlling parameters gotten based on the calibrated PEM E and F, do not give a decisive conclusion in term of which model adjusts, or is more or less sensitive to pressure or fluid saturation.

I compare in a quantitative manner the 4D maps obtained from the deterministic PEMs versus the ones obtained from the proxy model. The errors are calculated for the areas where both maps display softening and where both maps display hardening. For the Schiehallion field (figure 5.20b) the percentage of fit varies from 1% to 20%in the hardening areas for all the PEMS, meanwhile the softening areas shows the highest variability with errors from 1% up to +70%, the biggest errors occurring in softening areas due to pressure build up where the change in pressure reaches up to +14MPa. As for the Norne Field, the error fit (figure 5.21b) in the hardening areas varies between +1% and +50% and in the softening areas the error between both maps is from 1% up to

90%. The highest errors occur in the pressure build up zones where the pressure change between the 2004 monitor and the 2001 baseline is between +11 and +15 MPa. However, patches are observed in the error maps that correspond to areas of disagreement in polarity between the predicted impedances maps calculated through the deterministic PEM and those obtained using a simple proxy model. This disagreement observed in figure 5.21b agrees with the areas where an increase in gas saturation occurs (figure 5.13c).

For the carbonate Field X, figure 5.17a obtained from the deterministic PEMs compared to the figure 5.22a using a proxy model shows the least similarity of the three fields investigated in this thesis. When the polarity agrees in both maps, the errors are between 10% and 90% in the softening areas, and less than 10% in the hardening (figure 5.22b). The proxy model maps for the Field X, fails to reproduce the hardening areas observed in the predicted maps using deterministic PEMs due to gas coming back into solution after production, where the negative gas saturation change varies from -0.03 to -0.25 (figure 5.18c) and the pore pressure change is less than +5 MPa (figure 5.18b).

The resultant 4D maps using the proxy model for all fields, show a clear pattern of the distribution of pressure and water saturation from the simulation model, indeed the zones where both effects are competing display the same boundary shape in all the impedances change maps, since the controlling parameters act just as scale factors to provide the right 4D response. The biggest errors in the softening areas may be related to the complexity of the stress sensitivity term, and the difficulty to define a numerical value for C_P (Alvarez 2014). The proxy model presented in this work was designed for an oil-water system (i.e. no gas), where pressure increase softens the reservoir and gives the opposite polarity to water saturation increase or reservoir hardening via pressure depletion. The availability of the data will drive the study also, for Norne and Field X only preproduction seismic data is available, therefore gas presence is observed initially and after years of production and injection some of this gas will go back into solution affecting the time-lapse response. Consequently using only a 2 parameters proxy model that accommodates for the changes in pressure and water saturation, it will not be able to reproduce the entire 4D response laterally across the entire field in the presence of gas.

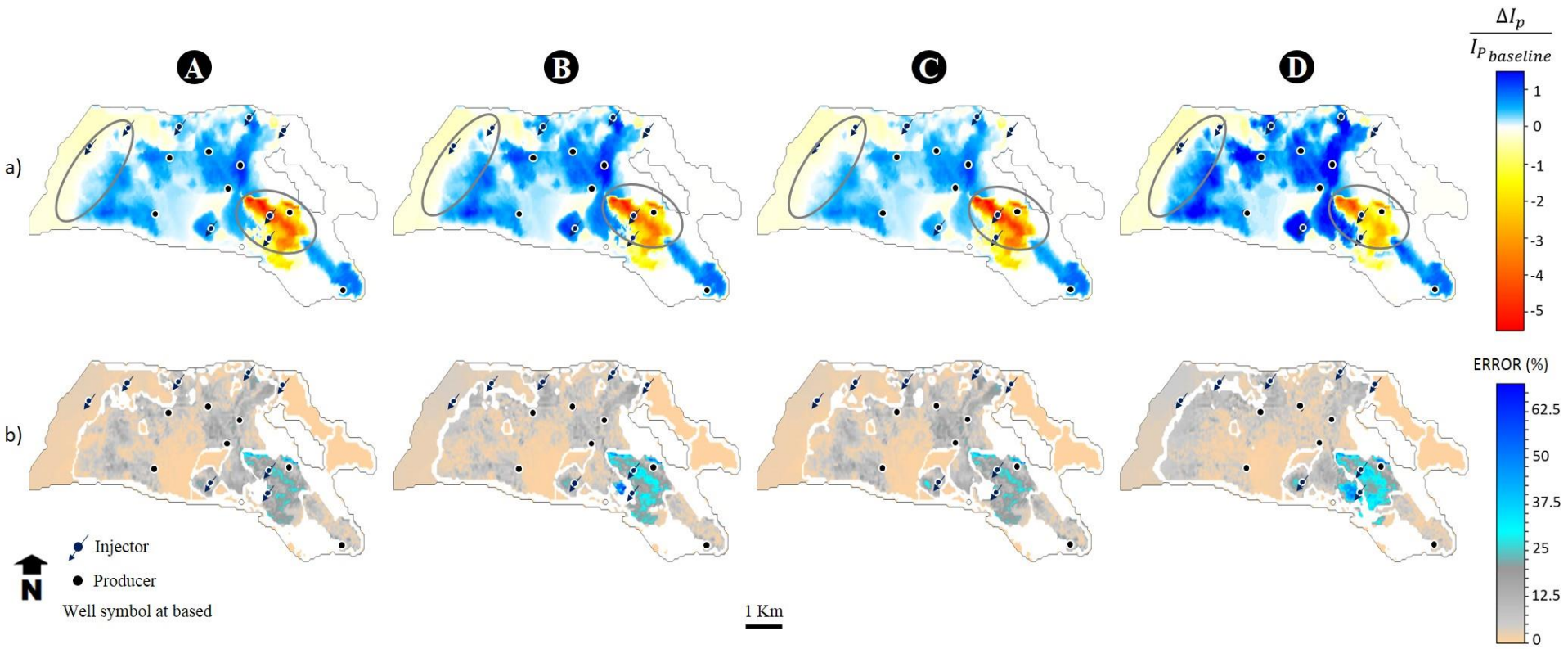

Figure 5.20 *(a) Maps of impedance change predicted using the reduced parameters proxy model for the Schiehallion field. (b) Error maps between the maps of impedance change predicted by calibrated deterministic PEMs A, B, C and D and the ones predcited by the proxy model.*

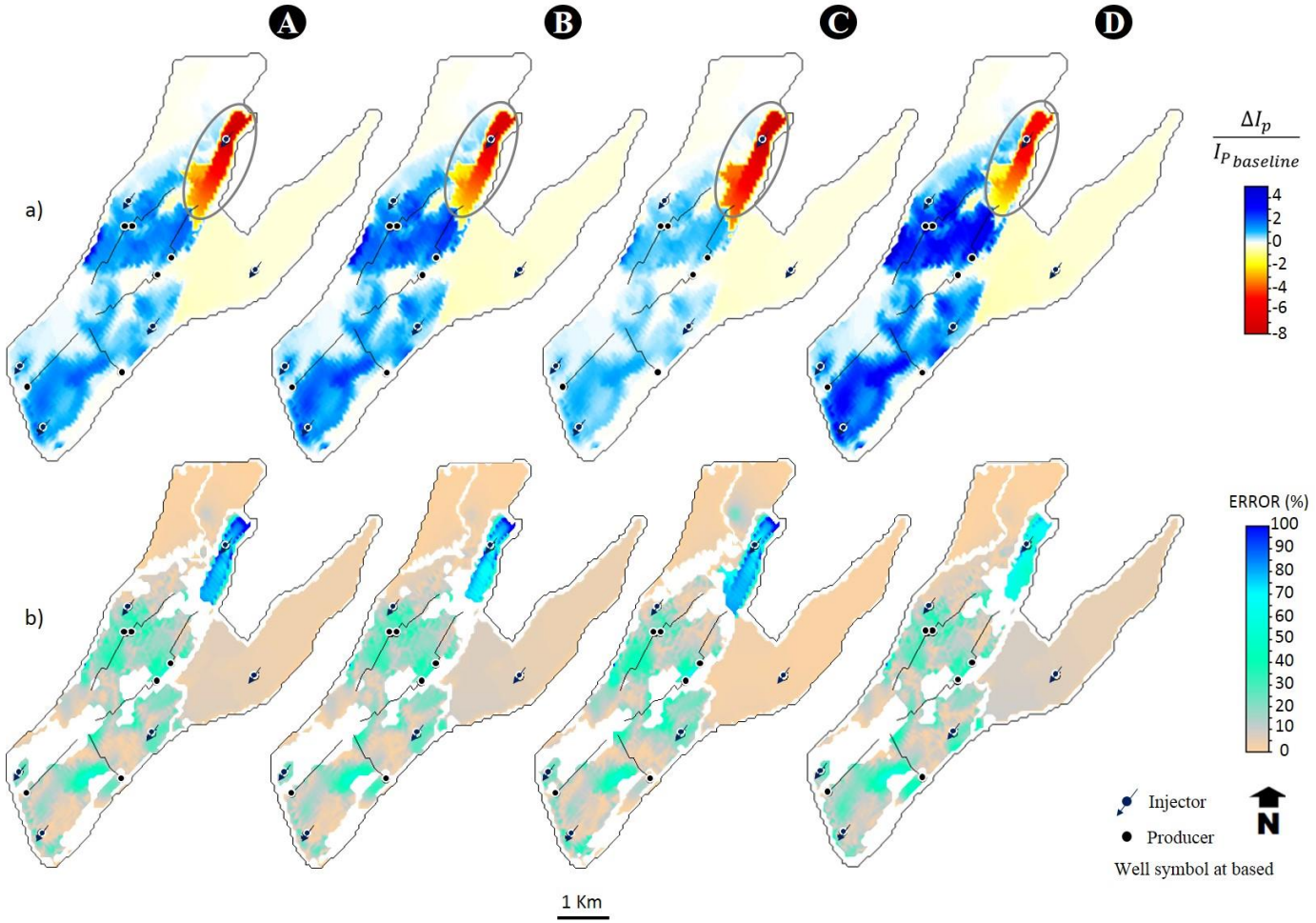

Figure 5.21 *(a) Maps of impedance change predicted using the reduced parameters proxy model for the Norne field. (b) Error maps between the maps of impedance change predicted by calibrated deterministic PEMs A, B, C and D and the ones predcited by the proxy model.*

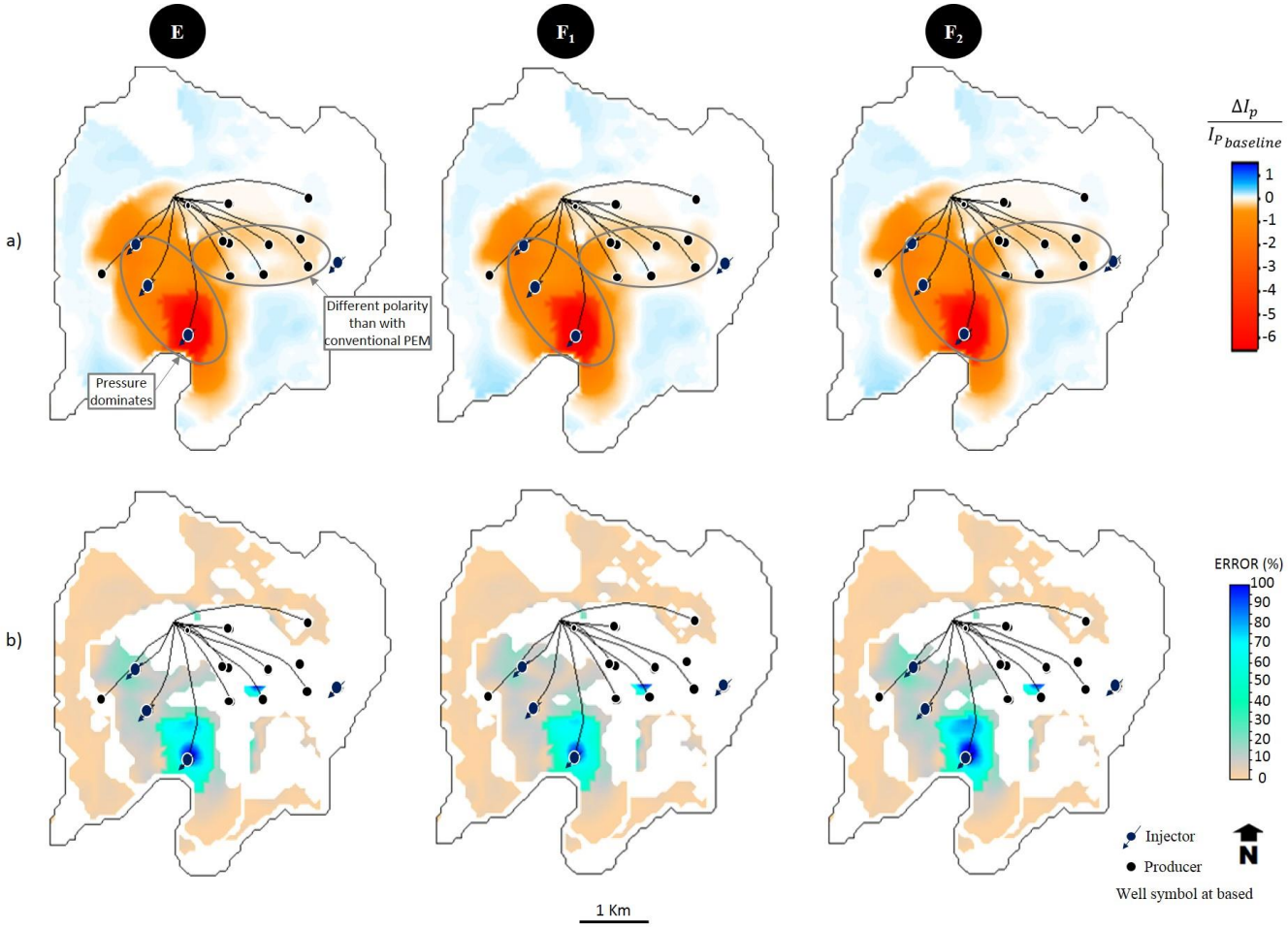

Figure 5.22 *(a) Maps of impedance change predicted using the reduced parameters proxy model for the Field X. (b) Error maps between the maps of impedance change predicted by calibrated deterministic PEMs E, F_1 and F_2 and the ones predcited by the proxy model.*

5.6 Conclusions

From all the observations from Schiehallion, Norne and Field X, in general and within a certain tolerance, the conclusion is that any of here presented conventional PEM may be appropriate, especially in a qualitative way. However, the calibration of the vast amount of parameters can be challenging and create uncertainty across the different models. In this sense, each PEM appears as a reasonable choice, no matter its complexity. In this work, the reduction of inputs parameters used in the deterministic PEMs was tackled using a proxy model whose downfall is that only can be applied to obtain time-lapse maps. The proxy model applied in this work cannot be used by itself, the calibration of such proxy must be achieved using a fully deterministic PEM model calibrated to the logs. Certainly the controlling parameter C_S carries the static log calibration but C_P's major influence comes from laboratory and core measurements. Actually a correct numerical assignment on the C_P term should depend on a range of factors that may enhance or diminish the stress sensitivity relative to the calibration offered by laboratory core plug measurements.

Based on a qualitative comparison between the deterministic PEMs and the proxy model, it is found that the two-parameter proxy model is satisfactorily close to the multi-parameters model results to replicate most of the 4D seismic response; such non-uniqueness makes the choice of the "best model" challenging.; indeed, any PEM may act as a "prime" for the proxy. However, from a quantitative point of view, considerations and attention must be taken into consideration. The proxy model works for an oil-water system, although big errors were shown in the time-lapse maps because of the uncertainty related to the stress sensitivity term in the PEM. Another uncertainty is the flow simulator model itself, if the reservoir model has a poorly history matched pressure and production and injection fluid data, then errors will be carried on through the entire 4D seismic study, indifferently of the rock physics model chosen and its associated calibrated input parameters. A progress on this issue is investigated in Chapter 6 by developing a practical tool for simultaneous analysis of 4D seismic data, PEM and the simulation model.

Keeping in mind that I am searching for a rock physics model that is accurate, robust and simple for time lapse interpretation, judging the models based on the concept of

Occam's razor seems appropriate: choosing the least complex PEM with the least number of parameters that fits the data well. Based on this philosophy the simplified linear proxy model with two parameters, may work well in practice to resolve this difficulty of building and choosing the right PEM, especially for an oil-water system (i.e. no gas). The presence of gas in any field, increases the uncertainty and predictability of the 4D maps using a simple two parameter mathematical equation.

Chapter 6

A practical tool for simultaneous analysis of 4D seismic data, PEM and simulation model

One of the main focuses of the geoscience industry is to constrain reservoir models to 3D and 4D seismic data using quantitative workflows that are suitable for model updating and history matching. This chapter focuses on the integration of 4D seismic data with reservoir engineering, with particular emphasis in the role of the petroelastic model and its associated uncertainties.

6.1 Introduction

The growth of history matching involving not only production data but also 4D seismic data has become a very active field (Gosselin et al. 2003; Roggero et al. 2007; Obidegwu 2015). This integration helps to reduce the uncertainty of the final reservoir model solutions and improve the reliability of production forecasts (Walker et al. 2006). Seismic history matching (SHM) closes the loop and minimizes the misfit between the observed data and that predicted by the reservoir model (figure 6.1). In SHM, the misfit can be computed at three different levels across the seismic and reservoir-engineering domains, namely, the simulation model domain, the acoustic impedance domain and the seismic amplitudes domain.

At the simulation model domain, a comparison is done between the pore pressure and saturation changes from the 4D observed data and to those predicted by the simulation model. This type of comparison is very complex as it requires two inversions that involve non-uniqueness issues (Landrø 2001). The comparison at the level of seismic impedances requires an inversion for impedances of the observed seismic amplitude data, and the synthetic impedances requires to be computed through a petroelastic model (PEM), using the saturation and pressure distribution from the fluid flow simulation model as inputs (Gosselin et al. 2001; Gosselin et al. 2003; Stephen et al. 2006; Roggero et al. 2007; Ayzenberg et al. 2013). Finally, if we are comparing at the level of seismic traces there is no need for seismic inversions of the observed seismic data, but to generate the synthetic seismic an additional procedure of seismic modelling is required after elastic properties calculation using a PEM coupled to a simulator model. The generated synthetic seismic is then compared to the observed seismic data (Dadashpour et al. 2007; Landa and Kumar 2011).

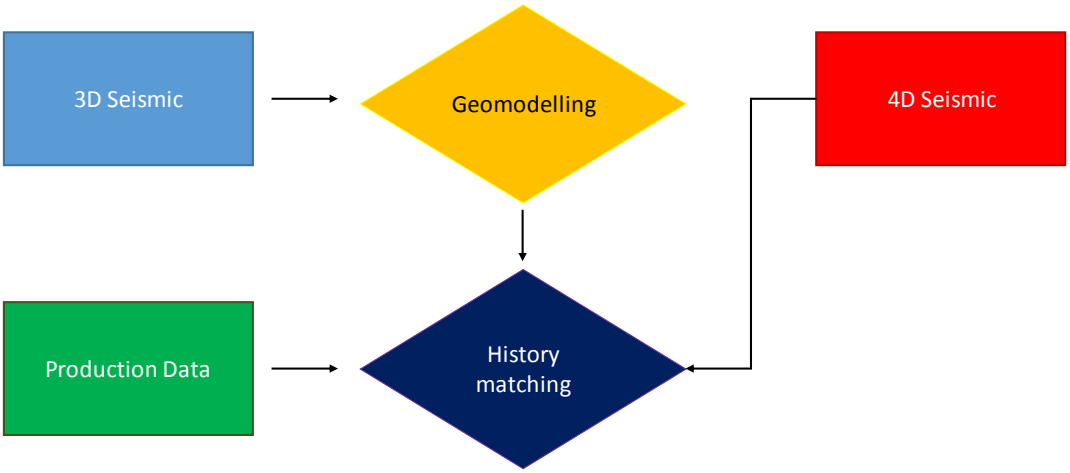

Figure 6.1 *Schematic workflow for Seismic History Matching (SHM) (Tian 2014)*

The SHM workflow relies on the petroelastic model (PEM) when computing the synthetic seismic from the simulated pressure and saturation changes. Many previous studies have pointed out the difficulty of selecting a PEM, the challenges in calibrating the model to the in situ response, and in particular the uncertainties involved. This non-uniqueness in the PEM, together with data and model uncertainties creates the need for time-consuming comparisons in the SHM workflow. The current chapter, further explores the two parameters proxy model presented in chapter 4 in relationship to PEM, with the objective of translate these two parameters into an interactive SHM domain. This study presents a simple and interactive way of visualizing uncertainties related to the simulation model, seismic data and PEM, whilst optimizing the SHM. The approach is illustrated by application initially to synthetic data and then to three different field applications from the UKCS, Norwegian Sea and offshore Brazil.

6.2 Methodology

Chapter 3, 4 and 5 showed that there are numerous PEM choices available for 4D seismic studies. However, the calibration of its vast amount of parameters can be challenging and with significant uncertainty across the different models. In this sense, each PEM (A, B, C, D, E and F) appears as a reasonable choice, no matter its complexity. For time-lapse seismic maps in particular, it has been suggested that the main response may be captured by a simplified empirically based proxy model with two parameters (equation 2.32), where C_S and C_P represent the PEM parameters, which provide the balance between the relative contributions of saturation (ΔS_w) and pore

pressure (ΔP) change to the overall time-lapse seismic signature (ΔA). Alvarez and MacBeth (2013) has shown that the fundamental parameter in 4D interpretation is actually the relative magnitude of C_S which is unit less and C_P with unit of MPa^{-1}, defined as the ratio C_P/C_S.

The approach presented in this thesis consists of a simple cross-plot of all changes in water saturation and pore pressure between the two time periods of interest in the reservoir history (usually pre-production baseline and a monitor). An example of this cross-plot is shown in Figure 6.2. The position of each point is defined by the simulation model predictions. Simulation models with a different selection of history matching parameters such as fault transmissibility multipliers, porosity multipliers, barrier locations, will have different simulation predictions and hence population of points on the cross-plot. Next, each point on the cross-plot is colour-coded according to the polarity of the 4D seismic signature (impedance or any other seismic mapping attribute). The input 4D seismic data are in the form of a difference between maps for the monitor and baseline data. For the applications we have chosen for an oil-water system (i.e. no gas), pressure increase softens the reservoir and gives the opposite polarity to water saturation increase or reservoir hardening via pressure depletion. Pressure depletion is normally linked to gas breakout, however for simplification the effect of gas in the proxy model is not considered in this thesis. Finally, the deterministic PEM can be overlain on top of this cross-plot by recognizing the result of Alvarez and MacBeth (2013), who proposed a proxy for the PEM.

The PEM is now defined as a straight line $\Delta A = 0$ passing through the origin of the cross-plot with the gradient C_P/C_S. From equation 2.32 it can be immediately observed that the line is a boundary that divides the cluster of points into two groups with different polarities. In practice the coefficients C_P and C_S are obtained by a calibration exercise previously shown in chapter 5, and if several equally-likely models are used then several lines need to be drawn on this plot. Thus the points are divided by a wide sector rather than single sharp boundary. Uncertainty in the seismic data is expressed by a change in the polarity of the points, which in turn changes the relationship with the PEM boundary. An incorrect simulation model changes the positions of the points which also changes the relationship to the PEM. In both cases the mismatch may be easily visualized for future corrective action.

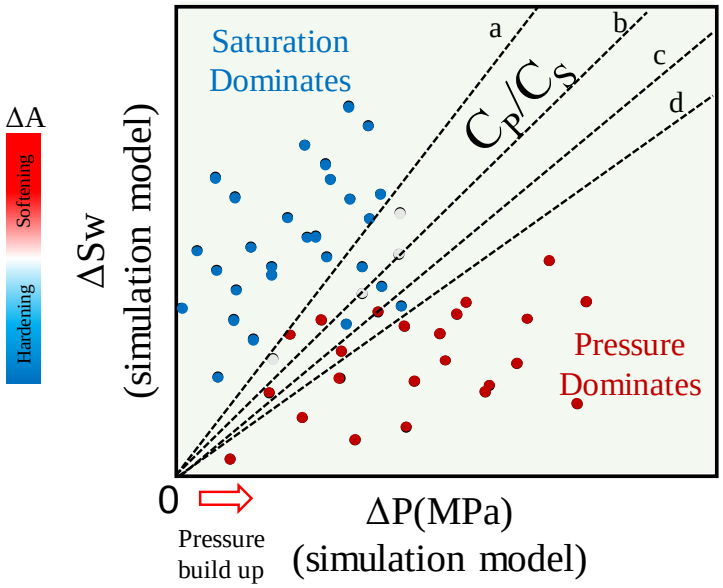

Figure 6.2 *Schematic plot of ΔSw versus ΔP from the simulation model, colour coded based on the polarity of the 4D response and with a selection of PEMs "a" to "d" overlain as straight lines. A red point corresponds to pressure increase, whilst blue is for water saturation increase.*

6.3 Synthetic data applications

The simple cross-plot tool is firstly applied to synthetic 4D seismic datasets generated from two clastic field models and a carbonate field model. The ΔP-ΔS_w points from each flow simulation model are colour coded using the 4D P-wave impedance change maps, calculated from all selected deterministic PEMs(A, B, C and D) coupled to a simulator model previously displayed in chapter 5 (figures 5.6, 5.12 and 5.17); in term of colour bar, red represents softening areas while blue the hardening ones. Figures 6.3, 6.6 and 6.7 shows the cross-plots for the synthetic 4D signature generated from the Schiehallion field, Norne field and Field X respectively.

In the case of the clastic fields, figures 6.3(a) and 6.6(a) gives the results for a synthetic 4D response calculated using a previously field-calibrated PEM A, and the boundary line relates to this model. Figures 6.3(b) and 6.6(b) gives the corresponding results for another model, PEM B. In the same manner, figures 6.3(c), 6.6(c) and 6.3(d), 6.6(d) give the corresponding results for the models PEM C and PEM D respectively. All the cross-plots for both clastic fields illustrate the division between the regions that are dominated by pressure and those dominated by saturation, indeed all chosen calibrated PEMs define a narrow fan with different C_P/C_S ratio for each rock physics model.

For the Schiehallion field, the cross-plots in figure 6.3 represent the entire sand reservoir of the T31 formation, which in the simulation model available for this study is defined between the layers 49 and 84. As for the time-lapse response and the dynamic changes from the simulation model, the monitor-baseline pair represented in the plot are 2004 monitor and 1996 preproduction baseline. All plots in figure 6.3 show a clear distinction and consistency between the two polarity groups, however there is a variation in the gradient C_P/C_S after approximately +2MPa pore pressure change due to the non-linearity of the stress sensitivity model used in the deterministic PEMs. For the gentle slope, C_P/C_S ratio varies between 0.014 and 0.05 MPa^{-1} and for the steepest slope the ratio is between 0.06 and 0.13 MPa^{-1}.

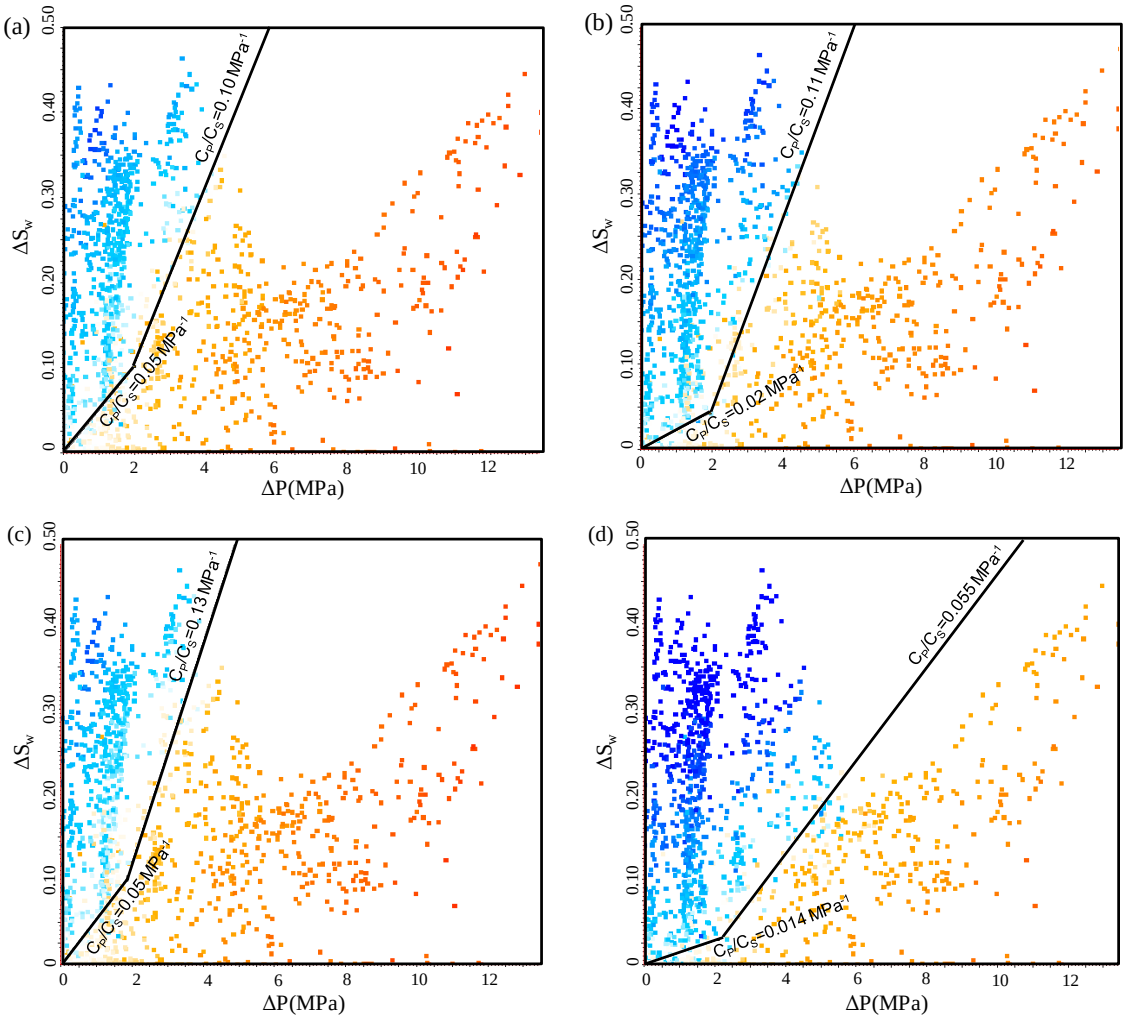

Figure 6.3 *Example of ΔSw versus ΔP cross-plot, colour coded using P-wave impedance changes (2004-monitor) maps calculated from deterministic PEMs based on mixing before fluid substitution previously displayed in chapter 5: (a) using the results from PEM A; (b) using the results from PEM B; (c) using the results from PEM C and (d) using the results from PEM D for the T31 sands of the Schiehallion Field.*

In the case of the Norne field, the cross-plots in figure 6.4 represent the reservoir of the Ile formation, which in the simulation model available for this study is defined between the layers 5 and 11. As for the time-lapse response and the dynamic changes from the simulation model, the time frame illustrated is between the 2004 monitor and the 2001 postproduction pseudo-baseline. The decision to use the 2001 pseudo-baseline time is subjected to the accessibility of the observed seismic data for the Norne field; indeed, exploring the practicality and usability of the cross-plot together with the observed seismic data will be shown later in this chapter. Consequently it is important to be consistent between the monitor-baseline pair used in the synthetic 4D calculation and the observed seismic data.

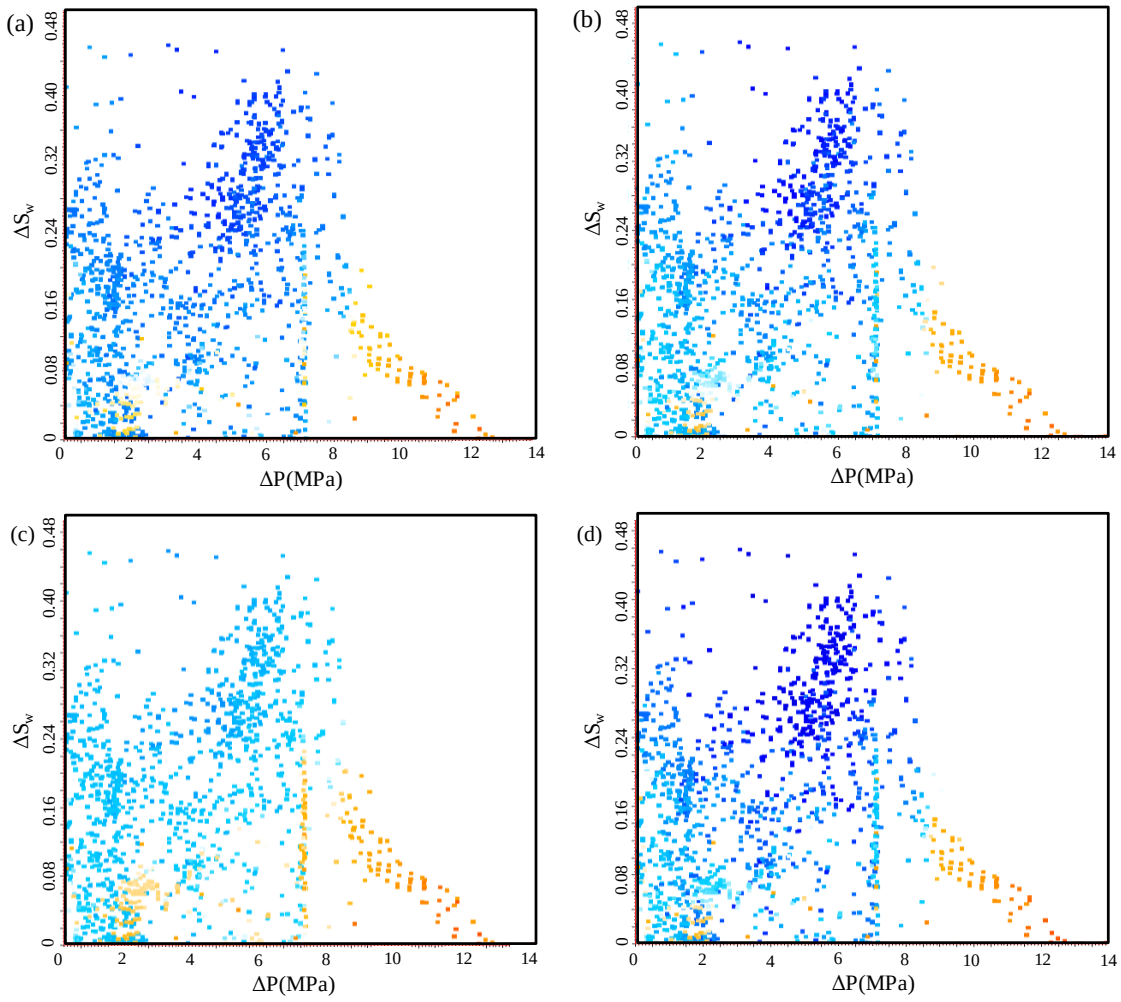

Figure 6.4 *Example of ΔSw versus ΔP cross-plot, colour coded using P-wave impedance changes (2004-2001) calculated from deterministic PEMs based on mixing before fluid substitution previously displayed in chapter 5: (a) using the results from PEM A; (b) using the results from PEM B; (c) using the results from PEM C and (d) using the results from PEM D for the Ile formation of the Norne Field.*

All plots in figure 6.4 do not exhibit a clear visible distinction between both polarity regions (softening and hardening), this is understood through the presence of gas in the reservoir by 2001 due to de-pressuring around the producing wells in Norne. At the 2001 pseudo-baseline time, the field has already been under production therefore pre-existing gas is found through the entire field and after years of injection, part of that gas will go back into solution. This is observed in figure 6.5 where the cross-plot of the changes of water saturation versus pore pressure is colour coded using the gas saturation change. Black dots in this case mean no presence of gas, red dots mean an increase in gas saturation with time, and the green/blue dots represents a decrease in gas saturation with time, hence gas going back into solution followed by a pressure build up.

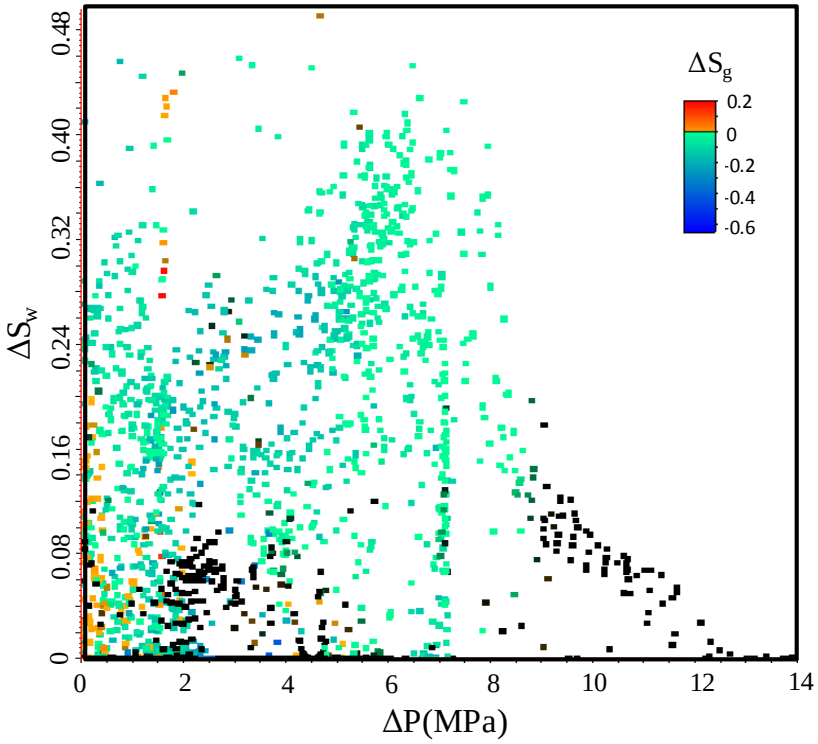

Figure 6.5 *ΔSw versus ΔP cross-plot, colour coded using ΔSg, all the dynamic change properties displayed in this cross-plot is between 2004-2001 for the Norne Field.*

Although for the applications we have chosen for an oil-water system (i.e. no gas), pressure increase softens the reservoir and gives the opposite polarity to water saturation increase or reservoir hardening via pressure depletion; thus a second set of cross-plots for Norne field where only the areas without gas saturation are displayed in figure 6.6. Visually the cross-plots in figure 6.6 show a division between the two 4D polarities,

even though the amount of data plotted is significantly reduced compared to the plots from figure 6.4. The new scenario, where gas is not shown, since the proxy model does not accommodate the time-lapse response associated to the presence of gas, shows a ratio C_P/C_S that varies between 0.016 and 0.039 MPa^{-1} for the clastic deterministic PEMs (A, B, C and D), which is consistent with the average values obtained from the controlling parameters for the proxy model previously shown in chapter 5 in table 5.1.

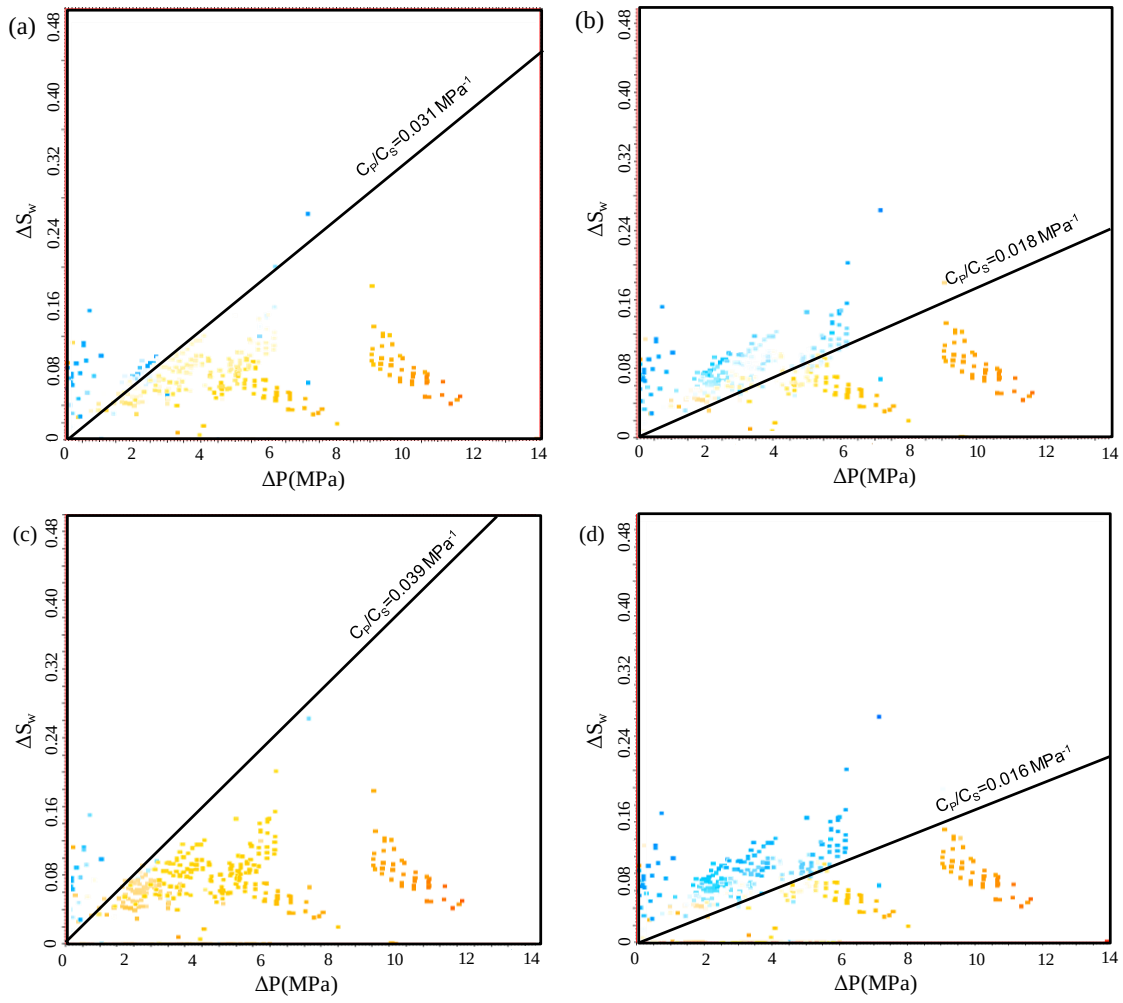

Figure 6.6 *Example of ΔSw versus ΔP cross-plot, colour coded using P-wave impedance change calculated from deterministic PEMs based on mixing before fluid substitution previously displayed in chapter 5: (a) using the results from PEM A; (b) using the results from PEM B; (c) using the results from PEM C and (d) using the results from PEM D for the Ile formation of the Norne Field.*

Moving to the carbonate field example, figure 6.7(a) gives the results for synthetic 4D response calculated using a previously field-calibrated PEM E, and the boundary line relates to this model. Figure 6.7(b) gives the corresponding results for another model, PEM F_1 where the inclusion pore shapes were modelled as spheres, and figure 6.7(c) provides the resultant outcome for the PEM F_2 where the inclusion pore shapes were modelled as needles. All the cross-plots for the carbonate Field X show the division between the regions that are dominated by pressure and those dominated by saturation. Contrary to the clastic fields results, the slope when $\Delta A=0$ which represents the ratio C_P/C_S and separates both domains does not pass by the origin, for all the PEMs approximately in the first +8MPa pore pressure change only hardening is observed. This observation can be associated with the gas going back into solution that occurs between 2011 and 2002 after years of production and injection. Indeed after gas going back into solution due to an increase in pressure support, the time-lapse signature is observed to be softening only if the pressure change is sufficiently big or hardening in the negative gas saturation change regions when the pore pressure change is not large enough, the latter case seems to be the situation illustrated in the plots from figure 6.7

For the Field X, the cross-plots in figure 6.7 represent the first 15ms of the carbonate reservoir, which in the simulation model available for this study is defined between the layers 1 and 13. As for the time-lapse response and the dynamic changes from the simulation model plotted, the time frame represented in the plots is between the 2011 monitor and the 2002 postproduction pseudo-baseline. In the three cross-plots of figure 6.7 there is a variation in the gradient C_P/C_S after approximately +13MPa pore pressure change due to the non-linearity of the stress sensitivity model used in the deterministic PEMs. Between +8 and +13 MPa changes in pore pressure the cross-plots shows a gradual C_P/C_S slope with an average value of 0.013 MPa^{-1} for all rock physics models, as for the second and steeper slope the C_P/C_S ratio is 0.030 MPa^{-1} on average for all the deterministic PEMs results.

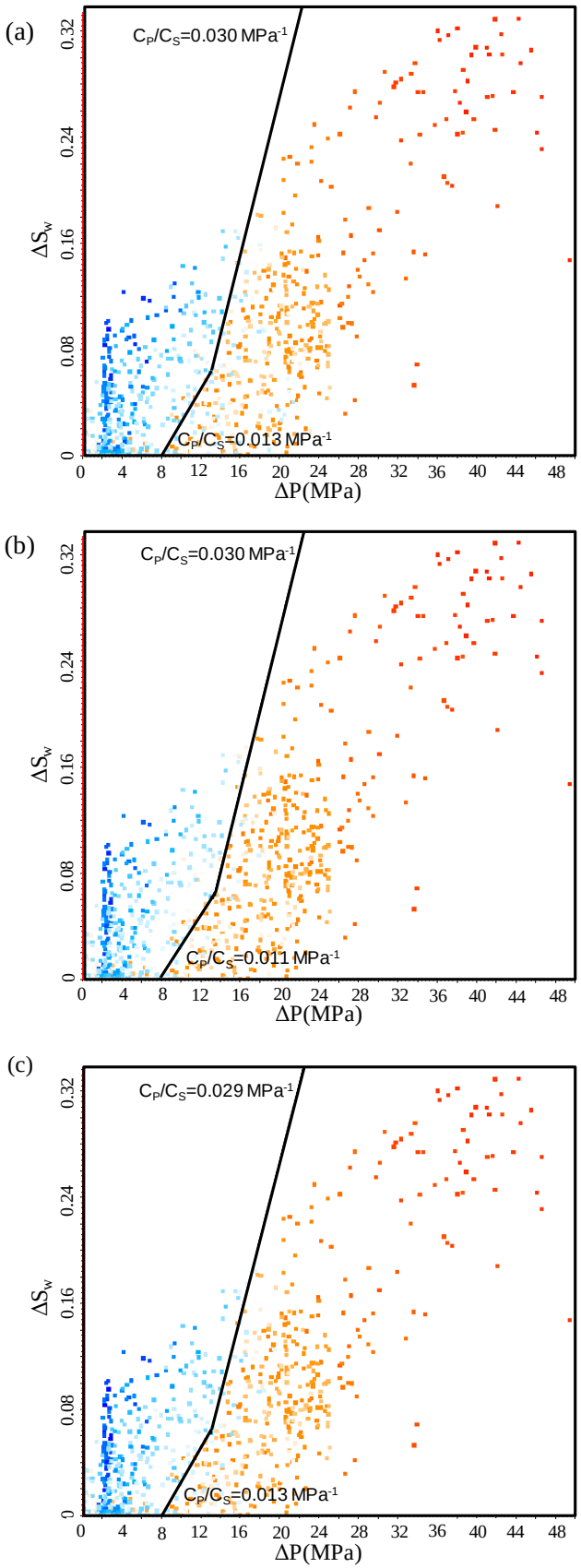

Figure 6.7 *Example of ΔSw versus ΔP cross-plot, colour coded using P-wave impedance changes (2011-2002) calculated from different deterministic PEMs based on mixing before fluid substitution previously displayed in chapter 5: (a) using the results from PEM E; (b) using the results from PEM F_1 and (c) using the results from PEM F_2 for the Field X.*

Similar to the case of the Norne field, the analysis is tied to the data; the only observed seismic data available for Field X are two monitors in 2002 and 2011, with the former acting as pseudo-baseline, which was the time-lapse response also modelled with synthetics. At the 2002 pseudo-baseline time, the field has already been under production for 23 years therefore pre-existing gas is found through the entire field and after some years of injections, the gas will go back into solution. This is observed in figure 6.8 where the cross-plot of the changes of water saturation versus pore pressure is colour coded using the gas saturation change between 2011 and 2002. The majority of the points on the plot are green/blue dots which represent a decrease in gas saturation with time - a negative change, hence gas going back into solution followed by a pressure build up. After gas goes back into solution due to an increase in pressure support, we can observe a hardening response in the negative gas saturation changes areas when the pore pressure change is not large enough, which agrees with the dynamic property maps (figure 5.18) of Field X in chapter 5. When comparing the gas saturation change scales from figure 6.5 and 6.8, they indicate that more gas goes back into solution after production in Norne than for the carbonate field. However the 4D gas effect in Field X is not as pronounced as in Norne; hence, there is no need to remove the negative gas saturation change points from the cross-plots in figure 6.7.

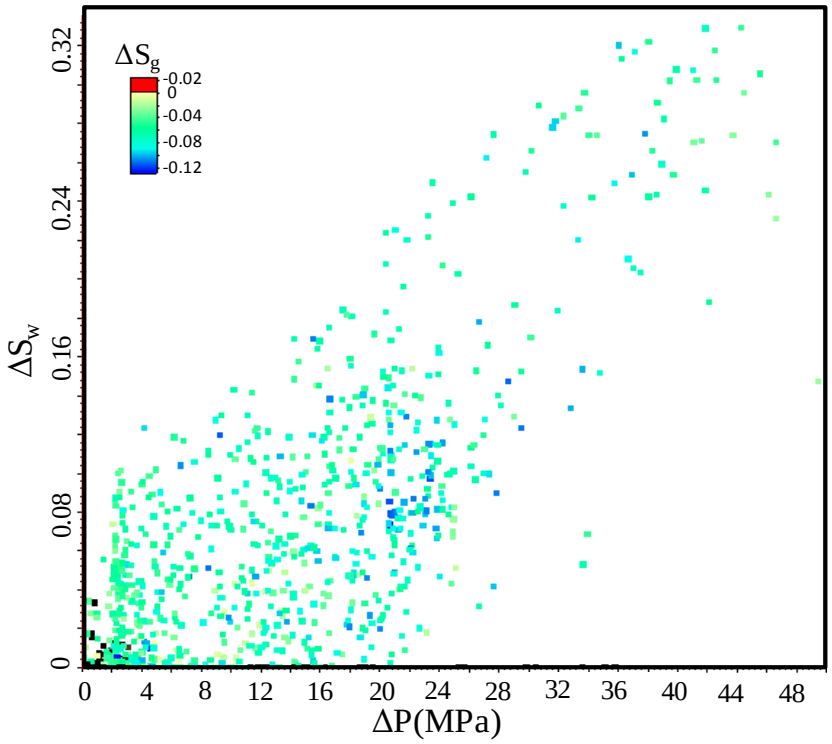

Figure 6.8 *ΔSw versus ΔP cross-plot, colour coded using ΔSw, all the dynamic change properties displayed in this cross-plot is between 2011-2002 for the carbonate Field X.*

6.4 Observed Data Examples

The cross-plot is applied to three fields in the UKCS, Norwegian Sea and offshore Brazil with distinctly different geological settings. First of all, the ratio C_P/C_S for all three fields is calculated using different log calibrated deterministic PEMs (A, B, C and D for the clastic reservoirs and E, F_1 and F_2 for the carbonate reservoir) at baseline and monitor times. The ΔP-ΔS_w cross-plot points are then colour-coded using the mapped 4D observed seismic amplitudes for each field. On top of the plots, the different boundaries C_P/C_S obtained from the deterministic PEMs (figures 6.3, 6.6 and 6.7 for each field) are displayed since they give a range of variability, and set the limits that represent softening and hardening of the reservoir.

For the Schiehallion field, the available data is the preproduction baseline seismic data and three monitor surveys (2004, 2006 and 2008). The observed Time Lapse seismic data maps observed in figure 6.9 are calculated using sum of negative amplitude (SNA) where an increase in the observed amplitudes indicates an influx of water while a decrease in the amplitudes indicates pore pressure up in the reservoir. The attribute sums all negative amplitudes between the top T31a and base T31b. This attribute is used since previous work has shown SNA to be sensitive to reservoir conditions when the sand are softer than the shales, this means giving a high to low seismic impedance contrast and a negative relative impedance (Jack et al., 2010).

As for the Norne Field, the first seismic survey was acquired in 1992, however the surveys available for this study were shot in 2001, 2003, 2004 and 2006. To evaluate the time-lapse response of the observed seismic data, 4D maps based on the difference of root mean square (RMS) between monitor and baseline ($RMS_{monitor} - RMS_{baseline}$) (Stammeijer and Hatchell, 2014) are calculated (figure 6.10). From the 4D maps in figure 6.10a to c, an increase in the observed amplitudes indicate a softening response related to a decrease in impedance (red areas) due to pore pressure up or gas presence in the reservoir, while a decrease in the amplitudes (blue areas) indicates a hardening response related to an increase in impedance where the water saturation change response dominates the seismic signature

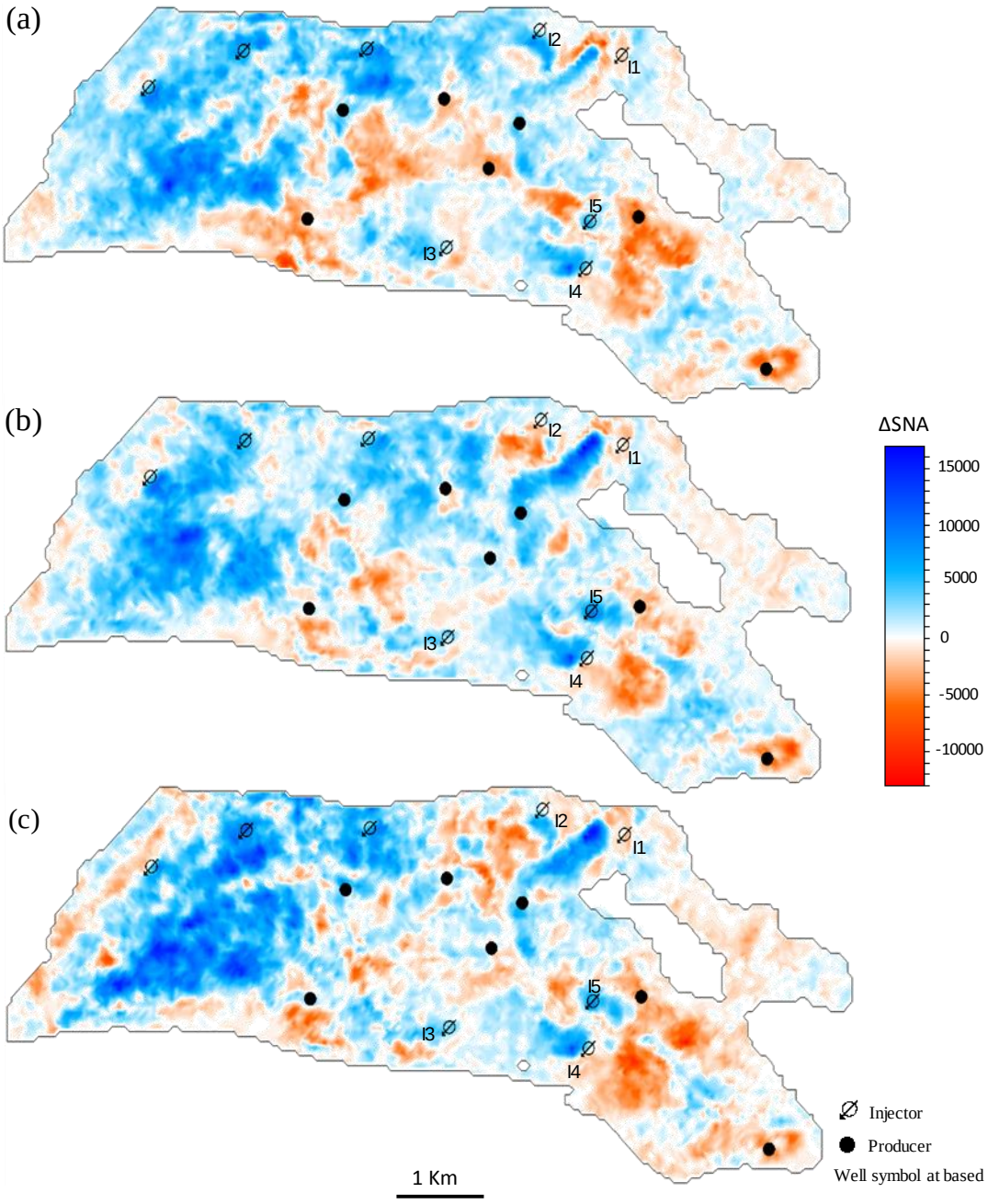

Figure 6.9 *Observed Time-Lapse maps using Sum of Negative Amplitude attribute over the entire T31 formation of the Schiehallion field for the following periods: (a) 2004-baseline; (b) 2006-baseline and (c) 2008-baseline. Red areas represent softening while blue hardening. An example of a vertical section of the seismic data with the horizons (T31a top and T31b base) used for the attribute mapping is shown in figure 5.3 (chapter 5)*

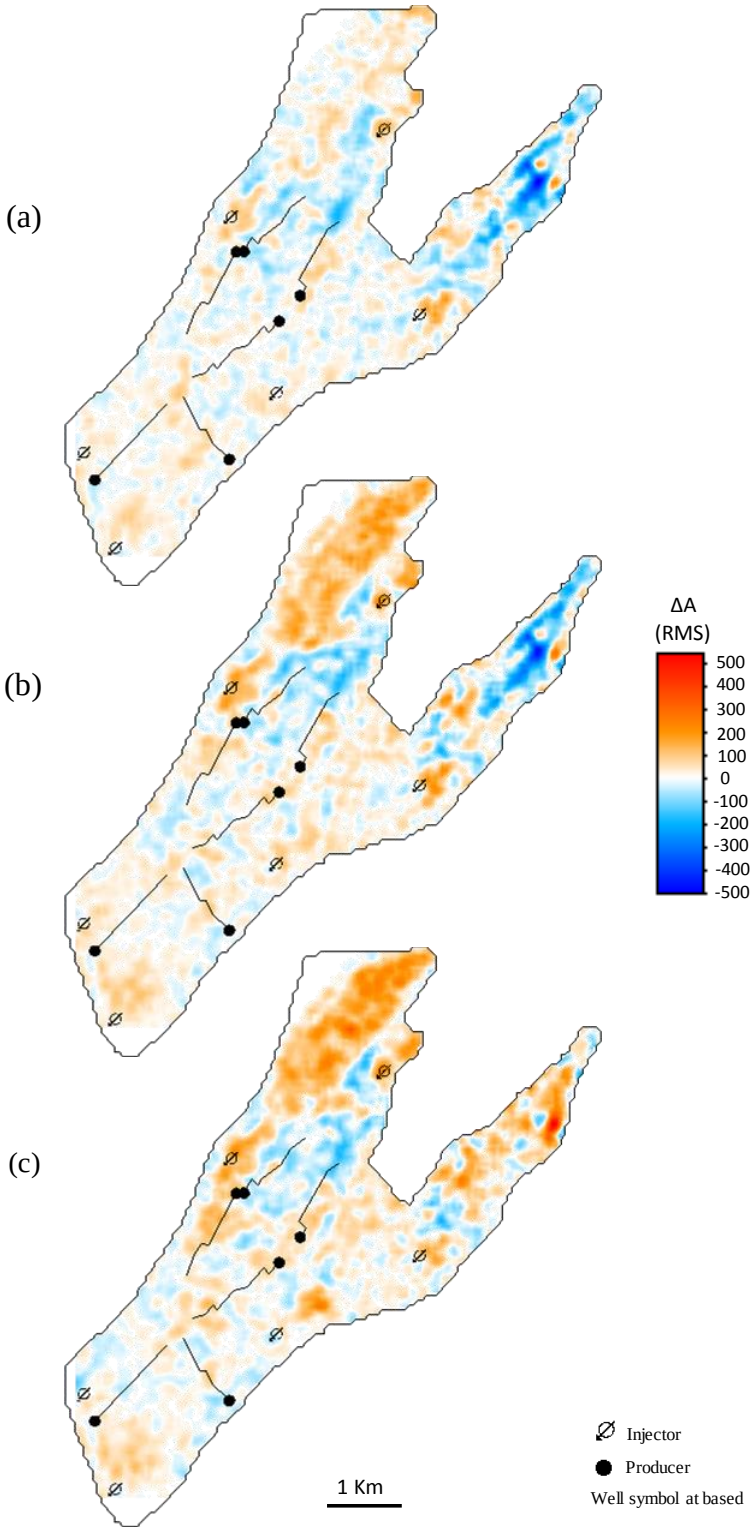

Figure 6.10 *Observed Time-Lapse maps using RMS attribute over the entire Ile formation of the Norne field for the following periods: (a) 2003-2001; (b) 2004-2001 and (c) 2006-2001. Red areas represent softening while blue hardening. An example of a vertical section of the seismic data with the horizons (top and base of the Ile formation) used for the attribute mapping is shown in figure 5.11 (chapter 5)*

Lastly, the Field X has a thickness of approximately 130ms and the seismic signature consist of several cycles of peaks and troughs. Indeed the analysis of the 4D signal for this kind of reservoirs is challenging, since the right optimal window must be chosen to extract the seismic attribute. To take into account the ambiguity related to the extraction of the 4D signal, RMS amplitude at the top of the reservoir for two windows, 15ms and 45ms below the top horizon, is extracted for the 3D seismic cubes (2002 pseudo-baseline and 2011 monitor). To evaluate the time-lapse response of the observed seismic data, 4D map based on the difference of RMS between baseline and monitor ($RMS_{baseline} - RMS_{monitor}$) is calculated (figure 6.11a and b). The decision to obtain the 4D map for baseline minus monitor survey is to preserve the polarity of the 4D response in the maps as in the seismic volume since we are in presence of a high to low seismic impedance contrast and a negative relative impedance.

From the time-lapse maps in figure 6.11, an increase in the observed amplitudes indicates a hardening response related to an increase in impedance (blue areas) while a decrease in the amplitudes indicate softening response related to a decrease in impedance (red areas) where the seismic signature is dominated by pressure up or the presence of gas. From the water injection rate data for the wells, it is understood that in the wells I_1 and I_3 the injection rate increases between 2002 and 2011, hence we are expecting to observe hardening around those injectors. On the other hand, for well I_2 there is a drop of around 25% in water injection by 2011 and the effect of pressure overwrite the saturation response (softening). The time-lapse map from figure 6.11a with a small window of 15ms shows a better agreement to the 4D signature anticipated around the wells than when using a bigger window (figure 6.11b)

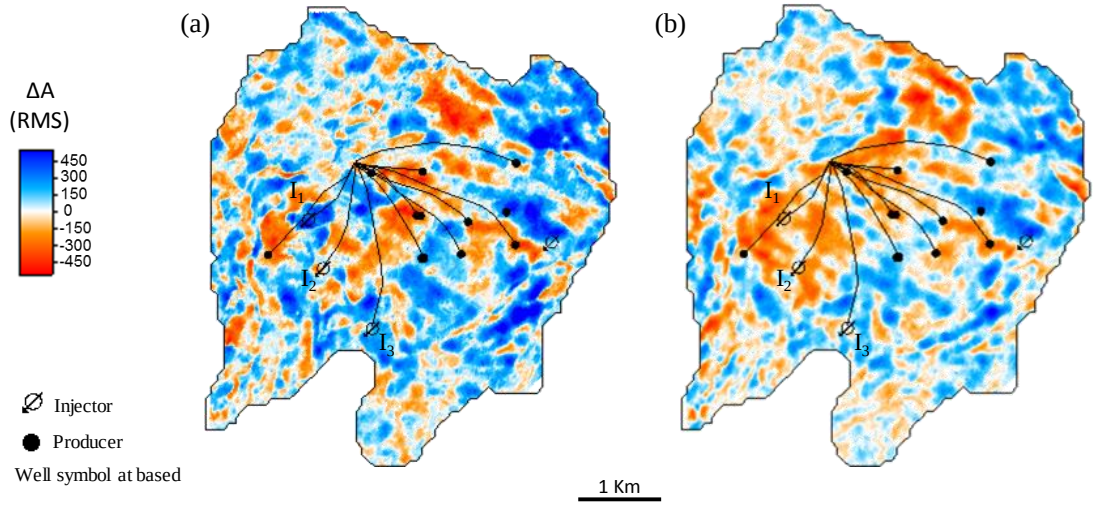

Figure 6.11 *Observed Time-Lapse maps using RMS attribute for the carbonate Field X between the 2002-2011 periods. (a) Over a 15ms window below the top of the reservoir and (b) 45ms window below the top of the reservoir. Red areas represent softening while blue hardening. An example of a vertical section of the seismic data with the horizon (top of the reservoir) used for the attribute mapping is shown in figure 5.16 (chapter 5)*

The cross-plot based on the observed 4D seismic response for the Schiehallion field (Figure 6.12) does not display a clear distinction between pressure and saturation domains in comparison with the calculated synthetic impedance changes (figure 6.3), the latter does not include wave interference concerns which could mask the real 4D seismic signature. Indeed, the link between the impedance and the seismic amplitude domains is missing since the full computation of the sim2seis workflow to obtain synthetic seismic data was not performed in this work. Even when the exercise is applied to a water-oil system by excluding all the gas cells from simulation model in the cross-plots, the seismic observations show the occurrences of gas dissolution and gas production during the life of the reservoir (Obidegwu 2015) which may not be predicted by the current simulation model, which can explain the points with softening on the left hand side of the PEM separation lines.

From figure 6.12 we can observe incorrect polarities (or wrong position) at the right top corner, meaning that decisions to update the model must be taken if the seismic data are accepted as accurate. By plotting the entire dynamic changes of the simulation model, we can review the simulation model in terms of: how accurate the model represents the reality of the reservoir in the subsurface. In this way, we can assess how truthful and physical plausible the distribution of pressure and the fluids in the reservoir between

wells is, where the absence of measured data represents a major uncertainty (Palke et al. 2012).

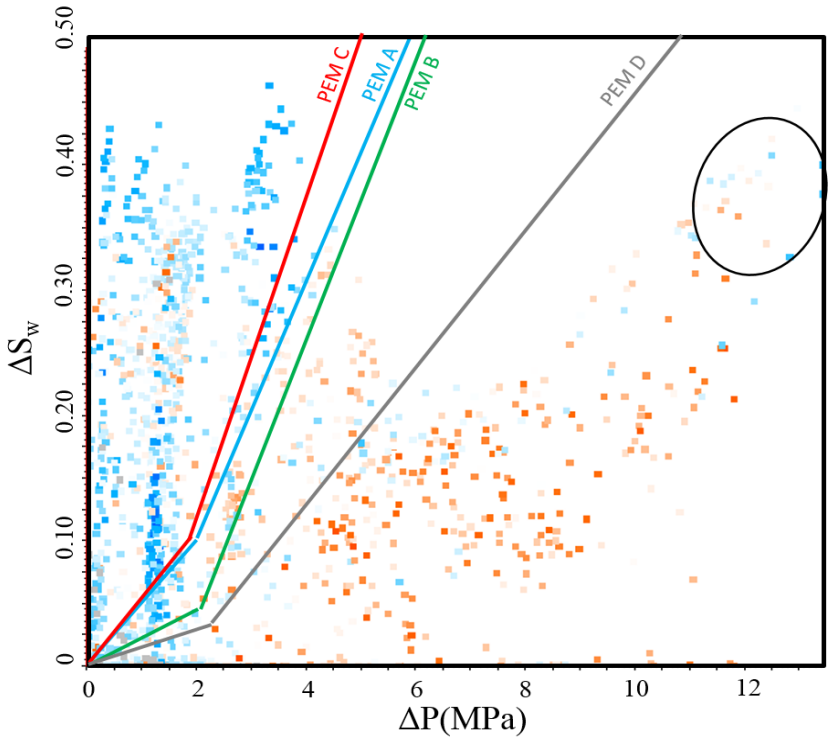

Figure 6.12 *ΔSw versus ΔP cross-plot using the original simulation model for the Schiehallion field and colour-coded with the polarities of observed 4D seismic response. The PEM separation lines were obtained at the impedance domain, which may represent a point of uncertainty in our interpretation.*

The 4D seismic amplitudes are interpreted as a weighted combination of pore pressure and water saturation changes, therefore if the methodology is applied only around the injectors where the saturation and pressure counteract, it is possible to back out the C_P/C_S ratio in situ (Alvarez 2014) since the well location can be seen as a trustworthy position. Given the polarity of the changes in amplitude (ΔA), and knowing what the changes in water saturation and pressure for sets of monitor-baseline, then it is possible to obtain inequalities of the form $C_S\Delta S_w > C_P\Delta P$ or $C_S\Delta S_w < C_P\Delta P$ based on whether saturation or pore pressure changes dominate the seismic response. Around water injection wells an increase on pore pressure, which translates into softening of the reservoir, has an opposing physical effect on the reservoir than an increase in water saturation, hence reservoir hardening. In this scenario $C_S\Delta S_w$ compete against $C_P\Delta P$ making the determination of the data polarity and the general dominance of the 4D seismic signal clear. In the case where no pore pressure increase is observed

(depletion), both pressure and saturation affect the rock in the same way, by increasing the impedances; this results in changes with the same polarity and renders the discrimination of which signal dominates the seismic difficult.

For the Schiehallion field we use a total of five injector wells (I_1, I_2, I_3, I_4 and I_5) which are active over the chosen 1998-2008 period. Simulation results between baseline (1998) and 2004 show a pore pressure change of +3 MPa around I_1, +0.3 MPa at well I_2, +2 MPa at well I_3, +3.5 MPa around well I_4 and +13 MPa around I_5. As for the saturation changes during this period we find +0.25, +0.20, +0.35, +0.35 and +0.40 respectively. During the 2004-baseline period, Figure 6.9a shows an amplitude decrease at I_1 which yields the relation $0.25C_S < 3C_P$ where the pressure effect is dominating the seismic signature. At well I_2 a decrease in the amplitude signal is consistent with a dominating saturation effect, which gives the relation $0.20C_S > 0.3C_P$. The same approach is followed for the remaining wells, thus we obtain more inequalities for C_S and C_P, $0.35C_S > 2C_P$, $0.35C_S > 3.5C_P$ and $0.4C_S > 13C_P$ at the wells I_3, I_4 and I_5 respectively.

Further inequalities are obtained from the remaining set of monitor-baseline data. The 4D amplitude map (figure 6.9b) between 2006 and the baseline reveals a decrease in amplitude around the wells I_1 and I_2 hence a dominance of the pressure response. It also shows an increase in amplitude around the wells I_3, I_4 and I_5 associated with saturation dominating over pore pressure. These lead to the inequalities $0.26C_S < 7.2C_P$, $0.24C_S < 5.2C_P$, $0.23C_S > 0.58C_P$, $0.30C_S > 1.18C_P$ and $0.40C_S > 3.2C_P$ around the wells I_1, I_2, I_3, I_4 and I_5 respectively. For the final monitor-baseline set (2008-baseline) the pore pressure change is negative at wells I_1, I_2 and I_3, and as a consequence no useful information can be extracted for this study. The only injectors that lead to an equality are wells I_4 and I_5 where the time-lapse map in figure 6.9c shows that the water saturation change dominates, yielding $0.31C_S > 0.7C_P$ and $0.42C_S > 2.35C_P$ respectively.

All of the equalities or inequalities are then brought together on the cross-plot of saturation changes versus pressure changes, where each dot represents a specific well at a specific monitor-baseline pair. Figure 6.13 shows the cross-plot obtained at the water injector wells location where it is possible to fit a straight line between both polarities

with slope C_P/C_S of approximately 0.09 MPa^{-1}. Because of the simplicity of this method to obtain C_P/C_S from the observed data, it represents a metric to compare and back out the different multi-parameters PEM paradigms from all the data sets available for this study. On top of the plot in figure 6.13, we display four different boundaries C_P/C_S obtained from the deterministic PEMs (A, B, C and D) since they give a range of variability, and set the limits representing softening and hardening of the reservoir. As a reminder the PEM C_P/C_S lines were obtained by using the entire distribution of the dynamic properties in the simulation model and hence may aid understanding the lateral variation of the 4D response.

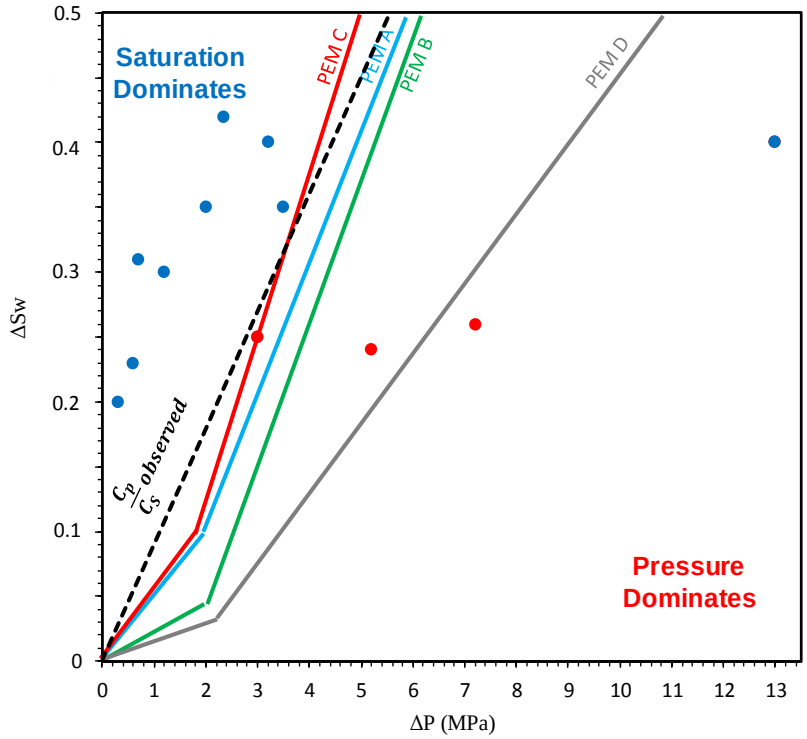

Figure 6.13 *ΔSw versus ΔP cross-plot at the water injector wells position for the Schiehallion field and colour-coded with the polarities of observed 4D seismic response. Blue dots the 4D signature is dominated by saturation while red dots are dominated by pore pressure.*

The plot for the Schiehallion field (Figure 6.12) shows incorrect polarities (or wrong position) at the right top corner, which is corroborated at the injector well position (figure 6.13) meaning that decisions to update the model must be taken if the seismic data are accepted to be correct. The connectivity across the reservoir is the primary factor in understanding the well performances and the reservoir sweep in the Schiehallion field, therefore the simulation model available for this study allows the

adjustment of the connectivity and shows the lithological heterogeneity through a detailed geobody characterization. Updating of the simulation model is performed by altering the transmissibility multipliers between geobodies in the areas of the model relating to the incorrect clusters of data, using the keyword MULTREGT in the Eclipse data file. Figure 6.14 shows an example of the transmissibility multipliers for the geobodies surrounding the area in question. These effectively reduce the pressure change for that specific area as can be seen in the reservoir pressure profile for a couple of wells in the affected area (figure 6.15a and c), as well as in the new dynamic maps from the updated model (figure 6.16). This updating is qualitative but can be guided carefully with the defined PEM and seismic uncertainties in the cross-plot. Different scenarios for the simulation model are run, and here we show the most optimal model which provides optimal separation of softening/hardening 4D signatures, in agreement with the C_P/C_S regions determined from the seismic data (figure 6.17).

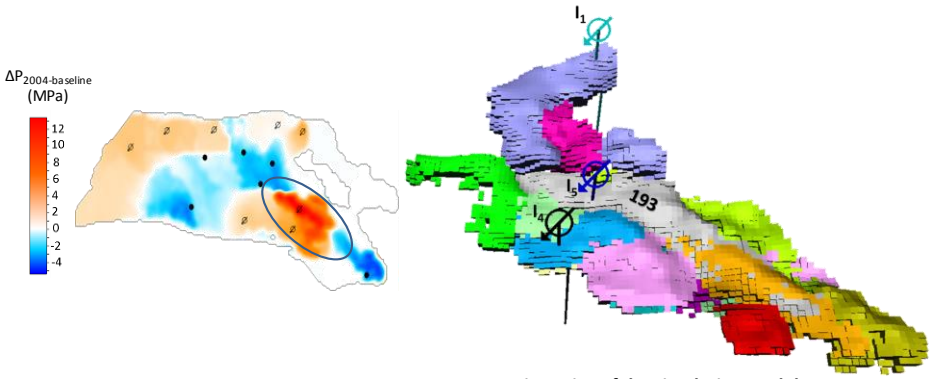

Original Simulation Model
Transmissibility multipliers between geobody pairs
MULTREGT
193 275 0.0040818 /
193 276 0.018105033 /
193 201 0.011242467 /
37 193 0.006158467 /
44 193 0.59858 /
193 361 0 /
40 193 0 /
174 193 0 /
187 193 0 /
193 198 0 /
193 206 0 /
193 219 0 /
193 224 0 /
193 226 0 /
193 231 0 /
193 253 0 /
193 272 0 /
193 279 0 /
193 324 0 /
193 358 0 /
193 282 0 /
157 193 0 /
33 193 0 /

New iteration of the Simulation model
Transmissibility multipliers between geobody pairs
MULTREGT
193 275 0.0040818 /
193 276 0.018105033 /
193 201 0.55 /
37 193 0.55 /
44 193 0.8 /
193 361 0.004 /
40 193 0.004 /
174 193 0.004 /
187 193 0.004 /
193 198 0.004 /
193 206 0.004 /
193 219 0.004 /
193 224 0.004 /
193 226 0.004 /
193 231 0.004 /
193 253 0.004 /
193 272 0.004 /
193 279 0.004 /
193 324 0.004 /
193 358 0.004 /
193 282 0.004 /
157 193 0.004 /
33 193 0.004 /

Figure 6.14 *Keyword MULTREGT in Eclipse is used to set the transmissibility multiplier between the geobody pairs around the area of conflict.*

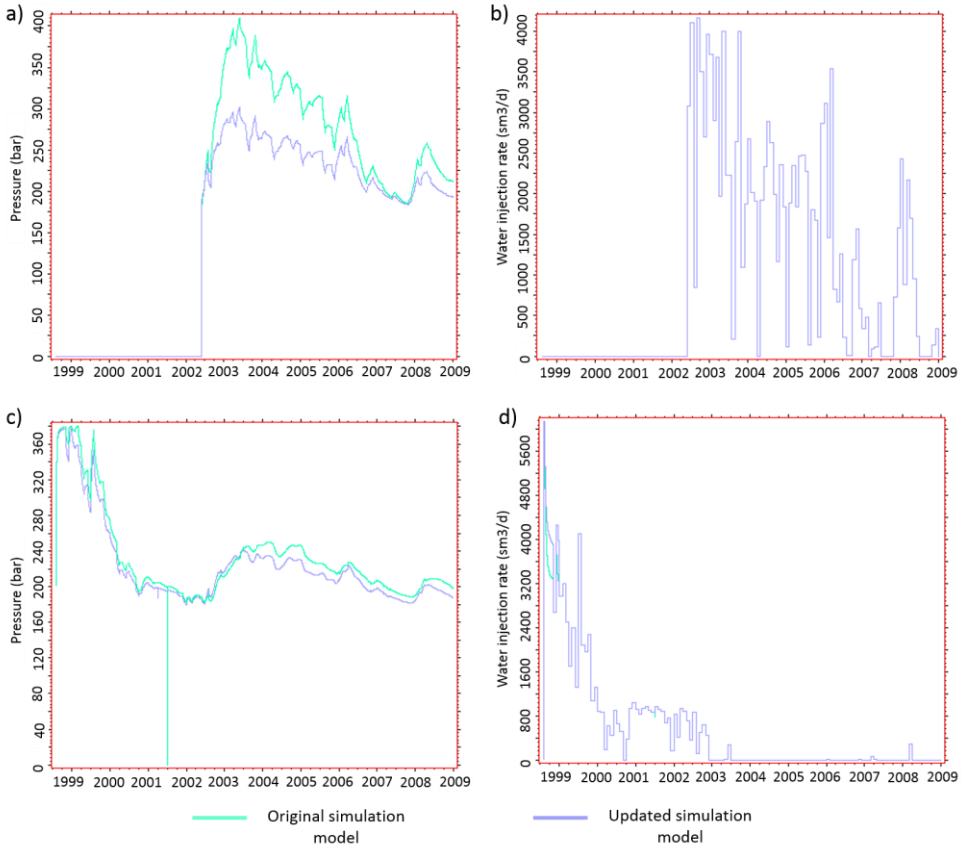

Figure 6.15 *(a) and (b) reservoir pressure and water injection rate respectively, prior and after model update for well I_5. (c) and (d) as in (a) and (b) but for a different injector well (I_4) around the affected area for the Schiehallion field.*

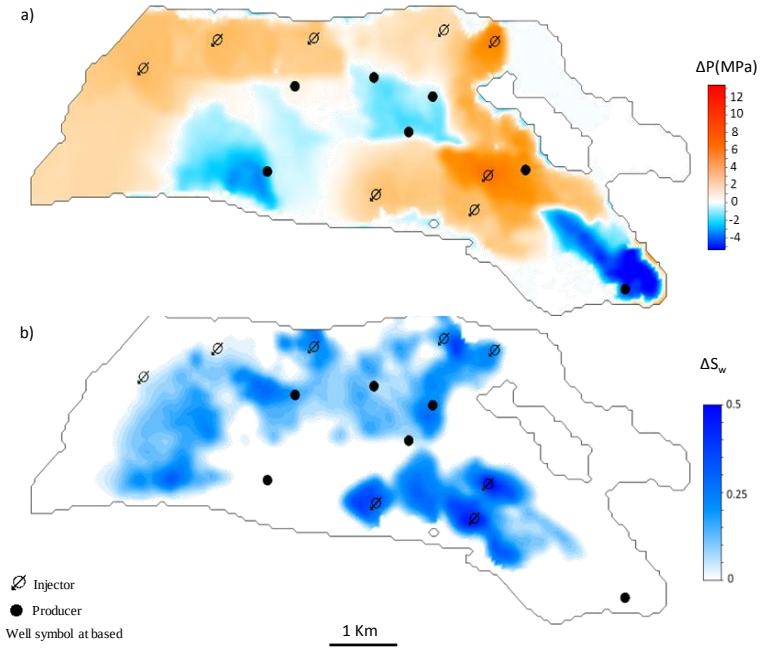

Figure 6.16 *Change in dynamic property maps between the 2004 monitor and 1996 baseline obtained from the more optimal simulation model after updates are performed. (a) Pore pressure change map. (b) Water saturation change map for the T31 formation of the Schiehallion Field.*

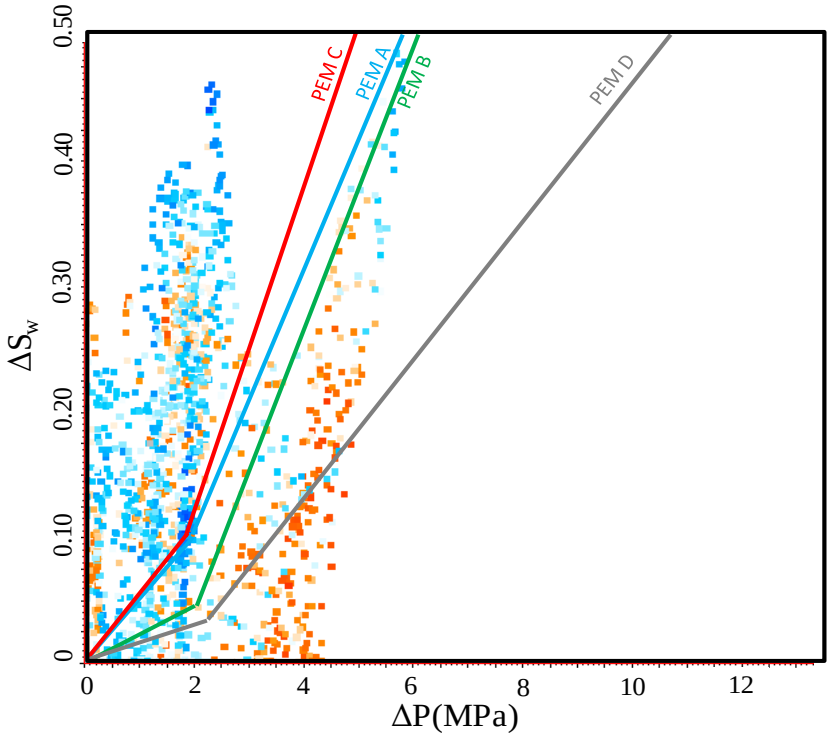

Figure 6.17 *ΔSw versus ΔP cross-plot using a more optimal simulation model for the Schiehallion field after updates are performed and colour-coded with the polarities of observed 4D seismic response (Blue = hardening; Red = softening). The PEM separation lines were obtained at the impedance domain, which may represent a point of uncertainty in our interpretation.*

The same approach is applied to the Norne field, the ΔS_w versus ΔP plot (Figure 6.18) shows clusters of points where there is a disagreement between the pressure and saturation regions. In the Norne field the seismic signature consist of several cycles of peaks and troughs. In this thesis the time-lapse response was extracted from the Ile formation, but the interpretation of the 4D signal for this kind of reservoirs is still challenging. Contrary to the Schiehallion Field, from the nine injector wells available for the Norne field, none of them can be used to demonstrate the separation of pressure and saturation, because four of them are water alternating gas injector wells, and from the remaining five water injectors only two of them perforate the Ile formation. Both wells are located in the water leg, hence no competition between pressure and saturation occur in such areas that can yield useful results.

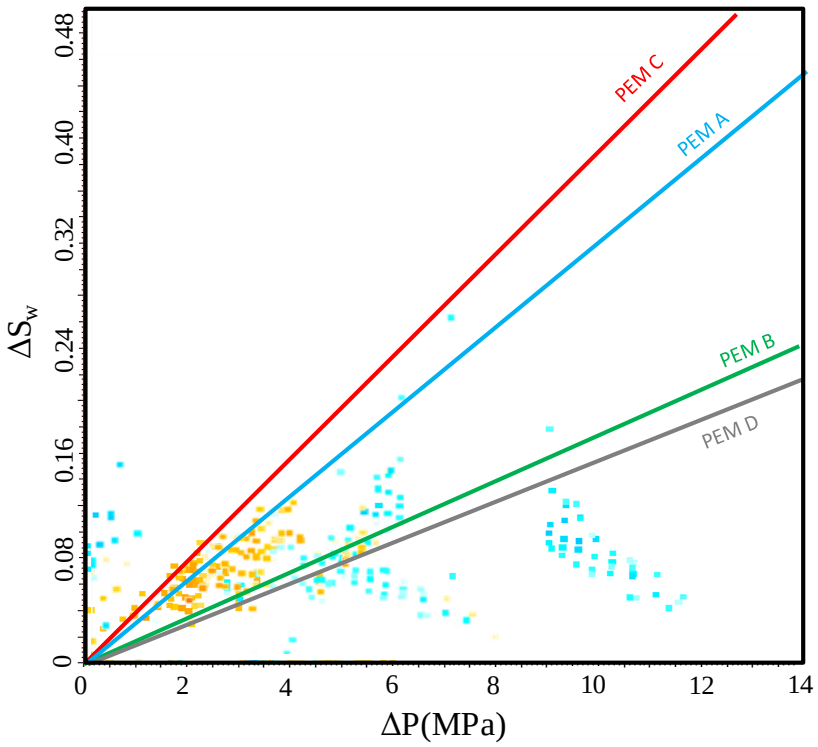

Figure 6.18 *ΔSw versus ΔP cross-plot using the original simulation model for the Norne field and colour-coded with the polarities of observed 4D seismic response.(Blue =hardening and Red = softening). The PEM separation lines were obtained at the impedance domain, which may represent a point of uncertainty in our interpretation.*

A potential reason for the observed scatter in the domains of pressure versus saturation separation may be the seismic data itself. Firstly, Norne suffers from higher NRMS compared to the other clastic dataset analysed in this work, this may result in more scattered 4D signatures in terms of hardening/softening and more uncertainty in the polarity of small 4D signals. Santos (2017) also distinguishes the remaining 4D noise as an uncertainty source in the seismic available for Norne. They noted that the reservoir signal contains overlapping between signal due to production and noise (figure 6.19), which results in ambiguous 4D interpretation in the reservoir. Aside from noise considerations, interference from side-lobes and also interference from thin bed sequences (tuning) renders 4D amplitude comparisons of observed data challenging. In fact, Barrett-Crosdill (2015) showed the effect of tuning from single and multiple layers is quite complex depending on the relative polarities of impedances, contrast, bed thickness and seismic data frequency.

Finally, as discussed by Omofoma and MacBeth (2015), there are seismic acquisition considerations that may result in a time-lapse aspect in the binning of traces that are considered as concurrent. In effect, the seismic data that is interpreted as baseline, or from a single monitor, may not be acquired at the same time. As a result, the observed data may contain different snapshots of the pressure field, which is varying during acquisition, which means that the amplitudes from the observed seismic data may not correspond to the pressure field conditions simulated from the flow simulation model.

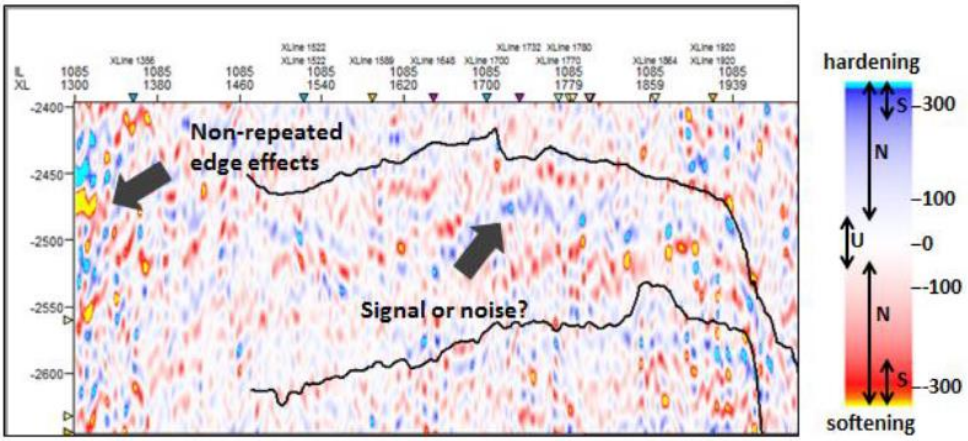

Figure 6.19 *Example of 4D section between 2004-2001 of Norne field where the magnitude of the signal may be the same as the noise. Arrows in the colour bas show the amplitude difference intervals for unchanged amplitude (U), noise (N) and signal (S) (Santos 2017).*

Another reason for uncertainty in our simple cross-plot is the simulation model itself, since the position of the data plotted is related to the distribution of pressure and fluids in the model. Therefore, the way in which the model is history matched may have a significant impact on the forecast predictions of the flow simulator model and consequently the position of the data on the C_P/C_S plots. Assuming that the observed 4D response might offer a reasonable degree of confidence for a model update, then it should be possible to perform multiple runs of the simulation model by altering fault transmissibility multipliers (using the keyword MULTFLT in the Eclipse data file). Figure 6.20 shows an example of the fault transmissibility multipliers for the area in question. These effectively reduce the pressure change and a slightly increment in water saturation change for that specific area as can be seen in the pressure and water injection rates profiles (figure 6.21), and the new dynamic maps from the updated model (figure 6.22). Figure 6.23 shows the new cross-plot, this time using the updated simulation

model, where the data points display a better position and agreement with the lines of C_P/C_S representing the boundary between the pressure and saturation domains.

Fault Multipliers (include file)
MULTFLT

Original Simulation Model	New iteration of the Simulation Model
DE_2 → 0.015 (partially open)	DE_2 → 0.5 (open)
DE_1 → 3.9 (open)	DE_1 → 8 (open)
E_01 → 0.01 (partially open)	E_01 → 0.2 (open)
E_01_F3 → 0.01(partially open)	E_01_F3 → 0.2 (open)
EF → 1.0 (open)	EF → 0.15 (partially open)

Figure 6.20 *Keyword MULTFLT in Eclipse is used to set the multiplier between faults in areas of uncertainty in the simulation model guided by the observed seismic data.*

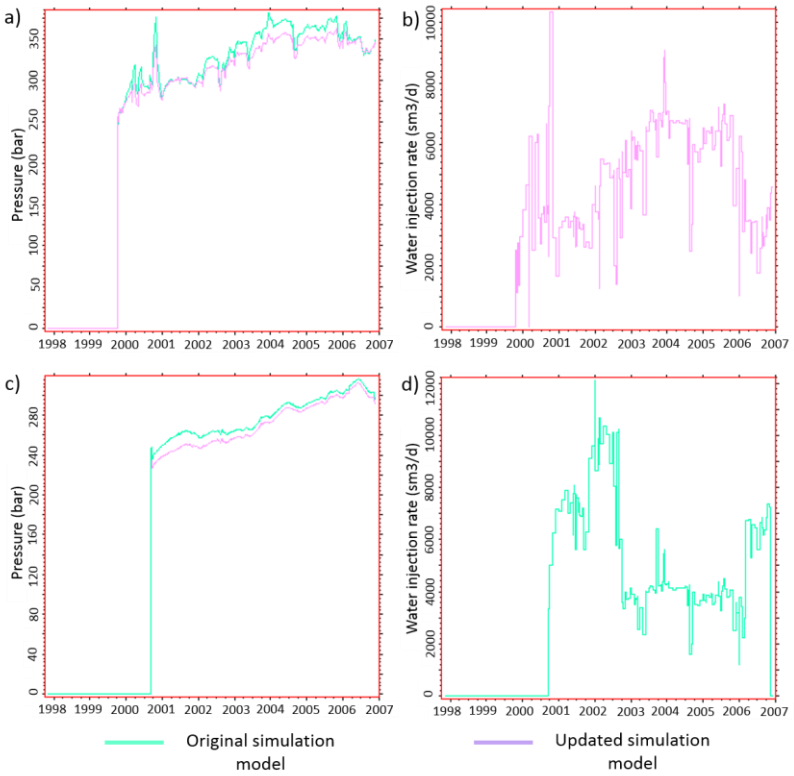

Figure 6.21 *(a) and (b) reservoir pressure and water injection rate respectively, prior and after model update for an injector well around the affected area. (c) and (d) as in (a) and (b) but for a different injector well around the same area in the Norne Field.*

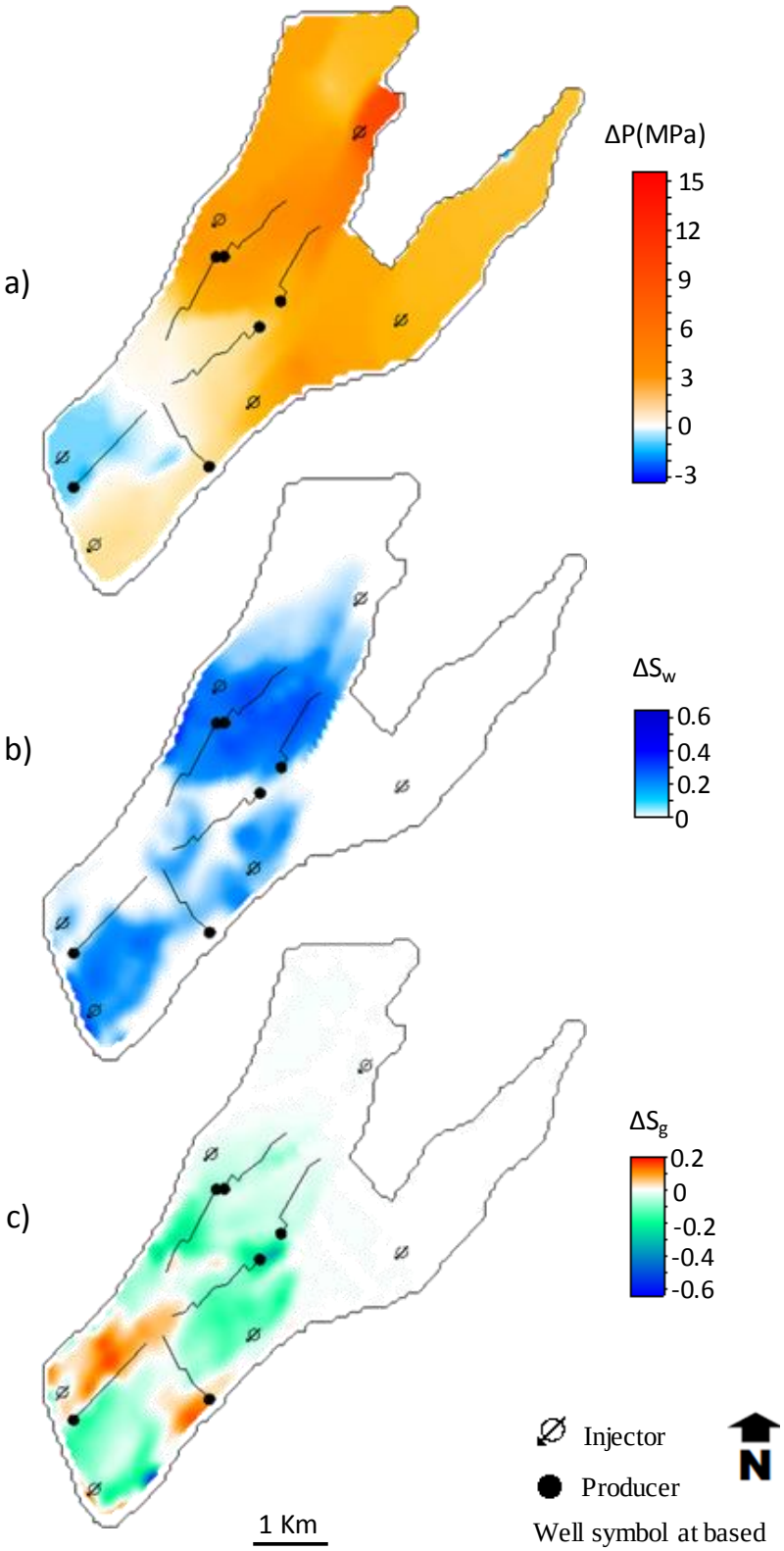

Figure 6.22 *Change in dynamic property maps between 2004 monitor and 2001 pseudo-baseline obtained from a more optimal simulation model after updates are performed. (a) Pore pressure change map. (b) Water saturation change map and (c) gas saturation change map for the Ile formation of the Norne field.*

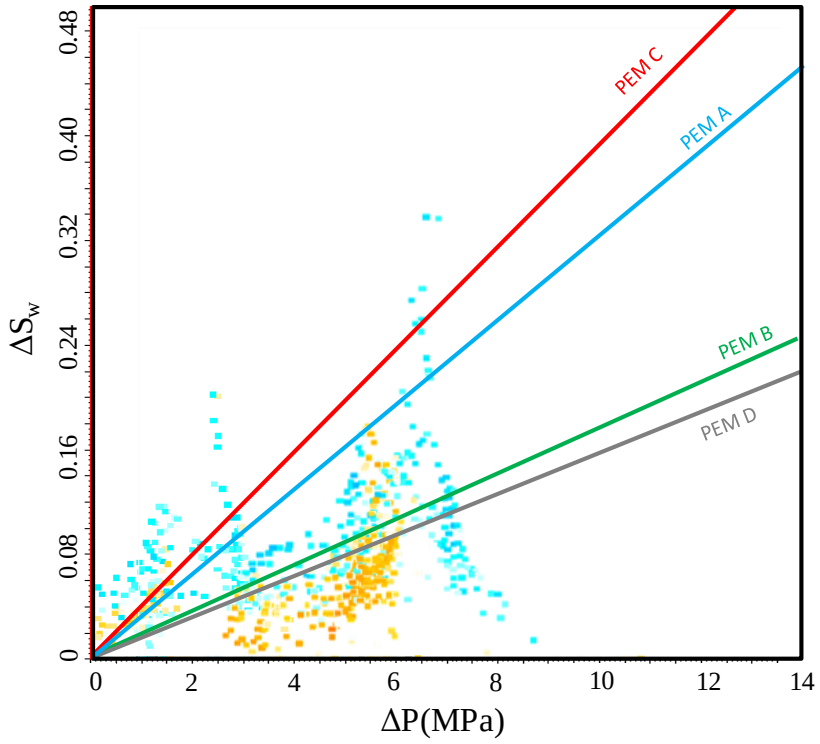

Figure 6.23 *ΔSw versus ΔP cross-plot using a more optimal simulation model for the Norne field after updates are performed, and colour-coded with the polarities of observed 4D seismic response.(Blue =hardening and Red = softening). The PEM separation lines were obtained at the impedance domain, which may represent a point of uncertainty in our interpretation.*

A second simulation model for the Norne Field was also available, which was history matched to production data only through an iterative ensemble smoother (Chen and Oliver 2013) which uses all the available data simultaneously but updates the model variables iteratively. The model parameters updated include porosity, net-to-gross (NTG), depth of oil-water contacts, permeability, fault transmissibility multipliers, transmissibility multipliers between flux regions, relative permeability of four different reservoir zones and vertical transmissibility (Chen and Oliver 2014). Figure 6.24 shows an example of the dynamic property change maps for the new history matched model, which translate to a new distribution of pore pressure and fluid change distribution in our simple cross-plot (figure 6.25). The new cross-plot using the history matched simulation model, still does not display a clear position separation in polarity between pressure and saturation domains, suggesting that not only the simulation model, but the observed seismic data itself must also be taken into consideration, including issues such as noise versus signal, signal interference and time-shifts corrections.

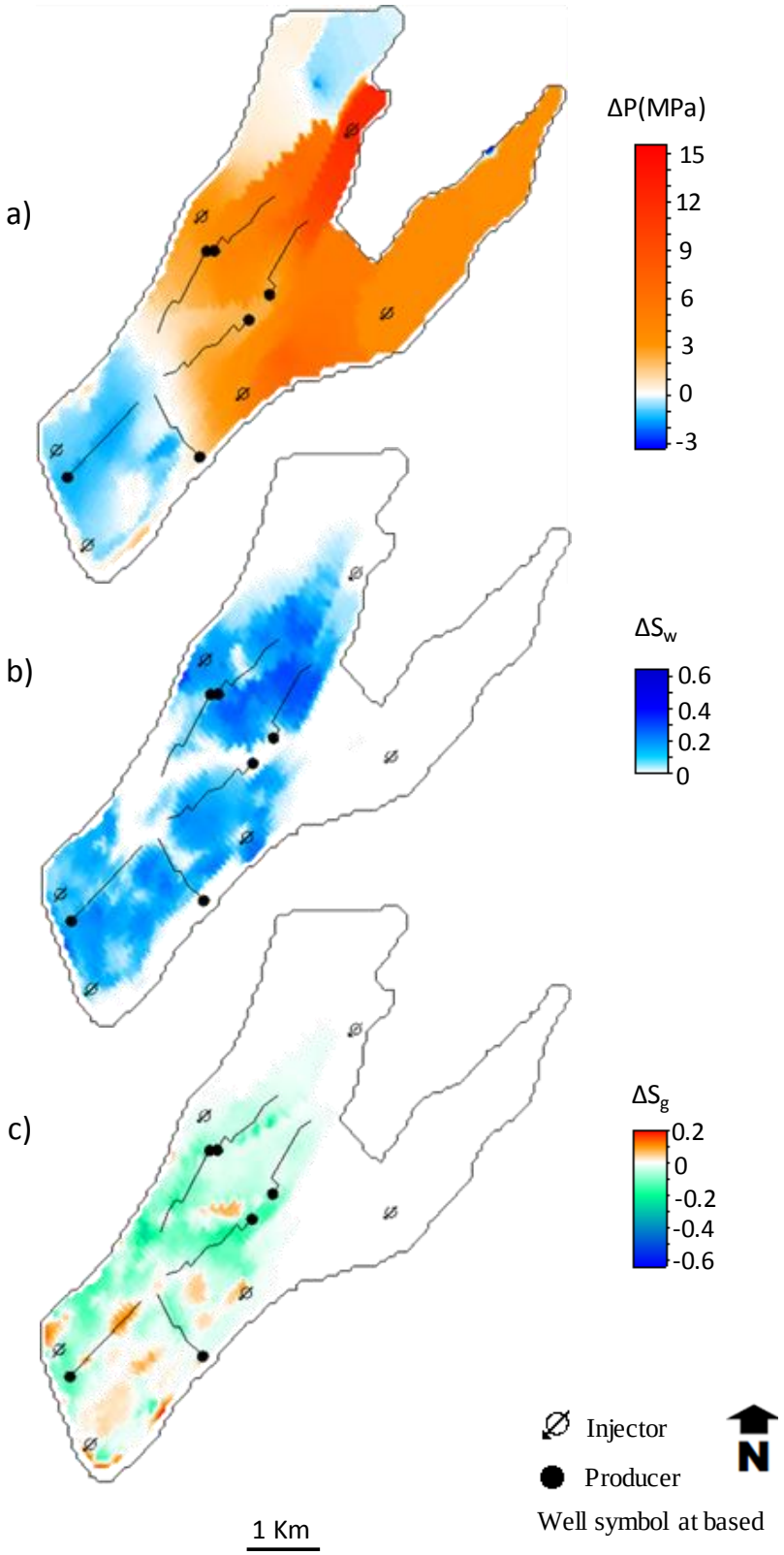

Figure 6.24 *Change in dynamic property maps between 2004 monitor and 2001 pseudo-baseline obtained from a new history matched simulation model (Chen and Oliver, 2014). (a) Pore pressure change map. (b) Water saturation change map and (c) gas saturation change map for the Ile formation of the Norne field.*

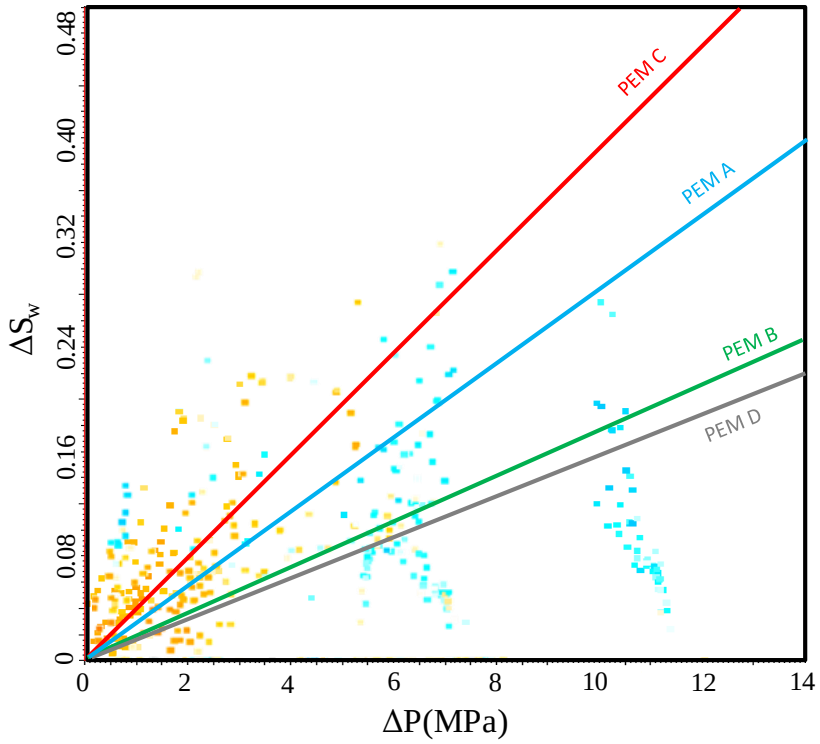

Figure 6.25 *ΔSw versus ΔP cross-plot using a more optimal simulation model for the Norne field after updates are performed, and colour-coded with the polarities of observed 4D seismic response.(Blue =hardening and Red = softening). The PEM separation lines were obtained at the impedance domain, which may represent a point of uncertainty in our interpretation.*

Moving to the final dataset used, the same methodology is applied to the carbonate Field X. Previously it was shown that the observed 4D map (figure 6.11a) using RMS amplitudes extracted for a small window of 15ms below top reservoir shows a better agreement to the 4D signature anticipated around the wells based on the water injection rate data. The ΔS_w versus ΔP cross-plot (Figure 6.26) is for the first 13 layers of the simulation model and colour coded according to the dRMS map from figure 6.11a. From the cross-plot there is no a clear distinction between the pressure (red points) and saturation (blue points) regions. Reasons for the lack of separation between pressure and saturation domains, include the presence of gas which might be poorly predicted in the simulation model and second, a poor history match performance on the flow simulator model available for this study. Conducting seismic history match (SHM) loop is out of the scope for this thesis, however our findings show that for SHM to be efficient, it involves understanding of the three domains: observed data, simulation model and PEM before going into a complex and time-consuming SHM algorithm.

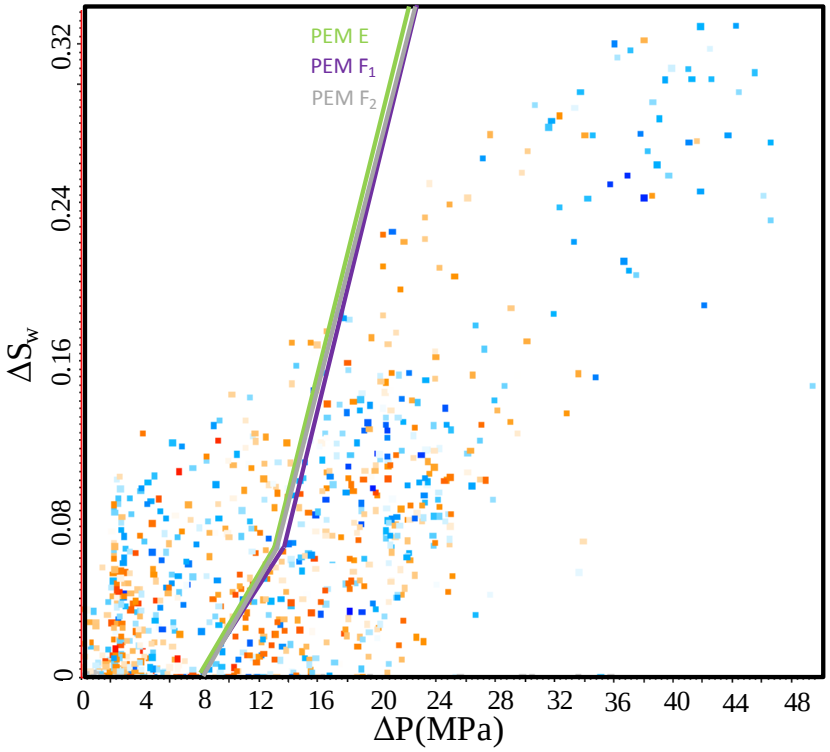

Figure 6.26 *ΔSw versus ΔP cross-plot using the original simulation model for the Norne field and colour-coded with the polarities of observed 4D seismic response.(Blue = hardening, Red=softening).*

6.5 Summary

The ΔSw-ΔP cross-plot is found to be a simple yet effective tool to simultaneously visualize the uncertainties associated with three different domains: the simulation model, the seismic data and the PEM. The plot allows us to discriminate between regions in the reservoir that are dominated by pressure or saturation change using a straight-line boundary corresponding to the selected PEM. A synthetic example has verified the usefulness of this approach, and the sensitivities to both data and the model. Application to three field datasets has confirmed the utility of the cross-plot as a way of guiding updating of the simulation model to agree with the observed seismic data. This interactive method is useful as a step prior to a full quantitative seismic history matching.

Although it is not feasible to determine the best PEM, the suggested cross-plot of ΔSw-ΔP can highlight the consistency of the different PEM paradigms compared to the observed data. Another point for future research relates to the use of the comparison

between C_P/C_S derived from observed data versus C_P/C_S derived from synthetic data. Indeed this comparison allows tuning of the stress sensitivity term during forward modelling, such that the C_P/C_S ratio from the PEM can collapse to that computed from the observed data, given that the seismically derived C_P/C_S is more representative and trustworthy of the 4D seismic signature than the C_P/C_S ratio derived from laboratory measurements and complex theoretical models.

Chapter 7

Conclusions and Recommendations

All models are still wrong, but some are still useful. This chapter summarizes exactly that usefulness and applicability of the comprehensive rock physics model applied during this thesis for 4D seismic studies. This thesis just scratches the surface of topics and issues related to the PEM definition and uncertainties as a key ingredient in time-lapse interpretation, however there are many more directions to uncover for future research.

From a reservoir management perception, different domains can be used to assess the simulation model against the 4D seismic data, including seismic amplitudes, impedance and pressure-saturation domains. Qualitative comparison between domains, comprise calculation time-lapse maps of seismic attributes which are later compared to the dynamic property (pressure and fluid saturations) maps from the simulation model and well activity to understand the 4D seismic signature. Nevertheless, when moving from a qualitative into a quantitative analysis the comparison between "observed" and "predicted" models can be fed into closing the loop seismic history matching (SHM) workflows, therefore a rigorous calibration and serious awareness of the uncertainties in the different steps of the workflow must be considered.

One of the major objectives for 4D seismic studies is to quantify pressure and saturation changes in the reservoir with confidence over time. The geocellular simulator flow model represents the main input in term of the static and dynamic properties of the reservoir from which any time-lapse study evolves. A key ingredient of 4D seismic interpretation is the petroelastic model (PEM), which links fluid saturations and pore pressure changes to the elastic property changes required for seismic modelling, time-lapse feasibility studies, 4D inversion and also seismic history matching. Numerous past studies have now pointed to the limitations and uncertainties that can exist within current rock physics models, also the difficulty of selecting an appropriate model and the need to calibrate to the *in situ* response.

The scope of this research reaches essentially the simulator to seismic process, where the 3D and 4D PEMs represent fundamental constituents in seismic constrained modelling. In a general sense, simulator to seismic modelling, hereafter referred to as sim2seis, connects two different domains together, the fluid flow simulation and the seismic domains. Sim2seis modelling is a process that creates the synthetic seismic response from a reservoir simulator during different stages of production. Forward modelling has different components including petroelastic modelling and seismic modelling. The former represents the main subject of this thesis. The degree of utility, and overall accuracy of the PEMs shown in this work, are based on their effectiveness for 4D seismic interpretation guided by sim2seis. The following summary shows the findings and challenges of the current work and recommendations for future research.

7.1 Deterministic PEM implementation in 4D Seismic

The ever present objective and challenge of this thesis was to build a PEM suitable for simulator to seismic (sim2seis) applications within the 4D seismic framework. The specific PEM must be sufficiently accurate, which stresses the importance of such model. The present thesis tackled a variety of rock physics models in term of calibration against logs and lab measurements, the number of inputs parameters, high degree of uncertainty due to non-uniqueness nature and the resultant outputs in the time-lapse impedance domain.

The conventional PEM (3D and 4D) is a series of relationships and equations based on theoretical principles and empirical laws with parameters calibrated against well logs and core data. The PEM relates rock and fluid properties to the elastic moduli distribution in the reservoir and hence determines P-wave and S-wave velocities and density. There are numerous PEM choices available for 4D seismic studies, the conventional deterministic PEM consist of two parts: the static rock components by which the saturated rock frame moduli and density in their initial state are specified, and the dynamic component which is defined by the fluid substitution model, effect of pressure changes on each fluid phase, and finally the stress dependency of the rock frame density and moduli. In this thesis, when building the conventional PEM for time-lapse purposes, efforts were directed to include rock properties and pressure variations in the dry frame moduli characterization through different equations as shown in chapter 3, which together with Gassmann fluid substitution model, then reflect the combined effects of pressure and fluid saturation changes in the reservoir due to production and recovery.

In terms of the PEM parameterization, Amini (2014) showed that the predicted 4D response in term of change of P-impedances, offer the same story in a qualitative manner indistinct if the parameters were calibrated or not. Meaning same areas are predicted for softening due to pressure build up or gas coming out of solution, and hardening for an oil being replaced by water (figure 7.1). In practice the PEM is uncertain and without calibration of the input data (lithology, porosity, and fluid saturation) it becomes more so (Amini 2014), with the uncertainty carried on through the entire process of the synthetic seismic computation. Precisely, the main goal of the

PEM is to envisage the right balance between pressure and saturation signals in the reservoir with time, for which is required a realistic calibration of the PEM parameters.

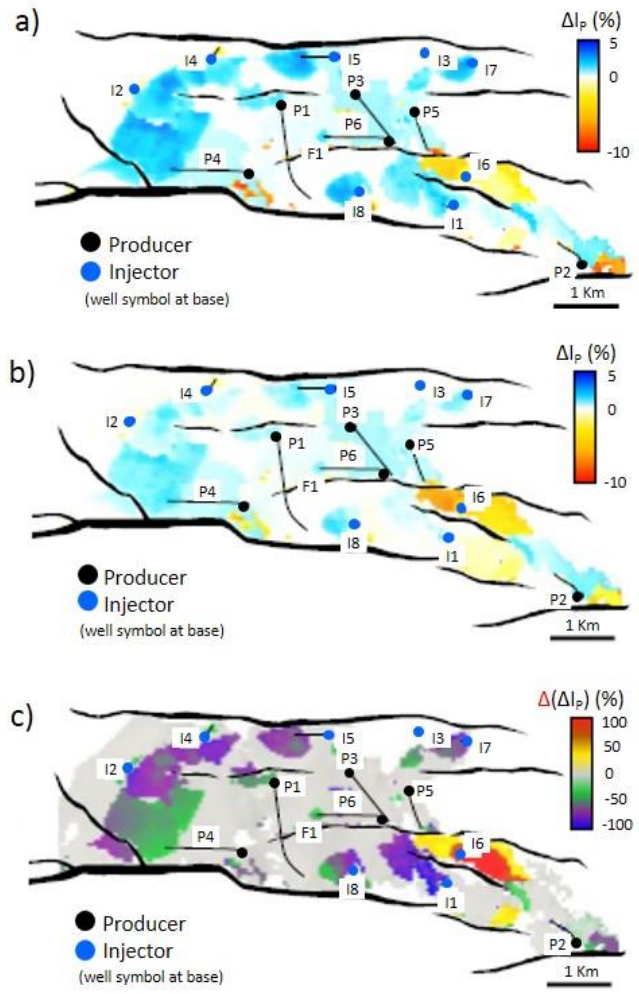

Figure 7.1 *Impedance changes maps for different PEM parameters scenarios: (a) calibrated parameters against log data and (b) using values from look up tables from the literature (no calibration); and (c) the associated error in the predictions between the calibrated and no calibrated PEM (After Amini 2014).*

The examples herein presented (UKCS, Norwegian Sea Field and offshore Brazil), showed that the PEM parameters are tied to the field characteristics, which implies that they need to be calibrated for each field, taking into account the geology specifics, and how structures and heterogeneities compare between the log and reservoir simulation domains. Chapter 4 showed that the parametrization of the PEM helps to outline the accuracy and confidence of time-lapse studies, indeed chapter 4 focused on the calibration of the PEM parameters to the in-situ response for each studied fields. The static calibration against log data was performed through an optimization algorithm to

reconstruct the elastic logs (velocities and bulk density) and derive the calibrated input parameters of each PEM. For all three fields of study there is a reasonably good fit between measured and predicted logs, implying that no rock physics model can in fact be considered as the best and all fit well. The dependence on pressure change was then added using coefficients derived from the laboratory based on the modified equations from MacBeth (2004).

The log optimization performed in Chapter 4 suggests that all the PEMs may be adequately calibrated to wireline log data for interpretation purposes, probably as a consequence of the high number of available free parameters. Indeed for each PEM a large number of free parameters were determined (nine parameters for PEMs A, B, C and E. eight for model D and six for model F), plus four laboratory coefficients in common since all the PEMs share the same stress sensitivity model (table 3.2). The calibration of its vast amount of parameters is challenging and created high degree of uncertainty across the different models, which makes the choice of the "best" model appear not to be possible, as all provide a satisfactory match to the logs in the three field datasets considered in this study.

The degree of utility, and overall accuracy of the PEMs, are based on their effectiveness for 4D seismic interpretation guided by simulator to seismic modelling. In chapter 5, each cell in the flow simulation model specified by a particular shale volume (V_{sh}) and porosity (ø) together with fluid saturation and pressure changes were then transformed into a corresponding V_P, V_S, and ρ using the estimated input parameters calibrated to wireline logs and core data. The calculation of the acoustic elastic properties of the reservoir leads to the resultant impedance change maps for producing units in each field. The time lapse change of impedances can be cast as a function of pressure and saturation changes, simulation model properties such as porosity, NTG, SATNUM (saturation regions), and the PEM. Certainly, each of the PEMs balance the changes of the dynamic properties of the reservoir differently, which is reflected in the 4D amplitudes response. On the other hand, having a good fit to the logs, does not necessarily translate in a good 4D impedance response in the simulation domain, as was observed for some of the models used for the Schiehallion field. The optimized to log data set of PEM parameters might be unrealistic affecting the entire synthetic seismic computation and its direct comparison to the observed data,

From all the observations from Schiehallion, Norne and Field X, in general and within a certain tolerance, qualitatively all the PEMs presented in this work may be appropriate and due to the high uncertainty nature across the different models, each PEM appears as a reasonable choice, no matter its complexity. However considerations must be taken to evaluate a PEM as good or bad based on the absolute values of the 4D seismic signature, being said impedances domain or any other seismic attribute, or through comparison between observed seismic data and synthetic seismic, this final observation is out of the scope presented in this thesis.

7.1.1 Rock Stress sensitivity

From a time-lapse point of view, the PEM consists of three main categories: fluid substitution model, fluid related pressure effects and the stress-dependency of the rock frame. The 4D PEM takes into consideration the effective stress dependency of the rock frame density and moduli; this need in this thesis was addressed through theory and core based laboratory measurements. From Gassmann's equations we can observe that there are three parameters we need to consider which depend on pressure changes and are part of a conventional petroelastic model: the bulk and shear modulus of the rock frame (K_{dry}, μ_{dry}), which define the rock stress sensitivity, and the bulk modulus of the fluid (K_{fl}) which controls the effect of pressure on fluids. One of the most problematic areas in the application of Gassmann fluid substitution model is in the calculation of the dry frame moduli. In the 4D domain, studies on dry frame modelling must incorporate the static dependence of the dry-rock moduli on porosity as well as relations that show the pressure dependence in the dry frame moduli. The stress sensitivity term of the dry rock frame remains the highest uncertainty in the PEM (Amini 2014) especially since the majority of studies on stress sensitivity are based on laboratory core measurements and they may not represent the in-situ field scale stress response (Ness et al. 2000, Fürre et al. 2009, Alvarez 2014).

7.2 Proxy petroelastic modelling for time-lapse studies

The time-lapse response is indeed a combination of changes in both pressure and fluid saturation during production, therefore has been critical in the industry to discriminate both effects (pressure and saturation) that characterized the seismic signature. In the

research community there has been an interest in obtaining the 4D seismic response independently from the conventional PEM recipe by using trend or simplified equations, like in the work of Floricih et al. (2006). However, Alvarez and MacBeth (2013) extended the use of the simplified equation to derive the time-lapse response by associating the coefficients of the simple mathematical model to the conventional PEM, which means constants with a clear physical meaning.

Alvarez and MacBeth (2013) developed a simplified equation where the elastic constants from such equations are related to the petroelastic model. The overall objective of Alvarez (2014) work was to devise a simple formula that can relate seismic, engineering and rock/fluid physic domains for ease of interpretation. Such simplified mathematical expressions is ruled by C_S and C_P known as the controlling parameters, which provide the balance between the relative contributions of saturation (ΔS_w) and pore pressure (ΔP) change to the overall time-lapse seismic signature (ΔA). When working with maps of 4D seismic attributes in particular, a good practical alternative is a two-parameter model linear in the pressure and saturation changes. It has been demonstrated in chapter 5 that this proxy model must still however be referenced to the full deterministic PEM. Thus simulator to seismic modelling may incorporate a single generic model with parameters linked directly back to the PEMs and data.

In chapter 5, the reduction of inputs parameters used in the deterministic PEMs was tackled by using a proxy model which is included into our sim2seis calculations. The proxy model applied in this work cannot be used by itself, the calibration must be achieved using a fully deterministic PEM model calibrated to the logs. Certainly the controlling parameter C_S carries the log calibration but C_P's major influence comes from laboratory data. Actually a correct numerical assignment on the C_P term should depend on a range of factors that may enhance or diminish the stress sensitivity relative to the calibration offered by laboratory core plug measurements.

In this thesis, from a qualitative comparison between the resulting time-lapse map of the simplified formulation, and those obtained through the conventional rock physics modelling (paradigms A, B, C and D for the siliciclastic fields, and E and F for the carbonate field example), I can conclude that is not necessary to have a lot of parameters to fit the behavior of the 4D signature response; such practical non-

uniqueness makes the choice of the "best model" in sim2seis studies challenging. Indeed, any PEM may act as a "prime" for the proxy, which can then be used in sim2seis modelling calculations on its own. Keeping in mind that the goal is searching for a rock physics model that is accurate, robust and simple for time lapse interpretation, judging all the models based on the concept of Occam's razor seems reasonable: choosing the least complex PEM with the least number of parameters that fits the data well. Based on this philosophy the simplified linear proxy model with two parameters, may work well in practice to resolve this difficulty of building and choosing the right PEM, especially for an oil-water system (i.e. no gas). The presence of gas in any field, increases the uncertainty and predictability of the 4D maps using a simple two parameters mathematical equation. Nevertheless, from a quantitative point of view, considerations and attention must be taken into consideration. The proxy model works for an oil-water system, although big errors were shown in the time-lapse maps in Chapter 5 because of the uncertainty related to the laboratory stress sensitivity term in the PEM. Another uncertainty is the flow simulator model itself, if the reservoir model has a poorly history matched pressure and production and injection fluid data, then errors will be carried on through the entire 4D seismic study, indifferently of the rock physics model chosen and its associated calibrated input parameters.

Finally, it should be understood that the PEM question is a simplification of a very complex system, and as such, is only approximate. However, I am seeking to provide a simple, yet precise PEM, which will be computationally possible and which can fulfil the requirements of the industry for Time Lapse interpretation.

7.3 Bringing together Simulation model, Seismic data and PEM knowledge

The integration of 4D seismic and engineering data has been primarily in a qualitative sense, by simple visualisation of the seismic signature to the changes associated to production in the reservoir, as was shown in chapter 5. However, the interest and development towards a more quantitative use of time lapse seismic data in the reservoir modelling workflow has increased in the geoscience industry. Indeed, a comprehensive literature review showed the growth of history matching using production and 4D seismic data. Seismic history matching (SHM) closes the loop and minimizes the misfit between the observed data and that predicted by the reservoir model. In SHM, the misfit

can be computed at three different levels across the seismic and reservoir-engineering domains, including the simulation model domain, acoustic impedance domain and the seismic amplitudes domain.

Alvarez (2014) used the simplified mathematical equation together with field data observations from a North Sea field dataset available in ETLP and from several published studies, to define a constraint in the stress sensitivity term. His study showed that the ratio of the controlling parameters C_S/C_P is a fundamental parameters that can be extracted from time-lapse maps at the injector wells location where the pressure is supported by water injection. Nevertheless, in this thesis, I decided to use the entire inter-well space of the 4D amplitude map and the dynamic properties maps of the simulation model. With the aim of capturing the ratio C_P/C_S associated for each deterministic rock physics model together with the lateral distribution of pressure and saturation in the simulation model.

The present thesis have highlighted the importance of the PEM in 4D seismic interpretation, including the contribution and key role for reservoir model updating and history matching. In Chapter 6, the ΔSw-ΔP cross-plot is found to be a simple yet effective tool to simultaneously visualize the uncertainties associated with three different domains: the simulation model, the seismic data and the PEM. The plot allows us to discriminate between regions in the reservoir that are dominated by pressure or saturation change using a straight-line boundary corresponding to the selected PEM. Indeed, the results from chapter 6 have confirmed the utility of the cross-plot as a way of guiding updating of the simulation model to agree with the observed seismic data. This interactive method is useful as a step prior to a full quantitative seismic history matching.

7.4 Recommendations

This thesis just scratches the surface of rock physics models and their role and applicability in 4D seismic studies, nevertheless there are more to bare and find for future research. The results presented here was always in the impedances domain, however it is a normal evolution for future research to compute the synthetic seismic

and add a new uncertainty level to the workflow though seismic modelling (convolution and finite difference).

From PEM perspective, the stress sensitivity term carries the highest uncertainty, therefore a better calibration must be achieved. A good area for further exploration would the effect of clay content on the stress sensitivity, and even though activation of the shale cells in the simulation model, since Rangel (2016) shows that they have an implication on the polarity and magnitude of the 4D seismic signature.

Although it is not feasible to determine the best PEM from the models herein exhibited; the suggested cross-plot of ΔSw-ΔP highlighted the consistency of the different PEM compared to the observed data. Another point for future research relates to the use of the comparison between C_P/C_S derived from observed data versus C_P/C_S derived from synthetic data. Indeed this comparison allows tuning of the stress sensitivity term during forward modelling, such that the C_P/C_S ratio from the PEM can collapse with that computed from the observed data, given that the seismically derived C_P/C_S is more representative and trustworthy of the 4D seismic signature than the C_P/C_S ratio derived from laboratory measurements and complex theoretical models.

It is understood that in reality, reservoirs are complex and presence of gas due to a drop in pressure after years of production cannot be ignored. Such challenge is recognised and therefore is highly recommended to be incorporated in the proxy model (equations 7.1), still having a physical meaning. In that way a more accurate quantitative approach can be achieved.

$$\Delta A = C_s \Delta S_w - C_p \Delta P + C_g \Delta S_g \tag{7.1}$$

Even in this thesis a carbonate reservoir was scrutinised, I acknowledge for future research the extension of the application in carbonate fields from conventional rock physics models, to proxy models, with the intention of understand its complexity and grow the knowledge of such fields.

Finally, the ΔSw-ΔP cross-plot is found to be a simple yet effective tool to simultaneously visualize the uncertainties associated with three different domains: the

simulation model, the seismic data and the PEM whilst optimizing the SHM. Certainly for future research, it would be interesting to use such an interactive tool inside an assisted history matching workflow as a guide. Therefore to impose constraint on the PEM and revise the model simultaneously with the results of the history match procedure in an interactive manner, until one finds a successful solution that fits the "observed data" and the "predictions" from the model.

7.5 Final Remarks

During this work, I have explored the conventional PEM build up stage together with the calibration of its multiple parameters, all in the context of simulator to seismic modelling. The resultant 4D impedance change maps have been compared on a qualitative point of view, drawing attention to the non-uniqueness nature of the rock physics models. Moving into a more quantitative stage seems to be the clear choice, and its support and applicability in the research community has increased with the years. Here in this research work I recognised a novel simplified linear proxy model for 4D studies and its controlling parameters as a metric to compare PEM but also to recognise uncertainties in the data and reservoir model. This thesis highlights the key role of the PEM in 4D studies (figure 7.2) but only shows a small portion of its applicability and complexity. Indeed, such an important topic can go further with the objective of fulfilling the closing the loop workflow (seismic history matching and updating of the reservoir model) requirements for time-lapse interpretation inside the oil and gas industry.

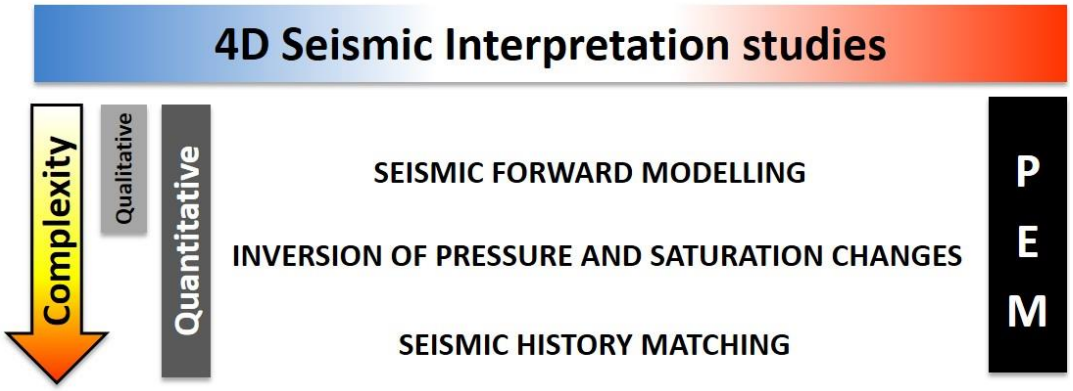

Figure 7.2 *Different applications of 4D seismic interpretation studies, which analysis can be performed in a qualitative or quantitative manner, therefore increasing its complexity and uncertainties associated. However, the PEM represents a key ingredient in whatever desired route or objectives that want to be reached.*

Appendix A: Publications

Th LHR2 08

Towards an Effective Petroelastic Model for Simulator to Seismic Studies

A. Briceno* (Heriot-Watt University), C. MacBeth (Heriot-Watt University) & M.D. Mangriotis (Heriot-Watt University)

SUMMARY

One of the major objectives for 4D seismic studies is to quantify pressure and saturation changes in the reservoir. A key ingredient of this interpretation is the petroelastic model (PEM), which links fluid saturations and pore pressure changes to the elastic property changes required for seismic modelling, time-lapse feasibility studies, 4D inversion and also seismic history matching. In this work we study the use of four different deterministic PEMs for simulator to seismic modelling. The models are calibrated to field data from a UKCS and Norwegian Sea with distinctly different geological settings. We find that there is no best choice of PEM, any may suffice, and that the number of input parameters for each is unnecessarily high. An alternate model for simulator to seismic modelling is suggested which uses only two parameters without loss of accuracy when predicting the mapped seismic response.

78th EAGE Conference & Exhibition 2016
Vienna, Austria, 30 May – 2 June 2016

Introduction

The petroelastic model (PEM) is an essential cornerstone of quantitative 4D seismic interpretation. This model links fluid saturations and pore pressure changes in the reservoir rock to the elastic property changes required for seismic modelling, time-lapse feasibility studies, 4D inversion and also seismic history matching (Falcone et al. 2004). Numerous past studies have now pointed to the limitations and uncertainties that can exist within current models, also the difficulty of selecting an appropriate model and the need to calibrate to the *in situ* response (for example, Amini 2014). To address the latter two issues in particular, here we study the use of four different deterministic PEMs for simulator to seismic modelling. These models are applied to two fields in the UKCS and Norwegian Sea with distinctly different geological settings. For each model, the static rock frame components are calibrated using a range of wireline log data acquired prior to production. The dependence on pressure change is then added using coefficients derived from the laboratory. Based on comparisons across field and model, the number of parameters, degree of utility, and overall accuracy of the PEMs, conclusions are drawn on their effectiveness for 4D seismic interpretation guided by simulator to seismic modelling.

Description of models

As our ultimate end-goal is simulator to seismic modelling for the reservoir prior and then after production and recovery. The PEM models selected for the study are therefore influenced by the choices made when building the cellular fluid simulation model and its subsequent predictions. For our two chosen fields each model cell is specified by a net-to-gross *NTG* (or volume of shale $V_{shale} = 1\text{-}NTG$). This therefore assumes that facies variations for these reservoirs can be represented by only variations in the sand/shale fraction. This is true of the reservoirs used in our study but may not of course be fully representative of all reservoirs, and for the most general case PEMs may need to be constructed for each distinct lithofacies (Alfred et al. 2008). Our PEMs consist of two parts: first the static rock components by which the saturated rock frame moduli and density in their initial state are specified, and secondly the dynamic component which is defined by the fluid substitution model, effect of pressure changes on each fluid phase, and finally the stress dependency of the rock frame density and moduli. For the purpose of our study, four different recipes described here as models A, B, C and D, are used to build the static component that is then calibrated directly by the wireline logs. All models employ some aspects in common: Gassmann fluid substitution equations and semi-empirical relations for reservoir fluid properties (Batzle and Wang 1992). Also in common is the volume averaging of the solid and liquid phases for calculation of the density, and Voigt-Reuss-Hill averaging of the mixing of sand and shale mineral moduli. PEMs A, B and C use MacBeth (2004) for the stress-sensitivity, modified for log calibration. Assuming isotropic loading, the stress-dependent moduli are

$$\mu_{dry} = \mu_{dry\_log}\left(\frac{1+E_\mu e^{-P_{res\_eff}/P_\mu}}{1+E_\mu e^{-P_{eff}/P_\mu}}\right) \qquad K_{dry} = K_{dry\_log}\left(\frac{1+E_K e^{-P_{res\_eff}/P_K}}{1+E_K e^{-P_{eff}/P_K}}\right) \tag{1}$$

where E_K, P_K, E_μ and P_μ are the rock stress sensitivity constants estimate from a selection of core measurements (MacBeth 2004), P_{res_eff} is the initial effective pressure of the reservoir at pre-production time, and P_{eff} is the effective isotropic stress at the monitor survey time. For PEM D, the rock-frame stress-sensitivity is specified using the Hertz-Mindlin theory (Mavko et al. 2009).

The main difference between models A, B, C and D lies in the modelling of the dry frame bulk and shear moduli, K_{dry} and μ_{dry}, in terms of the corresponding mineral moduli K_{min} and μ_{min}, porosity ϕ, and volume of shale V_{shale}. Thus, PEM A follows Lee (2005) by specifying $K_{dry} = K_{min}\,(1\text{-}\phi)/(1+\alpha\phi)$ and $\mu_{dry} = \mu_{min}\,(1\text{-}\phi)/(1+\alpha\phi)$, where α is a consolidation factor $\alpha = aV_{sand} + bV_{shale} + c\phi$ lying in the approximate range $2 < \alpha < 20$, a, b and c are coefficients to be determined. PEM B follows the concept of critical porosity ϕ_c (Nur 1998, Mavko et al. 2009) to specify the dry rock frame according to $K_{dry} = K_{min}\,(1\text{-}\phi/\phi_c)$ and $\mu_{dry} = \mu_{min}\,(1\text{-}\phi/\phi_c)$, where our clastic fields ϕ_c lies between 36 and 40%. PEM C is based on Krief et al. (1990) model, which describes $K_{dry} = K_{min}\,(1\text{-}\phi)^{m(\phi)}$ and $\mu_{dry} = \mu_{min}\,(1\text{-}\phi)^{m(\phi)}$

where m(ϕ) = 3/(1- ϕ). Finally, PEM D is based on the intermediate stiff-sand model (Mavko et al. 2009) determined by the functional form of the soft sand model with Hertz-Mindlin contact theory taking the pressure effect into account and the modified Hashin-Shtrikman lower bound to obtain the dry frame moduli which consider the porosity dependence.

Application to field data

Use of the PEMs A, B C and D above comes with the cost of many free parameters to be constrained for the particular dataset. These parameters are determined using an optimisation algorithm to fit each model to the sonic, shear, and density logs (after careful editing and petrophysical evaluation). For each field, the optimisation is performed for the entire depth interval that intersects the simulation model, for a range of wells and also for individual segments of the logs sampling similar geology. For the UKCS field, data from five wells are considered, with two of the logs subdivided to give a total of seven segments to match. For the Norwegian Sea field, logs from three wells are divided to obtain a total of six log segments. Figure 1 shows an example of log prediction from the optimisation algorithm for both study fields, with the corresponding model parameters given in Table 1. In general, prediction errors for the UKCS field are less than 5%, 3% and 1% for V_P, V_S and ρ respectively. For the Norwegian Sea field corresponding velocity errors are a slightly higher 8% due to geological heterogeneity, but density prediction error is still less than 1%.

Field	PEM paradigm	Scenario	K_{sand} (GPa)	K_{shale} (GPa)	β_{sand} (GPa)	β_{shale} (GPa)	ρ_{sand} (g/cc)	ρ_{shale} (g/cc)
UKCS	PEM A	1	24	15	20	4	2.718	2.403
	PEM B	2	33	14	28	4	2.722	2.407
Norne	PEM A	1	23	22	16	12	2.689	2.635
	PEM B	2	29	16	25	7	2.728	2.637

Table 1 Example of parameters obtained from model fit to the logs.

PEM	Elastic Moduli	Coefficient of Variation (CV) UKCS	Coefficient of Variation (CV) Norne
PEM A	K_{sand}	0.1525	0.1699
	G_{sand}	0.2483	0.1521
	K_{shale}	0.1022	0.2699
	G_{shale}	0.1715	0.2806
PEM B	K_{sand}	0.0333	0.0751
	G_{sand}	0.0980	0.0589
	K_{shale}	0.1544	0.0882
	G_{shale}	0.2296	0.1422
PEM C	K_{sand}	0.0266	0.0741
	G_{sand}	0.1443	0.0564
	K_{shale}	0.1854	0.0869
	G_{shale}	0.3534	0.1322
PEM D	K_{sand}	-	-
	G_{sand}	0.0564	0.0634
	K_{shale}	0.4318	0.1606
	G_{shale}	0.3212	0.1378

Table 2 Coefficients of variation for the input parameters obtained from log calibration.

The exercise of parameter optimisation yields estimates for a variety of different logs segments. To make a comparison between the models, the coefficient of variation (sample standard deviation divided by sample mean) is calculated for each field and model parameter (Table 2). Values range from 0.03 to 0.3, indicating a reasonable overall consistency between fits laterally across the field and with depth. As might be anticipated, the shear moduli are observed to be more variable than the bulk moduli, and the shale parameters are more variable than those for sand, which agrees with the literature. Interestingly however, no model shows a particularly strong tendency of either low or high dispersion. We conclude from our analysis that no model can in fact be considered as the best. After the statistical analysis, each

set of estimated input parameters are now used in simulator to seismic modelling. Thus, each cell in the flow simulation model specified by a particular V_{shale} and ϕ together with saturation and pressure changes can be transformed into a corresponding V_P, V_S, and ρ. Figure 2 shows the resultant impedance change maps for producing units in either field. The log calibration deals with the dry fame characterisation in the static domain and impacts the amplitudes via Gassmann fluid substitution but it will not impact strongly on the pressure sensitivity.

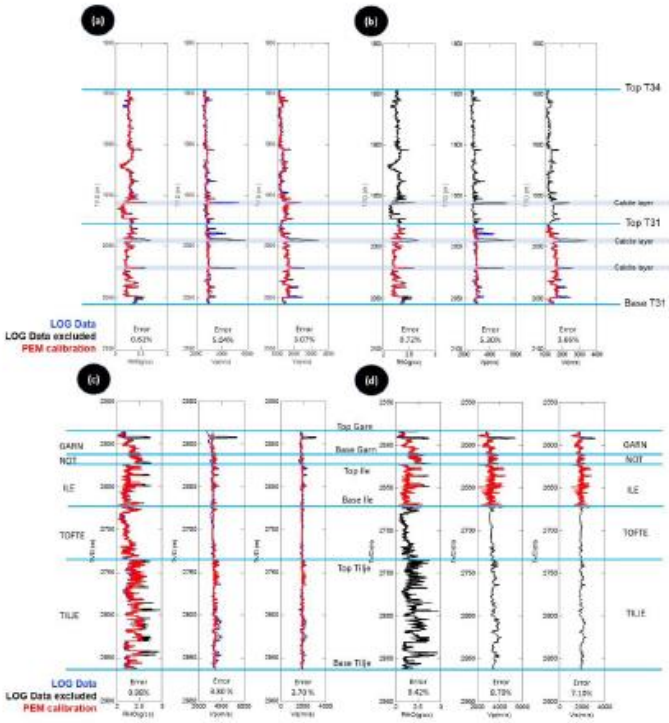

Figure 1 Example of fit of PEMs to log segments from the fields of interest in our study. UKCS field: (a) PEM A for entire log segment, (b) PEM B only for the lower sands. Norwegian Sea field: (c) PEM A for an entire log segment and (d) PEM B only for the top sands.

Discussion

For each PEM a large number of free parameters are required to be determined by the log optimisation procedure (9, 7, 6 and 8 for PEMs A, B, C and D respectively), plus four lab coefficients in common for PEM A, B and C as they share the same stress sensitivity model. Despite the data points available with which to calibrate effectively and the adequate degree of fit to almost all log segments, such models still however carry significant non-uniqueness which makes 4D seismic interpretation less intuitive. For time-lapse seismic maps in particular, it has been suggested that the main response may be captured by a simple two parameter equation $\Delta A = C_S \Delta S_w - C_P \Delta P$, where C_S and C_P are now the PEM parameters, which provide the balance between the relative contributions of saturation ΔS_w and pore pressure ΔP change to the time-lapse seismic signature ΔA (Alvarez and MacBeth 2013).

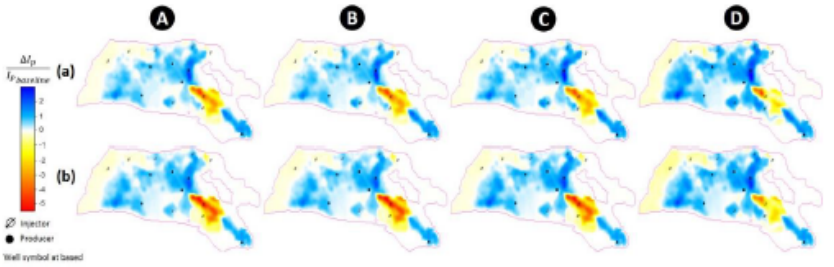

Figure 2 (a) Maps of impedance change predicted by calibrated PEMs A, B, C and D for our UKCS field. (b) As in (a), but maps of impedance change predicted using our reduced-parameter model.

Whilst this approach provides a framework that maps intuitive feel to a mathematical model, to be useful it still needs to be calibrated and linked to the simulation model. The calibration of the different PEMs above shows how this can be done. Based on our results, it is possible to select any of the PEMs A, B, C or D, and perform a calibration. After this, model predictions are directly inspected to yield the required C_P and C_S parameters. It is found that the two-parameter model is sufficiently close to the model results to replicate most of the 4D seismic response (see Figure 2).

Conclusions

There are numerous PEM choices available for 4D seismic studies. Our results suggest that all may be adequately calibrated to wireline log data for interpretation purposes, probably as a consequence of the high number of available free parameters. Indeed, the choice of a 'best' model appears not to be possible, as all provide a satisfactory match to the two field datasets considered in this study. When working with maps of 4D seismic attributes in particular, a good practical alternative is a two-parameter model linear in the pressure and saturation changes. It has been demonstrated that this must still however be referenced to the full PEM. Thus simulator to seismic modeling may incorporate a single generic model with parameters linked directly back to the PEMs and data.

References

Alfred D., Atan S., Hamman J.G., Caldwell D.H. 2008. Petro-Elastic Models: How Many and at What Scale?. 70th EAGE meeting, Rome, Italy, Expanded Abstracts. SPE No. 11354

Alvarez E., and MacBeth C. 2013. An insightful parametrization for the flatlander's interpretation of time-lapse seismic data. EAGE, Geophysical prospecting.

Amini H, 2014. A Pragmatic Approach to Simulator to Seismic Modelling for 4D Seismic Interpretation. Thesis.

Batzle M. and Wang Z. 1992. Seismic properties of pore fluids. Geophysics 57, 1396-1408

Falcone G, Gosselin O, Marrauld J, and Zhakupov M. 2004. Petroelastic modelling as key element of 4D History Matching: A field example. SPE 90466.

Krief M., Garat J., Stellingwerff J. and Ventre J. 1990. A petrophysical interpretation using the velocities of P and Swaves (full-waveform sonic). Log Analyst 31, 355-369.

Lee M.W. 2005. Proposed moduli of dry rock and their application to prediction elastic velocities of sandstones. U.S Geological Survey Scientific Investigations Report 2005-5119.

MacBeth C. 2004. A classification for the pressure-sensitivity properties of a sandstone rock frame: Vol. 2, No. April, p. 497–510.

Mavko G., Mukerji T., Dvorkin J. 2009. The Rock Physics Handbook: Tools for Seismic Analysis of Porous Media. Cambridge University Press

Nur A., Mavko G., Dvorkin J. and Galmundi D. 1998. Critical porosity: A key to relating physical properties to porosity in rocks. The Leading Edge17, 357-362.

Th A1 08

A Practical Tool for Simultaneous Analysis of 4D Seismic Data, PEM and Simulation Model

A. Briceño* (Heriot-Watt University), C. MacBeth (Heriot-Watt University), M.D. Mangriotis (Heriot-Watt University)

Summary

One of the main focuses of the geoscience industry is to constrain reservoir models to 3D and 4D seismic data using quantitative workflows that are suitable for model updating and history matching. Seismic history matching (SHM) closes the loop and minimizes the misfit between the observed 4D seismic and that predicted by the reservoir model. A key problem in formulating this misfit function is a lack of understanding as to how uncertainties in the seismic data, petroelastic model and simulation model interact. This can lead to lengthy and time consuming workflows. This study presents a simple and interactive way of visualizing these uncertainties whilst optimizing the SHM. The approach is applied initially to a synthetic example, and then to two different field datasets from the UKCS and Norwegian Sea. The results demonstrate that qualitative updates can be successfully applied to the simulation model in the presence of uncertainty in the PEM and noise in the 4D seismic data.

79th EAGE Conference & Exhibition 2017
Paris, France, 12-15 June 2017

Introduction

The growth of history matching involving not only production data but also 4D seismic data is a very active field (Gosselin et al. 2003; Roggero et al. 2007). This integration helps to reduce the uncertainty of the final reservoir model solutions and improve the reliability of production forecasts (Walker 2006). Seismic history matching (SHM) closes the loop and minimizes the misfit between the observed data and that predicted by the reservoir model. This workflow relies on the petroelastic model (PEM) when computing the synthetic seismic from the simulated pressure and saturation changes. Many previous studies have pointed out the difficulty of selecting a PEM, the challenges in calibrating the model to the in situ response, and in particular the uncertainties involved. This non-uniqueness in the PEM, together with data and model uncertainties creates the need for time-consuming comparisons in the SHM workflow. This study presents a simple and interactive way of visualizing all of these uncertainties, whilst optimizing the SHM. The approach is illustrated by application initially to synthetic data and then to two different fields from the UKCS and Norwegian Sea.

Methodology

Our approach consists of a simple cross-plot of all changes in water saturation and pore pressure between the two time periods of interest in the reservoir history (usually pre-production baseline and a monitor). An example of this cross-plot is shown in Figure 1. The position of each point is defined by the simulation model predictions. Simulation models with a different selection of history matching parameters such as fault transmissibility multipliers, porosity multipliers, barrier locations, will have different simulation predictions and hence population of points on the cross-plot. Next, each point on the cross-plot is colour-coded according to the polarity of the 4D seismic signature. The input 4D seismic data are in the form of a difference between maps for the monitor and baseline data. For the applications we have chosen for an oil-water system (i.e. no gas), pressure increase softens the reservoir and gives the opposite polarity to water saturation increase or reservoir hardening via pressure depletion. Finally, the PEM can be overlain on top of this cross-plot by recognizing the result of Alvarez and MacBeth (2013), who proposed a proxy for the PEM

$$\Delta A = C_S \Delta Sw - C_P \Delta P \quad (1)$$

where C_S and C_P the only two parameters required, and which provide the balance between the relative contributions of saturation (ΔS_w) and pore pressure (ΔP) change to the overall time-lapse seismic signature (ΔA). The PEM is now defined as a straight line $\Delta A = 0$ passing through the origin of the cross-plot with the gradient C_P/C_S. From (1) it can be immediately observed that the line is a boundary that divides the cluster of points into two groups with different polarities. In practice the coefficients C_P and C_S are obtained by a calibration exercise, and if several equally-likely models are used then several lines need to be drawn on this plot. Thus the points are divided by a wide sector rather than single sharp boundary. Uncertainty in the seismic data is expressed by a change in the polarity of the points, which in turn changes the relationship with the PEM boundary. An incorrect simulation model changes the positions of the points which also changes the relationship to the PEM. In both cases the mismatch may be easily visualized for future corrective action.

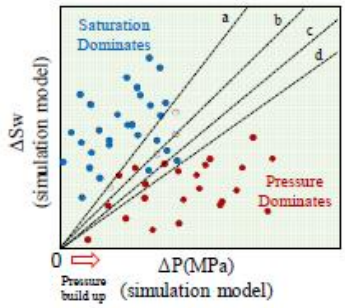

Figure 1 Schematic plot of ΔSw versus ΔP from the simulation model, colour coded based on the polarity of the 4D response and with a selection of PEMs "a" to "d" overlain as straight lines. A red point corresponds to pressure increase, whilst blue is for water saturation increase.

Synthetic Example

The cross-plot is firstly applied to a synthetic 4D seismic dataset generated from a North Sea field model. The ΔP-ΔS_w points are colour coded using the P-wave impedance, and are shown in Figure 2. Figure 2(a) gives the results for synthetic seismic calculated using a previously field-calibrated PEM A, and the boundary line relates to this model. Figure 2(b) gives the corresponding results for another model, PEM B. Both plots show a clear distinction and consistency between the two polarity groups.

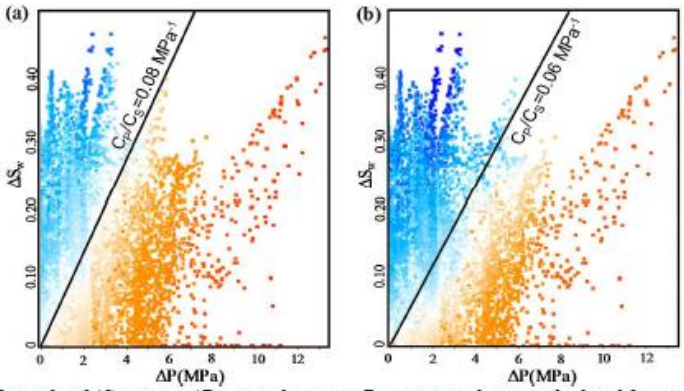

Figure 2 Example of ΔSw versus ΔP cross-plot, using P-wave impedances calculated from two different PEMS: (a) using the results from PEM A; (b) using the results from PEM B.

Observed Data Examples

The cross-plot is applied to two fields in the UKCS and Norwegian Sea with distinctly different geological settings. First of all, the ratio C_P/C_S for both fields are calculated using four different log calibrated deterministic PEMs (A, B, C and D) at baseline and monitor times following the work of Briceño et al. (2016). The ΔP-ΔS_w cross-plot points are then colour-coded using the mapped 4D seismic amplitudes for both fields. For the UKCS field the seismic attribute chosen is sum of negative amplitudes (SNA), and for the Norwegian Sea field is root mean square (RMS). On top of our plots, we display the four different boundaries C_P/C_S obtained from the deterministic PEMs since they give a range of variability, and set the limits that represent softening and hardening of the reservoir.

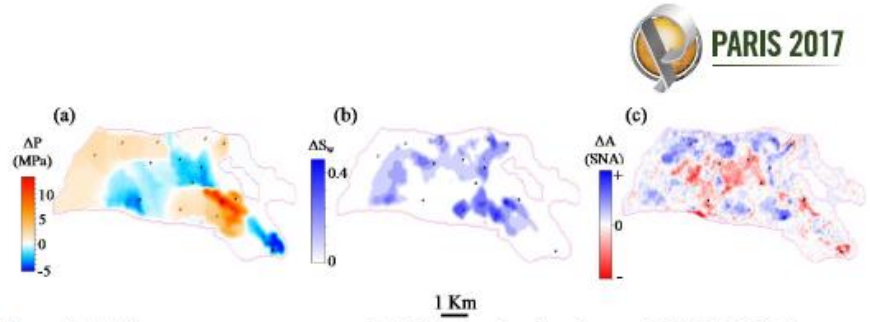

Figure 3 (a) Change in pore pressure map for 2004 minus baseline for our UKCS field. (b) Change in water saturation map. (c) 4D map using sum of negative amplitude attribute.

The plot for the UKCS field (Figure 4a) shows incorrect polarities (or wrong position) at the right top corner, meaning that decisions to update the model must be taken if the seismic data are accepted to be correct. Updating of the simulation model is performed by altering the transmissibility multipliers between geobodies in the areas of the model relating to the incorrect clusters of data. These effectively reduce the pressure change for that specific area. This updating is qualitative but can be guided carefully with the understanding PEM and seismic uncertainties in the cross-plot. Different scenarios for the simulation model are run, and here we show our most optimal model which provides the best all round agreement (Figure 4b).

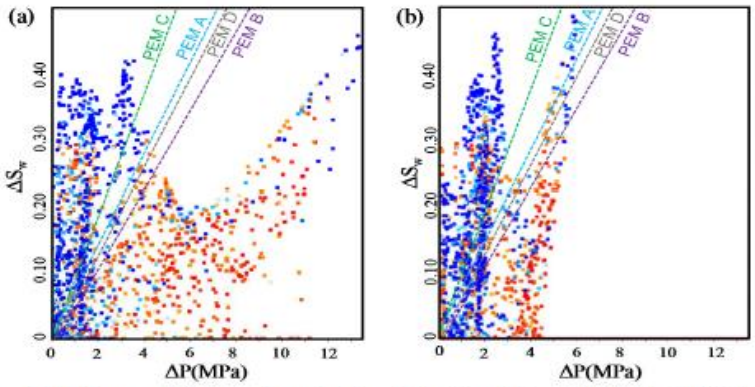

Figure 4 (a) ΔSw versus ΔP cross-plot using the original simulation model for the UKCS field and colour-coded with the polarities of observed 4D seismic response. (b) as in (a) but the points correspond to a more optimal simulation model after updates are performed.

The same approach is applied to the Norwegian Sea field, the ΔS_w versus ΔP plot (Figure 5a) shows clusters of points where there is a disagreement between the pressure and saturation regions. For this field, the updating of the simulation model is performed by altering fault transmissibility multipliers. Figure 5b shows our new cross-plot, this time using the updated simulation model, where the data points display a better position and agreement with the lines of C_P/C_S representing the boundary between the pressure and saturation domains.

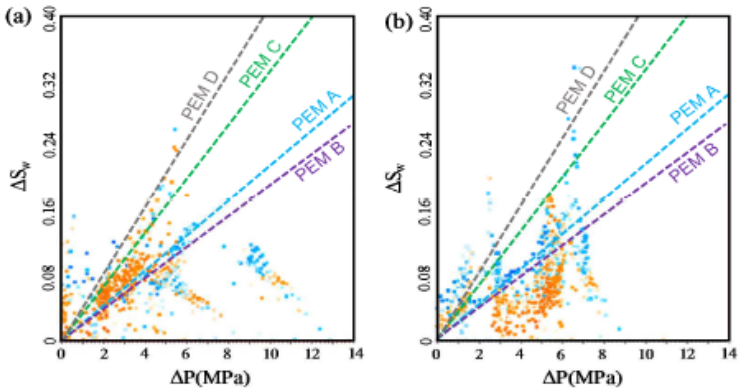

Figure 5 (a) ΔSw versus ΔP cross-plot using the original simulation model for the Norwegian Sea field and colour-coded with the polarities of the observed 4D seismic response. (b) as in (a) but the points correspond to the best simulation model after updates are performed.

Conclusions

The *ΔSw-ΔP* cross-plot is found to be a simple yet effective tool to simultaneously visualize the uncertainties associated with three different domains: the simulation model, the seismic data and the PEM. The plot allows us to discriminate between regions in the reservoir that are dominated by pressure or saturation change using a straight-line boundary corresponding to the selected PEM. A synthetic example has verified the usefulness of this approach, and the sensitivities to both data and the model. Application to two field datasets has confirmed the utility of the cross-plot as a way of guiding updating of the simulation model to agree with the observed seismic data. This interactive method is useful as a step prior to a full quantitative seismic history matching.

References

Alvarez E., and MacBeth C. [2013] An insightful parametrization for the flatlander's interpretation of time-lapse data. Geophysical Prospecting. **62**, 75-96.

Briceño A., MacBeth C. and M.D. Mangriotis. [2016] Towards an effective petroelastic model for simulator to seismic studies. *78th EAGE Conference and Exhibition*, Extended Abstracts, Th LHR2 08.

Gosselin O. Aanonsen S.I., Aavastmark I., Cominelli A., Gonard R., Kolasinski M., Ferdinandi F., Kovacic L., and Neylon K. [2003] History matching using Time-lapse Seismic (HUTS). SPE 84464. *SPE Annual Technical Conference and Exhibition*. Denver, Colorado, USA. DOI: 10.2118/84464-MS.

Roggero F., Ding D.Y., Berthet P., Lerat O., and Schreiber P.E. [2007] Matching of Production History and 4D Seismic Data – Application to the Girassol Field, Offshore Angola. SPE 109929. *SPE Annual Technical Conference and Exhibition*. Anaheim, California, USA. DOI: 10.2118/109929-MS.

Walker, G., Allan, P., Trythall, R., Parr, R., Marsh, M., Kjelstadli, R., Barkved, O., Johnson, D. and Lane, S. [2006] Three case studies of progress in quantitative seismic-engineering integration. *The Leading Edge*, **25** (9), 1161-1166.

Appendix B: log fitting results

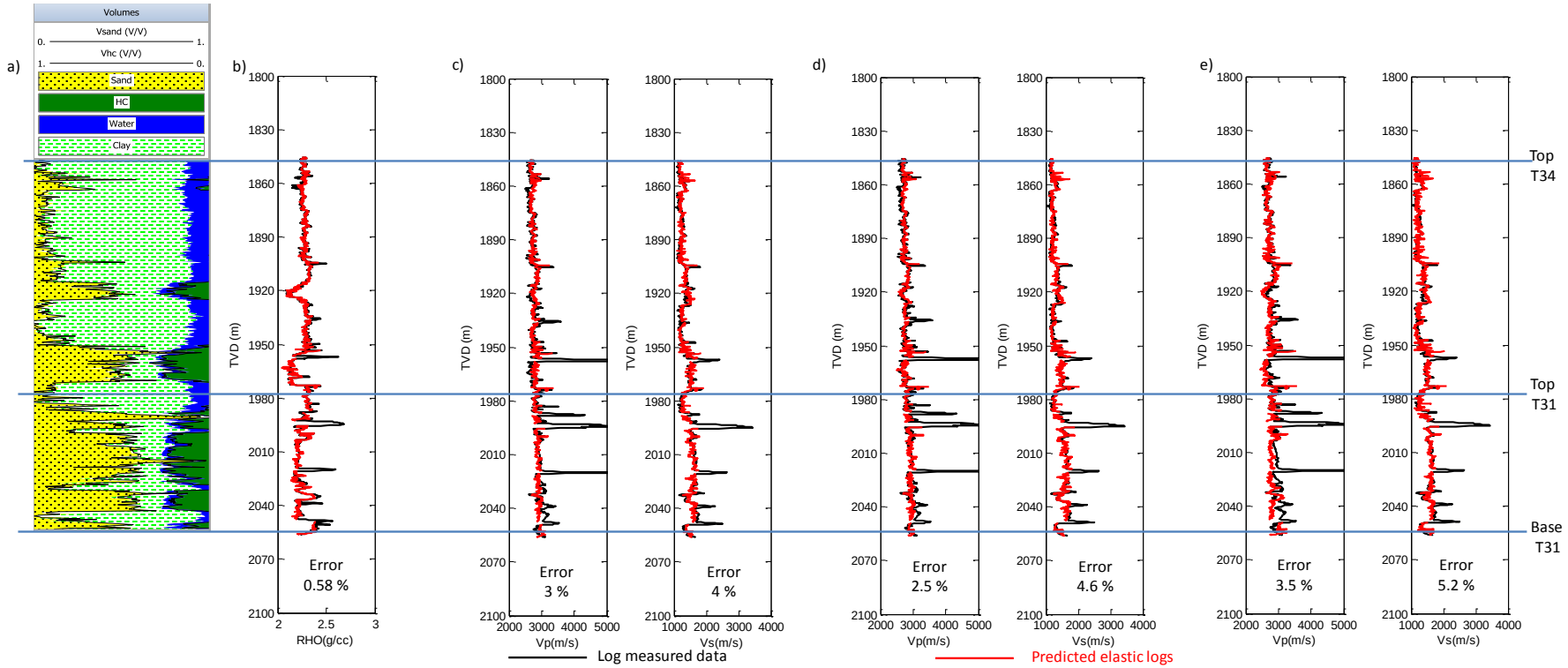

Figure B.1 *(a) sand/shale model from petrophysics analysis in well A1 (figure 4.3a). (b) Density fit which is invariable for all PEMs. (c) Mixing before fluid substitution PEM B fit to the velocity logs for the T34 and T31 reservoirs (A1, table 4.6) of the Schiehallion field, (d) as in (c) but fit based on PEM C and (e) as in (c) but fit based on PEM D (A1, table 4.7).*

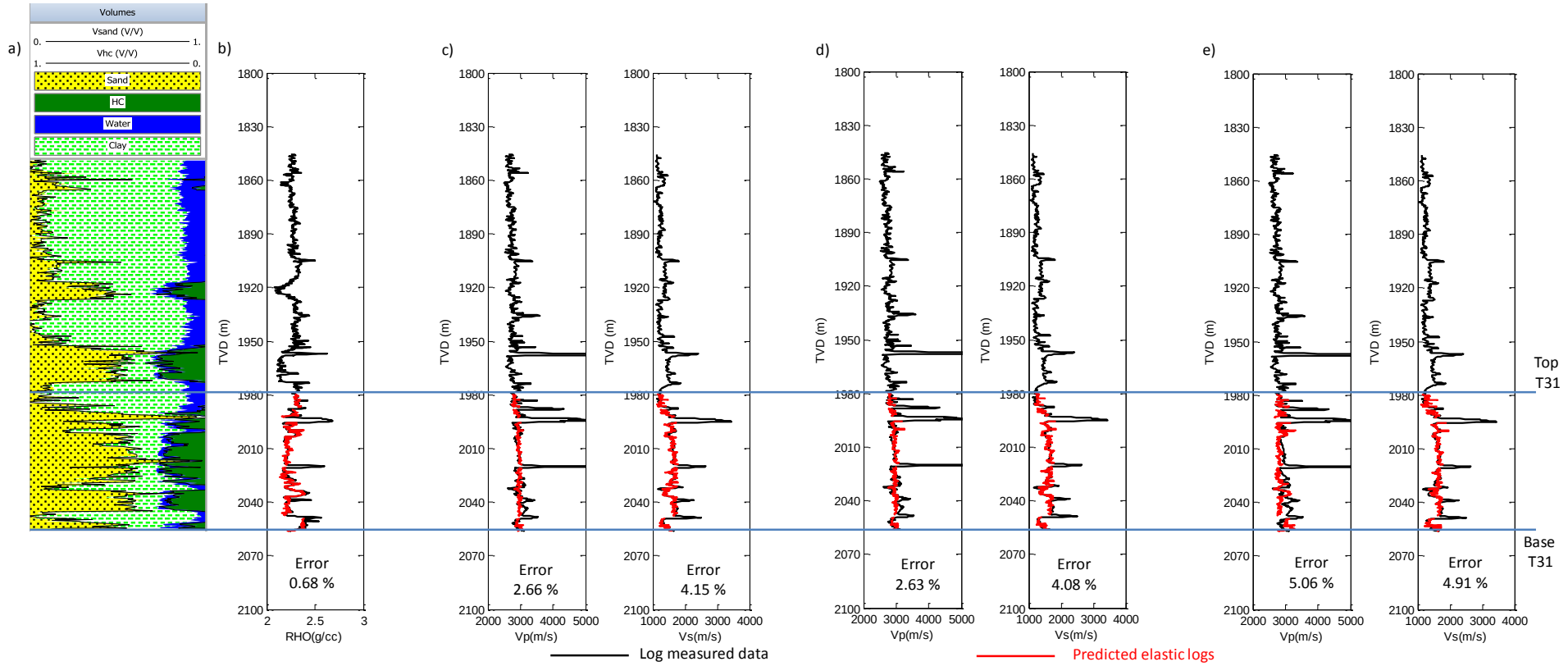

Figure B.2 *(a) sand/shale model from petrophysics analysis in well A1 from Schiehallion field (figure 4.3a). (b) Density fit which is invariable for all PEMs. (c) Mixing before fluid substitution PEM A fit to the velocity logs for the T31 reservoir ($A1_{low}$, Table 4.4); (d) as in (c) but fit based on PEM C ($A1_{low}$, Table 4.6) and (e) as in (c) but fit based on PEM D ($A1_{low}$, Table 4.7).*

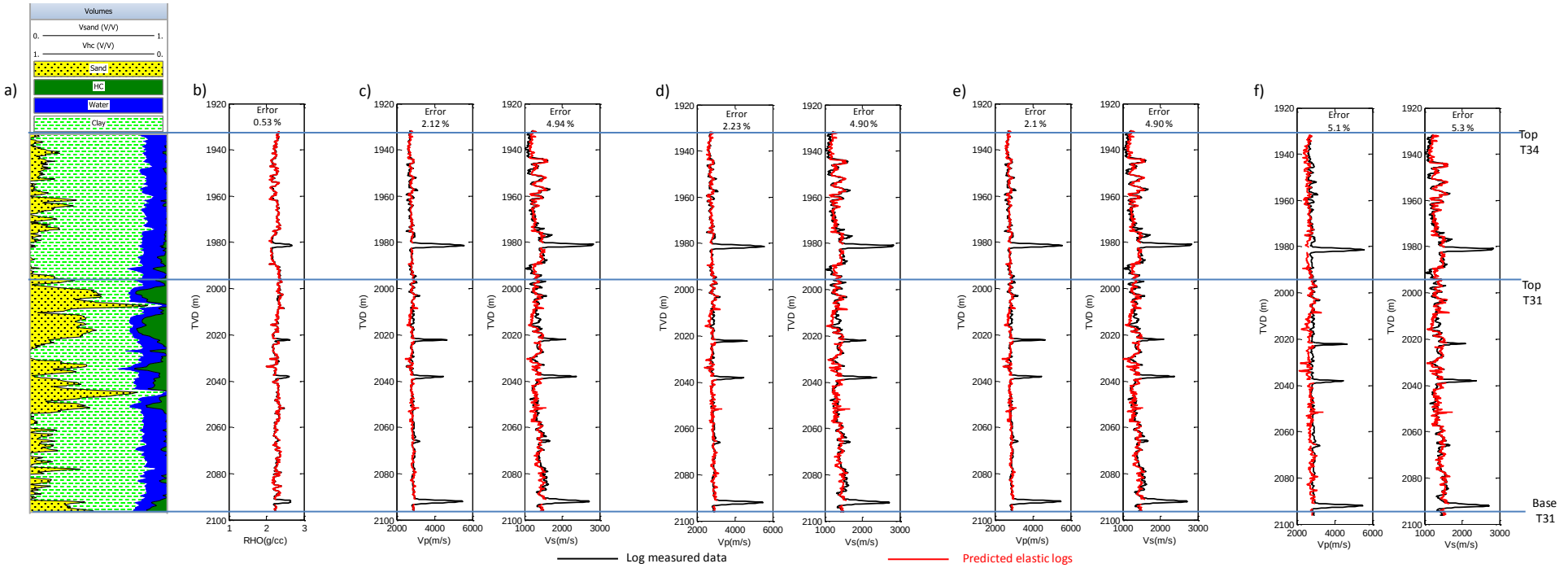

Figure B.3 *(a) sand/shale model from petrophysics analysis in well A2 from Schiehallion field (figure 4.3a). (b) Density fit which is invariable for all PEMs. (c) Mixing before fluid substitution PEM A fit to the velocity logs for the T34 and T31 reservoirs (A2, Table 4.4); (d) as in (c) but fit based on PEM B (A2, Table 4.5); (e) as in (c) but fit based on PEM C (A2, Table 4.6); and (f) as in (c) but fit based on PEM D (A2, Table 4.7).*

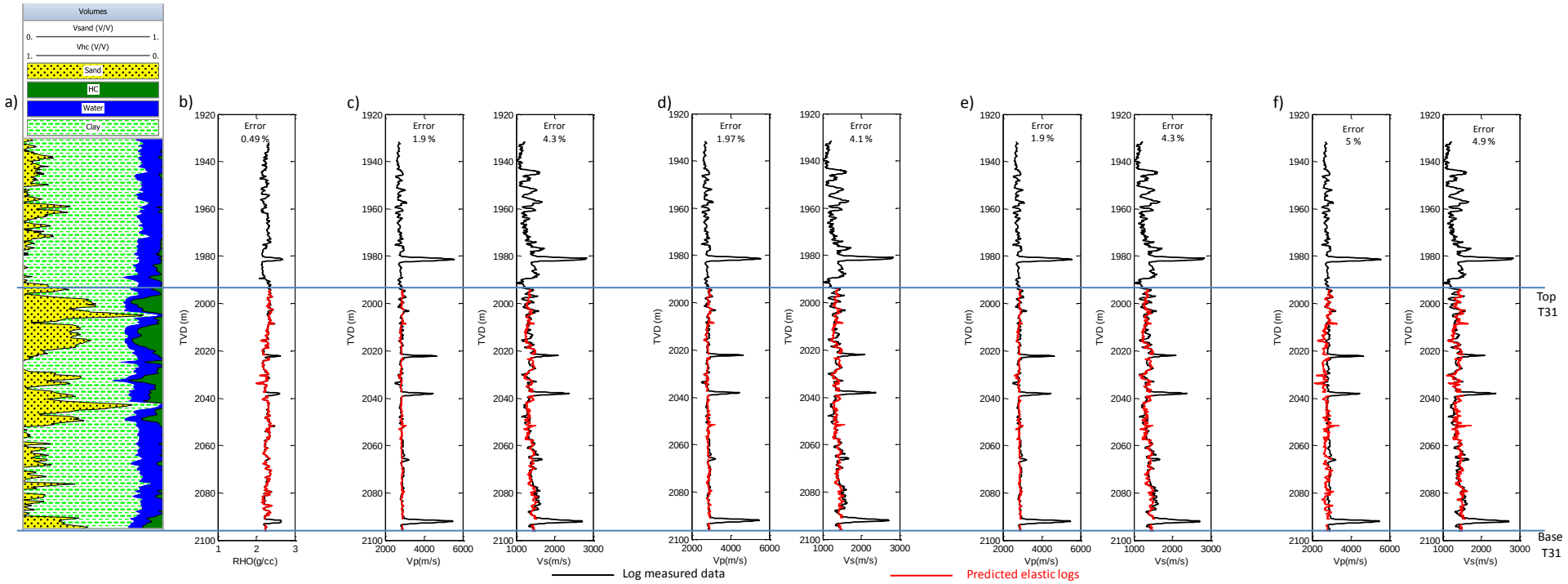

Figure B.4 *(a) sand/shale model from petrophysics analysis in well A2 from Schiehallion field (figure 4.3a). (b) Density fit which is invariable for all PEMs. (c) Mixing before fluid substitution PEM A fit to the velocity logs for the T31 reservoir ($A2_{low}$, Table 4.4), (d) as in (c) but fit based on PEM B ($A2_{low}$, Table 4.5); (e) as in (c) but fit based on PEM C ($A2_{low}$, Table 4.6) and (f) as in (c) but fit based on PEM D ($A2_{low}$, Table 4.7).*

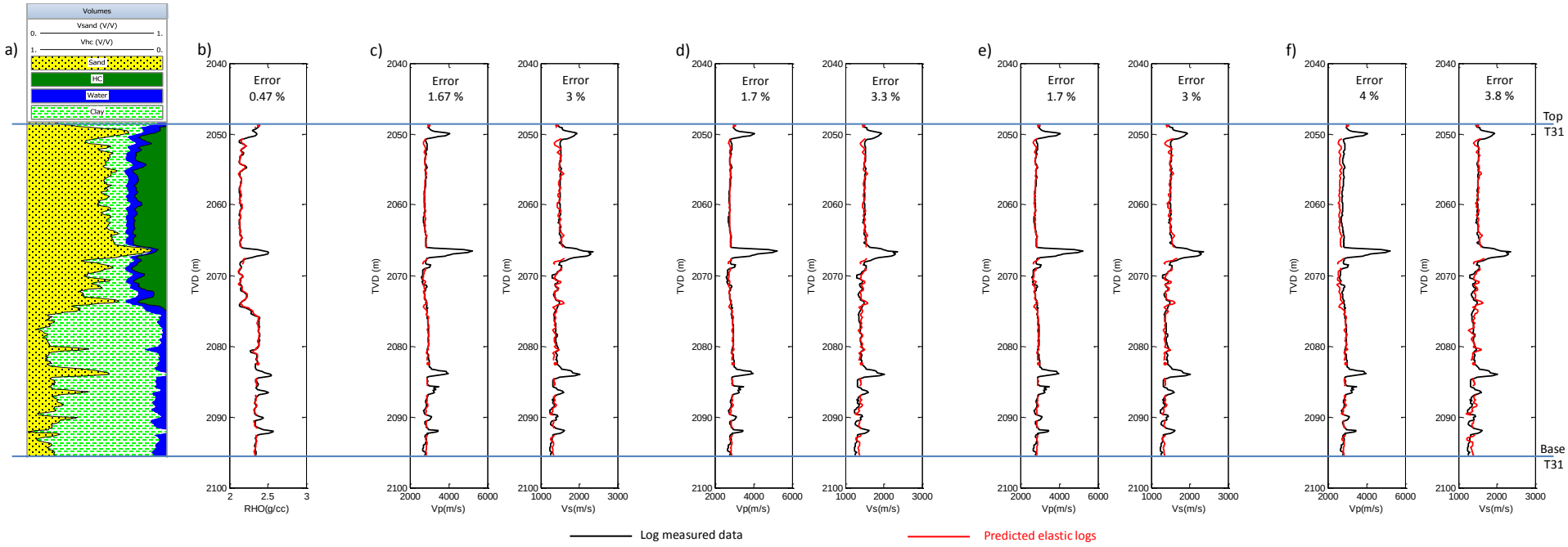

Figure B.5 (*a) sand/shale model from petrophysics analysis in well I1 from Schiehallion field (figure 4.3a). (b) Density fit which is invariable for all PEMs. (c) Mixing before fluid substitution PEM A fit to the velocity logs for the T31 reservoir (I1, Table 4.4); (d) as in (c) but fit based on PEM B (I1, Table 4.5); (e) as in (c) but fit based on PEM C (I1, Table 4.6) and (f) as in (c) but fit based on PEM D (I1, Table 4.7).*

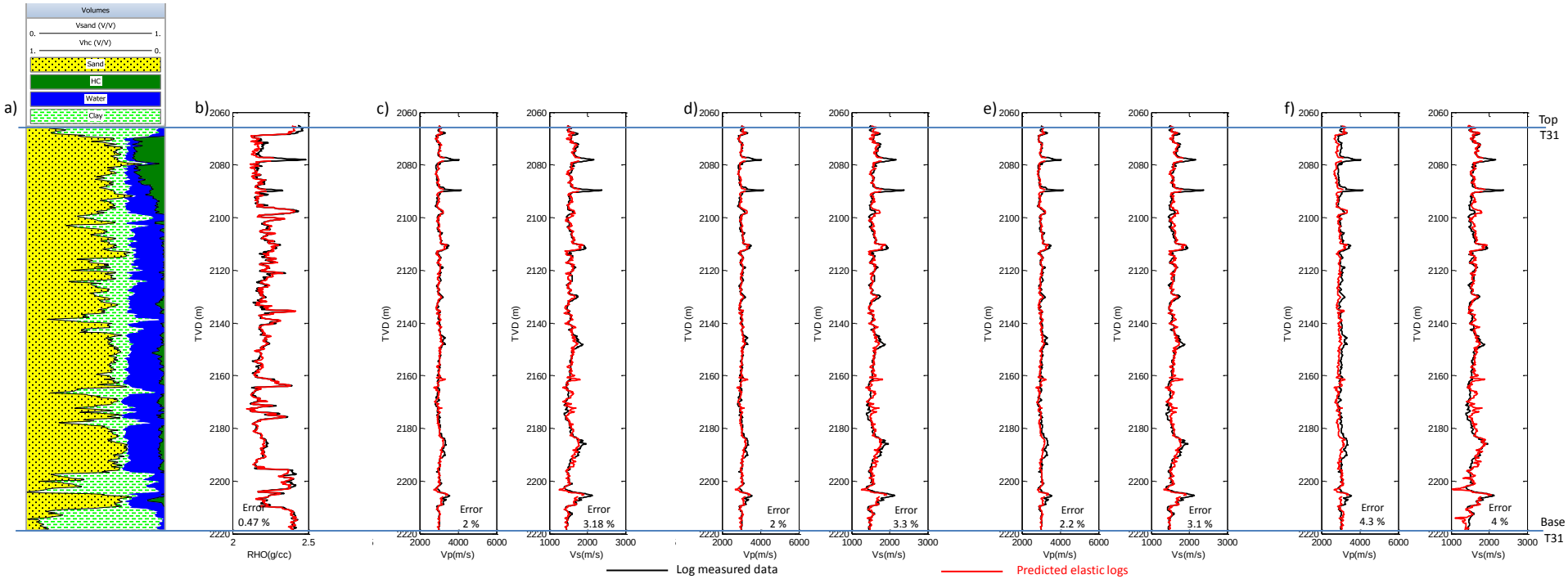

Figure B.6 *(a) sand/shale model from petrophysics analysis in well I2 from Schiehallion field (figure 4.3a). (b) Density fit which is invariable for all PEMs. (c) Mixing before fluid substitution PEM A fit to the velocity logs for the T31 reservoir (I2, Table 4.4); (d) as in (c) but fit based on PEM B (I2, Table 4.5); (e) as in (c) but fit based on PEM C (I2, Table 4.6)and (f) as in (c) but fit based on PEM D (I2, Table 4.7).*

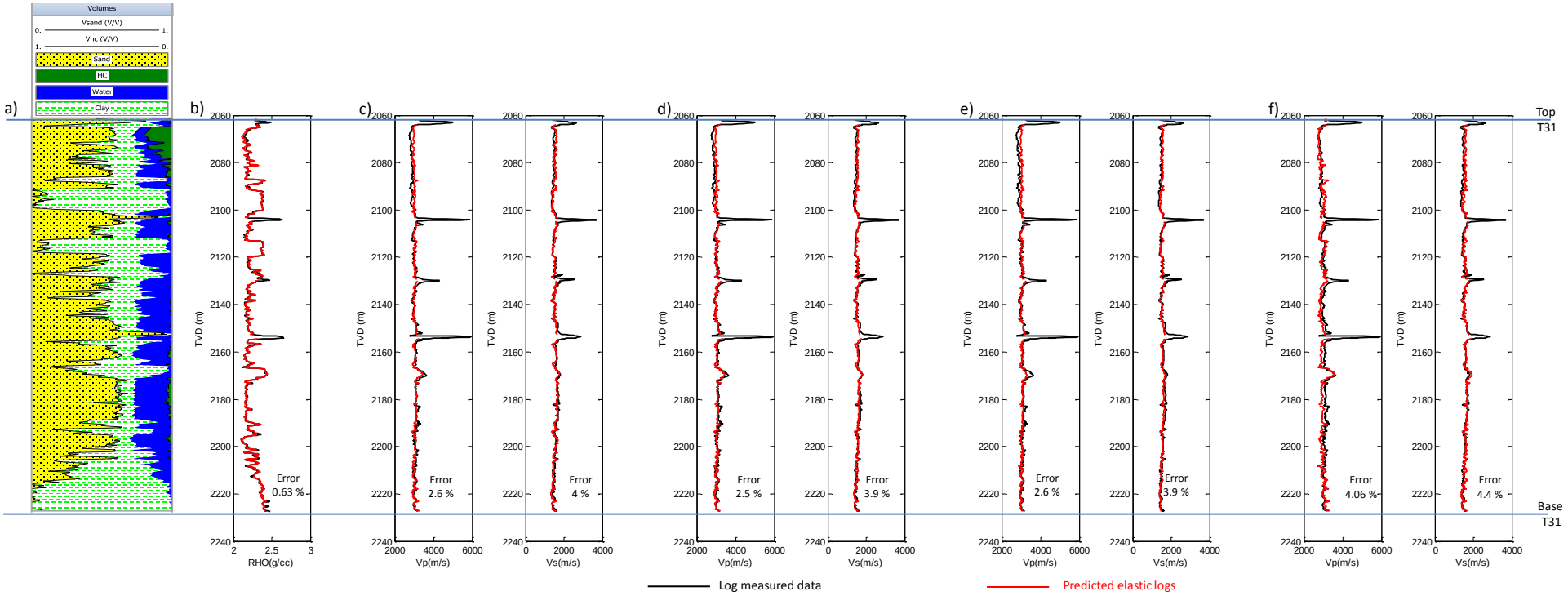

Figure B.7 *(a) sand/shale model from petrophysics analysis in well I3 from Schiehallion field (figure 4.3a). (b) Density fit which is invariable for all PEMs. (c) Mixing before fluid substitution PEM A fit to the velocity logs for the T31 reservoir (I3, Table 4.4); (d) as in (c) but fit based on PEM B (I3, Table 4.5); (e) as in (c) but fit based on PEM C (I3, Table 4.6) and (f) as in (c) but fit based on PEM D (I3, Table 4.7).*

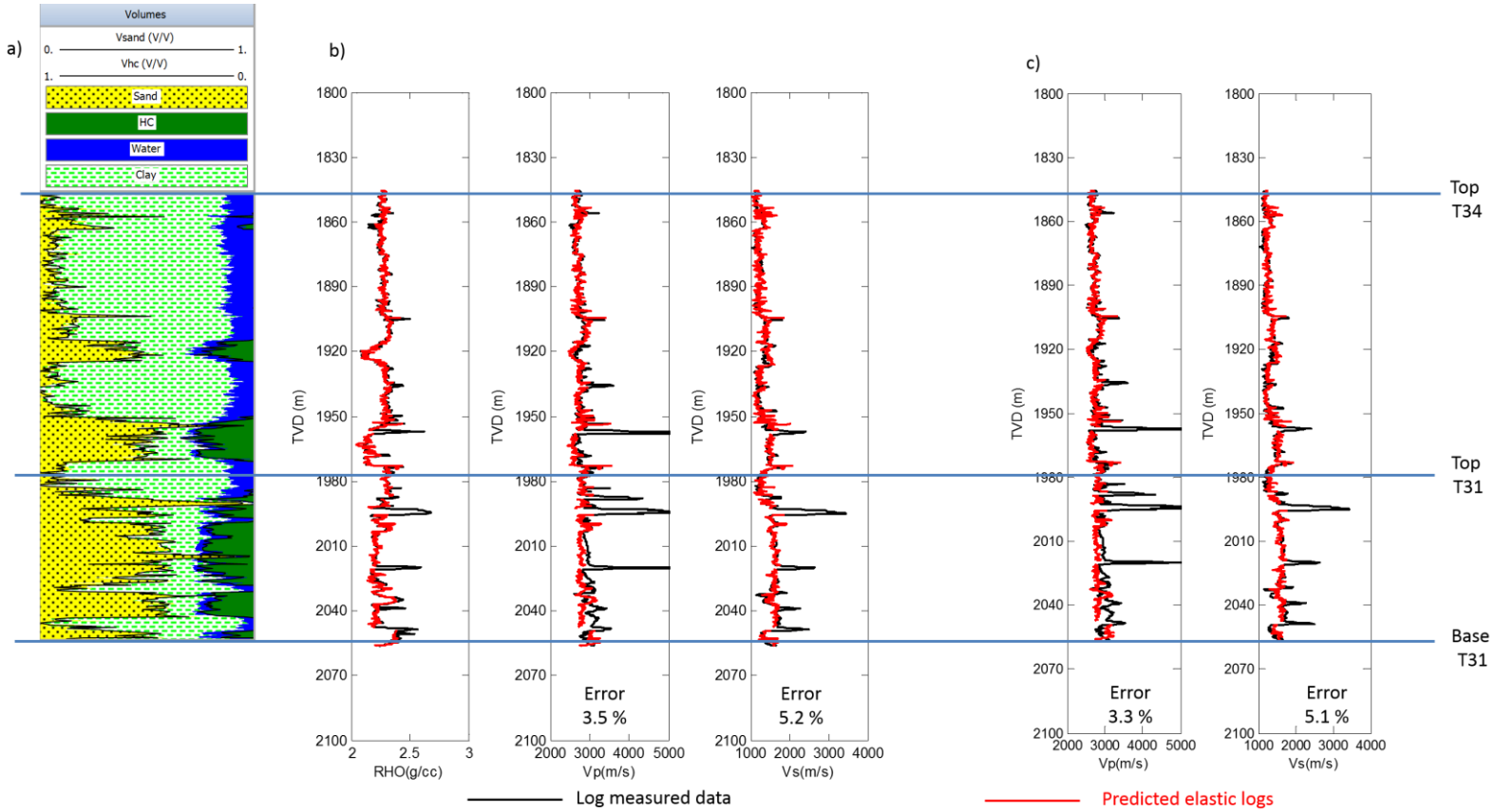

Figure B.8 *(a) sand/shale model from petrophysics analysis in well A1 (figure 4.3a). (b) Mixing before fluid substitution PEM D fit to the velocity logs for the T34 and T31 reservoirs of the Schiehallion field using a constant coordination number (c) and in (b) but using a simple linear regression for coordination number (a+bϕ) where a and b are constant obtained from log data.*

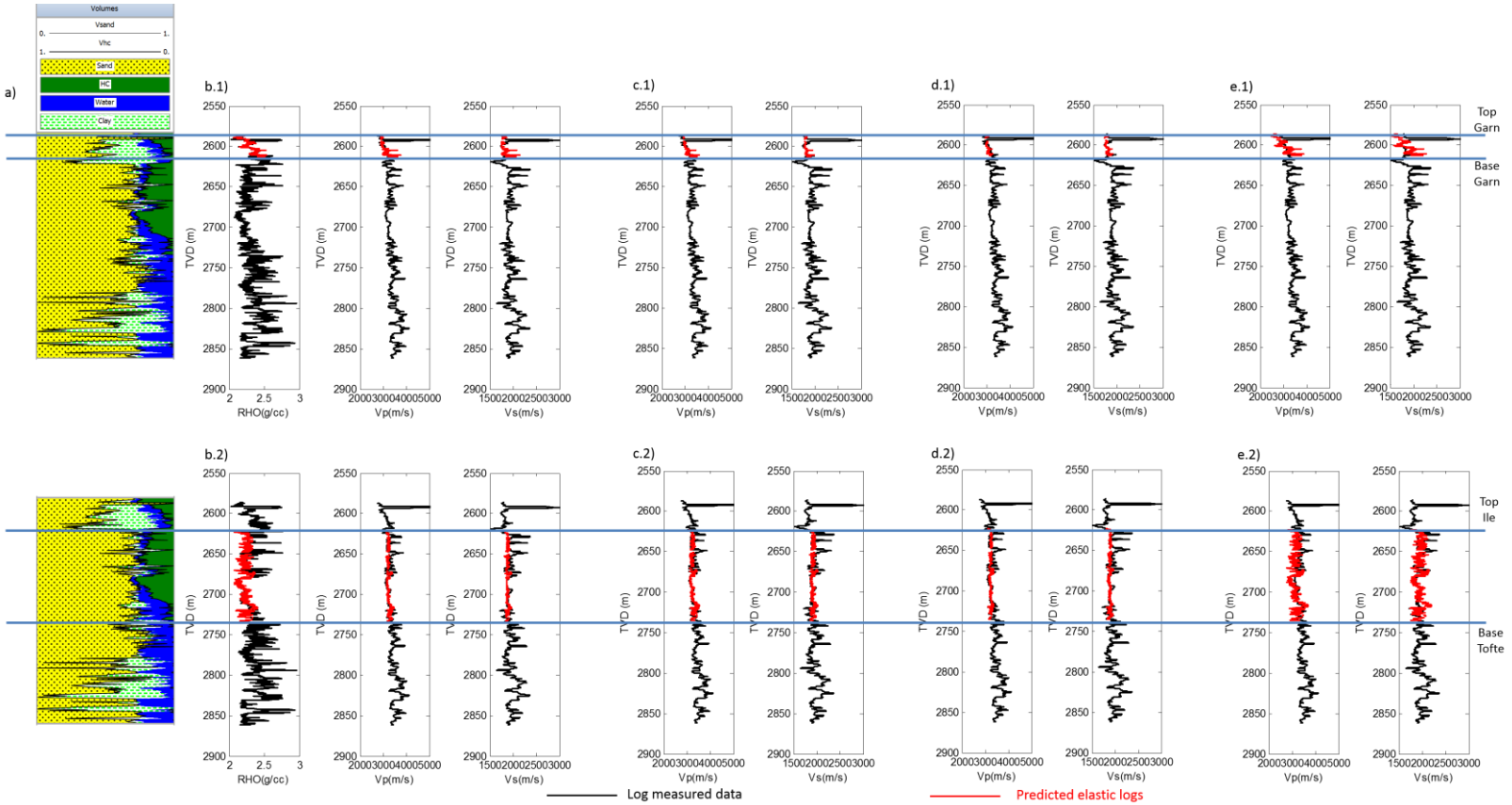

Figure B.9 *(a) sand/shale model from petrophysics analysis in well I2 from Norne field (figure 4.3b). (b.1) Mixing before fluid substitution PEM A fit to the density and velocity logs for only the top sand (Garn formation) (I2, Table 4.8); (b.2) Mixing before fluid substitution PEM A fit to the density and velocity logs for the second and third sands (Ile and Tofte formation) (I2, Table 4.8); (c.1) and (c.2) as in (b.1) and (b.2) respectively but fit based on PEM B (I2, Table 4.9); (d.1) and (d.2) as in (b.1) and (b.2) respectively but fit based on PEM C (I2, Table 4.10); (e.1) and (e.2) as in (b.1) and (b.2) respectively but fit based on PEM D (I2, Table 4.11).*

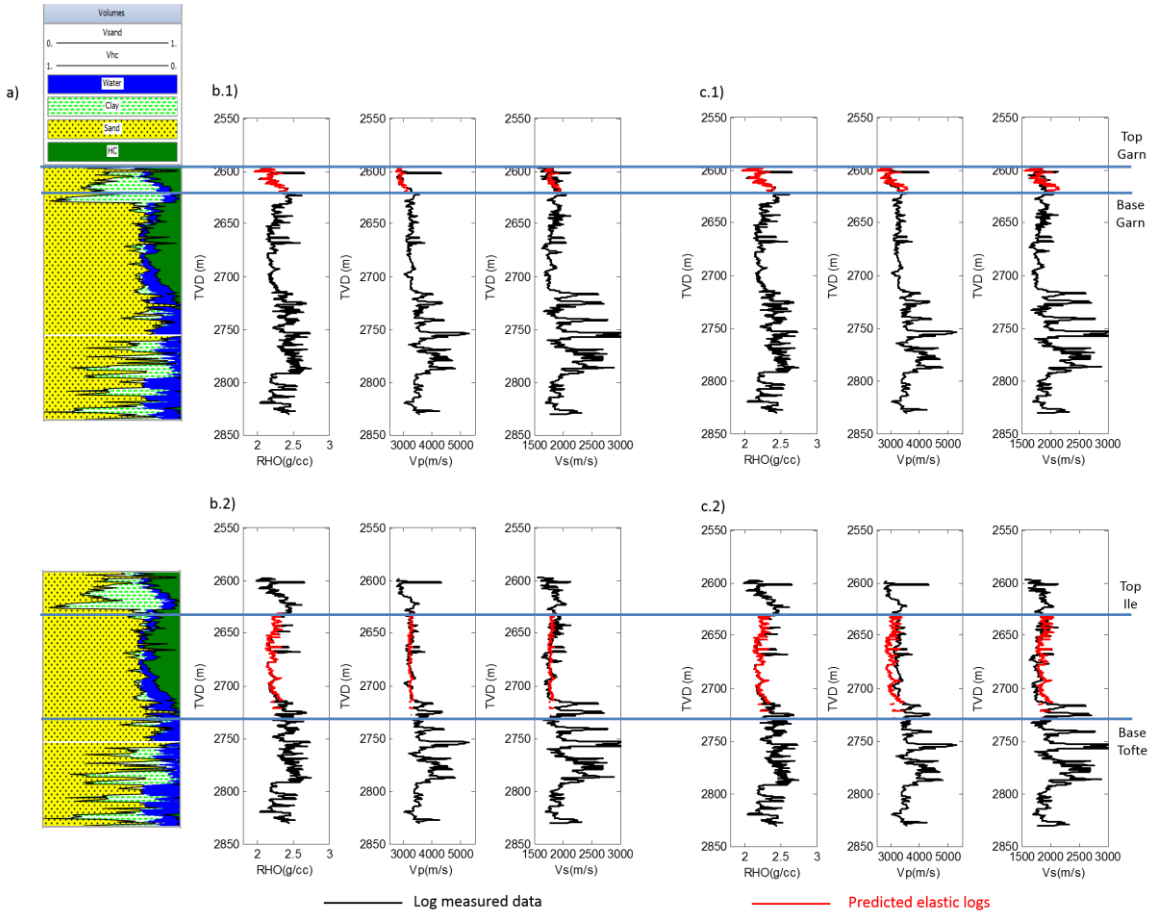

Figure B.10 *(a) sand/shale model from petrophysics analysis in well I1 from Norne field (figure 4.3b). (b.1) Mixing before fluid substitution PEM C fit to the density and velocity logs for only the top sand (Garn formation) (I1, Table 4.10); (b.2) Mixing before fluid substitution PEM C fit to the density and velocity logs for the second and third sands (Ile and Tofte formation) (I1, Table 4.10); (c.1) and (c.2) as in (b.1) and (b.2) respectively but fit based on PEM D (I1, Table 4.11).*

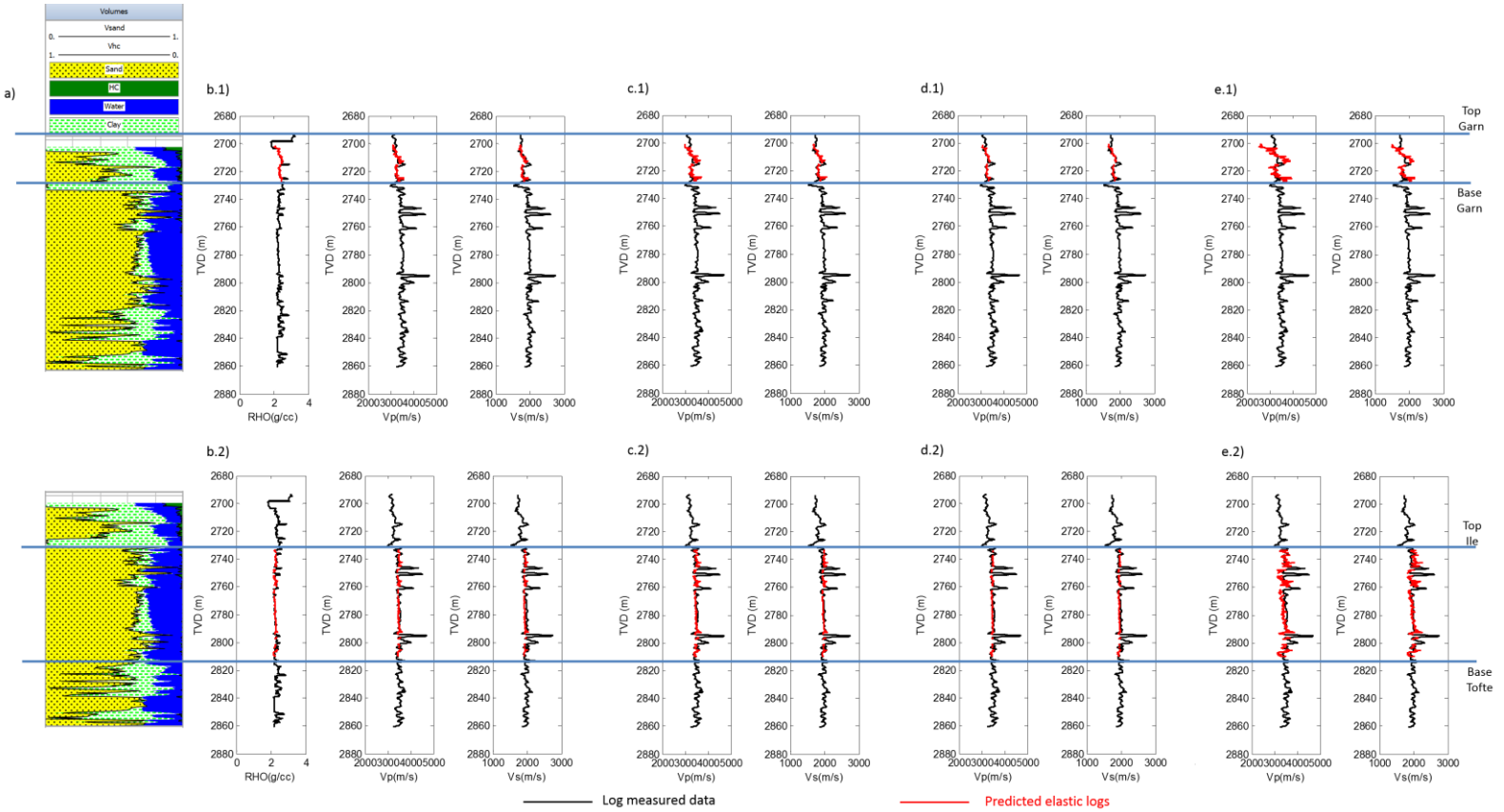

Figure B.11 *(a) sand/shale model from petrophysics analysis in well I3 from Norne field (figure 4.3b). (b.1) Mixing before fluid substitution PEM A fit to the density and velocity logs for only the top sand (Garn formation) (I3, Table 4.8); (b.2) Mixing before fluid substitution PEM A fit to the density and velocity logs for the second and third sands (Ile and Tofte formation) (I3, Table 4.8); (c.1) and (c.2) as in (b.1) and (b.2) respectively but fit based on PEM B(I3, Table 4.9); (d.1) and (d.2) as in (b.1) and (b.2) respectively but fit based on PEM C (I3, Table 4.10); (e.1) and (e.2) as in (b.1) and (b.2) respectively but fit based on PEM D (I3, Table 4.11).*

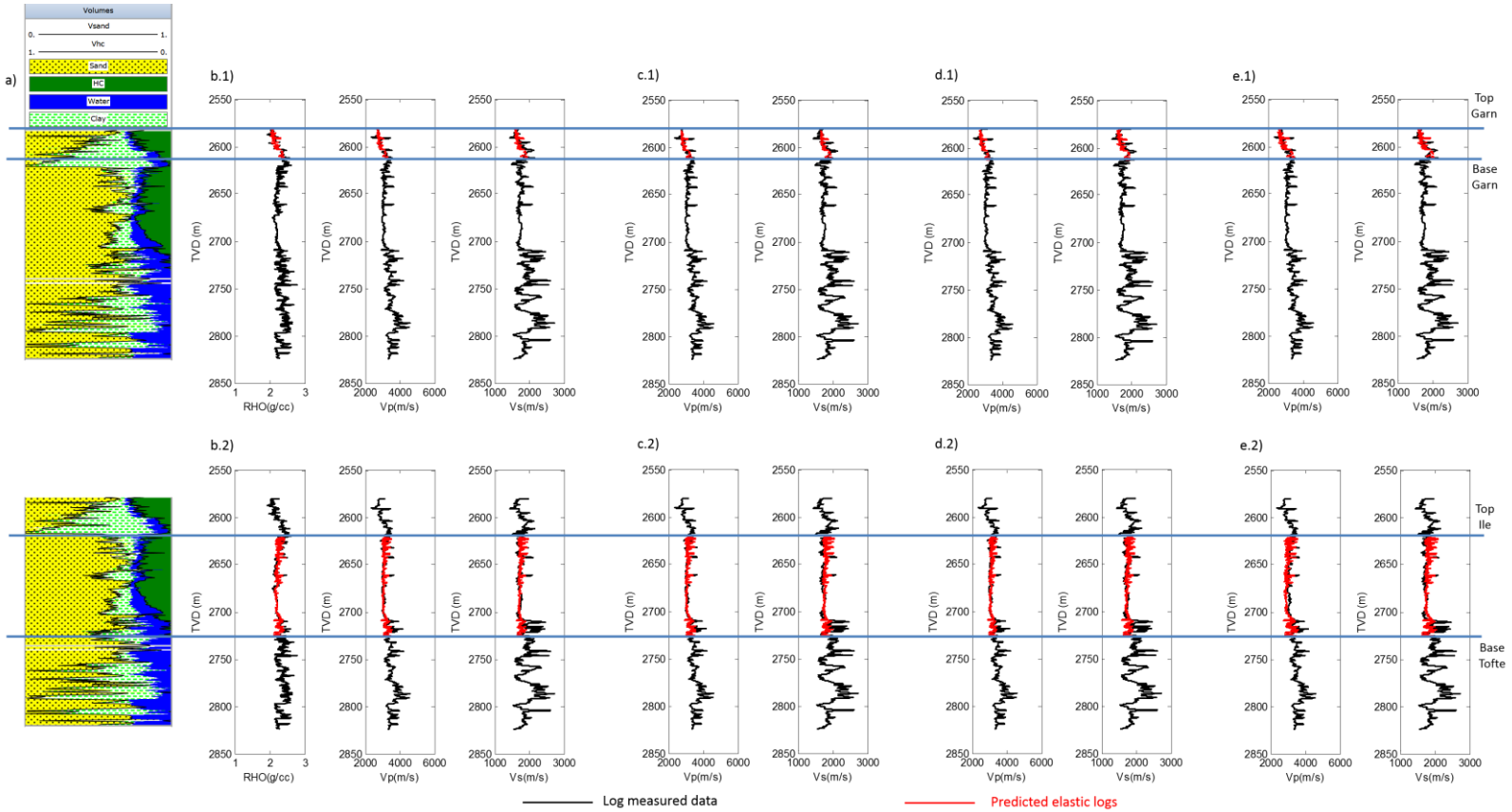

Figure B.12 *(a) sand/shale model from petrophysics analysis in well P1 from Norne field (figure 4.3b). (b.1) Mixing before fluid substitution PEM A fit to the density and velocity logs for only the top sand (Garn formation) (P1, Table 4.8); (b.2) Mixing before fluid substitution PEM A fit to the density and velocity logs for the second and third sands (Ile and Tofte formation) (P1, Table 4.8); (c.1) and (c.2) as in (b.1) and (b.2) respectively but fit based on PEM B (P1, Table 4.9); (d.1) and (d.2) as in (b.1) and (b.2) respectively but fit based on PEM C (P1, Table 4.10); (e.1) and (e.2) as in (b.1) and (b.2) respectively but fit based on PEM D (P1, Table 4.11)*

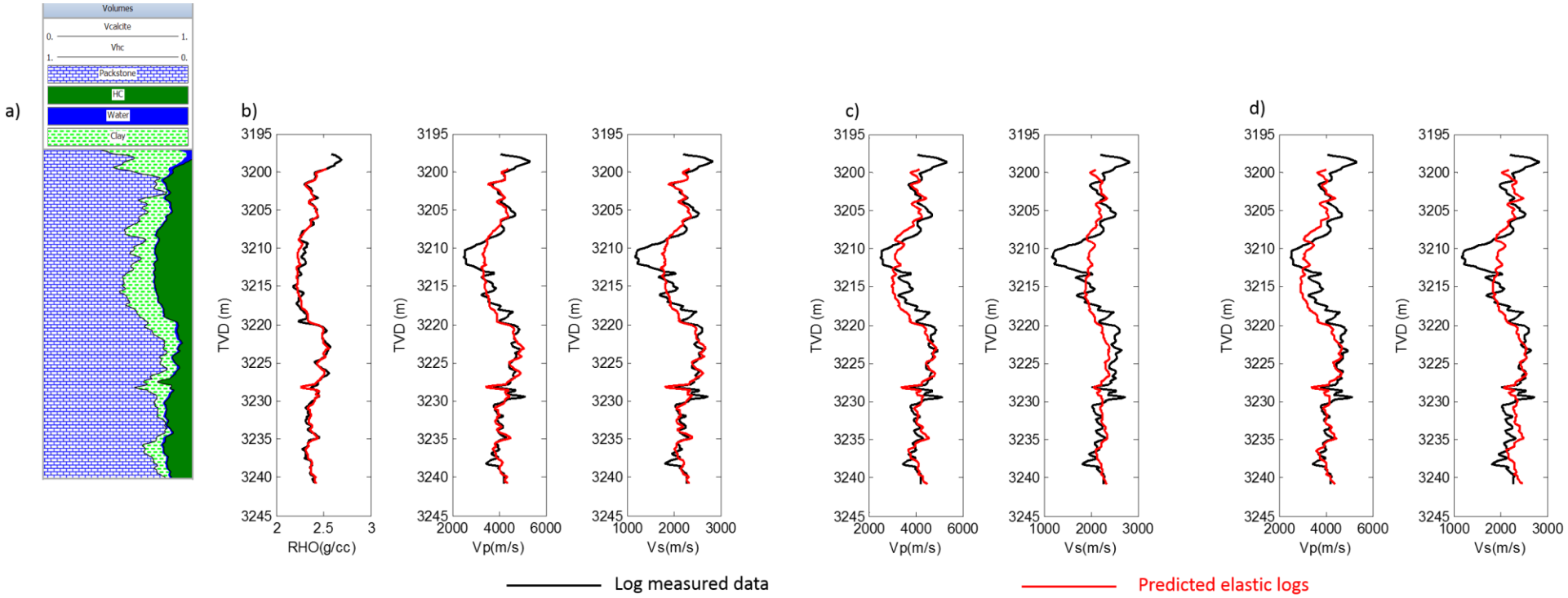

Figure B.13 *(a) calcite/shale model from petrophysics analysis in well I3 from carbonate Field X (figure 4.3c). (b) Mixing before fluid substitution PEM E fit to the density and velocity logs for the entire log segment (I3, Table 4.12); (c) as in (b) but fit based on PEM F using only spheres shape inclusions (I3, Table 4.13); and (d) as in (b) but fit based on PEM F using only needles shape inclusions (I3, Table 4.13)*

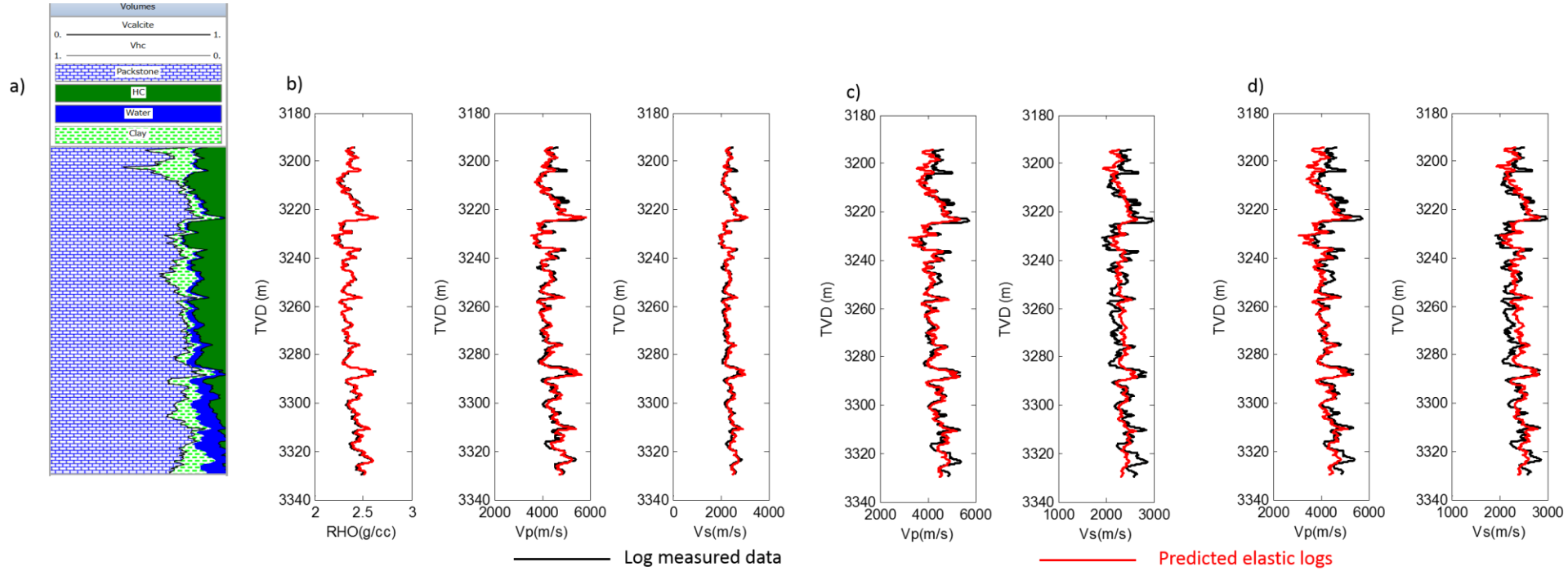

Figure B.14 *(a) calcite/shale model from petrophysics analysis in well I1 from carbonate Field X (figure 4.3c). (b) Mixing before fluid substitution PEM E fit to the density and velocity logs for the entire log segment (I1, Table 4.12); (c) as in (b) but fit based on PEM F using only spheres shape inclusions (I1, Table 4.13); and (d) as in (b) but fit based on PEM F using only needles shape inclusions (I1, Table 4.13)*

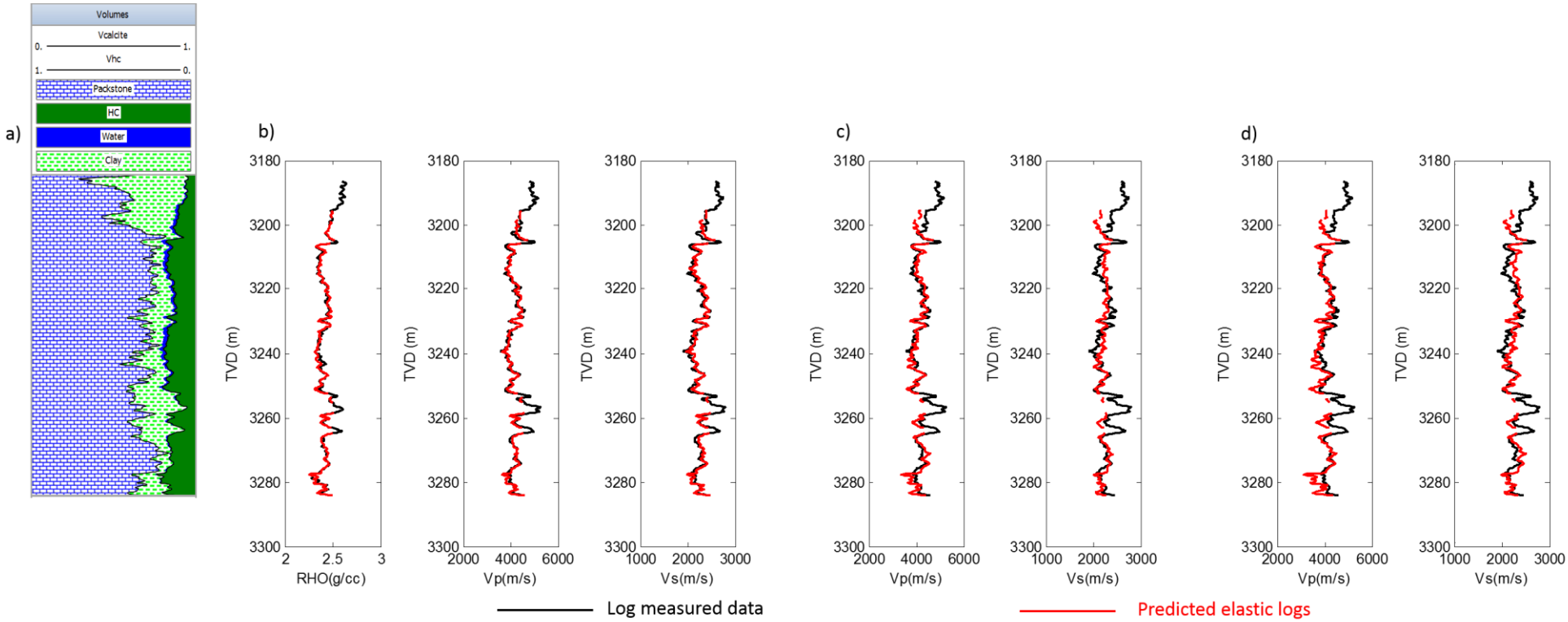

Figure B.15 *(a) calcite/shale model from petrophysics analysis in well P2 from carbonate Field X (figure 4.3c). (b) Mixing before fluid substitution PEM E fit to the density and velocity logs for the entire log segment (P2, Table 4.12); (c) as in (b) but fit based on PEM F using only spheres shape inclusions (P2, Table 4.13); and (d) as in (b) but fit based on PEM F using only needles shape inclusions (P2, Table 4.13)*

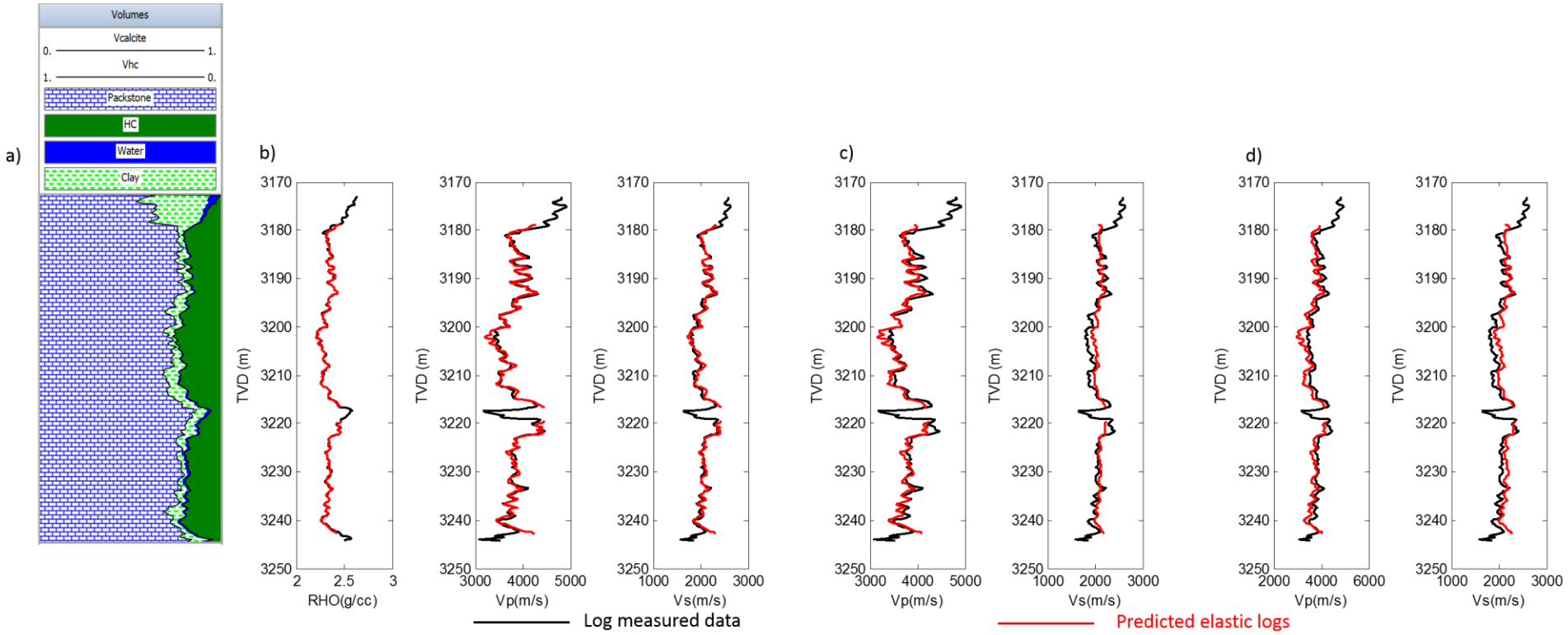

Figure B.16 *(a) calcite/shale model from petrophysics analysis in well P1 from carbonate Field X (figure 4.3c). (b) Mixing before fluid substitution PEM E fit to the density and velocity logs for the entire log segment (P1, Table 4.12); (c) as in (b) but fit based on PEM F using only spheres shape inclusions (P1, Table 4.13); and (d) as in (b) but fit based on PEM F using only needles shape inclusions (P1, Table 4.13)*

References

Aarre V. [2006] Estimating 4D velocity changes and contact movement on the Norne Field. *SEG Thecnical Program*. Expanded Abstracts. 3115-3119

Adam L., Batzle M., and Brevik I. [2006] Gassmann's fluid substitution and shear modulus variability in carbonates at laboratory seismic and ultrasonic frequencies. *Geophysics*, **71**, F173-F183.

Aleardi M., and Ciabarri F. [2017] Assessment of different approaches to rock-physics modelling: a case study from offshore Nile Delta. *Geophysics*, **82** (1), MR15-MR25.

Alerini M., Ayzenberg M., Feng T., Hustoft L., Lie E., Liu S., Skjei N., and Skjervheim J.A. [2014] Utilization of Time-lapse seismic for reservoir model conditioning. *76th EAGE Conference and Exhibition*, Extended Abstracts, We G102 10.

Alfred D., Atan S., Hamman J.G., Caldwell D.H. [2008] Petro-Elastic Models: How Many and at What Scale? *70th EAGE Conference and Exhibition*, Expanded Abstracts, SPE 11354.

Ali A., Taggart I., Mee B., Smith M., Gerhardt A., and Bourdon L. [2008] Integrating 4D seismic data with production related effects at Enfliield, North West Shelf, Australia. SPE 116916. *SPE Asia Pacific Oil & Gas Conference and Exhibition*. Perth, Australia

Allan P., Fowler S., Hill C., MacDonal C. and Campbell S. [2011] A decade of west of Shetland 4D seismic- The power of consistency, DEVEX conference.

Alvarez E. [2014] Petroelastic approximations for quantitative 4D seismic interpretations. *PhD Thesis*. Heriot Watt University.

Alvarez E., and MacBeth C. [2013] An insightful parametrization for the flatlander's interpretation of time-lapse data. Geophysical Prospecting. **62**, 75-96.

Amini H. [2014] A Pragmatic Approach to Simulator to Seismic Modelling for 4D Seismic Interpretation. *PhD Thesis*. Heriot Watt University.

Amini H., and Alvarez E. [2014] Calibration of the Petro-Elastic Model (PEM) for 4D seismic studies in multimineral rocks. *EAGE/FESM Joint Regional Conference Petrophysics meets Geoscience*. Kuala Lumpur, Malaysia.

Anderson J. K. [1999] The capabilities and challenges of the seismic method in chalk exploration. In: Fleet, A. J. & Boldy, S.A. R. (eds), Petroleum Geology of Northwest Europe. *5th Conference Geological Society*. London UK.

Askim O. J. [2003] Seismic forward modeling in a chalk reservoir with permanent monitoring. *65th EAGE Conference and Exhibition*. Extended Abstracts, A-16.

Assefa S., McCann C., and Sothcott J. [2003] Velocity of compressional and shear waves in limestones. *Geophysical Prospecting*, **51**, 1-13.

Avseth P., Mukerji T., and Mavko G. [2005] Quantitative Seismic Interpretation. Cambridge University Press

Avseth P., and Skjei N. [2011] Rock physics modeling of static and dynamic reservoir properties—a heuristic approach for cemented sandstone reservoirs. *The Leading Edge*, **30**(1), 90-96.

Ayzenberg M., Hustoft L., Skjei N. and Feng T. [2013] Seismic 4D inversion for quantitative use in automated History Matching. *75th EAGE Conference and Exhibition*, Expanded Abstracts, Tu 10 02.

Backus G. R. [1962] Long-wave elastic anisotropy produced by horizontal layering. *J. Geophysical Research*, **67** (11), 4427-4440.

Baechle G. T., Weger R. J., Eberli G. P., Massaferro J. L., and Sun Y-F. [2005] Changes of shear moduli in carbonate rocks: implications for Gassmann applicability. *The Leading Edge*, **24**, 507-510.

Bahkta T., Landrø M. [2013] Comparison of different rock physics model for chalk reservoir. *10th Biennial International Conference and Exposition*. Kochi 2013.

Barret-Crosdill B. [2015] An investigation into the seismic response of gassy marine sediments: a synthetic model study. Bangor University, Wales, UK.

Batzle M. and Wang Z. [1992] Seismic properties of pore fluids. *Geophysics* **57**, 1396-1408

Berryman J. G. [1980b] Long-wavelength propagation in composite elastic media. *J. Acoust. Soc. Am.*, **69**, 1809-1831.

Berryman J. G. [1992a] Effective stress for transport properties of inhomogeneous porous rock. *J. Geophys. Res.*, **97**, 17409 – 17424.

Berryman J. G., and Milton G. W. [1991] Exact results for generalized Gassmann's equation in composite porous media with two constituents. *Geophysics*, **56**, 1950-1960

Bogan C., Johnson D., Litvak M., and Stauber D. [2003] Building reservoir models based on 4D seismic & well data in Gulf of Mexico oil fields. SPE 84370 presented at the SPE Annual Technical Conference and Exhibition.

Bornard R., Allo F., Coleou T., Freudenreich Y., Caldwell D. H., and Hamman J. G. [2005] Petrophysical seismic inversion to determine more accurate and precise reservoir properties. SPE 94144. *SPE Europec/EAGE Annual Conference*. Madrid, Spain.

Brown R., and Korringa J. [1975] On the dependence of the elastic properties of a porous rock on the compressibility of the pore fluid. *Geophysics*, **40**, 608-616.

Carozzi A.V., and Falkenhein F.U.H. [1985] Depositional and diagenetic evolution of Cretaceous oncolytic packstone reservoirs, Macaé Formation, Campos Basin, offshore Brazil, in Roehl, P.O., and Choquette, P.W., eds., Carbonate petroleum reservoirs: Springer-Verlag, New York, p. 470-484.

Chao G., Lambert G., and Cumming H. [2009] Analysis of intrinsic uncertainties of petro-elastic models using simulated annealing. *71th EAGE Conference and Exhibition*, Expanded Abstracts, Z003.

Chapin M., Terwogt D., and Ketting J. [2000] From seismic to simulation using new voxel body and geologic modeling techniques, Schiehallion Field, West of Shetlands. *The Leading Edge*. 408-412.

Chen Y., and Oliver D. [2013] Levenberg-Marquardt forms of the iterative ensemble smoother for efficient history matching and uncertainty quantification. *Comput. Geosci.*, **17** (4), 689-703.

Chen Y., and Oliver D. [2014] History matching of the Norne full-field model with an iterative ensemble smoother. *SPE Reservoir Evaluation & Engineering*. 244-256.

Coléou T., Allo F., Bornard R., Hamman J., and Caldwell D. [2005] Petrophysical Seismic Inversion. *SEG Annual Meeting*.

Connolly P. [2007] A simple, robust algorithm for seismic net pay estimation. *The Leading Edge*, **26**, 1278-1282.

Cui Q., Hoffman T., and Davis T. L. [2013] Quantitative time-lapse seismic integrated history match in Delhi Field. SPE 165364. *SPE Western Regional and AAPG Pacific Section Meeting*. Monterey, California, USA.

Dadashpour M., Landrø M and Kleppe J. [2007] Porosity and permeability estimation by gradient-based history matching using time-lapse seismic data. SPE 104519. *15th SPE Middle East Oil & Gas Show and Conference*. Bahrain, Kingdom of Bahrain.

Davolio A., Maschio C., Schiozer D. J. [2011] Incorporating 4D seismic attributes into history matching process through an inversion scheme. SPE 142946. *SPE EUROPEC/EAGE Annual Conference and Exhibition*. Vienna, Austria.

De Brito. D., de Moraes R., and Emerick A. [2010] The Marlim Field: incorporating time-lapse seismic in the assisted history matching.

De Paula O. B., Pervukhina M., and Gurevich B. [2010] Testing Gassmann fluid substitution in carbonates: sonic log versus ultrasonic core measurements. *SEG Annual Meeting. Denver*, Colorado, USA.

Dejtrakulwong P., and Mavko G. [2011] Fluid substitution for laminated sand-shale sequences. *81st SEG Meeting*. Expanded Abstracts, 2183-2187.

Dong Y., and Oliver D. [2005] Quantitative use of 4D seismic data for reservoir description. March 2005 *SPE Journal*, 91-99.

Dong Y., and Oliver D. [2008] Reservoir simulation model updates via automatic history matching with integration of seismic impedance change and production data. IPTC 12550. *International Petroleum Technology Conference*.

Domenico S. N. [1974] Effect of water saturation on seismic reflectivity of sand reservoirs encased in shale. *Geophysics*, **39**, 759-769.

Dvorkin J., and Gutierrez M. A. [2002] Grain sorting, porosity and elasticity. *Petrophysics*, **43**, 185-196.

Dvorkin J., Mavko G., and Gurevich B. [2007] Fluid substitution in shaley sediment using effective porosity. *Geophysics*, **72**(3), O1-O8.

Dvorkin J., and Nur A. [1998] Acoustic signatures of patchy saturation. *International Journal of Solids Structures*, **35** (34-35), 1363-1370

Eberhart-Phillips D., Han D. H. and Zoback M. D. [1989] Empirical relationships among seismic velocity, effective pressure, porosity and clay content in sandstone. *Geophysics*, **54**, 82-89

Eberli G. P., Baechle G. T., Anselmetti F. S., Incze M. L. [2003] Factors controlling elastic properties in carbonate sediments and rocks. *The Leading Edge*, **22**, 654-660.

Eiken O., and Tøndel R. [2005] Sensitivity of time-lapse seismic data to pore pressure changes, is quantification possible? *The Leading Edge*, **24**, 1250-1254.

Elde R. M., Haaland A. N., Ro H. E., Ystad B., and Zachariassen E. [2000] Troll West – Reservoir monitoring by 4D seismic. *SPE European Petroleum Conference*. Paris, France.

Emerick A., de Moraes R. J., and Pereira Rodrigues J. R. [2007] History Matching 4D seismic data with efficient gradient based methods. SPE 107179. *SPE EUROPEC/EAGE Annual Conference and Exhibition*. London, UK.

Emerick A., and Reynolds A. C. [2013] History-matching production and seismic data in a real field case using the ensemble smoother with multiple data assimilation. SPE 163675. *SPE Reservoir Simulation Symposium*. The Woodlands, Texas USA.

Escobar I., Recordon M., and Williamson P [2006] Global Petro-Elastic Model (gPEM). *68th EAGE Conference and Exhibition*, Extended Abstracts, A023.

Fagervik K., Lygren M., Valen T.S., Hetlelid A., Berge G. V., and Sønneland L. [2001] A method for performing History Matching of reservoir flow models using 4D seismic. *SEG Exposition and Annual meeting*. San Antonio, Texas, USA.

Fahimuddin A., Aanonsen S. I. and Skjervheim J. A. [2010] Ensemble based 4D Seismic History Matching: Integration of different levels and types of seismic data. SPE 131453. *SPE EUROPEC/EAGE Annual Conference and Exhibition*. Barcelona, Spain.

Falcone G., Gosselin O., Marrauld J., and Zhakupov M. [2004] Petroelastic modelling as key element of 4D History Matching: A field example. SPE 90466. *SPE Annual Technical Conference and Exhibition*. Houston, USA.

Fanchi J. R. [1999] Predicting 4D seismic performance using an integrated flow model. SPE 56517. *SPE Annual Technical Conference and Exhibition*. Houston, Texas, USA.

Fanchi J. R. [2006] Principles of applied reservoir simulation. Third Edition, Elsevier-Gulf Professional Publishing, Boston.

Fanchi, J.R., T.A. Pagano and T.L. Davis [1999] State-of the-Art of 4D Seismic Monitoring. *Oil & Gas Journal*, in press (May 30).

Floricich M. [2006] An engineering-consistent approach for pressure and saturation estimation from time-lapse seismic data. *PhD Thesis*. Heriot Watt Univeristy.

Floricich M., MacBeth C., Stammeijer J., Staples R., Evans A. & Dijksman C. [2006] A New Technique for Pressure-Saturation Separation from Time-Lapse Seismic-Schiehallion Case Study. *68th EAGE Conference and Exhibition incorporating SPE EUROPEC*, Vienna, Austria.

Freund D., [1992] Ultrasonic compressional and shear velocities in dry clastic rocks as a function of porosity, clay content and confining pressure. *Geophysical Journal International*, **108**, 125-135.

Fursov I. [2015] Quantitative application of 4D seismic data for updating thin-reservoir models. *PhD Thesis*. Heriot Watt University.

Fürre A-K., Andersen M., Smalø Moen A., and Tønnessen R. K. [2009] Deriving effects of pressure depletion on elastic framework moduli from sonic logs. *Geophysical Prospecting*. **57** (3), 427-437.

Gassmann F. [1951] Elastic waves through a packing of spheres. *Geophysics*, **16** (4), 673 - 685

Geertsma J., and Smit D. C. [1961] Some aspects of elastic wave propagation in fluid-saturated porous solids. *Geophysics*, **26**, 169-181.

Gervais V., Roggero F., Feraille M., Le Ravalec M. and Seiler A. [2010] Joint history matching of production and 4D-seismic related data for a North Sea Field case. SPE 135116. *SPE Annual Technical Conference and Exhibition*. Florence, Italy.

Gommesen L., Fabricius I. L., Mukerlu T., and Pedersen J.M. [2007] Elastic behaviour of North Sea Chalk: A well-log study. *Geophysical Prospecting*. **55**(3), 307-322.

Gurevich B. [2004] A simple derivation of the effective stress coefficient for seismic velocities in porous rocks. *Geophysics*, **69**, 393-397.

Gurevich B., and Carcione J. M. [2000] Gassmann modeling of acoustic properties of sand/clay mixtures. Pure and Applied Geophysics, **57**, 811 – 827.

Gosselin O., van den Berg S., and Cominelli A. [2001] Integrated History-Matching of production and 4D Seismic Data. SPE 71599. *SPE Annual Technical Conference and Exhibition*. New Orleans, Lousiana, USA.

Gosselin O. Aanonsen S.I., Aavastmark I., Cominelli A., Gonard R., Kolasinski M., Ferdinandi F., Kovacic L., and Neylon K. [2003] History matching using Time-lapse Seismic (HUTS). SPE 84464. *SPE Annual Technical Conference and Exhibition*. Denver, Colorado, USA. DOI: 10.2118/84464-MS.

HajNasser Y. [2012] The implications of shale geomechanics and pressure diffusion for 4D interpretation. *PhD Thesis*. Heriot Watt University.

Hall J., and Alvarez E. [2014] Petrophysics for rock physics: what really matters at seismic scale? *SPWLA 55th Annual Logging Symposium*.

Han D-H., and Batzle M. [2000a] Velocity, density and modulus of hydrocarbon fluids – data measurement. *SEG Annual Meeting*. Extended Abstract. RPB 7.2.

Han D-H., and Batzle M. [2000b] Velocity, density and modulus of hydrocarbon fluids – empirical modeling. *SEG Annual Meeting*. Extended Abstract. RPB 7.3.

Han D-H., and Batzle M. [2004] Gassmann's equation and fluid-saturation effects on seismic velocities. *Geophysics*, **69** (2), 398-405.

Hashin Z., and Shtrikman S. [1963] A variational approach to the elastic behavior of multiphase materials. *J. Mech. Phys. Solids*, **11**, 127-140.

Hatchell P., Helly S., Muerz M., Jones T., Engbers P., van der Veeken J., and Staples R. [2002] Comparing time-lapse seismic and reservoir model predictions in producing oil and gas fields. *64th EAGE Conference and Exhibition*. Florence, Italy.

Haverl M. C., Aga M., and Reiso E. [2005] Integrated workflow for quantitative use of time-lapse seismic data in History Matching: A North Sea field case. SPE 94453. *SPE EUROPEC/EAGE Annual Conference and Exhibition.* Madrid, Spain.

Hill R. [1952] The elastic behavior of crystalline aggregate. *Proc. Phys. Soc.*, London A, **65**, 349 -354.

Hossain Z., Mukerji T., Dvorkin J., and Fabricius I. L. [2011] Rock physics model of glauconitic greensand from the North Sea. *Geophysics*, **76** (6), E199-E209.

Jack I., Barkved O., and Kommedal J. [2010] The life-of-field seismic system at Valhall, Norwegian Sea. Chapter, **6**, 483-625.

Jakobsen M., Johanesen T. A., and McCann C. [2003b] The acoustic signature of fluid flow in a complex porous media. *Applied Geophysics*, **54**, 219-246.

Japsen P., Høier C., Rasmussen K. L., Fabricius I., Mavko G., and Pedersen J. M. [2002] Effect of fluid substitution on ultrasonic velocities on chalk plugs, South Arne field, North Sea. *72nd Annual International Meeting, SEG*. Expanded Abstract, **21**, 1881-1884.

Johnston D. H. [2013] Practical applications of Time-lapse seismic data. Distinguished Instructor Series. Society of Exploration Geophysicist.

Jones S. M. [1995] Velocities and quality factors of sedimentary rocks at low and high effective pressures. *Geophysical Journal International*, **123**, 774-780.

Katahara K. [2004] Fluid substitution in laminated shaly sands. *74th SEG meeting*. Expanded Abstracts, 1718-1721.

Keys R., and Xu S. [2002] An approximation for the Xu-White velocity model. *Geophysics*, **67**(5), 1406-1414

Khaksar A., Griffiths C. M., and McCann C. [199] Compressional- and shear-wave velocities as a function of confining stress in dry sandstones. *Geophysical Prospecting*, **47**(4), 487-508.

Khazanehdari J., Curtis T., and Yi T. [2005] Combined seismic and production history matching. SPE 97100. *SPE Annual Technical Conference and Exhibition*. Dallas, Texas, USA.

Kittridge M., Taylor T. R., Braunsdorf N. R., Hathon L. A., and Taras Bryndzia L. [2004] Seismic Petrophysics for clean sandstones: integrated interrogation of lab- and well-based data for improved rock physics modeling. *SEG Annual Meeting*. Denver, Colorado, USA.

Kjelstadli R. M., Lane H. S., Johnson D. T., Barkved O. I., Buer K., and Kristiansen T.G. [2005] Quantitative History Match of 4D seismic response and production data in the Valhall Field. SPE 96317. *SPE Offshore Europe*. Aberdeen, Scotland.

Krief M., Garat J., Stellingwerff J. and Ventre J. [1990] A petrophysical interpretation using the velocities of P and S waves (full-waveform sonic). *Log Analyst*, **31**, 355-369.

Landa J., and Kumar D. [2011] Joint inversion of 4D seismic and production data. SPE 146771. *SPE Annual Technical Conference and Exhibition*. Denver, Colorado, USA.

Landrø M., Solheim O. A., Holde E., Ekren B. O., and Strønen L. K. [1999] The Gullfaks 4D seismic study. *Petroleum Geoscience*, **5**, 213-226.

Landrø M. [2001] Discrimination between pressure and fluid saturation changes from time-lapse seismic data. *Geophysics*, **66**, 836-844.

Landrø M. [2015] 4D Seismic. *In:* Bjørlykke K. (ed.) Petroleum Geoscience: From Sedimentary Environments to Rock Physics. Berlin, Heidelberg: Springer Berlin Heidelberg.

Leach, H. M., Herbert N., Los A., and Smith R. L. [1999] The Schiehallion development, *in* A. J. Fleet and S. A. R. Boldy, Petroleum geology of northwest Europe: Proceedings of the 5th Conference, 683–692.

Lee M.W. [2005] Proposed moduli of dry rock and their application to prediction elastic velocities of sandstones. U.S Geological Survey Scientific Investigations Report 2005-5119.

Lerat O., Adjemian F., Baroni A., Etienne G., Renard G., Bathellier E., Forgues E., Aubin F., and Euzen T. [2010] Modelling of 4D seismic data for the monitoring of steam chamber growth during the SAGD process. *Journal of Canadian Petroleum Technology*. **49** (6), 21-29.

Little A. J., Jutila H. A., and Fincham A. [2006] History matching with production uncertainty eases transition into prediction. SPE 100206. *SPE EUROPEC/EAGE Annual Conference and Exhibition*. Vienna, Austria.

Lumley D. E. and Behrens R. A. [1998] Practical issues of 4D seismic reservoir monitoring: What an engineer needs to know. *SPE Reservoir Evaluation and Engineering* **1**, 528-538

Luo X., Bhakta T., Jakobsen M., and Naevdal G. [2016] An ensemble 4D seismic history matching framework with wavelet multiresolution analysis – A 3D Benchmark case study. *ECMOR XV – 15th European Conference on the Mathematics of Oil Recovery*. Mo P076.

Lygren M., Husby O., Osdal B., El Ouair Y., and Springer M. [2005] History matching using 4D seismic and pressure data on the Norne Field. *67th EAGE Conference and Exhibition*, Extended Abstracts, We G102 10.

MacBeth C. [2004] A classification for the pressure-sensitivity properties of a sandstone rock frame. *Geophysics*. **69**, 497–510.

MacBeth C., and Schuett H. [2007] The stress dependent elastic properties of thermally induced microfractures in Aeolian Rotliegend sandstone. *Geophysical Prospecting*, **55**, 323-332.

MacBeth C., and Stephen K. D. [2008] Seismic scale saturation relations in turbidites undergoing water flood.

Machado A. F. [2009] Quantitative analysis of pressure and saturation maps into the history matching. Dissertation. State University of Campinas, Brazil.

Martin K., and Macdonald C. [2010] The Schiehallion Field: applying a geobody modeling approach to piece together a complex turbidite field. *DEVEX Conference*.

Mavko G., Mukerji T., Dvorkin J. [2009] The Rock Physics Handbook: Tools for Seismic Analysis of Porous Media Cambridge University Press

Menezes C., and Gosselin O. [2006] From logs scale to reservoir scale: upscaling of the petroelastic model. SPE 100233. *SPE EUROPEC/EAGE Annual Conference and Exhibition.* Vienna, Austria.

Mezghani M., Fornel A., Langlais V., and Lucet N. [2004] History Matching and quantitative use of 4D seismic data for an improved reservoir characterization. SPE 90420. *SPE Annual Technical Conference and Exhibition*. Houston, Texas, USA.

Mindlin R. D. [1949] Compliance of elastic bodies in contact. J. Appl. Mech., 16, 259-268.

Moyano B., Spikes K. T., Johansen T. A., and Mondol N. H. [2012] Modeling compaction effects on the elastic properties of clay-water composites. Geophysics, 77 (5), D171 –D183.

Ness O. M., Holt R. M., and Fjaer M. [2000] The reliability of core data as input to seismic reservoir monitoring studies. SPE 65180

Nur A., Mavko G., Dvorkin J. and Galmundi D. [1998] Critical porosity: A key to relating physical properties to porosity in rocks. *The Leading Edge*, **17**, 357-362.

Obidegwu D. [2016] Seismic History Matching using binary images. *PhD thesis*. Heriot Watt University.

Omofoma V., and MacBeth C. [2015] Intra-survey pressure variations – implications for 4D seismic interpretation. *77th EAGE Conference and Exhibition.*

Osdal B., and Alsos T. [2002] Seismic modelling of Eclipse simulations and comparison with real 4D data at the Norne Field. *64th EAGE Conference and Exhibition*.

Ouair, Y. E. I., Lygren M., Osdal B., Husby O., and Springer M. [2005] integrated reservoir management approach: from time-lapse acquisition to reservoir model update at the Norne field. IPTC 10894. *International Petroleum Technology Conference*.

Pagano T. A., Fanchi J. R. and Davis T. L. [2000] Integrated Flow Modeling: The Fusion of Geophysics and Reservoir Engineering. *SPE Annual Technical Conference and Exhibition*. Dallas, Texas, USA.

Palke M. R., Palmet B. A., and Rietz D. C. [2012] A novel simulation model review process. SPE 159274. *SPE Annual Technical Conference and Exhibition*. San Antonio, Texas, USA.

Pannett S., Slager S., Stone G. and Dekker S. [2004] Constraining a Complex Gas-Water Dynamic Model Using 4D Seismic. *SPE Annual Technical Conference and Exhibition.* Houston, Texas, USA.

Pride S. R. [2005] Relationships between seismic and hydrological properties. In Rubin Y. and Hubbard S. S. *Hydrogeophysics*. Springer, 217 – 255.

Ramamorrthy R., Murphy W. F., Coll C. [1995] Total porosity estimation in shaly sands from shear modulus. *SPWLA 36th Annual Logging Symposium.*

Rangel R. E. [2016] The impact of shale pressure diffusion on 4D seismic interpretation. *PhD Thesis*. Heriot Watt University.

Rasolofosaon P. N. J., and Zinszer B. [2012] Experimental verification of the petroelastic model in the laboratory – Fluid substitution and pressure effects. *Oil & Gas Science and Technology – Rev. IFP Enegies nouvelles*, **67** (2). 303-318.

Raymer L. L., Hunt E. R., and Gardner J.S. [1980] An improved sonic transit time-to-porosity transform. *21st Annual Logging Symposium*.

Roggero F., Ding D.Y., Berthet P., Lerat O., and Schreiber P.E. [2007] Matching of Production History and 4D Seismic Data – Application to the Girassol Field, Offshore Angola. SPE 109929. *SPE Annual Technical Conference and Exhibition*. Anaheim, California, USA. DOI: 10.2118/109929-MS.

Santos J. [2017] Semi-quantitative 4D seismic interpretation integrated with reservoir simulation: application to the Norne field. *Master Thesis*. State University of Campinas, Brazil.

Schön J. H. [2015] Physical properties of rocks. Fundamentals and Principles of Petrophysics. Volume 65. Second Edition.

Sedighi F., and Stephen K. D. [2009] Faster convergence in Seismic History Matching by efficient parameter searching. SPE 12210. *SPE EUROPEC/EAGE Annual Conference and Exhibition.* Amsterdam, Netherlands.

Shapiro S. A., and Troyan V. N. [2002] Stress dependences of seismic velocities in porous and fractured rocks. *64th EAGE Conference and Exhibition*.

Simm R. [2007] Practical Gassmann fluid substitution in sand/shale sequences. *First Break*, **25**, 61-68.

Skelt C. [2004] Fluid substitution in laminated sands. *The Leading Edge*, **23**, 485-488.

Skjervheim J.A., Evensen G., Aanonsen S.I., Ruud B. O., and Johansen T.A. [2007] Incorporating 4D seismic data in reservoir simulation models using Ensemble Kalman filter. SPE 95789. September 2007 SPE Journal. 282-292.

Smith T. M. [2011] Practical seismic petrophysics: The effective use of log data for seismic analysis. *The Leading Edge*, **30**, 1128-1141.

Smith T. M., Sondergeld C. H., and Rai C. S. [2003] Gassmann fluid substitutions: A tutorial. *Geophysics*, **68**, 430-440.

Souza R. M., Machado A. F., and Schiozer D. J. [2010] Iterative history matching technique for estimating reservoir parameters from seismic data. SPE 131617. *SPE EUROPEC/EAGE Annual Conference and Exhibition.* Barcelona, Spain.

Souza R. M., Santos M. S., and Schiozer D. J. [2011] Petro-Elastic parameters effects on history matching procedures. SPE 143384. *SPE EUROPEC/EAGE Annual Conference and Exhibition.* Vienna, Austria.

Souza R. M., Munerato F. P., and Schiozer D. J. [2011] Quantitative integration of time-lapse seismic derived information in a history matching procedure. SPE 143009. *SPE EUROPEC/EAGE Annual Conference and Exhibition*. Vienna, Austria.

Stammeijer J. G. F., Hatchell P. J. [2014] Standards in 4D feasibility and interpretation. *The Leading Edge*, **33** (2), 134-140.

Statoil. [2001c] PL128-Norne Field Reservoir Management Plan.

Stephen K. D., Soldo J., MacBeth C., and Christie M. A. [2005]. Multiple model seismic and production history matching: a case study. *14th Eurpec Biennial Conference*. Madrid, Spain.

Stephen K. D., and MacBeth C. [2006] Inverting for the petro-elastic model via seismic history matching. *SEG Annual Meeting*. New Orleans, USA.

Stephen K. D., Shams A., and MacBeth C. [2007] Faster seismic history matching in UKCS reservoir. SPE 107147. *SPE Europec/EAGE Annual Conference and Exhibiton.* London, UK.

Tian S. [2014] Closing the look by engineering consistent 4D seismic to simulator inversion. *PhD Thesis*. Heriot Watt University.

Tolstukhin E., Lyngnes B., and Sudan H. H. [2012] Ekofisk 4D seismic – Seismic History Matching workflow. SPE 154347. *EAGE Annual Conference and Exhibition incorporating SPE Europec*. Copenhagen, Denmark.

Trani M., Arts R., and Leeuwenburgh O. [2011] Estimation of changes in saturation and pressure from 4D seismic AVO and time-shift analysis. *Geophysics*, **76**, 1-17.

Trani M., Arts R.J. and Leeuwenburgh O. [2012] Seismic History Matching of Fluid Fronts Using the Ensemble Kalman Filter. SPE-163043. SPE Journal, **18** (1), 159-171

Trani M., Wojnar K., Moncorge A., and Philippe B. [2017] Ensemble-based assited history matching using 4D seismic fluid front parameterization. SPE 183901-MS. *SPE Middle East Oil & Gas Show and Conference*. Manama, Kingdom of Bahrain

Tura A., Hanitzsch C., and Calandra H. [1998] 3D AVO migration/inversion of field data. The Leading Edge, 17, 1578-1583

Vernik L., and Hamman J. [2009] Stress sensitivity of sandstones and 4D applications. *The Leading Edge*. **28** (1), 90-03.

van Gestel J.P., Best K. D., Barkved O. I. and Kommedal J. H. [2011] Integration of the life of field seismic data with the reservoir model at the Vallhall Field. *Geophysical Prospecting*, **59**, 673-681.

Verlo S. B., Hetland M. [2008] Development of a field case with real production and 4D data from the Norne Field as a benchmark case for future reservoir simulation model testing. Master Thesis. Norwegian University of Science and Technology.

Vernik L., and Hamman J. [2009] Stress sensitivity of sandstones and 4D applications. *The Leading Edge*, **28**, 90-93.

Vidal S. [2000] Integrating geomechanics and geophysics for reservoir seismic monitoring feasibility studies. SPE 65157. SPE Annual Technical Conference and Exhibition.

Waal D. H., and Calvert R. [2003] Overview of global 4D seismic implementation strategy. *Petroleum Geoscience*, **9**, 1-6.

Waggoner J. [1998a] Lessons learned from 4D projects. SPE 49144. *SPE Annual Technical Conference and Exhibition.* New Orleans, Louisiana, USA.

Waggoner J., Cominelli A., and Seymour R. [2002] Improved reservoir modelling with time-lapse seismic in a Gulf of Mexico gas condensate reservoir. SPE 77956. *SPE Asia Pacific Oil and Gas Conference and Exhibition*. Melbourne, Australia.

Walker, G., Allan, P., Trythall, R., Parr, R., Marsh, M., Kjelstadli, R., Barkved, O., Johnson, D. and Lane, S. [2006] Three case studies of progress in quantitative seismic-engineering integration. *The Leading Edge*, **25** (9), 1161-1166.

Walls J., Dvorkin J., and Smith B.A. [1998] Modeling seismic velocity in Ekofisk Chalk. *68th SEG Meeting*. Expanded Abstract.

Wang Z. [1997 Seismic properties of carbonate rocks. Carbonate seismology, Ed. Palaz I., Marfurt K. J., *Geophysical Developments*, **6**, 29-52.

Wang Z., and Nur A. [1989] Seismic and Acoustic Velocities in Reservoir Rocks, Volume 2, Theoretical and Model Studies. *SEG Geophysics reprint series*, **10**, 457.

Whitcombe D. N., Connoly P., Reagan R., and Redshaw T. [2002] Extended elastic impedance for fluid and lithology prediction. *Geophysics*, **67**, 63-67.

Wiggins, M. L., Startzman R. A. [1990] An approach to reservoir management. SPE 20747.

Wu T. T. [1966] The effect of inclusion shape on the elastic moduli of a two-phase material. *Int. J. Solids Structures*, **2**, 1-8.

Xu S., Chen G., Zhu Y., Zhang J., Payne M.A., Deffenbaugh M., Song L., and Dunsmuir J. [2007] Carbonate Rock Physics: Analytical Models and Validations Using Computational Approaches and Log/Lab Measurements: IPTC-112-8-PP.

Xu S., and White R. E. [1995] A new velocity model for clay-sand mixtures. *Geophysical Prospecting*, **43**, 91-118.